

Optical metasurfaces: synthesis, nanofabrication, and colorful applications

Présentée le 15 décembre 2022

Faculté des sciences et techniques de l'ingénieur
Laboratoire de nanophotonique et métrologie
Programme doctoral en photonique

pour l'obtention du grade de Docteur ès Sciences

par

Hsiang-Chu WANG

Acceptée sur proposition du jury

Prof. C. Moser, président du jury
Prof. O. Martin, directeur de thèse
Prof. D. P. Tsai, rapporteur
Dr G. Quaranta, rapporteur
Prof. R. Houdré, rapporteur

Acknowledgements

This incredible journey started with my involvement in Prof. Din Ping Tsai's PNSTL group in 2015. At that time, there were many distinguished researchers (Cheng Hong Chu, Ming Lun Tseng, Pin Chieh Wu, Yao Wei Hung, Hui Hsin Hsiao, Hui Jun Wu, Wei Yi Tsai, and so on, just to name a few) studying and investigating the plasmonic applications. I was working on a project regarding optical storage, which was considered a sunset industry. However, the more I investigated, the more potential I found in optical storage due to its low energy consumption for big data. It was after a project associated with metasurfaces (ultrathin planar cavity metasurfaces) that the idea of utilizing meta-atoms hatched in my mind. Thanks to Dr. Cheng Hong Chu, Pin Chieh Wu, Yao Wei Hung, Hui Hsin Hsiao, Yi-Chieh Lai, Jia-Wern Chen and Hui Jun Wu's assistance in the lab. It was a great time for me to research and explore phenomena at the nano scale. Within two years, I attended five international conferences (The 9th International Conference on Nanophotonics ICNP2016, the European Phase Change and Ovonic Symposium EPCOS2016, International Symposium on Optical Memory ISOM2016, The Asia-Pacific Conference on Near-field Optics APNFO2017, and the 8th International Conference on Surface Plasmon Photonics SPP8) and many talks, which helped broaden my horizons in nanophotonics and optics-related applications.

I still remember and appreciate the interview that I had with Prof. Olivier Martin in SPP8. It was a very pleasant occasion to interact and discuss with him and his colleagues (Debdatta Ray and Kuang-Yu Yang), who encouraged me to apply to this PhD program without hesitation. Fortunately, soon I was able to join Prof. Olivier Martin's Nanophotonics and Metrology Laboratory (NAM) in the same year, September 2017, with Prof. Din Ping Tsai, Prof. Snow Tseng, and Prof. Jong-Ching Wu's recommendation letters. In this year, there were many excellent researchers, including Christian Santschi, Toralf Scharf, Kuang-Yu Yang, Chen Yan, Xiaolong Wang, Madasamy Thangamuthu, Jérémy Butet, Gabriel David Bernasconi, Raziman Thottungal, Giorgio Quaranta, and so on.). They helped me a lot in all aspects of life and work, which allowed me to fit into the group and environment without any gap. The only problem is that there are only 24 hours a day. By the end of the first year, I was able to complete a study from an idea to a scientific report thanks to the solid training in Prof. Tsai's lab. In the following years, I spent most of my time communicating, brainstorming and polishing scientific writing skills, which established the bases for the research in the following years, such as "Optical force control using phase-gradient metasurfaces" with Karim Achouri, "Precise Capillary-Assisted Nanoparticle Assembly in Reusable Templates" with Henry S.C. Yu, "A Low-Temperature Annealing Method for Alloy Nanostructures and Metasurfaces: Unlocking a Novel Degree of Freedom" with Debdatta Ray, "Generative Adversarial Network Deep Learning for the inverse design of geometry-dependent plasmonic structural colors" with André-Pierre Blanchard-Dionne, just to name a few. Due to my curiosity and enthusiasm for research, and the surprising discoveries and productive discussions with Prof. Olivier Martin, studies such as "Pitfalls in the Spectral Measurements of Polarization-Altering Metasurfaces", "Metasurfaces Robustness Analysis: Perfect Structures are not always the Best", "Facile Design, Optical Characterization, and Performance of Metaholograms", and "Polarization-controlled chromo-encryption" were born.. There are still many ongoing projects not mentioned, I believe soon we will disclose the interesting findings in scientific journals.

Apart from Prof. Olivier Martin's support and supervision in research, the staff in CMi (Zdenek Benes, Rémy Juttin, Joffrey Pernollet, Guy-François Clerc, Philippe Langlet, Adrien Toros, and so on) and CMi friends (Yuji Takabayashi, Hamed Sattari, Dorian Herle, Marie Noël, Luca Nela, Silvia Demuru, Riyaz, Riyaz Mohammed Abdul Khadar, Taifang Wang, Ming Hua Chu) from different labs offered professional and empirical knowledge in fabrication, allowing me to fabricate sample smoothly. Friends of different backgrounds in the Photonics Chapter (Jan Krizek, Tania Palmer, Eirini Kakkava, Marie Bischoff, Jorge Madrid, Chiara Bonati, Pan Giulia, and so on.), Polydoc (don't remember their names), and Taiwanese Student Association (too many to list) made my PhD life colorful. Most of all, there were also good memories with my colleagues (Beatrice Raball, Cathy Buchs, Karim Achouri, Debdatta Ray, Maryam Yousefi, Sebastian Mader, Dong Cheon Kim, Jeonghyeon Kim, Marco Riccardi, Mintae Chung, Andrei Kiselev) and Quiz friends (Aleksa Djorovic, Juan Pablo Madrigal Cianci, Aurelian John-Herpin, Gabriele Bongiovanni, Valentina Paggi, Carlotta Gastaldi, Danica Milovanovic, and so on). In Switzerland, there are many interesting people (Alan Wu, Song-Lin Chan, Jeff Deng, Zhe-Xiu Andai, Branford Lu, Amanda Zhang, Henry S.C. Yu, Che Yang, Yi-Ru Yu, Venessa Chiu, Chin-Lin Chen, Sophia Hsieh, Chia-Jung Yang, just to name a few.) and my Swiss neighbor Stéphane. In the end, I would like to thank my family,

my wife, and friends far away in Taiwan for their emotional support. I believe this incredible journey in nanophotonics will never end and I look forward to further contributing to and exploring the field of optics.

Abstract

With the advance and progress of fabrication techniques in recent decades, researchers are able to reproduce artificial nanostructures, or meta-atoms, beyond the diffraction limit to manipulate the intrinsic properties of light, especially in the visible regimes. Hence, a diversity of proof-of-concept applications are demonstrated successfully in various fields for near-field enhancement, wavefront manipulation, and polarization conversion. These demonstrations used to be achieved with bulky materials, but nowadays they can be accomplished by two-dimensional thin flat structures, or metasurfaces, composed of a layer of meta-atoms, which are similar to molecules built from atoms. Therefore, it is fundamental but important to analyze the optical properties of meta-atoms for further applications.

In this thesis, we mainly utilize silver to construct the meta-atoms. Although suffering from easily oxidized, its excellent lossless property throughout the visible range makes it suitable for study. When preserved properly, silver-made metasurfaces can stay stable. To explore other potential materials for plasmonics, a cost-effective approach to fabricating gold and silver alloy is developed. Metalens and metaholograms are demonstrated as an example. Such alloy combines the stability of gold and the lossless property of silver. This low-temperature annealing approach can also apply to gold and palladium alloy when optimized.

In Chapter 2, approaches to study the subwavelength scaled meta-atoms are presented. We initially rely on numerical electromagnetics to obtain the reflectance and phase shift of a meta-atom. The meta-atoms are thus fabricated according to the design in simulation, and validate the optical responses with measurement. Because polarized light is applied in simulation, the measurement environment is reproduced by adding polarizers and analyzers in illumination and detection paths. This concept seems straightforward and easy, however, the chiral property of a structure and optical responses of elements can lead to unphysical results if not carefully considered, as presented in the last section. With many verified simulated spectra, we are confident in the observations in the simulations.

In Chapter 3, applications of metasurfaces in wavefront manipulation are demonstrated. With the increasing demands for flat optics make the proof-of-concept demonstrations step forward in mass production in the industry. Fabricating dimension-sensitive meta-atoms becomes challenging as a result of many complicated factors during fabrication. It takes much time to optimize the fabrication process to produce perfect structures as simulated. We found that perfect structures do not always guarantee the best, which relieves the restrictions in fabrication.

In Chapter 4, the cause of the spectrum from structural colors is investigated. With the understanding of our measurement setup and numerical simulations, we are able to analyze these polarization-dependent structures exhibiting different spectra. Those commonly used geometries of meta-atoms are sensitive to the polarized and exhibit polarization-induced chirality, leading to very diverse responses. We propose to utilize this property for optical encryption, which can easily support a quaternary coding system. At the end of this Chapter, the primary results of an ongoing project are presented, where we combine these polarization-sensitive meta-atoms and artificial intelligence for structural designs in encryption applications.

In Chapter 5, strong near-field enhancement of plasmonics is applied to increase the yield of luminescence. Rare-earth ion doped upconversion nanoparticles (NaYF_4 : Yb^{3+} , Er^{3+}) serve as matters on a platform of double resonance antennas. We utilize the optical properties of the plasmonic antennas to tailor the channels, leading to selectively enhance of the frequency upconversion process. This light and matter interaction can be applied in luminescence.

These theory-supported studies are simulated and demonstrated experimentally, displaying their abilities and facilities to harness the visible light. We believe this thesis can shed some light and offers inspiration in the field of flat optics.

Keywords: plasmonics, meta-atoms, metasurfaces, optical antenna, wavefront manipulation, spectral manipulation, structural colors, beamsteering, robustness, nanofabrication, polarization, alloy, near-field enhancement, frequency upconversion, metaholograms, phase modulation, optical encryption, chromo-encryption.

Résumé

Grâce aux progrès réalisés ces dernières décennies dans les techniques de nanofabrication, il est maintenant possible de fabriquer des nanostructures – des méta-atomes dans le contexte de cette thèse – avec des tailles plus petites que la limite de diffraction. Ces nanostructures permettent de manipuler les propriétés de la lumière sur l'entier du spectre visible et différentes applications ont été démontrées dans des domaines aussi variés que la déformation du front d'onde, l'exaltation du champ proche et la manipulation de la polarisation. Dans le passé, ces différentes fonctions étaient réalisées avec des composants optiques gros et encombrants; aujourd'hui, elles peuvent être réalisées avec de fines surfaces optiques, des métasurfaces, composées de couches de méta-atomes dont les propriétés déterminent la réponse optique du système.

Dans cette thèse, nous utilisons essentiellement l'argent pour construire des méta-atomes. Bien que ce métal souffre d'une propension à s'oxyder facilement, sa très faible absorption sur l'entier du spectre visible permet de réaliser des métasurfaces très performantes. Au-delà de l'argent, une méthode économique pour la fabrication de nanostructures en alliages d'or et d'argent est aussi développée et utilisée pour fabriquer des méta-lentilles et des méta-hologrammes. Ces alliages combinent la stabilité chimique de l'or avec les faibles pertes de l'argent et cette approche est aussi utilisée pour réaliser des alliages d'or et de palladium.

Le Chapitre 2 présente différentes études de méta-atomes de taille plus petite que la longueur d'onde. Des simulations numériques permettent de calculer le réflectance et le déphasage des méta-atomes qui sont ensuite fabriqués selon ces calculs et validés expérimentalement. Comme les simulations sont réalisées avec une polarisation spécifique, des polariseurs et analyseurs sont aussi inclus dans les mesures expérimentales. Bien que de telles mesures semblent triviales, il s'avère que les propriétés chirales des structures les plus simples peuvent produire des résultats non-physiques si on ne tient pas compte de la réponse de tous les éléments optiques se trouvant dans le microscope. Une comparaison détaillée entre expériences et simulations permet de valider ces résultats et démontre une méthode solide pour l'analyse des métasurfaces.

Le Chapitre 3 traite d'applications des métasurfaces pour la manipulation du front d'onde. La demande croissante pour des optiques planaires nécessite des démonstrateurs comme prérequis pour une implémentation industrielle. La fabrication de méta-atomes dont les dimensions sont très sensibles représente un véritable challenge, tant différents facteurs durant la nanofabrication peuvent influencer le résultat final. De façon surprenante, nous montrons que des métasurfaces "parfaites", ne produisent pas nécessairement les meilleures performances. Cette observation permet d'alléger les contraintes pour une fabrication industrielle des métasurfaces.

L'origine du spectre pour des couleurs structurelles est étudié en détail dans le chapitre 4. Grâce à la maîtrise acquise précédemment dans la simulation et la mesure des métasurfaces, nous étudions l'effet de la polarisation sur ces différents spectres et l'utilisons pour réaliser une cryptographie optique que nous implémentons dans un système quaternaire. Quelques résultats préliminaires sur l'utilisation de l'intelligence artificielle pour créer la forme de nanostructures qui produisent des couleurs vives sont aussi présentés à la fin du chapitre.

Le dernier chapitre étudie l'exaltation du champ proche produite par des nanostructures plasmoniques pour augmenter la luminescence. Des ions dopés avec des terres rares ($\text{NaYF}_4: \text{Yb}^{3+}, \text{Er}^{3+}$) sont combinés avec un substrat d'antennes doublement résonnants. Les propriétés optiques de ces antennes permettent d'accorder les différents canaux et d'augmenter de façon sélective la conversion ascendante.

Une combinaison de théories, simulations et expériences démontre les capacités des métasurfaces pour manipuler la lumière dans la partie visible du spectre et devrait inspirer d'autres travaux en optique planaire.

Mots-clés: plasmonique, méta-atomes, métasurfaces, antennes optiques, manipulation du front d'onde, manipulation du spectre optique, couleurs physiques, robustesse, nanofabrication, polarisation, alliages, exaltation du champ, conversion ascendante, méta-hologrammes, cryptographie optique, modulation de phase.

Content

Acknowledgements.....	ii
Abstract.....	iv
Résumé.....	v
Content.....	vi
Chapter 1 Introduction.....	1
Chapter 2 Methods.....	3
2.1 Simulation techniques.....	3
2.1.1 Surface integral equations	4
2.1.2 COMSOL multiphysics	5
2.1.3 Semi-analytical model	5
2.2 Nanofabrication.....	7
2.2.1 Materials	7
2.2.2 Substrates.....	10
2.2.3 Fabrication processes.....	12
2.3 Experimental setup.....	17
2.3.1 Optical imaging microscopy	20
2.3.2 Fourier space microscopy	22
2.3.3 Polarization spectral microscopy	28
2.4 Summary	35
Chapter 3 Wavefront manipulation	36
3.1 Introduction	36
3.2 Metalens	36
3.3 Metaholograms	39
3.3.1 Introduction	39
3.3.2 Results and discussion.....	43
3.3.3 Conclusion	46
3.4 Robustness analysis	47
3.4.1 Introduction	47
3.4.2 Results and discussion.....	48
3.4.3 Conclusion	55
3.5 Outlook	55
Chapter 4 Spectral manipulation.....	56
4.1 Introduction	56
4.2 Chromo-encryption.....	56
4.2.1 Introduction	56
4.2.2 Results and discussion.....	59
4.2.3 Conclusion	69
4.3 Machine learning structural color	70

4.3.1	introduction	70
4.3.2	Results and discussion.....	72
4.3.3	Conclusion	73
4.4	Outlook	73
Chapter 5	<i>Near-field enhancement</i>	74
5.1	Introduction	74
5.2	Results and discussion.....	75
5.3	Conclusion	81
Chapter 6	<i>Conclusion and outlook</i>.....	82
Chapter 7	<i>Appendix</i>	84
7.1	Matlab code of Semi-analytical model	84
List of figures	86
List of tables	89
References	90
Curriculum Vitae	102

Chapter 1 Introduction

Early in 1678, Huygens successfully explained the propagation of light with the property of waves. Later in 1818, Fresnel included amplitude and phase to explain the diffraction effect and in 1865, Maxwell published a unified theory showing that electromagnetism and light are closely connected. From then on, Maxwell's equations have been widely applied in all light-wave-related applications. Before the existence of computational electromagnetics, analytical solutions were restricted to simple structures and geometries in a homogeneous medium. However, even with limited tools, many amazing theories based on observations were proposed and demonstrated. Since its advent more than 5 decades ago, the field of computational electromagnetics has provided insights into optical phenomena using full-wave simulations. The realization of these subwavelength structures, however, was not possible until the existence of Electron-beam lithography and related infrastructure. In this thesis, we refer to these subwavelength structures as meta-atoms. The concept of achieving various functionalities with these artificial meta-atoms on surfaces leads to the term metasurfaces, which are different from bulky artificial structures also known as metamaterials. Since the first demonstration of metasurfaces in 2012 [1], which manipulated the propagating direction of light with a layer of plasmonic meta-atoms, a large number of research endeavors have sprung up in the past decade, all focused on manipulating the intrinsic properties of light. These artificial metallic meta-atoms appeared in various forms in different fields for near-field enhancement, wavefront manipulation, polarization conversion, and spectral control.

The pace of research progress in metasurfaces continues to increase thanks to the advances in computational and fabrication techniques. A tremendous number of proof-of-concept metasurface devices have been proposed, first in the microwave regime, and later in the near-infrared and visible regimes. For example, achromatic metalenses operating in the visible regime were realized in 2018 [2]. Metalenses working at shorter wavelengths were developed early this year in 2022 [3]. Metaholograms providing miniaturized analog encryption were proposed in 2013 [4], right after the first metasurface for anomalous reflection was demonstrated. Super density optical storage has now again been revisited [5] and paves the way for metasurfaces applications for optical encryption. The more demonstrated proofs-of-concept, the more robust and concrete the mechanism established. Therefore, these applications are moving toward commercial products in flat optics, unmanned aerial vehicles, and autonomous cars requiring miniaturized meta-devices for imaging. When information becomes big data, green optical storage for encryption with structural colors or metaholograms can be applied. In view of the processing speed of light and energy consumption of optical devices, the potential for manipulating light with metasurfaces is impressive and increasing demands for metasurface devices have encouraged the research presented in this thesis.

The objective of this thesis is to advance the state-of-the-art in the detailed characterization, optimized designs, and identification of potential applications for metasurfaces. The content provided in this thesis contributes to move applications for metasurfaces a step further toward industry. The contributions of this thesis are highlighted as follows:

First, measuring the optical responses under polarized light is widely applied in optical microscopy, but there is still no proper holder for polarization-insensitive beam splitters, which can lead to unphysical measurements. The content in Chapter 2 starts from basic concepts and continues with a demonstration that can guide readers to the core issue of how to conduct precise measurements with different polarized illuminations. Such precise characterization methods are then used for measuring structural colors in Chapter 4. The optical responses of structural colors are considered complicated, and as a consequence, the geometries of structural colors are mainly limited to discs. In addition, there is no clear explanation why the colors turn vivid as the rod rotates by 45° with respect to the illumination. The mechanism of this phenomenon is disclosed and is further applied in the fields of artwork reproduction and quaternary encryption. Based on this work, arbitrary shapes are then obtained from machine learning, such that a more complicated spectrum can be exploited for robust encryption.

Second, in Chapter 3, the conventional method to design metasurfaces for wavefront manipulation is revisited. Reflective metalenses and meta-holograms made of Au-Ag alloys are demonstrated and a cost-effective fabrication process using only thin film deposition and low temperature annealing is developed. This method can retain the geometry of nanostructures and combines the benefits of the two materials. In addition to the Au-Ag alloy, the recipe presented in Chapter 2 can also be applied to Au-Pd, which is widely used for photocatalysts. With the successful demonstration of wavefront manipulation, there is little doubt on the method of design. The study of robustness analysis in Chapter 3 presents insights into surprising results, which encourage us to revisit the design method to include some technological limitations. This could also be optimized with the assistance of machine learning algorithms.

Third, although their application has been widely reported, there is no literature describing how meta-holograms are designed and how pixel size affects the reconstructed images. In Chapter 3, to reduce the gap between implementation and application and to make the meta-holograms accessible to a larger number of researchers, the design details are presented step by step. The theoretical efficiencies achieved by different numbers of phase modulation are simulated. Such values are able to explain why the efficiency of binary, phase-modulated meta-holograms, can reach up to 80% under some circumstances. Additionally, the higher-order images of meta-holograms if they exist, are not completely reconstructed due to multi-slit diffraction. These details are not presented in the literature.

Fourth, in addition to the applications of light modulation, meta-atoms can also be used in energy upconversion for light harvesting. Chapter 5 presents a plasmonic antenna that can have a strong influence on the relaxation path of excited electrons, thereby demonstrating that plasmonics can manipulate excited electrons in matter.

Chapter 2 Methods

In this Chapter, numerical simulation approaches, such as the Surface Integral Equation (SIE) and the Finite Elements Method (FEM)-based multiphysics simulation software (COMSOL), are used to investigate the optical responses of subwavelength structures, called meta-atoms. Because the optical response of meta-atoms (i.e., the scattering cross-section for isolated structures and reflectance and phase shift for periodic unit cells) varies with the constituent materials and their geometric structure, full-wave numerical simulations are required for the structural design of meta-atoms.

Once the optical responses of meta-atoms are calculated, with the proper arrangement or design, these meta-atoms can be then assembled like lego bricks into a surface to provide functions equivalent to bulky optical components, like lenses. Such artificial surfaces, known as metasurfaces, can be composed of arbitrary geometries and rely on Electron-Beam Lithography (EBL) for precise fabrication. Fortunately, the commonly used materials are available in the Center of MicroNano Technology (CMi) at EPFL, where all the samples reported here have been fabricated. A few different techniques are utilized to fabricate metasurfaces in terms of the structure of the composing meta-atoms. The fabricated metasurfaces are first inspected using Scanning Electron Microscope (SEM) to obtain their physical features.

Optical microscopes offer then a reliable and stable platform for characterizing the optical functions of metasurfaces. The measurement setup that has been implemented includes an optical microscope with an additional excitation path and detection path for diverse requirements. The setup is able to measure the spectrum of a spot (5 μm in diameter) in the visible range or provide imaging in a Fourier plane for angular information. With all these tools, we are able to study and investigate meta-atoms for a variety of applications in the visible regime.

2.1 Simulation techniques

Numerical simulations of electromagnetic waves have been developed for more than four decades. In the field of computational electromagnetics, methods based on Maxwell's equations have been developed for calculating problems using different approaches, including the Finite Difference Time Domain method (FDTD), the Method of Moments (MoM), and the Finite Element Method (FEM) [6, 7].

The SIE method, based on the MoM, is used to calculate the scattering cross-section of an isolated plasmonic optical antenna in a homogeneous medium, where the refractive index of the environment is constant [8]. The Lorentzian-shaped scattering cross-section spectrum is proportional to the Local Density of Optical States (LDOS) of the optical antenna and shows the position around which there is strong near-field enhancement at the wavelength of interest [9-11]. The LDOS represents a channel for light coupling between near-field and far-field at a specific wavelength. With this approach, one is able to determine the dimension of plasmonic structures, which is useful for applications such as fluorescent enhancement.

An equivalent approach implemented by COMSOL multiphysics simulates periodic structures in inhomogeneous environments, such as plasmonic structures on a substrate. Reflectance, transmittance, and phase shift under the illumination of polarized light can be derived. However, sometimes COMSOL and SIE predict different results. In this case, one can either utilize another approach, such as FDTD, for comparison or fabricate the sample and characterize it.

2.1.1 Surface integral equations

In the SIE method, the surfaces of a structure are meshed into triangular patches, and Maxwell's equations are solved using Green's tensor in the frequency domain. Complex electromagnetic fields are thus calculated. Physical quantities such as scattering cross-section, absorption cross-section, near-field enhancement, scattering pattern, polarization state, surface charge, optical force, and multipolar moments, are then computed with post-processing.

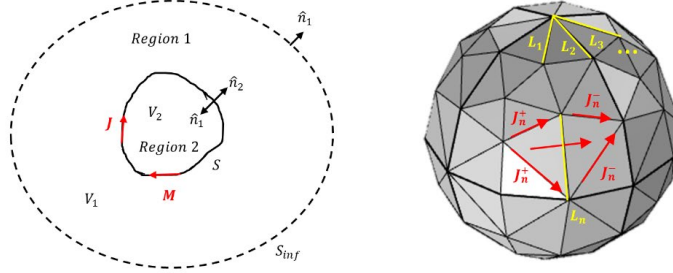


Figure 2.1-1 SIE method meshes only the surface of a structure into triangular patches. The interaction between each surface patch satisfies Green's function. With the interaction matrix, complex electromagnetic fields are obtained.

This approach is used for designing Double Resonance Optical Antennas (DROA), which are composed of two rods of different lengths. The isolated optical antenna is simulated in an effective homogeneous environment (given the average permittivity of air and silicon dioxide substrate) under polarized plane wave illumination as shown in Figure 2.1-2(a).

In Figure 2.1-2(b), the spectrum of one single rod exhibits a single peak (in red), while two antennas properly designed exhibit two peaks (in blue). The idea is to increase the scattering cross-sections simultaneously for two wavelengths in the spectrum such that the optical antenna can provide two channels of LDOSs for selective light-matter interaction. More details on the study of fluorescence enhancement via optical antennas are provided in Chapter 4.

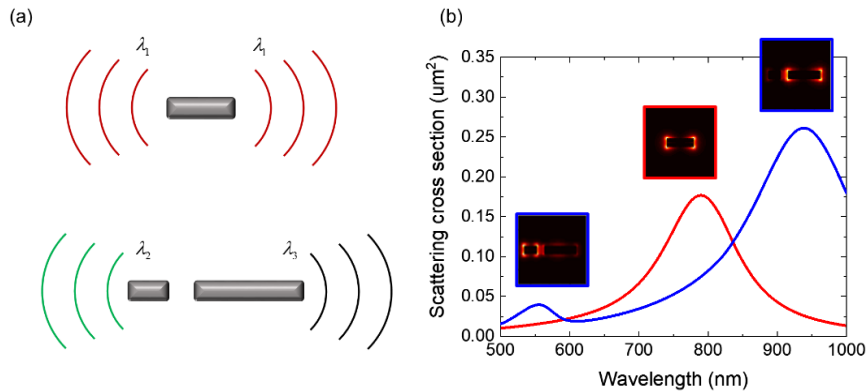


Figure 2.1-2 Optical antenna designs in SIE. (a) A single rod antenna and a double resonance antenna provide different numbers of channels of light coupling between near-field and far-field. (b) Spectral responses in scattering cross-section spectrum for antennas in (a) exhibit Lorentzian-shaped curves at the resonant wavelength. Insets show the position near the antennas where strong near-field enhancement occurs.

2.1.2 COMSOL multiphysics

Consider a complicated structure such as that shown in Figure 2.1–3(a), it consists of a plasmonic structure and metallic thin film separated by HSQ atop a silicon substrate. It is difficult to derive an effective refractive index for such an environment. Fortunately, the FEM-based software COMSOL (version 5.6) meshes the entire volume: it takes into account not only the structure itself (Figure 2.1–3(b)) but also its surroundings (Figure 2.1–3(c)), and partitions the regions into small tetrahedra in which Maxwell's partial differential equations are solved. Generally, smaller meshes provide better approximations, but the total number of mesh elements is restricted by the computer memory. Perfectly matched layers (PML) are applied to avoid an excessive calculation volume, as indicated by the green volumes in Figure 2.1–3(d). The mesh of the PML is different from the surroundings. In particular, periodic boundaries are applied for the computation of the periodic meta-atoms' reflectance. In Figure 2.1–3(e), x- and y-directions are individually assigned. A port is added for polarized plane wave illumination and detection. The refractive index for each domain is also determined so that the steady-state electromagnetic fields in the volume can be solved in the frequency domain. Through post-processing, the reflectance and phase shift information of a meta-atom is derived, which enables diverse proofs-of-concept to be designed in the following Chapters.

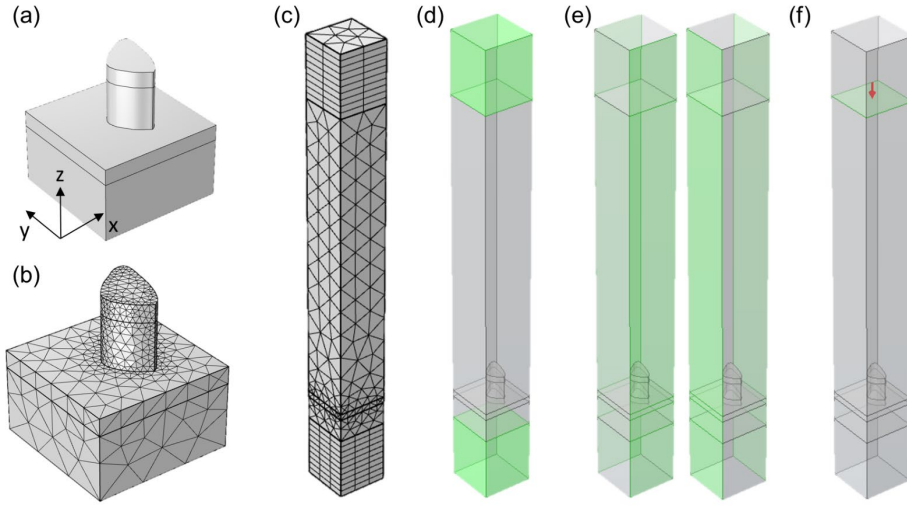


Figure 2.1–3 Computing the reflectance of a periodic meta-atom with COMSOL software requires meshing the entire environment and assigning boundary conditions in the frequency domain. (a) A complicated structure of interest atop a substrate. The entire volume, including (b) the structure and (c) the surroundings, is meshed into small tetrahedrons. (d) PML layers are assigned and meshed differently. (e) Periodic boundaries in the x and y directions are given individually. (f) A port is added for polarized plane wave illumination and detection.

2.1.3 Semi-analytical model

In wavefront manipulation, it is essential to analyze the propagation of light in space. The propagation vector is also known as the wavenumber k and is defined as $2\pi/\lambda$, where λ is the wavelength of light. When diffracted by a grating, incident light can be scattered into different diffraction orders, sometimes called channels. The diffraction angles follow

$$\theta_m = \sin^{-1} \left(\frac{n_1 \sin \theta_i}{n_2} - \frac{m\lambda_0}{n_2 d} \right), \quad (2.1.1)$$

where m is an integer representing the order, θ_i the incident angle, n_1 the refractive index of the environment for the incident light, n_2 the refractive index for the environment of diffraction and d the distance of repetition. These angles are affected by the spacial frequency of a grating. The Fourier transform of the complex amplitude on the surface reveals the parallel momenta. It can be also used to reverse-compute the desired complex electromagnetic field distribution on a surface [12].

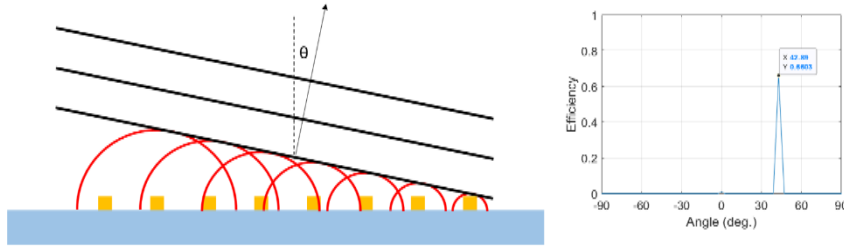


Figure 2.1–4 The wavefront reconstructed by a phase gradient withonly meta-atoms and its Fourier analysis. The amplitudes of the meta-atoms (yellow squares) are constant while their phase shifts (red lines) vary uniformly to span a 2π range. The reconstructed wavefront (black lines) shows the reflected light propagating at an angle θ with respected to the normal reflection.

Considering a reflection-type beamsteering meta-device under linearly polarized illumination, each meta-atom will absorb and re-radiate the plane wave, thus generating a new wavefront according to Huygens principle. This fundamental principle has been widely utilized in metasurfaces for wavefront manipulation. In the demonstration of beamsteering devices, the meta-atoms are usually chosen with uniformly discrete phase shifts covering 2π , while leaving the amplitudes constant and as large as possible. Such design choices follow the physical picture in a straightforward manner as shown in Figure 2.1–4. The generalized reflection law follows the equation

$$\sin \theta_r - \sin \theta_i = \frac{\lambda_0}{2\pi n_i} \frac{d\Phi}{dx}, \quad (2.1.2)$$

where θ_r is the reflection angle, θ_i the incident angle, n_i the refractive index of the environment in the incident space, λ_0 the wavelength of light in vacuum, and Φ the phase shift on the surface. Under normal incidence and working in air, $\theta_i = 0^\circ$ and $n_i = 1$. For a periodic surface with superlattice Λ , the phase gradient along the surface is 2π over Λ and the reflection angle is determined as

$$\sin \theta_r = \frac{\lambda_0}{2\pi n_i} \frac{2\pi}{\Lambda}, \quad (2.1.3)$$

A Matlab code has been designed to provide the response of a beamsteering device given the amplitudes and phases of the meta-atoms that compose one superlattice Λ (variable `Lattice`), which are then repeated ad infinitum. The code can be easily modified to model other types of metasurface unit cells by using other amplitudes (variable `a`) and phases (variable `p`) for the different meta-atoms. As explained in the corresponding publication, in this simple model, each meta-atom is considered as a point light source and the response is obtained by Fourier transform. The Matlab code is attached in Section 7.1.

2.2 Nanofabrication

As the feature sizes of the meta-atoms are less than 20nm, fabricating these subwavelength scale nanostructures requires EBL. Deep ultraviolet photolithography would be possible for fabricating dielectric meta-atoms of larger dimensions. However, the dimensions of metallic nanostructures in plasmonics are smaller than dielectric nanostructures because of the different excitation mechanisms. For plasmonic metals, the concentration of electrons is so high that within a small volume the oscillation can produce a very strong response. In general, the dimensions of metallic meta-atoms fall between a few to hundred nanometers, while dielectric meta-atoms have dimensions in the order of several hundreds of nanometers.

In this Section, the most widely used materials will be introduced, followed by a discussion of the potential alloys for plasmonics (AuAg and AuPd). The used substrates that unknowingly affect the morphology of alloys during annealing are also presented. Apart from the materials on the substrate, the substrate itself complies with the experimental conditions, such as the used objective and measurement setup. Fabrication processes such as lift-off and etching are also discussed. A process that only requires direct deposition after EBL is also applied for cost-efficient fabrication. 3D schematics and SEM images of the final structures are presented.

2.2.1 Materials

Localized surface plasmonic resonances for common materials such as gold and silver occur in the visible region [13]. This is also the case for aluminum [14] and copper [15]. The resonant frequency of plasmonics can be tuned by tailoring the dimensions of the structures. The general rule of thumb is to use aluminum for frequencies up to violet, silver in the visible, and copper and gold in the near-infrared with similar sizes of nanoparticles. A spectrum of the materials' resonant frequencies is summarized in Figure 2.2–1 [16]. Apart from the operating frequencies, their chemical properties vary. For example, aluminum and silver suffer from oxidization, but aluminum tends to be well-protected by a thin layer of alumina. Although gold has relatively stable characteristics, its poor adhesion to other materials necessitates the use of an additional layer to improve adhesion.

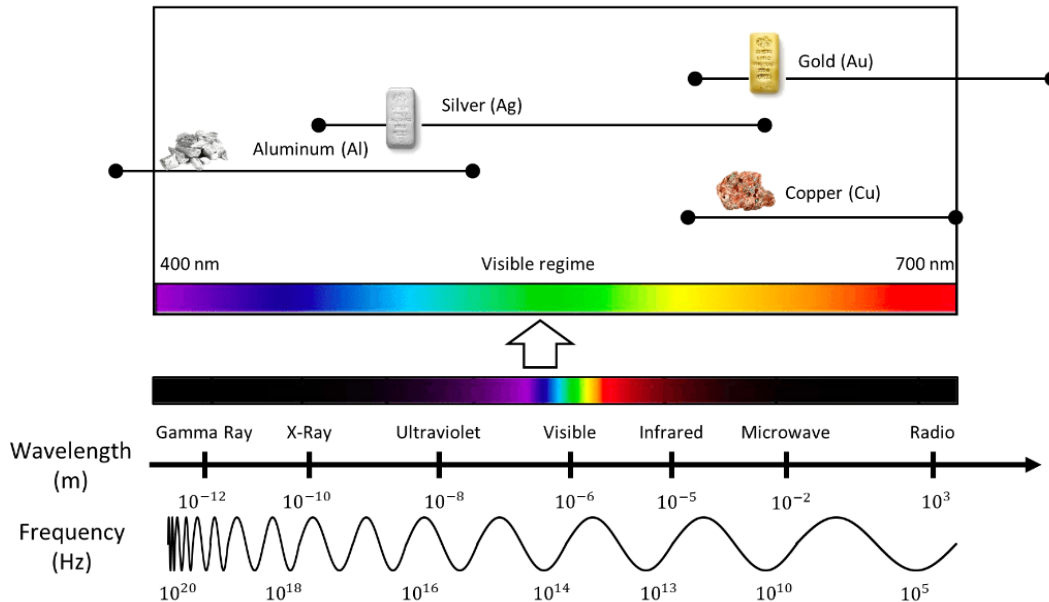


Figure 2.2–1 Resonant frequencies of common metallic materials for plasmonics in an electromagnetic spectrum.

Early in 2017, a treatment for the preservation of silver had been developed in Olivier's lab. This treatment prevented silver from oxidation, thereby allowing it to be used for a long time [17]. The need for new materials with favorable chemical properties increases as the field of plasmonics advances, and this need has encouraged recently the development of alloys. As a starting point, gold and silver are chosen due to their negligible lattice mismatch, opposite chemical properties, and tunable optical properties in the visible regime. The permittivity of gold and silver alloys from theory [18] are plotted in Figure 2.2–2. In the real part of the permittivity, the optical constant is tuned between gold and silver with different combination ratios; meanwhile, the imaginary part can be reduced, which shows great potential for gold and silver alloys to be used in plasmonics throughout the visible regime. Additionally, gold and silver alloy can combine the advantages of the two materials: the stability of gold and silver's ability to provide modulation in the visible wavelength range.

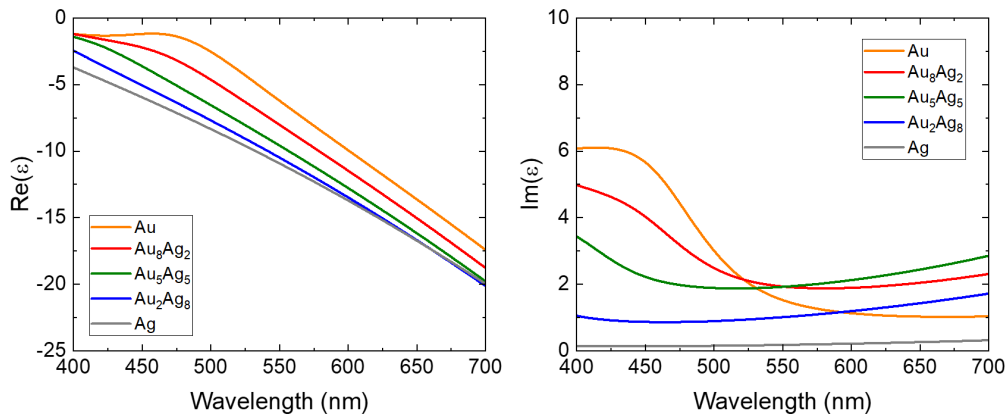


Figure 2.2–2 The permittivity of gold and silver alloys with different stoichiometry in the visible regime.

To fabricate plasmonic structures with desired geometries and arbitrary stoichiometry, a low-temperature annealing process based on diffusion has been developed [19]. The stoichiometry of the AuAg alloy is defined by the initial thicknesses deposited. The synthesis starts with the deposition of a pre-determined thickness of silver and then gold separately on top of a glass substrate. The bilayer film structure (silver below and gold atop) is then placed in an oven with nitrogen flow and annealed at 300° celsius for 8 hours with a final push at 450° celsius for 30 minutes. The atomic concentration ratios measured by X-ray photoelectron spectroscopy (XPS) before and after low-temperature annealing are plotted in Figure 2.2–3. Before annealing, the bilayer structure is observed to be made of 30 nm-thick gold on top and 120 nm-thick silver underneath. The separated bilayer structure is eliminated after the diffusion process wherein gold and silver are uniformly distributed through the depth above the substrate. The analysis is conducted for 150 nm-thick films, which represent with a solid safer margin the thickest limit for plasmonic structures. This annealing procedure is then applied with a lift-off process for fabricating alloy plasmonic structures in desired geometries with EBL. Demonstrations of metasurfaces made of different stoichiometric AuAg alloys are presented in Section 3.2.

The low-temperature annealing process is capable of retaining the nanostructure shape even with a high aspect ratio for plasmonic studies. In addition to utilizing the optical properties of the alloyed materials, the chemical properties of the alloy can promote research in different fields. For example, palladium (Pd) is famous for attracting hydrogen. Therefore, I made an attempt to fabricate AuPd alloys with such a low-temperature annealing process. The atomic concentration ratios through the film before and after annealing are plotted in Figure 2.2–4. Layers of gold and palladium with 37.5 nm each are deposited separately as was done for Au-Ag. However, using the same annealing conditions, the gold does not completely diffuse into the palladium layer, and thus the process needs further optimization, although these preliminary results are encouraging. Most importantly, alloys provide additional degrees of freedom when choosing materials for plasmonic applications.

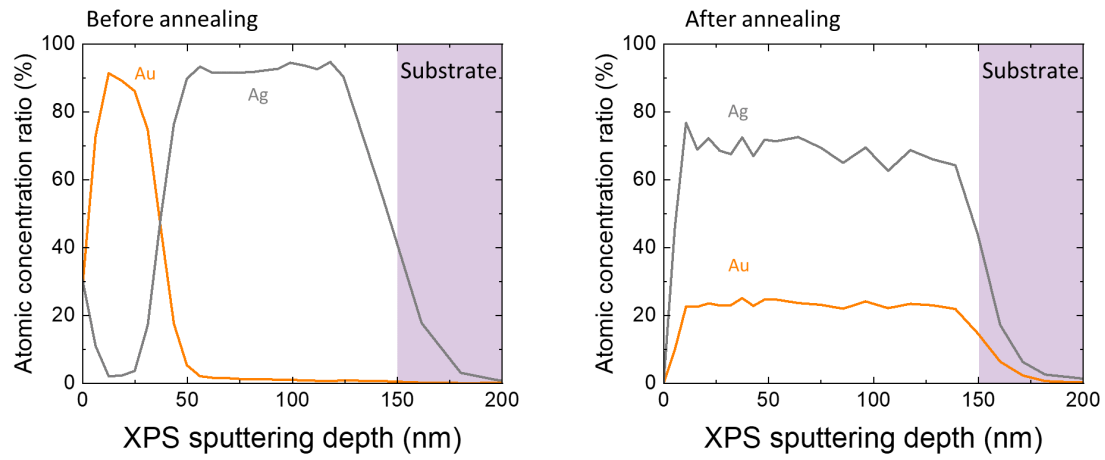


Figure 2.2–3 XPS images for a 150 nm-thick $\text{Au}_{0.2}\text{Ag}_{0.8}$ film before and after annealing. After bilayer deposition, annealing at 300 °C for 8 hours, followed by 30 min at 450 °C.

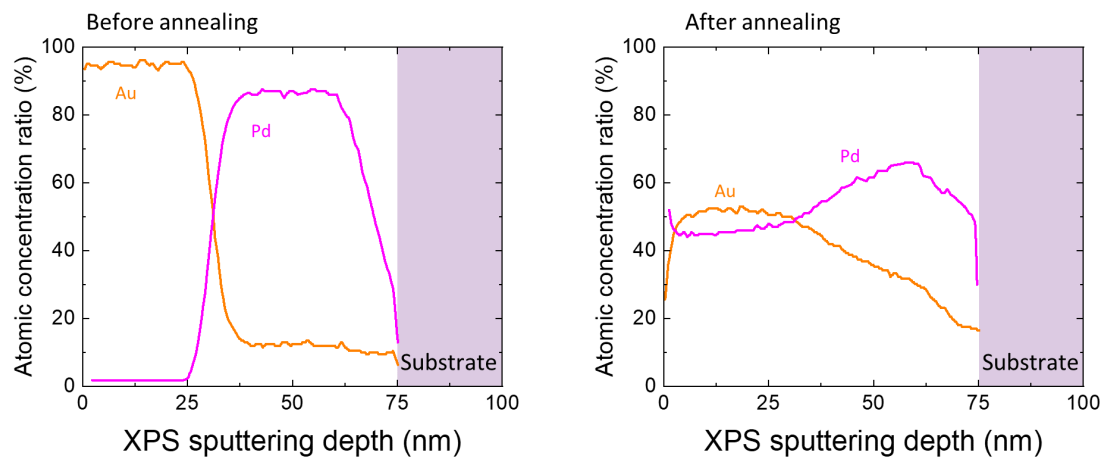


Figure 2.2–4 XPS images for a 75 nm thick $\text{Au}_{0.5}\text{Pd}_{0.5}$ film before and after annealing. After bilayer deposition, annealing at 300 °C for 8 hours, followed by 30 min at 450 °C. We observe partial annealing of the film. It is likely that with additional experiments Au-Pd alloys could be realized at low temperatures.

2.2.2 Substrates

The substrates, also known as wafers, used in this thesis to support the nanostructures, are listed in Table 2-1. Although there are other types of substrates provided by CMi for various purposes, the table is sufficient for fundamental studies analyzing the optical properties of metasurfaces. Generally, transparent glass wafers such as float glass wafers are used for transmission-type devices, while opaque silicon wafers are widely applied for reflective ones.

Substrate type	Name	Thickness	Thermal strain point
Glass wafer (amorphous)	Borosilicate wafers, D263T/DS	150 μm	529°C
	Float glass wafers, FLOAT/DS	550 μm	490°C
	Fused Silica	525 μm	1120°C
Silicon wafer (crystalline)	Silicon test wafers, 100/P/SS/01-100	100 mm	1100°C

Table 2-1 The substrates used in the thesis.

To be able to detect the light scattered by structures, interlinked factors such as the radiation patterns of the samples, the substrate, the objective used, and the environment require simultaneous considerations. These factors are summarized in Figure 2.2–5.

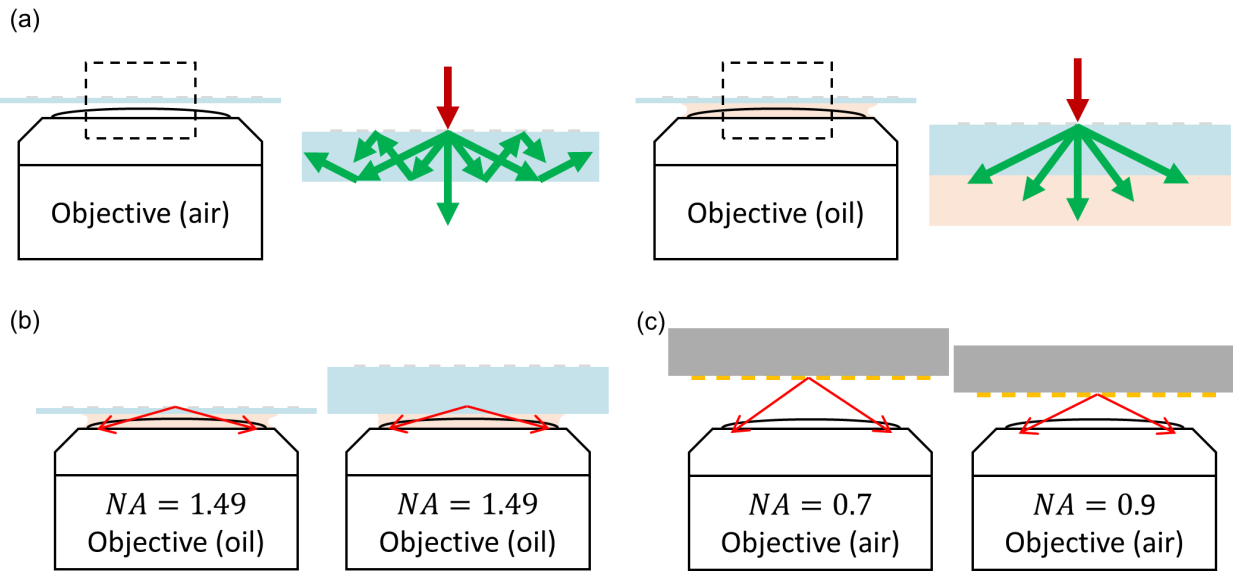


Figure 2.2–5 Factors affecting the measurement configuration in transmission and reflection. Detecting light scattered from a sample requires consideration of many interlinked factors, including the radiation patterns (isolated structures) or diffraction orders (periodic structures) of a sample, the substrate for structures, the objective used, and the environment for measurements. (a) Comparison of objectives operating in air and in oil for measuring samples atop glass substrates in a transmission manner. (b) A thinner transparent substrate is required for oil-immersed objectives when measuring transmission. (c) Configuration for measurement in reflection. The main factor is the numerical aperture of the objective used.

In Figure 2.2–5(a), an objective in the air is compared with one in oil for measuring periodic structures atop a glass substrate ($n = 1.5$) in transmission. Light scattered by periodic structures described with diffraction orders propagates in the glass substrate, where total internal reflection occurs for light propagating at angles larger than 41.8°. This restriction can be eliminated by using an oil-immersed lens with a comparable refractive index of oil ($n = 1.51$). This measurement configuration is necessary for measuring frequency upconversion signals with double resonance antennas due to the dispersion property of light crossing from $\lambda = 980 \text{ nm}$ to $\lambda = 525 \text{ nm}$ and the periodic antennas. In addition, a 150 μm -thick thin glass substrate (Borosilicate wafers, D263T/DS) is required for oil-immersed lenses because of the high

numerical aperture. As shown in Figure 2.2–5(b), a thick glass substrate prevents the lens from focusing on the structures, where the strong near-field enhancement for frequency upconversion occurs. For measurements in reflection as shown in Figure 2.2–5(c), the most important factor is the numerical aperture of the objective. The numerical aperture (NA), related to the acceptance angle θ and refractive index of the operating environment n , is defined as $NA = n \times \sin \theta$. More details associated with measuring reflective samples will be discussed in sub-Section 2.3.2.

Since float glass wafers can only sustain up to 500°C, when studying alloys under different annealing temperatures, fused silica glass wafers and silicon wafers were used in the beginning because they are stable at temperatures exceeding 1000°C. As the annealing temperature is optimized down to a maximum of 450°C, float glass wafers can be applied. An observation of annealing materials on different substrates is shown in Figure 2.2–6. The results imply that an amorphous substrate (float glass wafer) produces a more flat alloy surface, while materials on silicon substrates tend to build large crystalline structures after annealing.

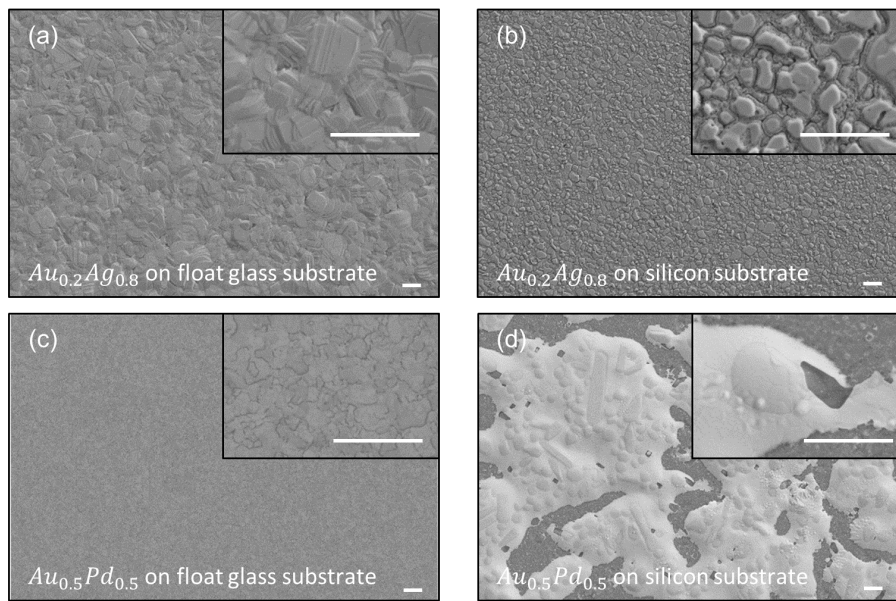


Figure 2.2–6 SEM images of Au-Ag and Au-Pd on different substrates after low-temperature annealing. Bilayer films of Au-Ag and Au-Pd in a total of 150 nm were deposited on amorphous and crystalline substrates, followed by low-temperature annealing process. Scale bars are 1 μm .

2.2.3 Fabrication processes

Fabricating meta-atoms in subwavelength scales requires the utilization of EBL, which usually contains three steps: spin-coating E-beam resist, E-beam exposure, and development as a final step. Depending on the resists used, the exposure area will be removed after development if the resist is positive, such as polymethylmethacrylate (PMMA). If the resist is negative, for example, hydrogen silsesquioxane (HSQ), the area will remain after EBL. In this sub-Section, three processes based on EBL together with anisotropic thin film deposition are utilized for fabricating meta-atoms.

2.2.3.1 Lift-off

A lift-off process removes the unwanted structures by "lifting" the positive resist above the structures "off" the substrate. This approach, used for fabricating double resonance antennas, is exhibited step by step in Figure 2.2–7:

- (a) A 150 μm -thick thin glass substrate (D263T/DS) is first cleaned with Tepla GiGAbath.
- (b) Bilayer of positive resists (the lower layer: 120 nm 495KA4 @6000rpm; the upper layer: 60 nm 950KA2 @6000rpm.) are separately spin-coated on the substrate. Each layer is baked for 5 minutes at a temperature of 180°C for dehydration.
- (c) Before E-beam exposure, a layer of 20 nm-thick Cr film is deposited with Leybold Optics LAB 600H, to prevent the sample from charging the sample during E-beam exposure.
- (d) The sample is patterned by Vistec EBP5000.
- (e) After the exposure step, the Cr layer is removed by a Cr acid wet etch for 10 seconds. To remove the acid completely, the sample is repeatedly immersed in DI water three times and each time for 2 minutes.
- (f) When the conductive Cr layer is removed, the sample is placed in a resist developer (MiBK: IPA 1:3) for 1 minute followed by an IPA rise for 1 minute and a drying step with nitrogen. As there might be some residues remaining, an 8-second oxygen plasma treatment with Oxford PRS900 is recommended.
- (g) After the area patterned by E-beam is completely cleaned and hollowed, a 40 nm-thick silver anisotropic thin film is deposited by Leybold Optics LAB 600H. A 1nm-oxide layer is first deposited for adhesion and then a 39 nm-thick silver film. After the anisotropic thin film deposition, the sample is placed upside down in Acetone for 24 hours. The PMMA resist will be dissolved and the attached silver flakes will be floating in the solution. A pipette can be used to blow off the floating flake or alternatively, an ultrasonic bath for 10 seconds removes the floating flakes.
- (h) The double resonance antenna is completed by rinsing the sample with IPA and drying the nitrogen. To avoid oxidization, samples are kept in a nitrogen chamber.

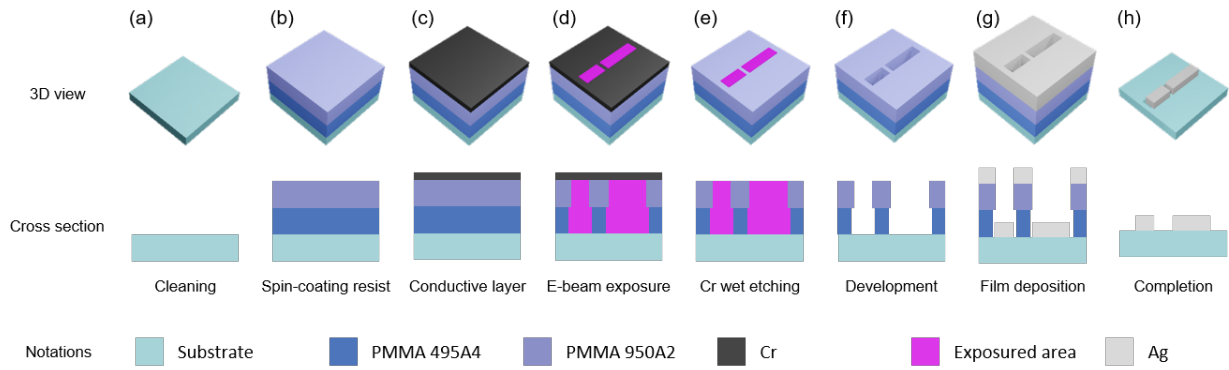


Figure 2.2–7 Schematic of fabricating double resonance antenna with lift-off method. (a) clean glass substrate. (b) spin-coated with bilayer PMMA. (c) Deposited with Cr as a conductive layer for E-beam exposure. (d) E-beam exposure. (e) Conductive layer removal. (f) Resist development and oxygen plasma treatment. (g) anisotropic thin film deposition. (h) Completion of double resonance antenna after removing the PMMA layer and atop silver flake.

The SEM images of the optical antennas fabricated with the lift-off approach are presented in Figure 2.2–8. These optical antennas exhibit resonance behaviors in the visible regime, which are used to generate strong near-field for fluorescent enhancement. The fluorescent particles, frequency upconversion nanoparticles ($\text{NaYF}_4: \text{Yb}^{3+}, \text{Er}^{3+}$, Sigma-Aldrich), are directly spin-coated on the substrates, so conductive layers for better imaging are not applied. A more comprehensive study and discussion of plasmonic enhancement for frequency upconversion are presented in Chapter 4.

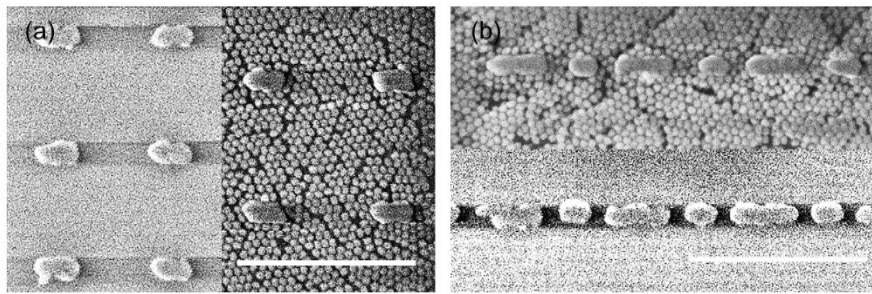


Figure 2.2–8 SEM images of optical antennas fabricated with the lift-off approach. These silver antennas are above 150 nm-thick nonconductive glass substrates. For better imaging, a layer of carbon or conductive metal can be deposited. However, these samples are directly spin-coated with a layer of frequency upconversion nanoparticles $\text{NaYF}_4: \text{Yb}^{3+}, \text{Er}^{3+}$ for experiments, so the conductive layers are not used. The scale bars are 500 nm.

2.2.3.2 Evaporation + HSQ + etching

Etching processes remove the unwanted structures by bombarding them with anisotropic electron beams. This method is a subtractive manufacturing method different from the additive Lift-off process. Instead of depositing the structure in the hallowed area, the hallowed region will be etched away. In this etching process, a negative resist like HSQ is used. The step-by-step process for fabricating phase gradient meta-atoms is presented in Figure 2.2–9:

(a) A Silicon wafer (100/P/SS/01-100) is first baked on a hot plate (fabricant) for 5 minutes at a temperature of 180 °C to dehydrate it (humidity is detrimental to nanofabrication).

(b) Thin film deposition is performed, including a 1 nm Ti adhesion layer for the subsequent 150 nm Au mirror, a second 1 nm Ti as the adhesion layer for the following 40 nm SiO₂ dielectric spacer, a third 1 nm Ti adhesion layer for the following 30 nm gold used for the meta-atoms. There is a 20 nm Cr layer serving as a sacrificial layer, which is used to remove the resist at the end. All films are deposited by Leybold Optics LAB600H.

(c) Negative tone electron beam photoresist hydrogen silsesquioxane (HSQ, XR-1541-006 DuPont) is then spin-coated on top at 6000 rpm.

(d) Electron beam exposure with Vistec EBP5000 system (100 keV and 100 pA)

(e) Development with Tetra Methyl Ammonium Hydroxide 25% (Honeywell) by immersing the sample for 1 minute and then rinsing with DI water and drying with nitrogen for removing the toxic chemicals.

(f) Ion beam etching by Veeco Nexus IBE350 (300V and 500mA collimated Ar ions beam) to reveal the meta-atoms while maintaining the SiO₂ substrate.

(g) The process is finished by isotropic wet etching the sacrificial Cr layer with TechniEtch Cr01 (Microchemicals GmbH), which removes the remaining HSQ. After the wet Cr etch, the sample is cleaned with isopropanol alcohol and deionized water.

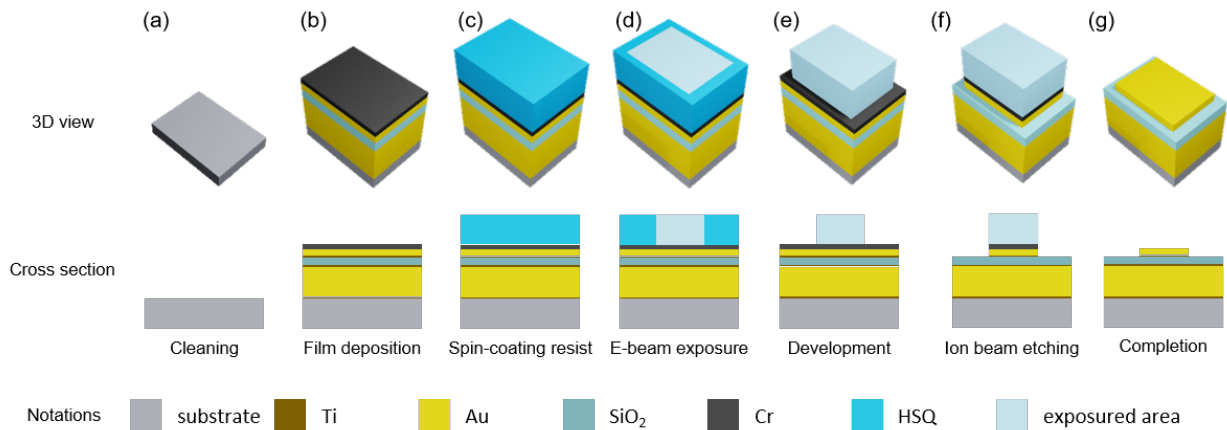


Figure 2.2–9 Schematic of a phase gradient meta-atom in the etching process. (a) Cleaning silicon substrate. (b) E-beam evaporation for sequential thin film deposition: 1nm Ti as an adhesion layer, 150nm Au as the back reflector, 1nm Ti as an adhesion layer, 40nm SiO₂ as a spacer, 1nm Ti as an adhesion layer, 30nm Au for the plasmonic nanorod, and 20nm Cr as a sacrificial layer. (c) Spin-coated with HSQ. (d) E-beam exposure. (e) E-beam resist development with Tetra Methyl Ammonium Hydroxide 25%. (f) Ion-beam dry etching. (g) a complete phase gradient meta-atom after removing the Cr layer and atop HSQ.

This etching process has been used to produce the meta-atoms for the robustness analysis of phase gradient metasurfaces. Based on the traditional design principle for beam-steering metasurfaces, used to redirect the incoming light without following Snell's law, two designs with the same function are compared, including their misfabricated samples, shown in Figure 2.2–10 and Figure 2.2–11. The performance of these devices is measured with Fourier space microscopy which is introduced in sub-Section 2.3.2.



Figure 2.2–10 Fabricated 8-level phase gradient beam-steering metasurface devices with intended misfabricated defects.

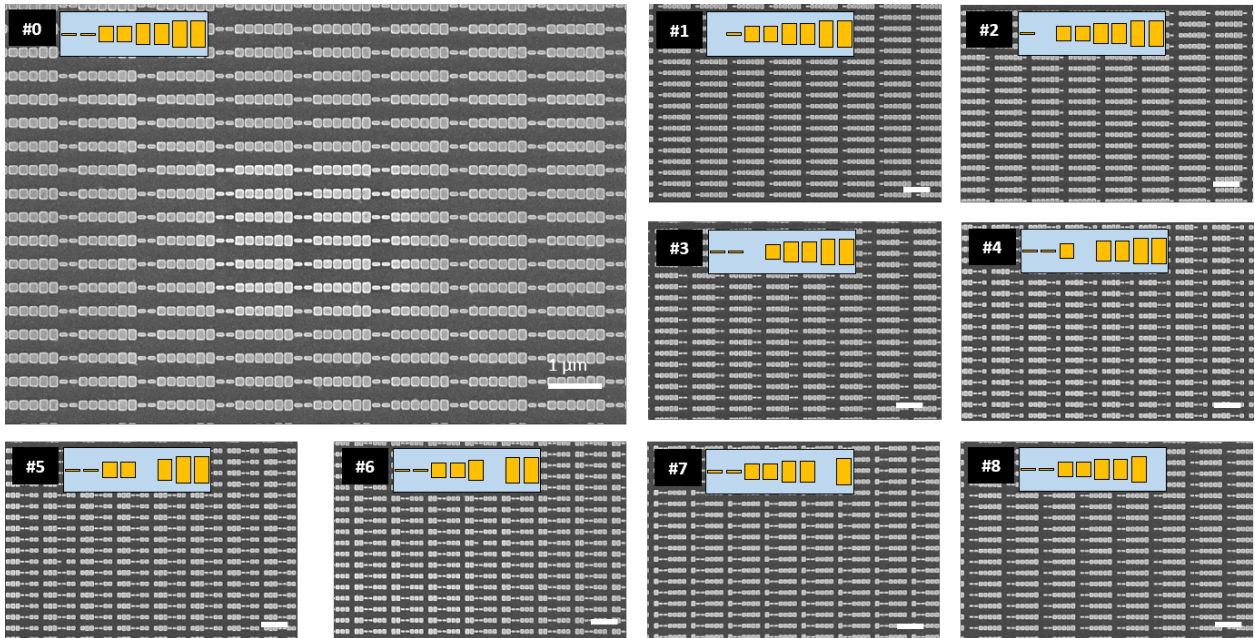


Figure 2.2–11 Fabricated 4-level phase gradient beam-steering metasurface devices with intended misfabricated defects.

2.2.3.3 HSQ + evaporation

This instant process, without lift-off or etching, is the most convenient and is accomplished by thin film deposition after EBL. A negative resist (HSQ) is used as a spacer, to separate the plasmonic structure patterned by E-beam and its complementary-shaped reflector. The step-by-step fabrication process is presented in Figure 2.2–12:

(a) A Silicon wafer (100/P/SS/01-100) is first baked on a hot plate (fabricant) for 5 minutes at a temperature of 180 °C to dehydrate it (humidity is detrimental to nanofabrication).

(b) Negative tone electron beam photoresist hydrogen silsesquioxane (HSQ, XR-1541-006 DuPont) is then spin-coated on top at 6000 rpm.

(c) Electron beam exposure with Vistec EBPG5000 system (100 keV and 100 pA)

(d) Development with Tetra Methyl Ammonium Hydroxide 25% (Honeywell) by immersing the sample for 1 minute and then rinsing with DI water and drying with nitrogen to remove the toxic chemicals.

(e) The sample is completed after a thin film deposition of 40 nm-thick Ag by Leybold Optics LAB 600H.

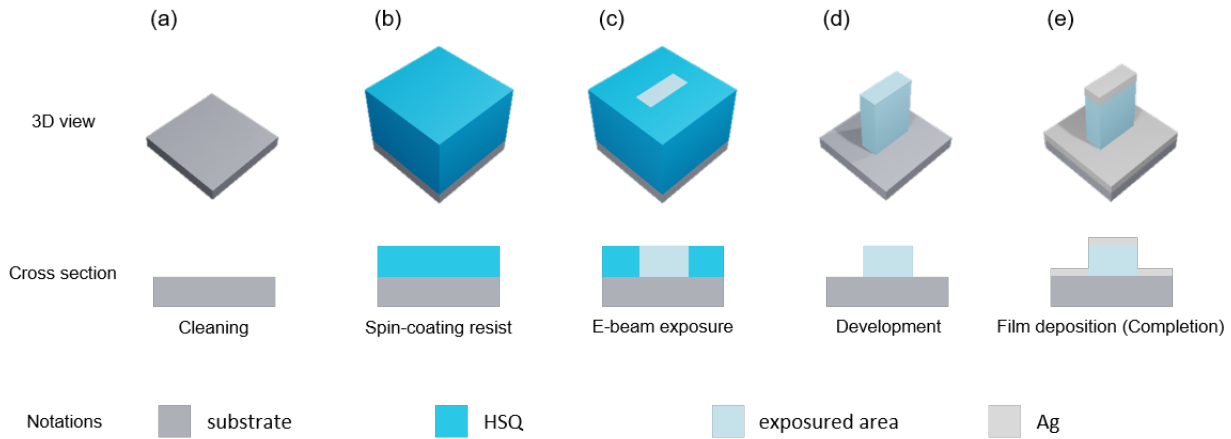


Figure 2.2–12 Schematic of a polarization-converting meta-atom, or a geometry-sensitive meta-atom, in the fabrication process. (a) clean silicon substrate. (b) spin-coated with 150 nm-thick HSQ. (c) Patterned with E-beam exposure. (d) Development to remove the unpatterned area. (e) The structure is complete after 40 nm-thick silver thin film deposition.

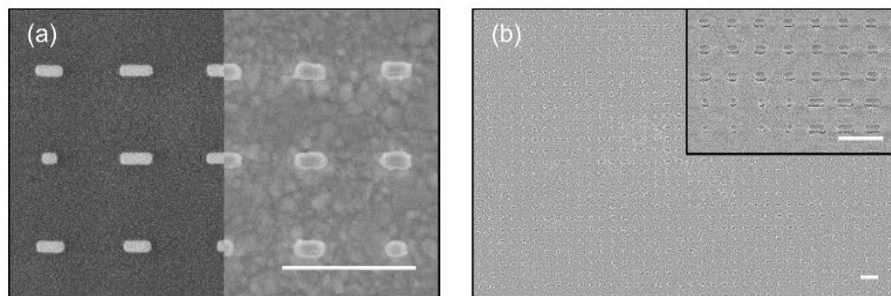


Figure 2.2–13 SEM images of fabricated plasmonic structures in the direct deposition process. (a) Before (left) and after (right) thin-film deposition after E-beam resist development. (b) The final structures. Scale bars are 500 nm.

The fundamental physical response of such nanostructures is discussed in Chapter 4, while the corresponding measurement method for such polarization converting meta-atoms will be discussed in Section 2.3.

2.3 Experimental setup

The most convincing proof for validating results from numerical simulations is to conduct measurements on fabricated samples. It is important to carefully examine each optical component in a measurement system before analyzing a functioning metasurface device. The introduced measurement setup is modified from an Olympus optical microscope and is mainly used for characterizing optical responses in the visible regime of the electromagnetic spectrum. The used wavelength is between 430nm and 750nm. The efficiency for other wavelengths is relatively poor since the optical components do not function properly at these wavelengths, and as a consequence, the measured signal decays quickly and is absorbed by the system. Optical images, Fourier plane analysis, and spectral responses can be measured using this approach. The optical image shows the appearance of the sample with proper magnification and can be directly observed by the naked eye with an optical microscope. Fourier plane analysis displays the spatial frequency information of the image; in other words, it takes an analog Fourier transform of the optical image. The spectrum, measured from the image plane, is used to analyze the intensity of light for each wavelength. This setup is optimized for two imaging modes: optical imaging microscopy and Fourier space microscopy, whereby simply flipping an optical component allows for switching between the two. Spatial filters are applied for necessary imaging processing, while spectral filters are used to get rid of undesired signals in the spectrum. A study on measuring structures for polarization conversion is presented in the last sub-Section.

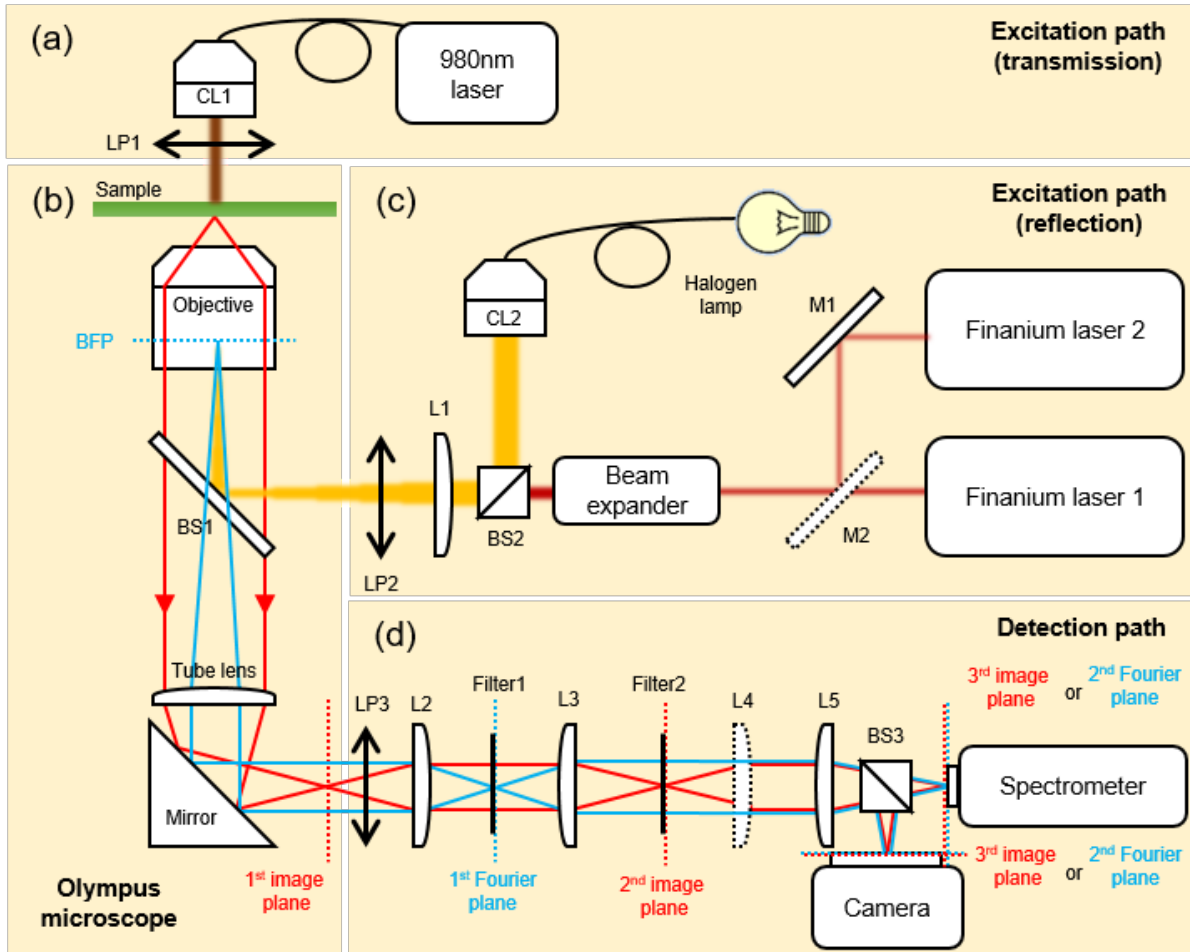


Figure 2.3–1 Schematic of the measurement setup for characterizing optical responses. There are four parts in the whole system: (a) Excitation path in transmission, (b) Olympus optical microscope, (c) Excitation path in reflection, and (d) detection path.

An overview of the measurement setup is schematically shown in Figure 2.3–1. The setup is separated into four parts: (a) Excitation path in transmission with a single wavelength laser at $\lambda = 980$ nm, (b) Imaging samples with an Olympus optical microscope (Olympus IX73), (c) Excitation path in reflection for three light sources, and (d) Detection path for imaging and spectral analysis.

- Excitation path in transmission in Figure 2.3–1(a)

The light source illuminates the double resonance antennas on a glass substrate, where a single wavelength laser emitting at $\lambda = 980$ nm is applied. Light is first coupled into a fiber, and collimated by a collimator (CL1). A linear polarizer (LP1) is then used to generate a polarized plane wave for illuminating the double resonance antennas and frequency upconversion nanoparticles (NaYF₄: Yb³⁺, Er³⁺). Frequency upconversion is a process that can efficiently convert two or more lower energy photons ($\lambda = 980$ nm) into a higher energy one ($\lambda = 540$ nm and 660 nm). Additional details are discussed in Chapter 4.

- Olympus optical microscope in Figure 2.3–1(b)

Optical microscopes are well-known systems for observing tiny objects difficult to examine with bare eyes. This inverted optical microscope holds the sample on top of a stage leaving the objectives underneath. The optical image of the sample is magnified and projected on the 1st imaging plane (red dashed line) by the lens pair (an objective and a tube lens). The red lines indicate the ray tracing for imaging; that is, the optical image of the sample is first coupled into the objective at its focal length, and afterward is focused onto the 1st image plane by the tube lens following reflection by the mirror at the bottom of the microscope.

- Excitation path in reflection in Figure 2.3–1(c)

There are three light sources: an incoherent light source (halogen lamp) and two coherent Finanium lasers. A flippable mirror (M2) is used to change the light source from a low-power laser (Finanium laser 2) to a high-power one (Finanium laser 1). The halogen lamp and coherent light sources are aligned and focused at the back focal plane (BFP) of the objective by a long focal length lens (L1) and two beam splitters (BS1 and BS2), such that a plane wave is generated on the sample side by the objective. By examining the position of the light spot on the BPF, one can determine the incident angle for plane waves. A linear polarizer (LP2) can be used to generate s- and p-polarized light for illumination at the entrance of the optical microscope.

- Detection path in Figure 2.3–1(d)

Two 4f systems made of two pairs of lenses (L2-L5) and two detectors (a spectrometer and a color camera) are used. The linear polarizer (LP3) is used as an analyzer to examine the polarization state of light exiting the optical microscope. In optical imaging microscope mode, four lenses are used. With the beam splitter (BS3), optical images of the sample are projected on the camera; meanwhile, the spectrum is analyzed by the spectrometer. Flipping the lens (L4) will switch the optical imaging mode to Fourier space microscopy mode. When L4 is flipped, three lenses (L2, L3, and L5) are used. In this mode, the analog Fourier transform of the optical image will be projected on the camera. The blue lines illustrate how the images on Fourier planes are projected on the camera. By applying filters at the 1st Fourier plane (blue dashed line) and at the 2nd image plane, analog imaging processing can be achieved.

The list of components regarding the labels in Figure 2.3–1 is exhibited below in Table 2-2 Table of optical components in Figure 2.3–1.

Optical setup	Labels	Items	Specifications
Excitation path (transmission)	980nm laser	Laser diode	Thorlabs: LP980-SF15-170621-52
		Laser mount	Thorlabs: LDM9LP
		Laser controller	Thorlabs: ITC 510
	CL1	Collimator	Thorlabs: F280FC-980
	LP1	Linear polarizer	Thorlabs: WP25M-UB
Olympus inverted microscope (IX73)	Objective	Objectives	Leitz Wetzlar PL AP0 50x/0.90 air
			Olympus LUCPlanFL N 60x/0.70 air
			Olympus UApo N 100x/1.49 oil
	BS1	Beamsplitters	Thorlabs: BS022
			Thorlab: BS014
			Chroma: AHF F21-020
	Tube lens	Tube lens	F = 180 mm (built-in)
	Mirror	Mirror	Dielectric mirror (built-in)
Excitation path (reflection)	Halogen lamp	Lamp	Olympus U-LH100IR
	CL2	Collimator	Objective 10x air
	L1	Lens	F = 400 mm (A-coating) LA1172-A
	BS2	Beamsplitter	Thorlabs: BS022
	LP2	Linear polarizer	Thorlabs: WP25M-UB
	Finanium laser 1	Laser controller	SuperK Fianium
		Wavelength modulator	SuperK VARIA
	Finanium laser 2	Laser controller	Fianium FemtoPower 1060, Serial No: 100627
		Acousto-optical tunable filter	Fianium AOTF-V1-N1-DD; VIS1 (400 nm to 750 nm) NIR1 (750 nm to 1100nm)
	Beam expander	Lens	F = 50 mm (A-coating)
		Pinhole	D= 50 μ m
		Lens	F = 100 mm (A-coating)
	M1	Mirror	Thorlabs: PF10-03-P01P
	M2	Flippable mirror	Thorlabs: PF10-03-P01P
Detection path	LP3	Linear polarizer	Thorlabs: WP25M-UB
	L2	Lens	F = 200 mm (A-coating) LA1979-A
	Filter1	Spatial filters	Beam blocker: D = 0.5 m
			Beam blocker: D = 2 mm
	L3	Lens	F = 200 mm (A-coating) LA1979-A
	Filter2	Spatial filter	Image plane pinhole: D = 0.2 mm
		Short pass spectral filter	Chroma: ET750sp-2p8
	L4	Lens	F = 50 mm (A-coating) LA1131-A
	L5	Lens	F = 75 mm (A-coating) LA1608-A
	BS3	Beamsplitter	Thorlabs: BS022
	Camera	Color camera	Flir: CM3-U3-50S5C-CS
	Spectrometer	Spectrograph	Andor Shamrock 303i
		Spectroscopy detector	Andor Newton 971 EM-CCD

Table 2-2 Table of optical components in Figure 2.3–1.

2.3.1 Optical imaging microscopy

Using a pair of lenses, including objectives, for imaging is widely employed in optical microscopes. The schematic of a $4f$ imaging system made of two lenses (Lens A and B with focal lengths f_1 and f_2 individually) is depicted in Figure 2.3–2. The sample is located at the image plane, or at the focal distance f_1 on the left side of Lens A. When the image of the sample is the input to Lens A, the output on the right side at the same distance f_1 is the Fourier transform of the input image. When the second lens (Lens B) is placed at a distance of its focal length f_2 from the Fourier plane, the original input image will be Fourier transformed twice and presented on the right side of Lens B at a distance f_2 from Lens B.

Mathematically, assuming the input image to be $f(x, y)$, the output image after a pair of lenses will become $f(-x, -y)$, which can be derived by applying the Fourier transform to a function twice. In reality, the output image $f(-x, -y)$ is inverted, i.e., upside down and left to right. As mentioned previously, the lens pair (an objective and a tube lens) in the optical microscope are used to project the image of the sample onto the 1st image plane at the exit of the microscope. Likewise, two $4f$ systems in the detection path, composed of two pairs of lenses, are used, generating 2nd and 3rd imaging planes in Figure 2.3–1.

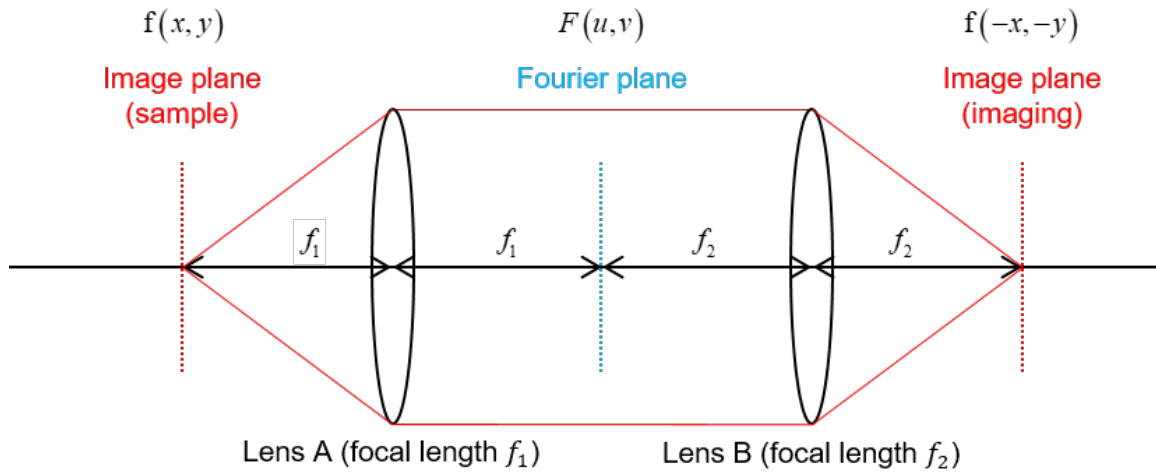


Figure 2.3–2 A $4f$ system with a pair of lenses is widely applied for imaging. The image of the sample will be projected on the other side of the $4f$ imaging system and becomes inverted upside-down.

The filters (Filter2) at the 2nd image plane can be applied together if needed. When measuring a spectrum, the spatial filter (pinhole of diameter of 0.2 mm) can be used to analyze the spectrum of an area 20 μm in diameter with the objective (50x), shown in Figure 2.3–3. This spatial filter is useful in measuring isolated or sparse optical antennas [20]. The two 3rd image planes are split by the beam splitter (BS3), which enables the setup to detect the optical image and analyze the spectrum simultaneously.

When an optical image enters the spectrometer, light is dispersed on a charge-coupled device (CCD) by a grating. The dispersed light detected on each column of pixels on the CCD is converted into electrons, which are proportional to the intensity of light. The spectrometer is calibrated with mercury vapor arc-discharge lamps, which have strong emission peaks at $\lambda = 546 \text{ nm}$ and $\lambda = 579 \text{ nm}$. Sometimes the signal on the spectrum is weaker than the noise, and when this occurs, a longer exposure time can be applied to increase the signal-to-noise ratio.

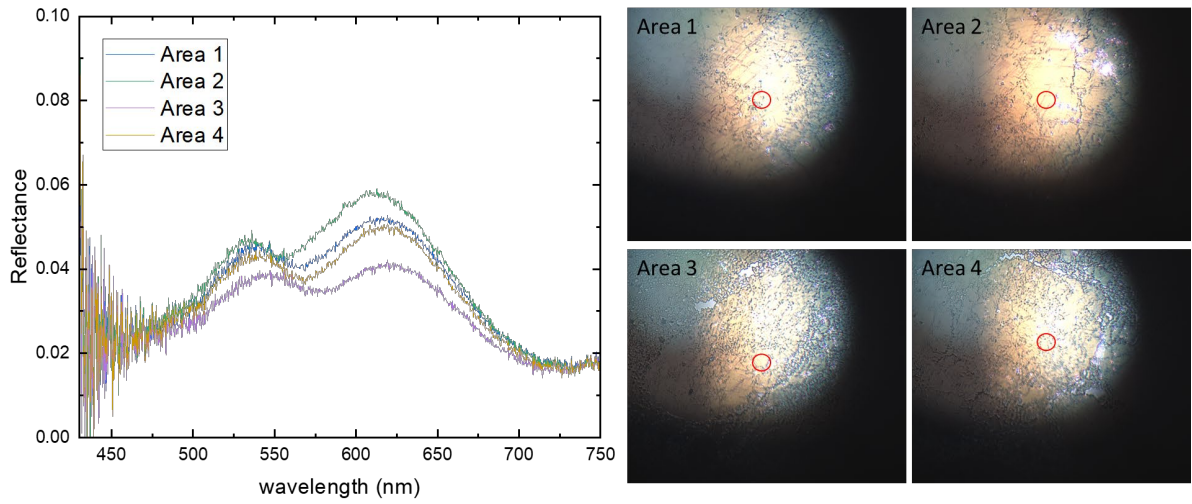


Figure 2.3-3 Spectra measurement with a spatial filter (pinhole) at the 2nd image plane. The spectrum of a smaller area at a specific position is analyzed. The reflectance is derived by dividing it with the spectrum from a silver mirror. The images on the right side are without a spatial filter, while the red circles indicate regions that are not blocked by a pinhole.

In measuring the scattering light of a sample, the numerical aperture (NA) of an objective plays a crucial role. The NA not only affects the choice of substrates used (as discussed in sub-Section 2.2.2) but also influences the detected information. It is defined as $NA = n \sin \vartheta$, where n is the refractive index of the operating environment and ϑ is the acceptance angle. Only the scattered light within the acceptance angle ϑ can be coupled into the component and detected. For example, an objective with $NA = 0.7$ in air can detect signals within $\vartheta = \sin^{-1}(0.7) = 44.4^\circ$, while an oil-immersed lens with $NA = 1.49$ is capable of collecting signals within $\vartheta = \sin^{-1}(1.49/1.51) = 80.6^\circ$. When an image contains broader spatial frequency information, it possesses sharper edges than one with narrower and lower angular information. A comparison of optical images observed by similar magnification objectives with different NA is presented in Figure 2.3-4. The spatial frequency information will be discussed in sub-Section 2.3.2.

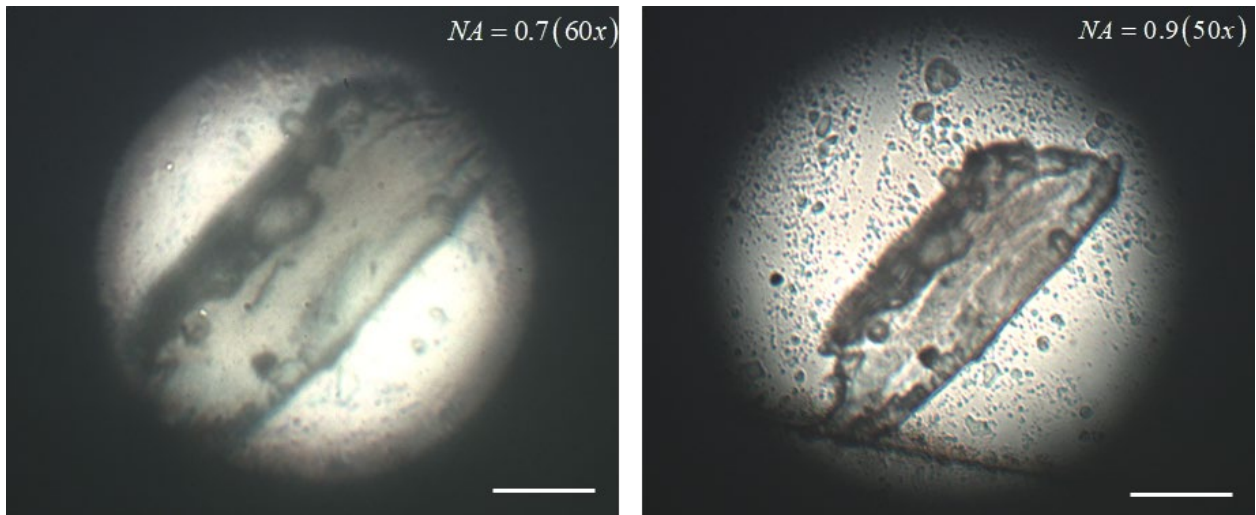


Figure 2.3-4 Optical images collected by objectives with $NA = 0.7$ and $NA = 0.9$. The edges are sharper with higher NA values due to higher spatial frequency information is contained. The scale bars are $50 \mu\text{m}$.

2.3.2 Fourier space microscopy

Fourier transform (FT) is a method that transforms a function of a certain variable into a function of the variables' conjugate. For example, a function of time t will be expressed as a function of frequency f ($f = 1/t$) after Fourier transform. The FT of a function $f(t)$ is defined as:

$$F(f) = \int_{-\infty}^{\infty} f(t) e^{-i2\pi ft} dt, \quad (2.3.1)$$

and its inverse Fourier transform (iFT):

$$f(t) = \int_{-\infty}^{\infty} F(f) e^{i2\pi ft} df \quad (2.3.2)$$

The conjugate variables can also apply to the position. That is, a function of positions x in space will be transformed into a function of spatial frequency u ($u = 1/x$). By extending the function of position from 1D FT to 2D FT, the transformation is capable of processing 2D information, which refers to the optical images obtained from the microscope. The 2D FT and 2D iFT are defined as:

$$F(u, v) = \int_{-\infty}^{\infty} \int_{-\infty}^{\infty} f(x, y) e^{-i2\pi(ux+vy)} dx dy, \quad (2.3.3)$$

$$f(x, y) = \int_{-\infty}^{\infty} \int_{-\infty}^{\infty} F(u, v) e^{i2\pi(ux+vy)} du dv$$

Sometimes, normalization factors are also applied to the function and its transform [21]. One can mathematically post-process images obtained by a detector for analysis, or directly apply a lens to perform analog transformation without digital distortion. The concept of an analog Fourier transform is depicted in Figure 2.3–5.

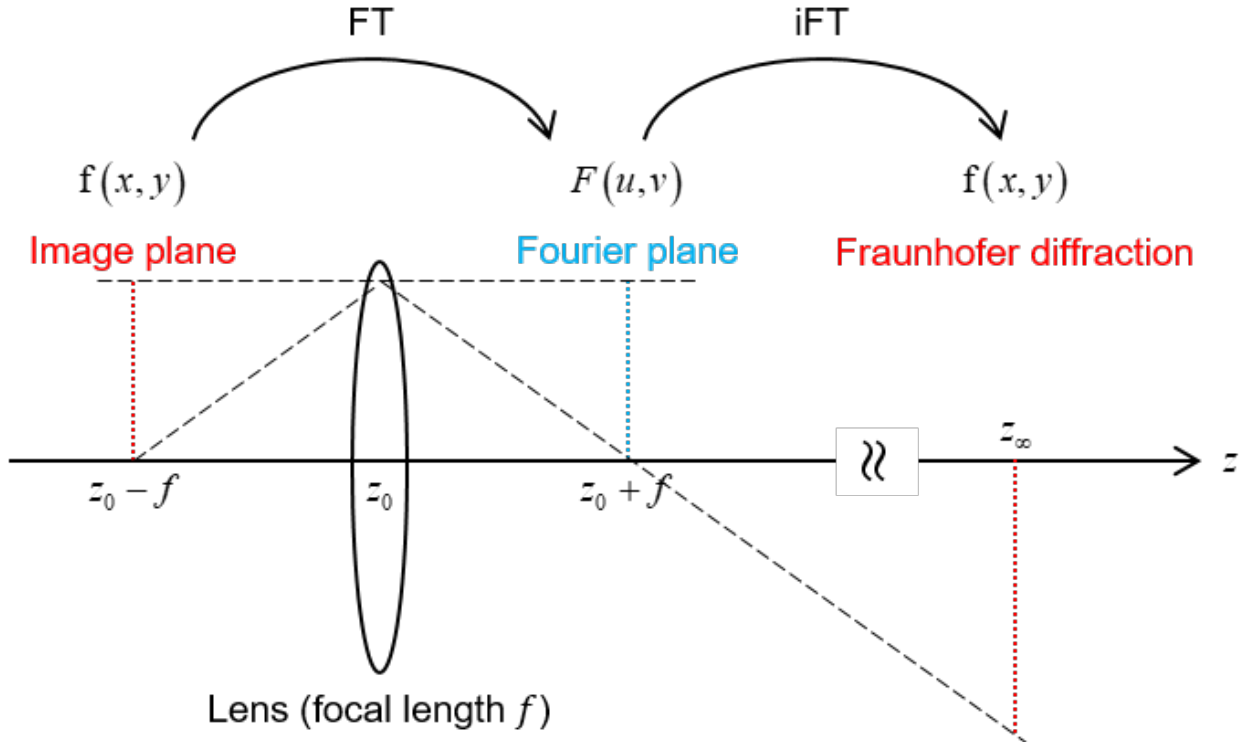


Figure 2.3–5 The concept of the analog Fourier transforms in an optical system. The Fourier transform is accomplished by applying a lens. The image on the image plane, viewed as a function of positions $f(x, y)$, is Fourier transformed to $F(u, v)$ and projected at the focal distance f on the other side of the lens, or the Fourier plane. As the distance becomes infinite, Fraunhofer diffraction is applied, which can be approximated as the inverse Fourier transform of the image on the Fourier plane.

Considering a lens at z_0 with focal distance f , the optical image of a sample represented by a function of $f(x,y)$ is at z_0+f . On the other side of the lens z_0-f , which is at the same focal distance from the lens, is the Fourier plane. The information of the image on the Fourier plane is transformed and can be expressed as $F(u, v)$. As the distance increases to infinity z_∞ , the iFT can be applied due to the Fraunhofer diffraction approximation. The schematic of Fraunhofer diffraction for reconstructing metaholograms will be discussed in Section 3.3.

Using a lens, one can produce the analog FT of images, and a pair of lenses are used for imaging in an optical system. In order to project a Fourier transformed image on the detector, odd numbers of lenses are used. Similar to projecting a sample image in an optical imaging microscope, the $4f$ system is applied to project Fourier plane images, as shown in Figure 2.3–6. If Lens A is at a focal distance f_1 from the Fourier plane, the $4f$ imaging system will project the Fourier plane image on the other side of the $4f$ system at a focal distance f_2 of the second lens (Lens B).

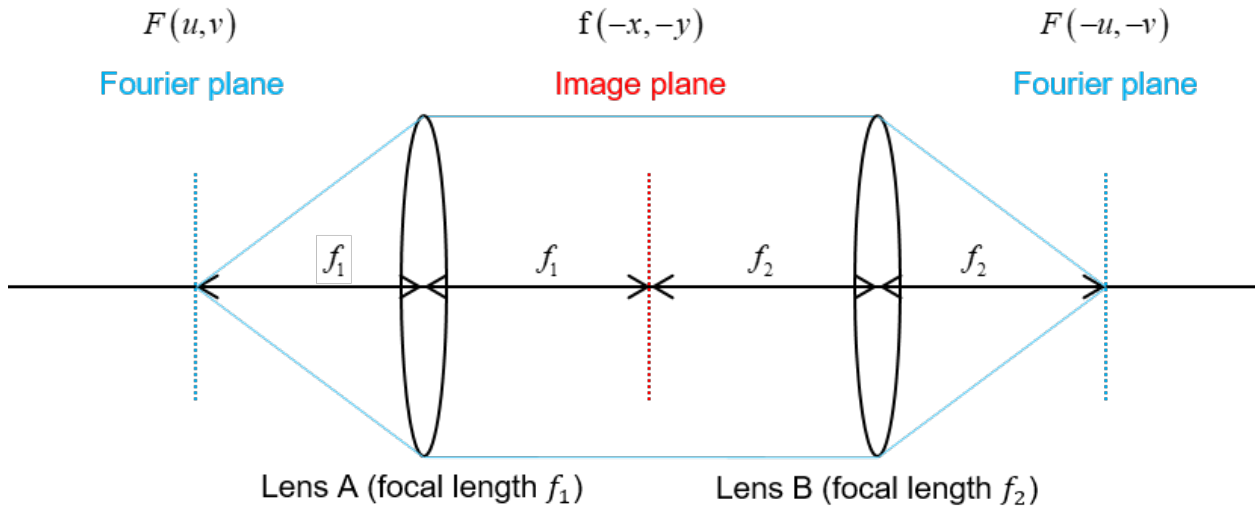


Figure 2.3–6 Images on the Fourier plane are projected with a $4f$ imaging system. When Lens A is at a focal distance from the Fourier plane, the image on the Fourier plane is generated at the focal distance of Lens B on the other side.

The ray-tracing for Fourier plane images is drawn with blue lines in Figure 2.3–1. When the component L4 in the detection path is flipped (i.e., not used), both imaging modes on the detectors (the spectrometer and the camera) are switched from the 3rd imaging plane to the 2nd Fourier plane. The image on the 2nd Fourier plane is projected from the 1st Fourier plane by the lens pair (L3 and L5) and processed by filters (Filter1 and Filter2) if applied. The separation between L3 and L5 does not necessarily need to be the sum of both focal lengths, since the image on the 1st Fourier plane becomes collimated with L3 and then focused (or Fourier transformed) by L5 onto the detectors. One can consider that the image on the 1st Fourier plane is a result of the lens L2 as discussed in Figure 2.3–5. Nevertheless, it is actually from the BFP of the objective in the microscope by the lens pair (the tube lens and L2). The BFP is the Fourier transform of the sample image acquired by the objective.

Since the image of a sample on the Fourier plane is a result of a Fourier transform, a measurement for observation can be conducted with a metahologram. Metaholograms, composed of discretized subwavelength pixels, are designed based on Fourier transforms. (More details are discussed in Section 3.3.) When a metahologram is under coherent illumination, the encoded image can be reconstructed on the Fourier plane or in the far field (far away from the sample). The images of a metahologram on the image plane and on the Fourier plane are displayed in Figure 2.3–7.

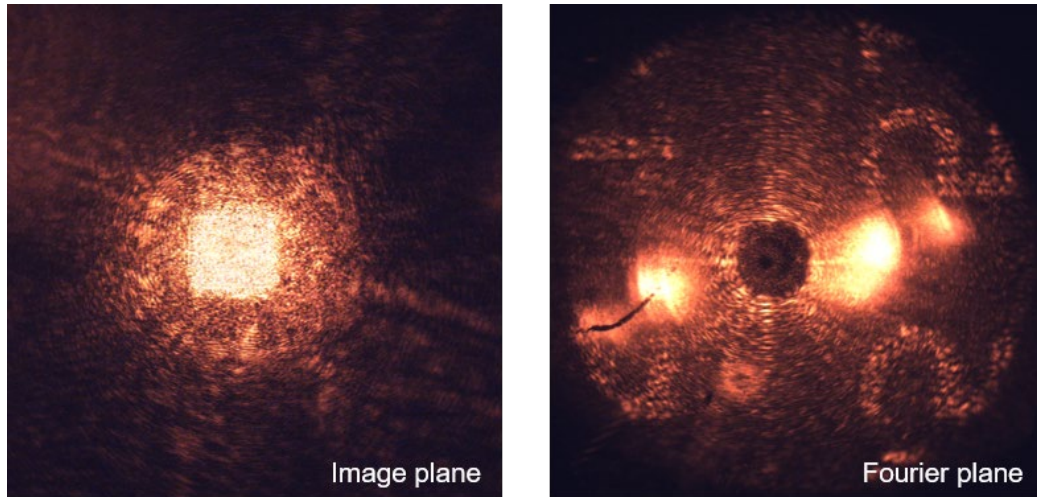


Figure 2.3-7 Metahologram sample on the image plane and on the Fourier plane. When illuminated with a polarized plane wave at $\lambda = 632$ nm, metahologram sample (a smaller brighter square in the image plane) on the image plane is observed. Meanwhile, the encoded image is reconstructed on the Fourier plane. The faint circle at the center in the Fourier plane image is due to the spatial filter (Fourier plane beam blocker) on the 1st Fourier plane, blocking the incident light.

Although a whole area of the metahologram is illuminated, the reconstructed image on the Fourier plane in Figure 2.3-7 does not cover the entire reconstructed area due to the limitation of numerical apertures of the used lenses in the detection path. Although the acceptance angle of an objective in the air ($NA = 0.9$) can reach up to 64° by definition, the other lenses (L2, L3, and L5) will also cut off the higher angular information. For example, L2 is a lens of 50 mm in diameter with a focal length of 200 mm. By definition, it has a numerical aperture $NA = 0.25$, so the acceptance angle is about 15° . Therefore, the reconstructed image on the Fourier plane only covers up to 15° , leaving the angular information above 15° cut off by the measurement system.

This imaging process is also applied in the Fourier plane. Edge detection on an image can be achieved by placing a spatial filter (beam blocker) as done in Figure 2.3-7 on the Fourier plane. The marker on the imaging plane is altered from a bright-field image (the image on the left in Figure 2.3-8) to a dark field image (the image on the right in Figure 2.3-8), which is due to low angular information of light (and incident light under normal incidence) is blocked.

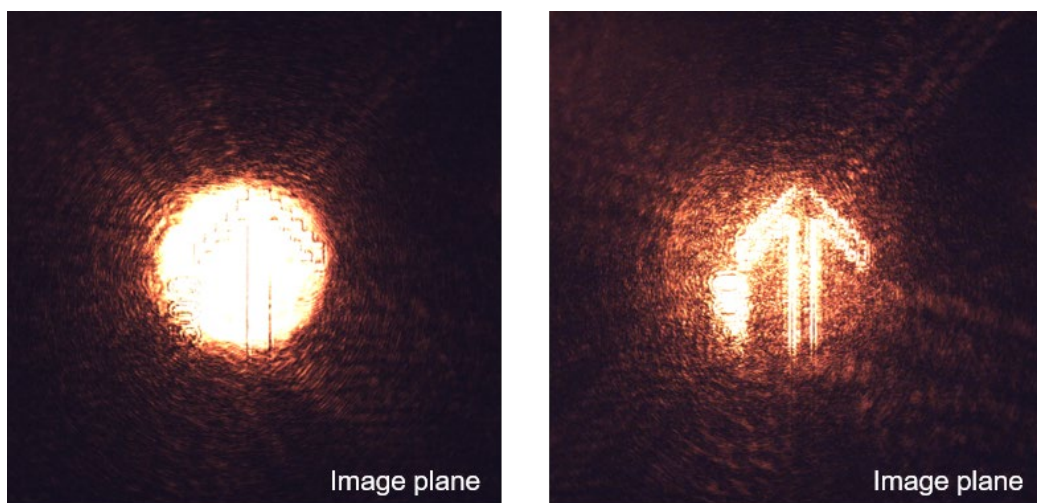


Figure 2.3-8 Image processing for dark-field images and edge detection. The image on the left shows a marker under normal incidence with a laser at $\lambda = 632$ nm. When the normal incident light is blocked in the Fourier plane (the faint central area in the Fourier plane as shown in Figure 2.3-7), the edge of the marker is observed, which mainly comes from the light in higher spatial frequency.

The image on the Fourier plane reveals not only the spatial frequency information of an image as shown in Eq. (2.3.3) but also the angular information of light. Angular information is the angle of light propagating with respect to an axis normal to the lens. When light propagating in all angles is coupled into a lens, light in different directions will be projected on different positions on the Fourier plane image, as shown in Figure 2.3–9.

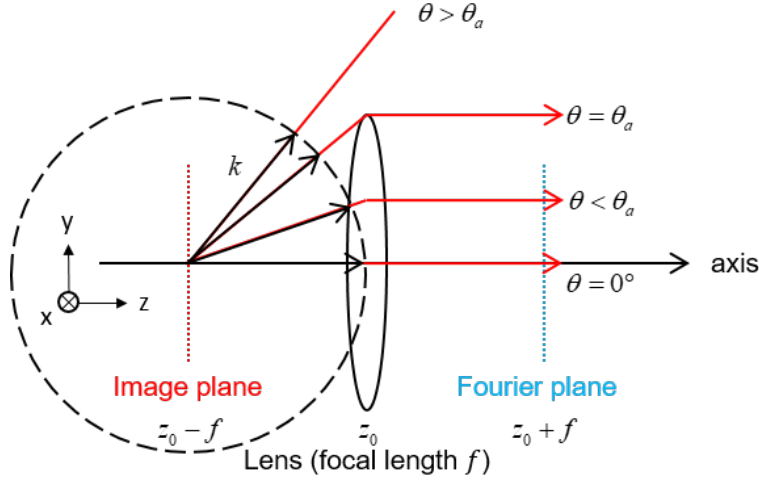


Figure 2.3–9 Angular information of light on the Fourier plane. The image in the Fourier plane contains the information of light propagating in different angles with respect to the axis normal to the lens. The acceptance angle of the lens θ_a is the boundary of the image on the Fourier plane. The dashed circle indicates the wave vector of light.

Although the spatial frequency of an image u and the angular information of light ϑ seem to be different concepts, they are closely related and can be described with the following equation:

$$2\pi \times u = k \times \cos \theta, \quad (2.3.4)$$

where $u = 1/x$ is the spatial frequency of an image on the Fourier plane, k is the wave number of light defined as $k = 2\pi/\lambda$, λ is the wavelength of light, and ϑ is the angular information of light.

Measurements on the angular information of light scattered from structures on the Fourier plane are used to characterize the performance of metasurface devices such as beam-steering devices [22] and Fresnel zone plates with gold and silver alloys [19]. It is also used in measuring the radiation pattern of nanostructures [23].

The beam-steering metasurface devices are opaque (e.g., the SEM images are shown in Figure 2.2–10 and Figure 2.2–11.), so the single wavelength laser is placed in the reflection excitation path as shown in Figure 2.3–10. Collimated light is focused at the BFP of the objective, producing plane wave illumination. Together with the linear polarizer (LP1), the plane wave becomes linearly polarized. When the focused spot is aligned at the center of the BFP, it is guaranteed that the sample is under normal incidence by polarized plane waves. Placing a silver mirror allows for observation of the normal reflected light on the Fourier plane, which is aligned at the center of the BFP of the objective, as shown in Figure 2.3–10. The intensity of light (incident and reflected light) is integrated as a reference for calculating the efficiency of devices. Since a silver mirror has up to 99.7 % reflectance at $\lambda = 980$ nm in air, this could be why the measured efficiencies in the paper are only half of the values obtained in the simulations. When the mirror is replaced with beam-steering metasurface devices, normal incident light is redirected to the designed angle. On the Fourier plane, the reflected light is mainly steered at 43° , which is the acceptance angle of the objective. Some normal reflection light can be observed at 0° , which can be the light reflected by the device or the objective. More analyses of the performance of beam-steering metasurface devices including dielectric ones in transmission are discussed in Section 3.4. Robustness analysis.

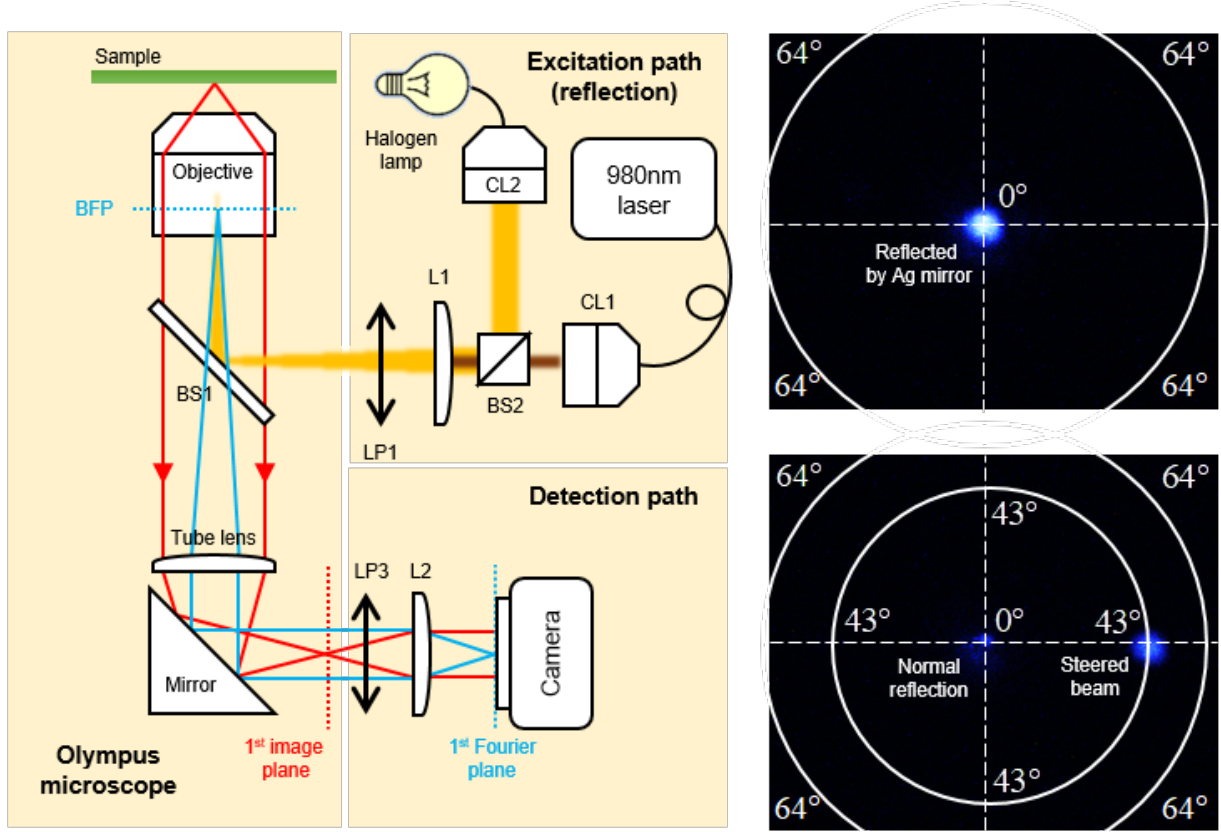


Figure 2.3-10 Measurement setup for analyzing beam-steering metasurface devices modified from Figure 2.3-1. A single wavelength laser emitting at $\lambda = 980$ nm is in the reflection excitation path. A polarized plane wave illuminates the sample under normal incidence. The objective (Leitz Wetzlar PL APO 50x/0.90 air) is used, which collects scattered light up to 64° . The image on the BFP is projected onto the camera. Polarized light is analyzed by a linear polarizer (LP3). Images on the Fourier plane are detected with a color camera.

The focal spot of the reflecting Fresnel zone plate (FZP) lens, made of two stoichiometric gold and silver alloys ($\text{Au}_{0.2}\text{Ag}_{0.8}$ and $\text{Au}_{0.8}\text{Ag}_{0.2}$), is taken on the 3rd image plane with the camera. The scenario is as presented in Figure 2.3-1 with the supercontinuum laser emitting at $\lambda = 532$ nm in the reflection excitation path. For convenient illustration, the focal spot of a lens in the transmission is provided. In Figure 2.3-11, the Lens with focal length f is on the sample side, and the pair of lenses (Lens A and Lens B) is for imaging. When a plane wave impinges on the sample, light is focused at a focal distance f . The camera detects the image where Lens A is focused. By adjusting the position of Lens A, the image plane can shift from the surface to the focal spot of the sample. The focal spot is thus measured on the camera. However, incident light and the focused spot of a reflective lens will overlap under normal incidence.

In measuring the reflective FZP, the simplified schematic is shown in Figure 2.3-12(a). Collimated incident light is first focused on the BFP with a lens (L1) and a beam splitter (BS), generating plane wave illumination on the lens sample. When the sample is under normal illumination, the incident light and focused spot overlap, which makes it difficult to distinguish the two. To get rid of the normal incident in the measurement, a small trick is applied. The objective is first focused on the sample, and the image mode is switched to the Fourier plane by flipping the L4 (not being used). The overlap of incident light and focused beam on the Fourier plane is presented in Figure 2.3-12(b). When the lens sample is tilted a few degrees, the focal spot deviates from the axis. A beam blocker is then applied to block the incident light at the center on the 1st Fourier plane. When switching back to the optical microscope mode, edge detection on the FZP is observed. The focal spot is measured when the image plane matches the focal distance of the Lens sample.

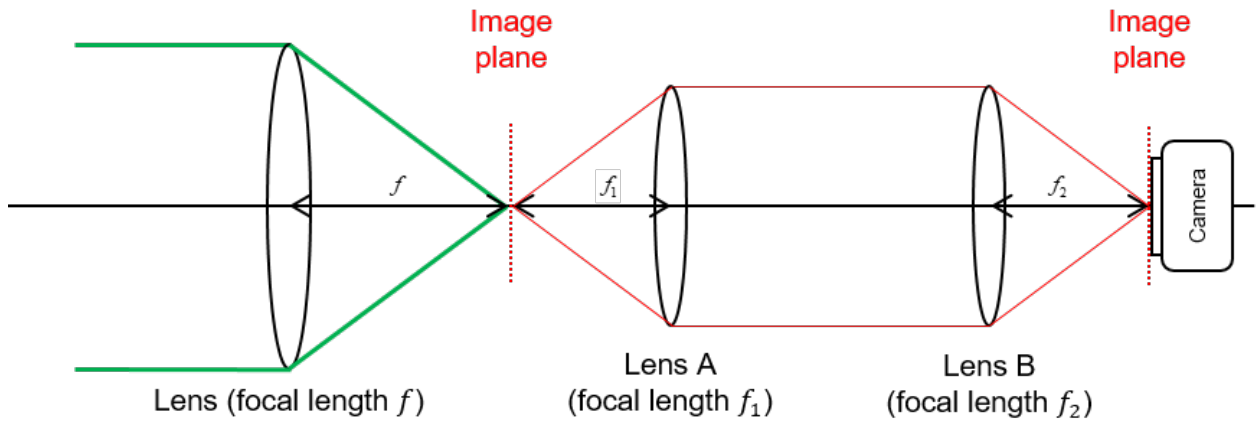


Figure 2.3-11 The scenario of measuring the focal spot of a lens in transmission type. A collimated beam impinges on the sample (lens) and is focused at a focal distance f from the sample. The camera with the pair of lenses (Lens A and Lens B) detects the intensity of light on the image plane.

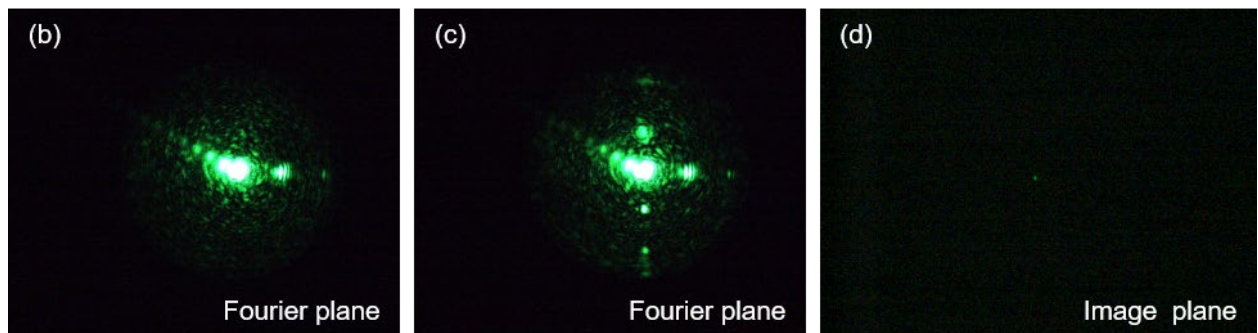
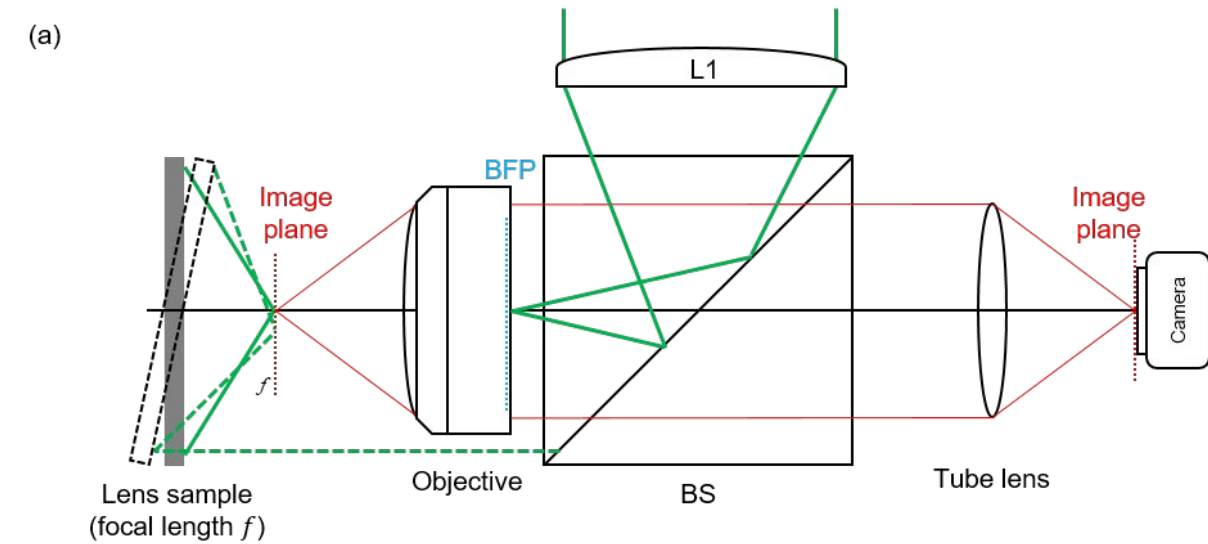


Figure 2.3-12 Measurement on the Fresnel zone plate lens in a reflection manner. (a) The scenarios of measuring the focal spot of a reflective lens sample with and without tilting. (b) The image on the Fourier plane without tilting the sample, where the normal incident light overlaps with the focused light. (c) The image on the Fourier plane when the sample is tilting at a small angle. (d) The focal spot on the image plane after blocking the normal incident light.

2.3.3 Polarization spectral microscopy

Previously, measuring a spectrum with an incoherent and unpolarized light source (halogen lamp) was introduced in sub-Section 2.3.1. However, in numerical simulations, polarized light is applied instead. That is, the oscillating direction of electric fields needs to be assigned. Besides, the geometries of plasmonic structures are mostly polarization-sensitive except for disk-shaped or square structures. In order to match the measured and simulated spectra, a linear polarizer (LP2) and an analyzer (LP3) are required to duplicate the simulation surroundings. Quarter waveplates are needed to produce circularly polarized light, and are placed after the linear polarizer (LP2) and before the analyzer (LP3). The function of a quarter waveplate is to convert linearly polarized light into circularly polarized light. To analyze the circularly polarized light, a quarter waveplate can convert the circularly polarized light into linearly polarized light. The outcome of polarized light can be calculated with Jones calculus by taking the product of the Jones matrix of the optical element and the Jones vector of the incident polarized light.

There are six major polarization states of light, including x -, y -, $+45^\circ$ -, -45° -, right circular (RC), and left circular (LC) polarizations. These oscillation patterns can be clearly observed when projected onto a plane perpendicular to the propagation direction of light. Figure 2.3–13(a) shows the electric field oscillates on the XY plane as polarized light propagates in the $+z$ direction. Take x - and y -polarized light for example; here, the electric field oscillates either along x -axis or y -axis. In each case, only the E_x or E_y component of the electric field is involved. $+45^\circ$ and -45° polarizations are generated when both E_x and E_y components exist in phase with equal amplitude. When the phase difference between E_x and E_y components is $\pm\pi/2$, circularly polarized light will be produced ($+$ for right circular and $-$ for left circular). These polarization states can also be described with Stokes parameters, which include S_0 , S_1 , S_2 , and S_3 . On the Poincaré sphere, as shown in Figure 2.3–13(b), a Stokes vector (S_0 , S_1 , S_2 , S_3) indicates the composition of polarization states of polarized light. In this sphere, polarization states on both sides of each axis are orthogonal.

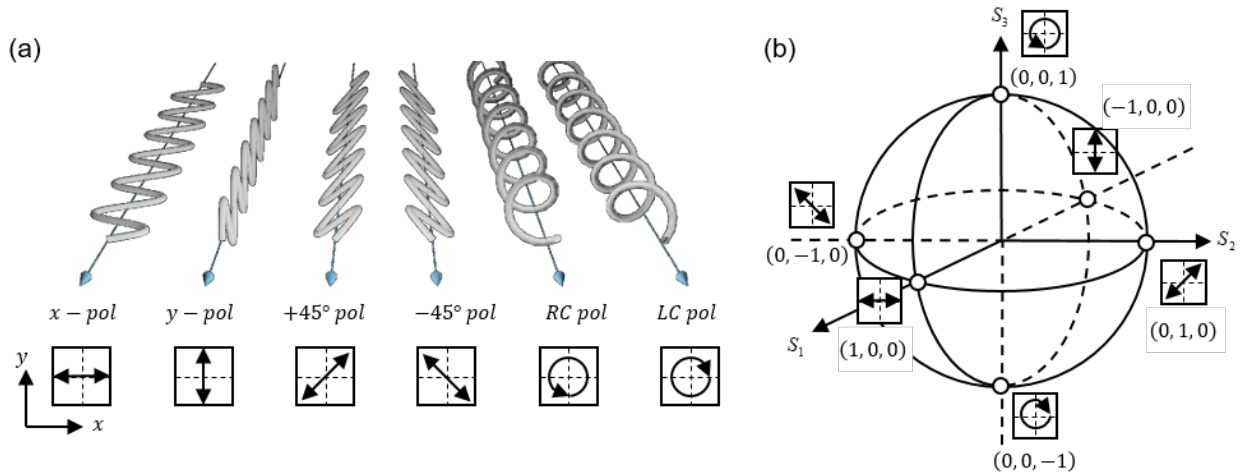


Figure 2.3–13 Polarization states on a Poincaré Sphere. Projecting the entire cycle of the oscillation path on a plane perpendicular to the propagating direction of light can clearly observe the pattern of polarization states.

In fact, optical components are still polarization-sensitive even if they are originally designed for unpolarized light. Metasurfaces composed of structures with low symmetry also have different reflectance and transmittance depending on polarization states. In the following, spectral measurements on polarization converting metasurfaces are presented.

The following section has been accepted for publication in Applied Optics (2022), <https://doi.org/10.1364/AO.469399>

Title: Pitfalls in the Spectral Measurements of Polarization-Altering Metasurfaces

Authors: Hsiang-Chu Wang and Olivier J.F. Martin*

Abstract: The optical characterization of metasurfaces and nanostructures that alter the polarization of light is tricky and can lead to unphysical results, like a reflectance beyond unity. We track the origin of such pitfalls to the response of some typical optical components used in a commercial microscope or a custom-made setup. The beam splitter or some mirrors in particular have a different response for both polarizations and can produce wrong results. A simple procedure is described to correct those erroneous results, based on the optical characterization of the different components in the optical setup. With this procedure, the experimental results match the numerical simulations perfectly. The methodology described here is simple and will enable the accurate spectral measurements of nanostructures and metasurfaces that alter the polarization of the incoming light.

Introduction:

Since its inception in the 17th century, the optical microscope has become the key instrument to investigate light-matter interactions [24]. Over the last decade, it has enabled the development of metasurfaces: artificial optical components built from sub-wavelength nanostructures, the so-called meta-atoms [25-29]. Here, by optical microscope, we refer to any type of platform, from the most sophisticated commercial device, to its simplest counterpart built from an illumination path, a sample holder, an objective and a tube lens.

Among the demonstrated, the meta-atoms geometries and materials play a key role in determining the metasurface function. The geometries come in a variety of shapes. For the materials, plasmonic metals [30-32], or high permittivity dielectrics [3, 33-41] are utilized, with some emerging alternative routes such as hybrid meta-atoms that combine metal and dielectrics [42-44], or alloyed nanostructures [19].

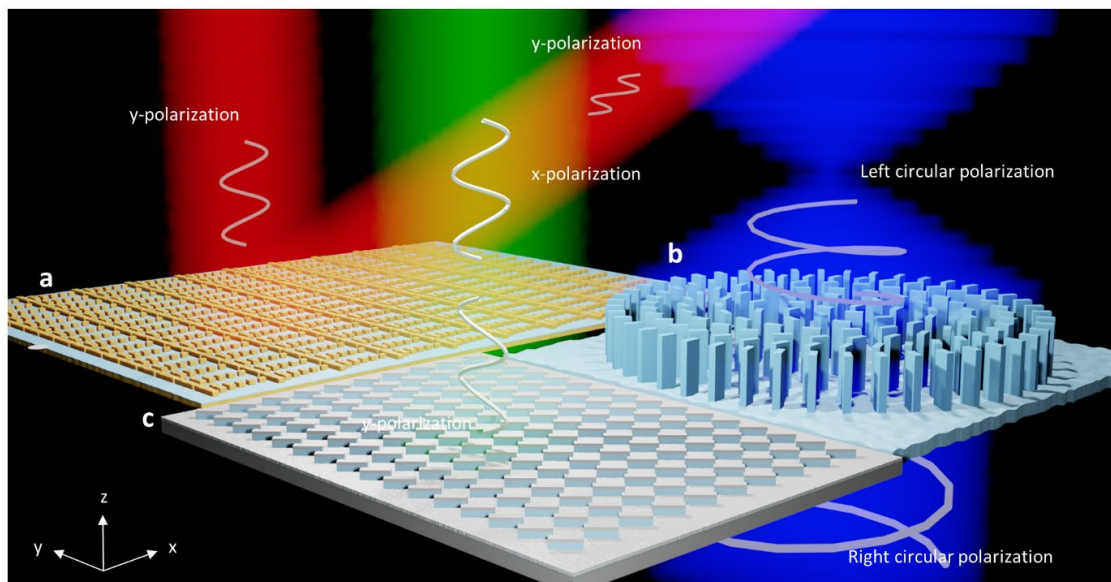


Figure 2.3–14 Examples of metasurfaces and the way they modify the polarization of light. (a) polarization-sensitive meta-atoms for wavefront manipulation, requiring specific polarized light for excitation and detection. (b) Metalens based on Pancharatnam-Berry phase that transforms right circular polarization into left circular polarization and vice versa. (c) Structural metasurface built from protruding nanorods rotated by 45° that convert white light into a specific color upon reflection.

To mimic classical optical elements, metasurfaces usually manipulate the phase of light, which in turn requires manipulating its polarization [45]. Thus, most metasurfaces produce reflected or transmitted light with a polarization that is different from that of the incoming light. This polarization altering can cause some difficulties when measuring metasurfaces in an optical microscope and the objective of this paper is to document those difficulties and describe workarounds. Figure 2.3–14 shows some popular metasurfaces that are sensitive to polarization: (a) beam-steering devices utilizing phase gradients that operate only for a specific polarization direction [23, 46, 47]; (b) a metalens that uses the Pancharatnam-Berry (PB) phase and is excited with a given circular polarization, while the resulting light phase has the opposite handedness [2, 48-50]; (c) and some structures even alter the incident polarized light into another polarization [51-55]. From these examples, we observe that the corresponding meta-atoms have a low symmetry, like a rectangular shape that responds differently to incident orthogonal polarizations [56] and causes complications in their optical characterization. For completeness, we must also mention another class of metasurfaces that are built from high symmetry meta-atoms, like for example disks, and are polarization insensitive [19, 57-59]. We are not concerned with such metasurfaces in this work.

Optical microscope system:

The custom-built microscope system used in this work is shown in Figure 2.3–15, it is constructed around a commercial inverted optical microscope and includes a spectrometer and a camera. Our aim is to measure the metasurface spectral response over the entire visible range and compare it with numerical simulations. Indeed, during the design of a metasurface, full-wave simulations are used to compute the amplitude and phase produced by a meta-atom. Here we resort to Comsol Multiphysics vers. 5.6 for this task. For numerical simulations, it is straightforward to select one specific illumination polarization and then analyze the polarization of the scattered light: this process is entirely numerical and requires only projecting the electromagnetic field on a basis like the Jones vectors to obtain the amplitude, phase and polarization of the scattered light [60]. The procedure is more complicated in an experiment since physical components such as polarizers, analyzers, beam splitters, mirrors and wave plates must be used and these components have a response that changes over the spectral range of interest [45].

The measurement setup shown in Figure 2.3–15 is operated in reflection mode, with two additional key components: a linear polarizer (LP) in the excitation path and an analyzer (LP) in the detection path. By adding these two linear polarizers, we intend to illuminate the metasurfaces with linear polarized light and analyze the polarization states of reflected light. This system can be separated into three parts: the optical microscope in Figure 2.3–15(a), the illumination in Figure 2.3–15(b), and the detection in Figure 2.3–15(c). The microscope is an inverted microscope (Olympus, IX73) composed of four components in brief: a 50/50 plate beam splitter (Chroma, AHF F21-020), an objective (LUCPLFLN 60X, NA = 0.7), a tube lens, and a dielectric mirror. When the halogen lamp is on, light first couples into the fiber and becomes collimated by the Collimator (Objective 10x air). Afterwards, the lens L1 (Thorlabs, LA1172-A) and LP (Thorlabs, WP25M-UB) are used to focus the beam at the back focal plane (BFP) of the objective, producing a plane wave excitation on the sample metasurface. To ensure normal incidence, we examine in the Fourier plane on the camera (Flir, CM3-U3-5055C-CS) that the beam is at the center of the objective. Light reflected by the sample is collected by the same objective with numerical aperture NA = 0.7. The NA indicates the angle θ up to which the scattered light can be coupled into the objective: $NA = n \sin(\theta)$, where n is the refractive index of the environment (air in this case, $n = 1$). Hence, the scattered light between $\pm 44.4^\circ$ can be collected by the objective. After passing the 50/50 plate beam splitter, the sample image is projected on the first image plane with the assistance of the tube lens and the dielectric mirror belonged to the microscope. Generally, a camera is placed at the exit of the microscope for imaging. On the contrary, here we put LP (Thorlabs, WP25M-UB) instead to analyze the polarization state of the reflected light. Besides, we also implement a 4f system for post-processing the image in the first image plane. When the lens L4 in Figure 2.3–15(c) is removed, images on the Fourier planes such as the BFP of the objective and the first Fourier plane will be projected onto the second Fourier plane. On the other hand, the first and second image planes will be projected onto the third image plane when all the lenses are in place. This 4f imaging system is optimized with four lenses L2-L5 (Thorlabs, LA1979-A, LA1979-A, LA1131-A, LA1608-A) for special-selective spectral measurements, high-pass or low-pass imaging, and for Fourier plane

imaging. Here, we only need to analyze the spectrum of the sample under polarized illumination, so we use this 4f system only to extend the image onto the spectrometer with the LP on the first image plane to analyze the polarization.

Building the measurement setup from a commercial microscope provides stability, robustness and positioning accuracy, which is important for small samples, like metasurfaces; on the other hand, there might be some "hidden" optical components within the microscope body that require detailed characterization to fully understand the optical path within the microscope.

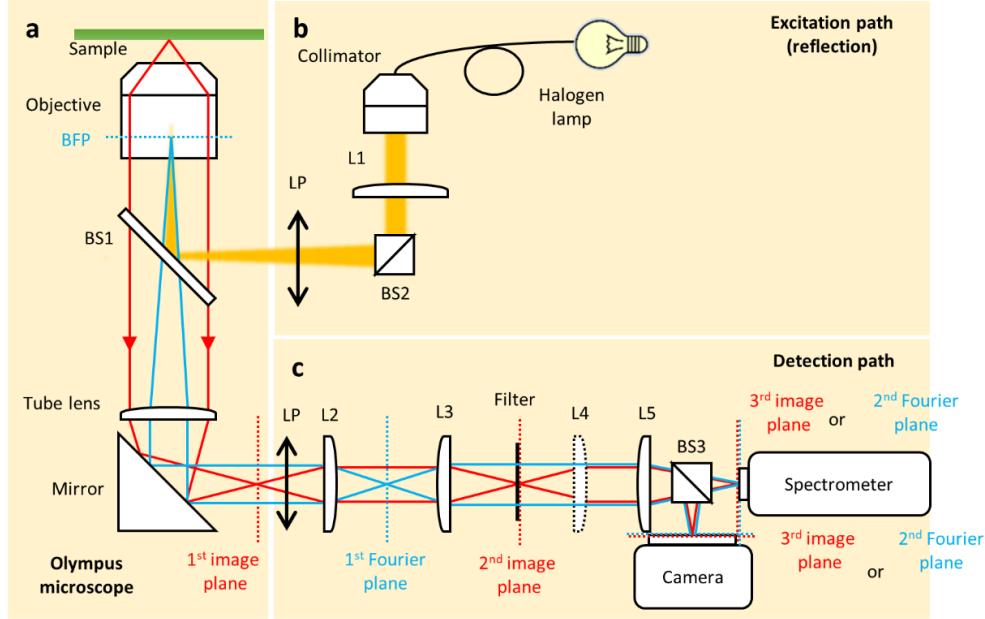


Figure 2.3–15 Schematic of the optical system for measuring spectrum of metasurfaces under polarized illumination. (a) The schematic of an inverted microscope (Olympus IX73). (b) Excitation path by a halogen lamp in reflection type. (c) Detection path composed of a 4f system and a spectrometer with a CCD camera.

Metasurface measurements

We consider a metasurface built from silver nanorod, which has been used by several authors [61-68]. This simple geometry exhibits a chirality that arises from the polarization of the incident light, as soon as it is not parallel to one of the structure's symmetry axes [69]. When this is the case, part of the incident polarization is converted into the orthogonal polarization, producing a dichroic response. We will show that special care must be taken when measuring such a metasurface and unexpected, polarization-related, effects might occur in the experiment, which are not present in the full-wave simulation, since for the latter, there are no additional polarization-sensitive optical components like mirrors or beam splitters to retrieve the optical signal.

The schematics of the meta-atom is described in the inset of Figure 2.3–16(a): it is a rectangular silver rod ($W = 40$ nm, $L = 110$ nm) inside a square lattice with period $P = 300$ nm in both directions. A 150 nm thick negative photoresist HSQ (DuPont, Hydrogen Silsesquioxane) written with electron beam lithography defines the nanostructure on a Si substrate. 40 nm thick silver is evaporated (Leybold Optics, LAB 600H) on the entire structure, producing an Ag nanorod that protrudes from an Ag background with complementary geometry. This simple fabrication approach has been used to build a variety of plasmonic nanostructures and metasurfaces [70-79]. This meta-atom is illuminated with polarized (x or y polarizations) light propagating in $-z$ direction, while the reflected light is collected with an analyzer (x or y polarizations). This leads to four combinations of reflectance spectra obtained from the combinations of incident and reflected lights: R_{xx} , R_{xy} , R_{yy} and R_{yx} . The first indices indicate the incident polarizations, while the second indices indicate the analyzer directions. Figure 2.3–16(a) shows the simulated spectra when the rod is aligned with the x -direction;

R_{xx} and R_{yy} are present while R_{xy} and R_{yx} vanish. The corresponding measurements, shown in Figure 2.3–16(b) together with the scanning electron microscope (SEM) image of the sample, agree well with the calculations. To distinguish between calculated reflectance and measured reflectance, we describe the latter with subscripts that correspond to the polarization used in the experiment: R_{ss} (corresponding to R_{xx}), R_{sp} (R_{xy}), R_{pp} (R_{yy}) and R_{ps} (R_{yx}).

When the rod is rotated by 45° , the cross-polarization term R_{xy} appears in the calculations, Figure 2.3–16(c). This cross-polarization term indicates that the metasurface exhibits chirality when the incident polarization is not parallel to the meta-atoms axes [69]. Besides, the R_{xx} (blue line in Figure 2.3–16(c)) exhibits now a deep trough and behaves in a complimentary way to R_{yy} . Due to the structural symmetry, the spectra R_{xx} and R_{yy} overlap with each other, and so do the spectra of R_{xy} and R_{yx} . This spectral change due to the rotation of the same structure caught our attention and we measured the original sample rotated by 45° , as indicated in the inset of Figure 2.3–16(d). Surprisingly, unphysical reflectance data are obtained in this case, with a reflectance larger than unity, Figure 2.3–16(d). This disagreement between simulations and measurement, prompted us to investigate the optical responses of the components used in the setup.

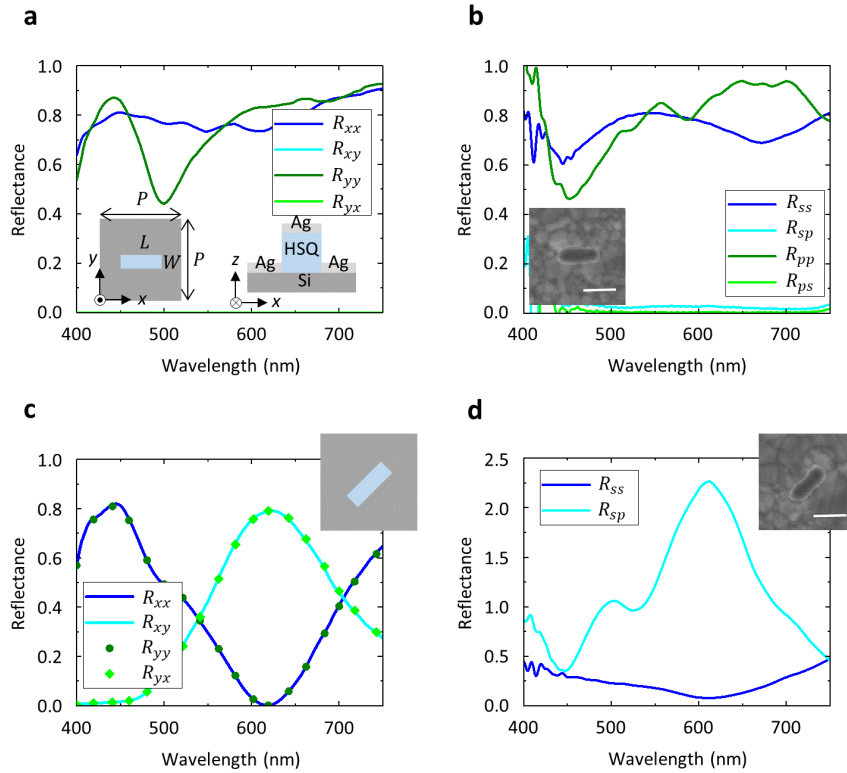


Figure 2.3–16 Simulated and measured spectra for the metasurface built from an array of Ag meta-atom rods. (a) Simulated and (b) measured reflectance spectra when the rods are aligned along the x-direction. The insets in panel (a) sketch the meta-atom, while the inset in panel (b) show the SEM image of the fabricated structure. (c) Simulated and (d) measured reflectance spectra when the sample has been rotated by 45° (Scale bars 100 nm).

It turns out that the optical responses of plate beam splitters is polarization-sensitive, i.e. their transmittance is different for s- and p-polarized light (s-polarization is defined as the electric field perpendicular to the plane of incidence, while p-polarization has the electric field parallel to the plane of incidence). The transmittance measured for the plate beam splitter used in our setup (Chroma, 50/50 AHF F21-020) is shown in Figure 2.3–17(a). The transmittance for unpolarized light (magenta line) in Fig. 4(a) is the average of s-polarization (purple line) and p-polarization (red line). This polarization-dependent transmittance gives rise to different intensities depending on the polarization of the light. Even for a halogen lamp with equal intensities in s- and p-polarizations, the measured spectra after the plate beam splitter deviate

from each other, as shown in Figure 2.3–17(b): at first sight the spectra appear comparable between $\lambda = 400$ nm and 550 nm, but when magnified they are still different. To quantify this difference, we plot in Figure 2.3–17(c) the intensity ratio for both polarizations. This ratio is overall larger than one and exhibits a fluctuation pattern; it indicates that the reflected light for p-polarization can have larger transmittance than for s-polarization. This explains the unphysical data observed in Figure 2.3–16(d): if the incident light is s-polarized and its polarization converted by the meta-atom, the reflected spectrum will be multiplied by a factor larger than one, producing a response where energy appears to have been generated! We will discuss this in greater details in the next section. Ideally, the transmittance ratio between both polarizations should be constant to avoid any polarization-dependency. It turns out that cube beam splitters do not have such a drawback, as shown in Figure 2.3–17(d) for the element (Thorlabs, 70/30 BS022): the transmittances for each polarization almost overlap. Similar plots to those presented in Figs. 4(b) and 4(c) for the plate beam splitter are shown for the cube beam splitter in Figure 2.3–17(e) and Figure 2.3–17(f). In that case, the transmittances for both polarizations are similar and their ratio a constant over the visible spectrum. Therefore, a cube beam splitter is a good option for measurements where polarization plays a role. Unfortunately, there are no commercial holders for cube beam splitters to be mounted in commercial microscopes; in our case, we fabricated one using 3D printing. Fortunately, it is still possible to correct the spectrum measured in Figure 2.3–16(d), as will be discussed next.

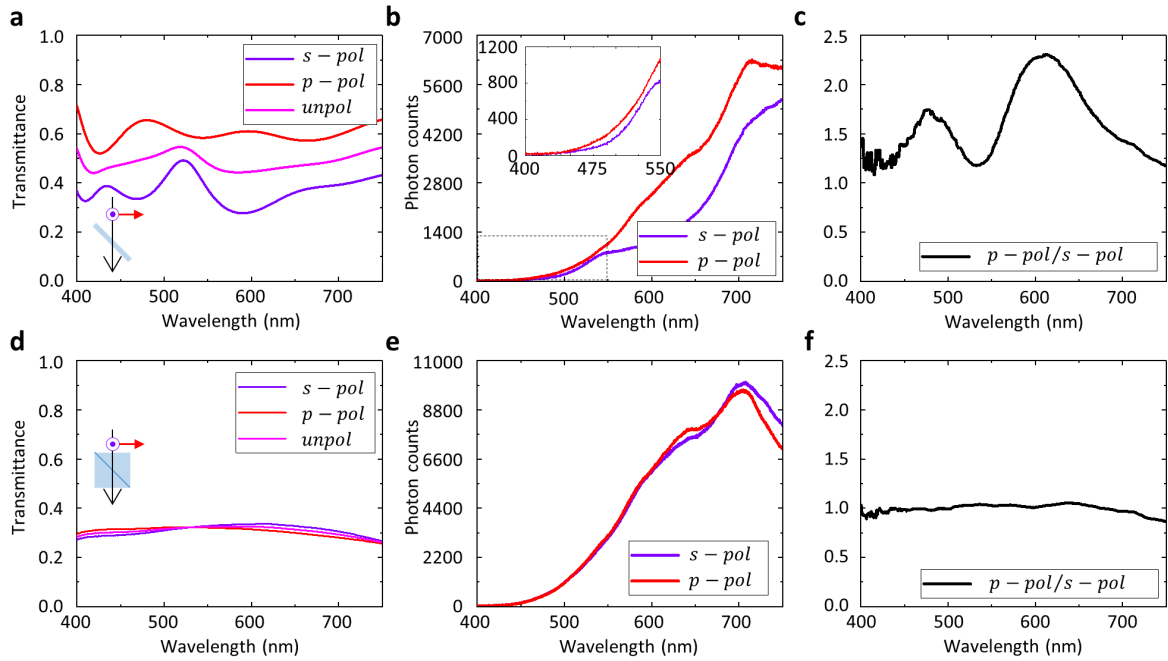


Figure 2.3–17 Comparison between the optical responses in terms of polarizations for a plate beam splitter and a cube beam splitter. (a) Transmittance of the plate beam splitter (Chroma, 50/50 AHF F21-020). (b) Transmittance for polarized light passing this plate beam splitter. (c) Corresponding transmittance ratio. (d) Transmittance of the cube beam splitter (Thorlabs, 70/30 BS022). (e) Transmittance for polarized light passing this cube beam splitter. (f) Corresponding transmittance ratio.

Let us dwell further into the details of the issues that can arise when measuring with the system shown in Figure 2.3–15 a sample that modifies the incident polarization, e.g. the situation shown in Figure 2.3–16(c) when the sample has been rotated by 45° . Figure 2.3–18(a) is the case when the sample reflects light without changing the polarization state. We consider s-polarized incident light with spectrum I_s that is first reflected by the beam splitter so the spectrum can be expressed as $R_s I_s$, where R_s is the reflectance of the beam splitter for s-polarization. We assume that the objective is lossless and polarization-insensitive. This polarized light reached the sample and is reflected without changes of polarization, with R_{ss} being the sample reflectance. Hence, the reflected spectrum becomes $R_{ss} R_s I_s$ and after passing through the beam splitter with transmittance T_s for s-polarization, the measured spectrum becomes $M_{ss} = T_s R_{ss} R_s I_s$. The reflectance of a sample is defined as the measured spectrum M_{ss} divided by the incident light. For the inverted

microscope, we obtain the incident light by placing a silver mirror with unit reflectance at the location of the sample. Since this silver mirror does not change the polarization of the normal incident light, the reference spectrum measured with the mirror is $M_{ss}^{ref} = T_s R_s I_s$ and the sample reflectance R_{ss} is obtained by dividing the spectrum with the sample by that reference spectrum.

On the other hand, considering the case shown in Figure 2.3–18(b) where the sample alters the incident s-polarized light into p-polarization, the measured spectrum becomes $M_{sp} = T_p R_{sp} R_s I_s$, where R_{sp} is the amount of light converted by the sample from s- to p- polarization upon reflection and T_p is the beam splitter transmittance for p-polarization. If one used the same definition for deriving the sample reflectance R_{sp} and divide the measured spectrum by the reference spectrum, one obtains $R_{sp} T_p / T_s$ instead of R_{sp} ; the properties of the beam splitter bias the response! It is however possible to retrieve the correct sample response by dividing the measured spectrum with the ratio T_p / T_s . For example, if one divides the spectrum in Figure 2.3–16(d) with the polarization ratio T_p / T_s shown in Figure 2.3–17(c), one retrieves the correct sample reflectance R_{sp} , see the cyan line in Figure 2.3–18(c). Note that the corrected reflectance R_{sp} shown in Figure 2.3–18(c) recovers around $\lambda = 600$ nm the broad resonance for R_{xy} and the dip for around R_{xx} computed in Figure 2.3–16(c).

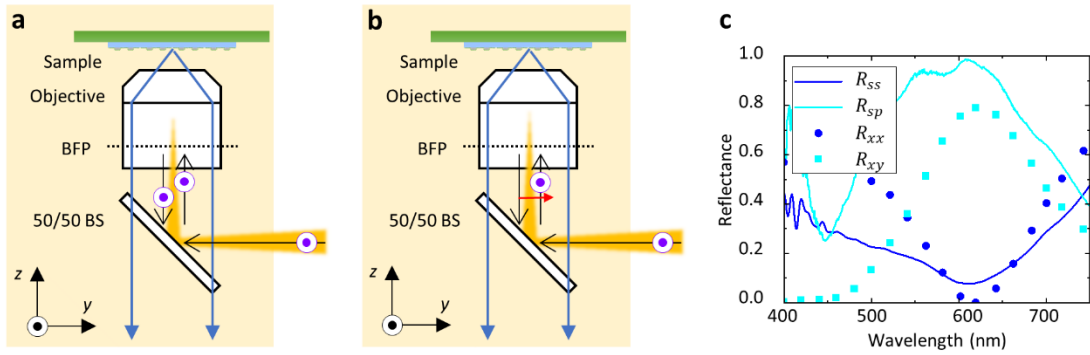


Figure 2.3–18 Schematic of polarized light propagating in a microscope with a polarization-sensitive plate beam splitter. (a) S-polarized light reflected by a sample and the reflected light polarized in the same direction as incident light. (b) S-polarized light reflected by a sample that alters the polarization into p-polarization as reflected. (c) Corrected spectra from measurements compared with the simulated.

In addition to beam splitters, mirrors used in the setup can affect the measurements. For example, silver mirrors serve as perfect reflectors since they are capable of reflecting the incident light over the entire spectrum, from the visible to the near infrared with little absorption. The reflectance of a silver mirror can be calculated with the Fresnel coefficients [80] using the permittivity from Johnson and Christy [81], as shown in Figure 2.3–19(a) for light incident at 0° or 45° as is the case in the optical setup used here. At normal incidence 0° , the reflectances overlap both polarizations. On the other hand, for 45° incidence the reflectance for s-polarized light increases up to 1% compared to the normal incidence, while it drops up to 1% for p-polarized light. Furthermore, the difference of phase shift between s- and p-polarized light reflected by the mirror and computed with the Fresnel coefficients increases with the angle of incidence, Figure 2.3–19(b). As a consequence, when both components are present, the reflected light becomes elliptically polarized. This is illustrated in Figure 2.3–19(c), where we show the polarization ellipse for light reflected from a silver mirror at $\lambda = 532$ nm. The angle of incidence is 45° and four different polarizations are considered: s- and p- polarizations, which are conserved upon reflection; while diagonal and anti-diagonal polarizations lead to elliptically polarized reflected light. This behavior originates from the complex dielectric function of silver and would not occur with a dielectric mirror. Therefore, when using silver mirrors in a measurement system, polarizations in horizontal and vertical directions can be retained without being modified while other polarization states need to be handled with care.

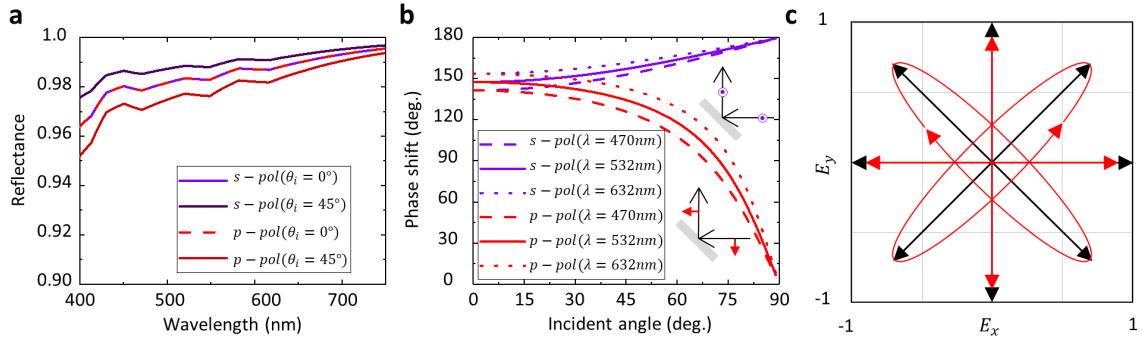


Figure 2.3–19 Reflectance and phase shift for polarized light reflected by a silver mirror derived from Fresnel coefficients. (a) Reflectance spectrum in the visible range for s- and p-polarized light incident at 0° and 45° . (b) Phase shift as a function of incident angle for s- and p-polarized light at three primary wavelengths. (c) Polarization patterns for the reflected light at 532 nm for light incident at 45° on a silver mirror for four different incident linear polarizations: s- and p- polarizations are conserved, while diagonal and anti-diagonal incident linear polarizations produce an elliptically polarized plane wave.

Conclusion

In summary, we have analyzed the fate of polarization as light propagates through a conventional microscopy setup used to measure optical nanostructures, metasurfaces, or polarization-altering optical components. When the sample alters the incident polarization, as is the case for most specimen, special care must be taken to avoid unphysical effects, such as a reflectance beyond unity or experimental measurements that do not match numerical simulations. These effects originate from the polarization-sensitive response of the components used to build the setup, especially the beam splitter. Especially, plate beam splitters can have a very different response for both polarizations, while cube beam splitters are much better for those measurements; unfortunately, their mounting into a commercial optical microscope requires a custom-made holder.

A simple procedure has been explained to correct for those optical components, such that correct results are obtained in spite of them. This procedure is based on carefully characterizing each optical component over the entire measurement spectrum. With this procedure, the experimental results match the numerical simulations perfectly. The analysis has been extended to other components in the measurement setup, like mirrors.

The procedures described here are simple and will enable the accurate spectral measurement of nanostructures and metasurfaces that alter the polarization of the incoming light.

2.4 Summary and outlook

These introduced simulation methods, fabrication approaches, and characterization tools establish the basis for studying meta-atoms and their applications in the following chapters. In Section 2.1, although SIE and COMSOL are introduced, other mentioned simulation methods can also be used, such as FDTD based Lumerical and CST studio. As for the materials, alloys serve as another degree of freedom in metasurfaces. It is of importance to develop a cost-efficient synthesis process for making alloys. For instance, Au-Pd can be fully synthesized with the proposed annealing recipe presented in Section 2.2.1 under conditions of thinner film structure, which can be further investigated. Optical characterization requires practice and experience. Although the concepts and theory in the Section 2.3.3 might appear trivial at first sight, many practical and subtle details associated with optical components make the measurements not straightforward. The provided content will be especially helpful for researchers not very familiar with characterizing metasurfaces composed of polarization-sensitive meta-atoms.

Chapter 3 Wavefront manipulation

In this Chapter, an approach to engineering the propagation direction of light using reflection is presented. In Section 3.1, the origin of wavefront manipulation with localized surface plasmonics is briefly reviewed. The theory based on Huygen's principle was the first successful demonstration that broke Snell's law, and is widely applied in artificial surface structures, i.e., metasurfaces. Devices based on this principle, including beam-steering phase gradient metasurfaces, metaholograms, and metalens, are thereafter developed. The principle of manipulating the wavefront of light involves tailoring the phase shift of light when re-emitted by scatterers. Polarization-insensitive reflective lens and metaholograms made of Au-Ag alloy are presented in Section 3.2. The approach to design phase-only modulation metaholograms and details of reconstructing the images are individually discussed in Section 3.3. These promising demonstrated devices have created a demand for metasurface devices in industry, which encourages the study of defect tolerance on metasurface devices. Reflective metallic structures and transmissive dielectric structures are examined in Section 3.4.

3.1 Introduction

The idea of wavefront manipulation stems from the Huygens–Fresnel principle, which states that every point of a wavefront is itself the source of spherical wavelets, and the secondary wavelets emanating from different points mutually interfere. The sum of these spherical wavelets forms the wavefront. This theory successfully explains many physical phenomena in wave optics, including Snell's law. In 2011, Yu et al demonstrated a layer of periodic structures on a surface that was capable of reflecting normal incident light toward another angle, achieving anomalous reflection [82][Yu_2011]. The same concept can be applied to simple structures [46][Sun_2012]. The core idea of anomalous reflection is that these subwavelength scatterers act as point sources with different phase shifts, such that a new wavefront can be generated at will under coherent plane wave illumination. The idea of utilizing subwavelength structures, or meta-atoms, in manipulating light was later applied in holograms and lens [49, 83][Huang_2013b, Wang_2017o]. Due to the strong scattering cross section of plasmonics, the long-held dream of miniaturizing bulky optical components became a practical possibility. Thereafter, intensive studies on different structures were investigated and proposed to modulate the phase shift, including adjusting the dimension of structures or rotating the same structure (Pancharatnam-Berry). Now there exist many devices, which perform a variety of functions, depending on the geometric structures used.

3.2 Metalens

The working principle of a bulky lens is to bend light by accumulating phase shift as it propagates in the lens. Light travels slower in the lens than in the environment, so a beam emerges when it exits the lens. A concept to fold the phase shift is demonstrated by a Fresnel lens. This idea of a metalens is to arrange meta-atoms in the form of a Fresnel lens [84][He_2022], where the phase shift on a xy plane follows:

$$\varphi(r, \lambda) = \frac{2\pi}{\lambda} \left(f - \sqrt{r^2 - f^2} \right), \quad (3.2.1)$$

where r is the radius of the lens ($r = \sqrt{x^2 + y^2}$), f is the focal length, and λ is the operating wavelength.

The following section represents my contribution to the article published in *Advanced Materials* **34**, 2108225 (2022).

Title: Low temperature annealing method for alloy nanostructures and metasurfaces: Unlocking a novel degree of freedom

Authors: Debdatta Ray¹, Hsiang-Chu Wang¹, Jeonghyeon Kim, Christian Santschi, Olivier J.F Martin*

Abstract: The material and exact shape of a nanostructure determine its optical response, which is especially strong for plasmonic metals. Unfortunately, only a few plasmonic metals are available, which limits the spectral range where these strong optical effects can be utilized. Alloying different plasmonic metals can overcome this limitation, at the expense of using a high temperature alloying process, which adversely affects the nanostructure shape. Here, we develop a low temperature alloying process at only 300°C and fabricate Au-Ag nanostructures with a broad diversity of shapes, aspect ratios and stoichiometries. EDX and XPS analyses confirm the homogeneous alloying through the entire sample. Varying the alloy stoichiometry tunes the optical response and controls spectral features such as Fano resonances. Binary metasurfaces that combine nanostructures with different stoichiometries are fabricated using multiple-step electron beam lithography, and their optical function as holograms or Fresnel zone plates is demonstrated at the visible wavelength of $\lambda = 532$ nm. This low temperature annealing technique provides a versatile and cost-effective way of fabricating complex Au-Ag nanostructures with arbitrary stoichiometry.

Alloyed metasurfaces

We apply the low-temperature annealing technique introduced in sub-Section 2.2.1 to fabricate disk-shaped meta-atoms made of gold and silver alloy atop reflective substrate. To achieve functions like holograms and Fresnel zone plates, alloyed nanostructures with different stoichiometries on the same substrate are first simulated. Generally, tuning the phase shift of a meta-atom is achieved by tailoring its geometry. Here, instead of varying the shape, we change the material while keeping the shape constant. Binary-phase metasurfaces are fabricated with two different alloys, $\text{Au}_{0.8}\text{Ag}_{0.2}$ and $\text{Au}_{0.2}\text{Ag}_{0.8}$. It should be noted that the meta-atoms shape is kept constant to emphasize the effect of changing the optical properties of the material; this nanotechnology can of course be applied to meta-atoms with different shapes as well as different stoichiometries, thus providing a very large number of degrees of freedom for the metasurface design. With Au–Ag alloys, it is straightforward to develop metasurfaces that operate in the visible; here we chose $\lambda = 532$ nm and fabricate a periodic array of meta-atoms with periodicity $P = 300$ nm to avoid any diffraction order. Alloyed discs $\text{Au}_x\text{Ag}_{1-x}$ with diameter $d = 110$ nm and thickness $h = 50$ nm, atop an Al mirror (thickness 150 nm) with a $t = 100$ nm thick SiO_2 spacer are used as meta-atoms, see the inset in Figure 3.2–1. Such a structure is polarization insensitive and supports a gap plasmon [85, 86], which enables the reradiation of the incident wave with a phase shift that can be controlled over a 2π -range [87]. The reflectance and phase shift are computed as a function of the wavelength using the periodic surface integral equation method [8, 88], Figure 3.2–1(a). The permittivity for Al and SiO_2 originate from the literature [89], whereas that for $\text{Au}_x\text{Ag}_{1-x}$ are computed using Rioux’s model [18]. Figure 3.2–1(a) indicates that at $\lambda = 532$ nm the reflectance is the same for $\text{Au}_{0.2}\text{Ag}_{0.8}$ and $\text{Au}_{0.8}\text{Ag}_{0.2}$ nanostructures, while the phase they produce is shifted by 165° ; this nano-structures pair can therefore serve as meta-atoms for a binary metasurface [90]. This is confirmed in Figure 3.2–1(b) by measurements on alloyed disc arrays with five different stoichiometries. The agreement between measurement and simulations is good, especially in the spectral locations of the reflection dip.

Having demonstrated the ability to manipulate the reflected light using arrays of alloyed nanostructures, we now fabricate a metahologram and a Fresnel zone plate using the stoichiometries $\text{Au}_{0.8}\text{Ag}_{0.2}$ and $\text{Au}_{0.2}\text{Ag}_{0.8}$ to realize the two different disc-shaped meta-atoms. For the metahologram, we calculate the phase distribution using the computer generated hologram method [91]. Since the metahologram is built from two different alloys, a 3-step EBL process is used to position the corresponding nanostructures with different compositions on the metasurface. In the first step, alignment marks are written and in the consecutive 2nd, respectively 3rd steps, nanostructures with $\text{Au}_{0.8}\text{Ag}_{0.2}$, respectively $\text{Au}_{0.2}\text{Ag}_{0.8}$, are deposited. A position accuracy in the order of 20 nm is achieved thanks to the alignment

¹ Both authors contributed equally to this work.

markers. The annealing is performed after the final step, once all the meta-atoms with different stoichiometries have been deposited on the surface. The SEM images of the hologram device in Figure 3.2–1(c) indicate that all the unit cells share the same physical dimensions and the different meta-atoms are well aligned over a very large area (the inset highlights with colors the two different stoichiometries used in the metasurface). This is quite remarkable since these nanostructures are written in two successive, independent steps, including electron-beam resist coating, EBL, development, two-layer metal deposition and lift-off. Images of the hologram projection under polarized laser illumination are shown in Figure 3.2–1(d),(e) for two different incident polarizations. The holograms are polarization-independent thanks to the symmetrical arrangement of the meta-atoms.

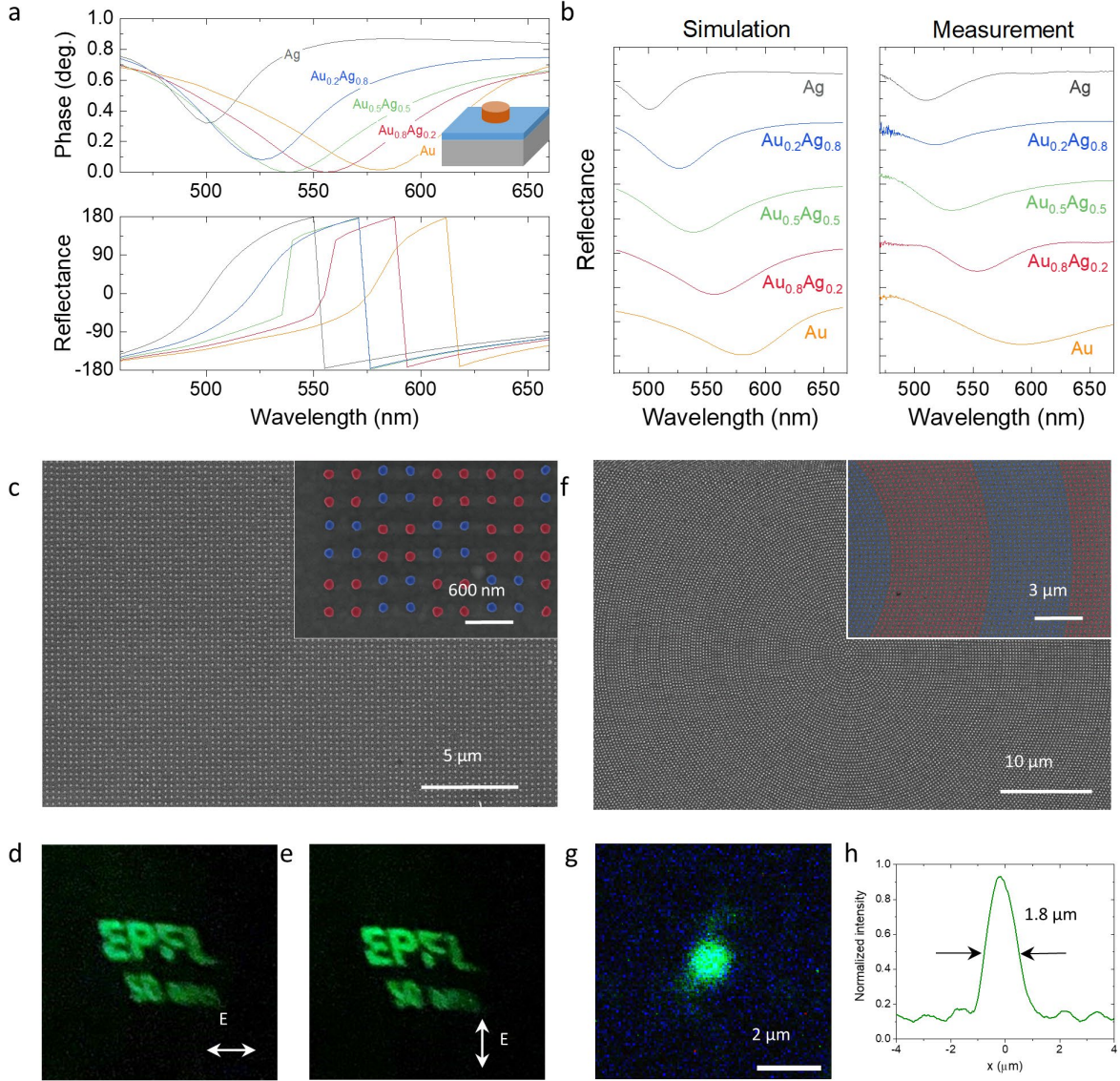


Figure 3.2–1 Wavefront manipulation achieved by Au-Ag alloy. a) Simulated reflectance and phase for alloyed meta-atoms with different stoichiometries. The inset shows the meta-atom composed of an alloyed disc with diameter $d = 110$ nm, height $h = 50$ nm, positioned atop an Al mirror with a SiO₂ spacer of thickness $t = 100$ nm. The period is $P = 300$ nm. b) Simulated and measured reflectance spectra for different disc stoichiometries. c) SEM image of the hologram device and d,e) its optical projection under horizontally (d) and vertically (e) polarized light. f) SEM image of the FZP with focal length $f = 400$ μm and NA = 0.35. g) Intensity distribution at the focal plane and h) normalized intensity profile at the center of the focal spot. The insets in (c) and (f) emphasize with colors the two different stoichiometries used for the meta-atoms.

For demonstration purposes, the lens is designed with a $NA = 0.35$ in air. The lens diameter is $D=300\text{ }\mu\text{m}$ and the focal length is $f = 400\text{ }\mu\text{m}$. Figure 3.2–1(f) shows the SEM image of the fabricated lens. The inset in Figure 3.2–1(f) provides a magnified view of the lens, which is composed of meta-atoms with the same dimensions but different Au–Ag stoichiometries. The focal spot, displayed in Figure 3.2–1(g), is measured in the Fourier plane, whereas the intensity profile, shown in Figure 4h, is determined in the focal plane. The full width at half maximum (FWHM) is $1.8\text{ }\mu\text{m}$, which agrees extremely well with the theoretical diffraction spot size $D_{FWHM} = 1.22\lambda/NA = 1.85\text{ }\mu\text{m}$. One may consider that metasurfaces built from bilayer meta-atoms instead of alloyed meta-atoms could provide the same optical functions. Furthermore, in the case of a bilayer, the response shifts in a rather intricate manner as a function of the wavelength. In addition to representing a disruptive approach to the design of optical metasurfaces, the utilization of alloyed nanostructures brings its own advantages compared to metasurfaces designed from a collection of meta-atoms with different shapes. First, the metasurfaces shown in Figure 3.2–1 are intrinsically polarization insensitive, which is not the case for traditional metasurfaces with, e.g., elongated nanostructures. Second, since all the meta-atoms have the same dimensions, the design can be extremely dense, thus enhancing the device efficiency.

3.3 Metaholograms

The following section has been submitted to Nanophotonics.

Title: Facile Design, Optical Characterization, and Performance of Metaholograms

Authors: Hsiang-Chu Wang and Olivier J.F. Martin*

Abstract: We combine numerical simulations and nanofabrication to describe a general method for the design of Fraunhofer metaholograms. A facile iterative procedure is used to obtain the metahologram phase distribution required to produce a specific target image. The discretization of this continuously varying phase using a limited number of levels strongly influences the image quality. Rarely mentioned details associated with the number of discrete levels are discussed, including the appearance of twin images for binary metaholograms. While these twin images dilute the energy, they can also be used to produce very efficient metaholograms. Additional subtleties associated with the utilization of the fast Fourier transform during the design procedure are considered. The image reconstruction from metaholograms is also discussed using experimental data from silver metasurfaces. The possibility to improve the viewing angle by repeating each meta-atom several times to form a super-pixel is demonstrated and explained in terms of multiple slits diffraction.

3.3.1 Introduction

Holography has recently evolved thanks to the emergence of metasurfaces, which replace conventional recording media with thin surfaces, and have been utilized for many holographic applications [25, 92-97]. Metaholograms – holograms built from meta-atoms – have the advantage of subwavelength pixel size, large space-bandwidth product [98], and a broad choice of meta-atom materials (plasmonic metals [19, 23, 91, 99, 100], dielectrics [101-105] and semiconductors [28, 33, 106, 107] for versatile purposes. They have become popular for applications such as highly efficient wavefront manipulation [108-110], high-density optical encryption [111-115], and optical data storage [116-118].

The physical principle of metaholograms is to replace diffractive optical elements with meta-atoms, or artificial structures, to achieve the same functionalities as those produced by a conventional digital hologram [119]. The subwavelength pixel size of a metahologram, on the one hand can increase the sampling rate, enabling an image to be reconstructed at a shorter distance [120]; on the other hand, it also increases the diffraction angle, which can lead to aberrations at the margin that need to be taken care of [121].

The growing popularity of metaholograms calls for a detailed generic analysis of their design, fabrication and optical characterization. In this work, we address this need by discussing the different issues pertaining to the synthesis, layout

and measurement of metaholograms. Their phase distribution is based on that of computer-generated holograms, which combines the Fraunhofer approximation with Gerchberg and Saxton's iterative algorithm to obtain the complex amplitude distribution in the hologram plane [122]. The hologram efficiency is also discussed; it is affected by the number of modulation levels. Although a large number of modulation levels increases the efficiency, it is possible to reach the highest efficiency with the minimum number of modulation levels. The positions and size of the reconstructed image are also affected by the metahologram synthesis and by the pixel size. To take full advantage of the reconstructed image for a given application, it is essential to understand how metaholograms manipulate the encoded image.

Calculation of the phase distribution

Let us set the scene by considering in Figure 3.3–1(a) the reconstruction of an image in the $x_1 - y_1$ plane using a hologram located in the $x - y$ plane and illuminated by a plane wave. The required complex amplitude in the hologram plane can be derived according to scalar diffraction theory since for practical purposes the incident light polarization is well-controlled. The most general approaches such as Rayleigh-Sommerfeld and Fresnel-Kirchoff diffractions are commonly used for that task. While they provide an accurate prediction for light propagating in space, such rigorous calculations are time consuming [123]. An efficient way to calculate the complex field amplitude is to use diffraction approximations. Depending on the distance where the image is generated, shown in Figure 3.3–1(b), the applicable approximations based on the diffraction theory are categorized in terms of Fresnel number N_f [124]. The Fresnel number can be expressed as $N_f = a^2/z\lambda$, where a is the hologram size, z the distance between the hologram and the image, and λ the wavelength of incident light. The Fresnel number distinguishes between the near- and far-field regions: the near-field region is from the hologram plane to the distances satisfying $N_f \geq 1$, while the far-field region is at the distances such that $N_f \ll 1$. In Figure 3.3–2, we describe the procedure for designing a metahologram with 300 by 300 pixels and choose a square pixel size of $P = 300$ nm, hence the size of the metahologram is $90 \mu\text{m}$ by $90 \mu\text{m}$. The distance from the hologram plan to the image plane is chosen as 30 cm. For a plane wave at the wavelength $\lambda = 632$ nm, the image will be reconstructed in the far-field region because $N_f = 0.0427 \ll 1$ in this case. In that region, the wavefront can be approximated as a plane wave, such that the required complex amplitude in the hologram plane is merely the inverse Fourier transform of the image in the image plane. As a result, the complex amplitudes in the image plane and the hologram plane are related by a Fourier transform (FT) and an inverse Fourier transform (IFT).

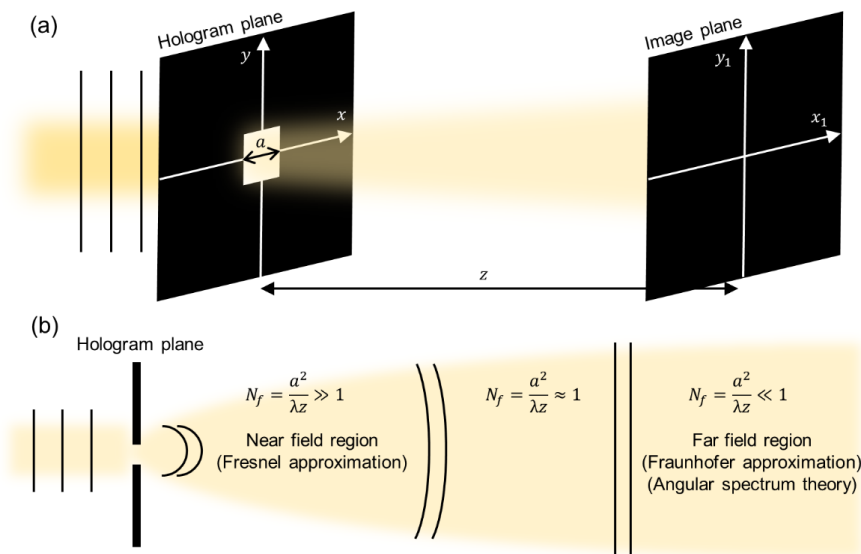


Figure 3.3–1 Diffraction theories and applicable approximations to reconstruct the image produced by a metahologram under plane wave illumination. (a) Hologram and image planes, the metahologram can be viewed as an aperture with dimensions $a \times a$. (b) Applicable approximations that can be used depending on the Fresnel number N_f . Waves in near-field region, $N_f \geq 1$, propagate as parabolic wavefronts, while in far-field region, $N_f \ll 1$, they can be approximated as plane waves.

Classical digital holograms usually modulate the amplitude or the phase of the light by means of a spatial light modulator, although some recent publications have reported improved performance by modulating both amplitude and phase [125]; which is also the case for metaholograms [126]. However, the vast majority of reported metaholograms are based on solely modulating the phase, while their reflectance or transmittance is constant and we will focus here on such phase-modulation metasurfaces. Although we aim for a device where the amplitude is constant, when we perform FTs, both the amplitude and the phase are modulated. Therefore, a phase iteration process, based on computer-generated holograms and proposed in 1988 [127], is needed to obtain a constant amplitude.

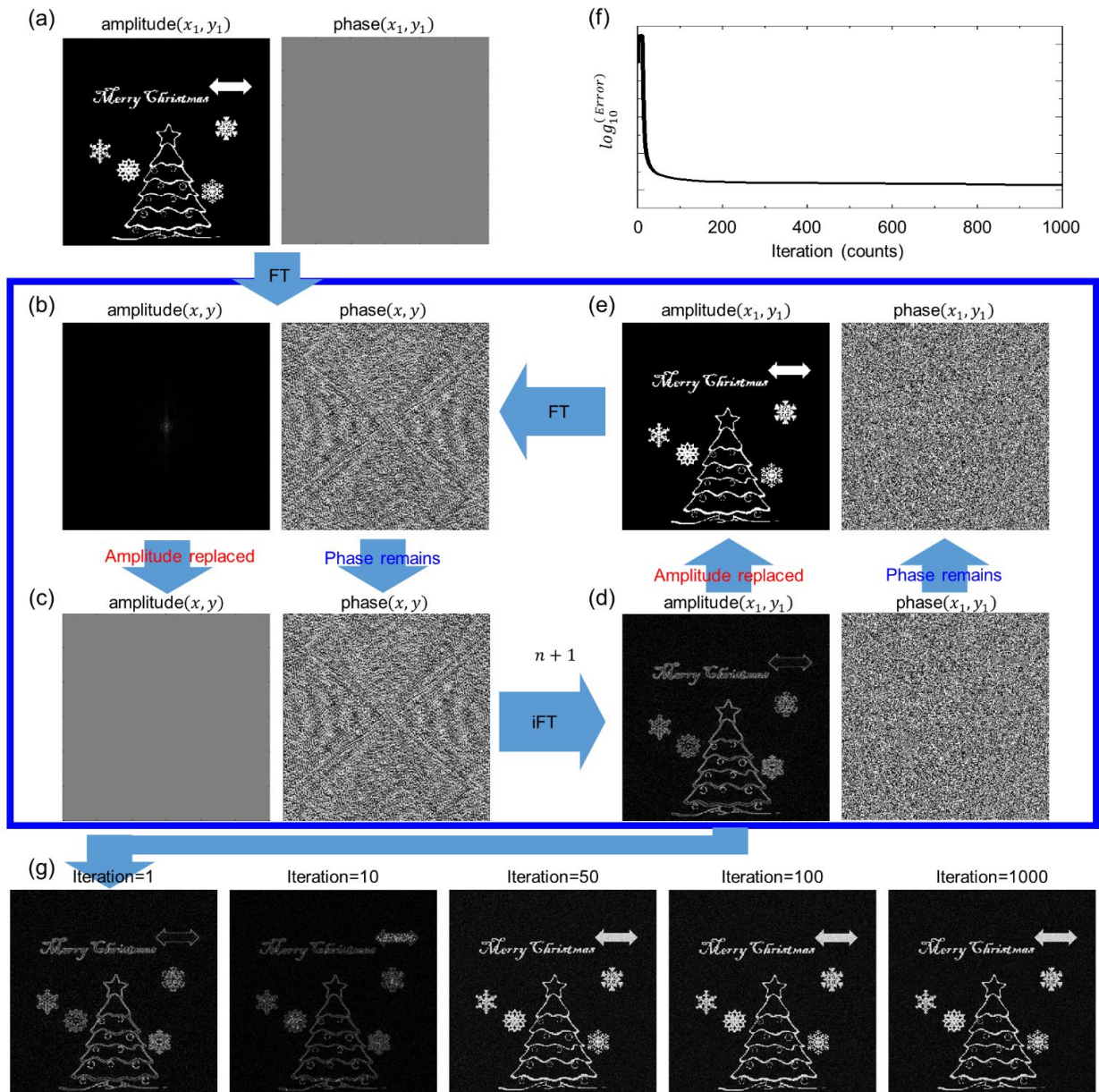


Figure 3.3–2 Algorithm for generating a phase-modulation-only metahologram. (a) The target image has only a modulated amplitude and a constant phase. (b) A first Fourier transform (FT) of the target image produces both amplitude and phase modulations. (c) Next, the amplitude is replaced with the constant value 1, whilst keeping the phase. (d) An inversed Fourier transform (iFT) produces the corresponding image. (e) The amplitudes of this image are replaced by that of the target image and the process (b)-(e) is repeated. (f) Root mean square difference between the amplitudes of the computed image at iteration n and the target image. (g) Reconstructed images for selected iteration numbers.

This process is illustrated in Figure 3.3–2, where we use the following notations for the complex amplitude $U_{image}^n(x_1, y_1) = A_{image}^n(x_1, y_1) \exp(i\phi_{image}^n(x_1, y_1))$, where U is the complex amplitude of a pixel, A its amplitude and ϕ its phase. The superscript n indicates the iteration number and the subscript refers to the image or the hologram plane. For illustration purpose, we keep our square image with 300 by 300 pixels. The process starts with the target image, which has a constant phase and a modulated amplitude, Figure 3.3–2(a). The first FT gives the complex amplitude in the hologram plane $U_{hologram}^0(x, y) = A_{hologram}^0(x, y) \exp(i\phi_{hologram}^0(x, y))$ shown in Figure 3.3–2(b). As mentioned, the amplitude is not constant and its distribution shows the strongest values mainly at the center of the hologram. To iterate on the phase such that we reach a hologram with constant amplitude, we keep the phase term $\exp(i\phi_{hologram}^0(x, y))$ and replace the amplitude in the hologram with a unit constant, such that $U_{hologram}^0(x, y) = 1 \exp(i\phi_{hologram}^0(x, y))$, as shown in Figure 3.3–2(c). At this stage, the complex amplitude represents the first iteration for the phase-modulation-only hologram. Unfortunately, the corresponding image obtained with iFT is very bleak: $U_{image}^1(x_1, y_1) = A_{image}^1(x_1, y_1) \exp(i\phi_{image}^1(x_1, y_1))$, Figure 3.3–2(d). To continue the iteration, the amplitude part of the complex amplitude is replaced by the target image amplitude $A_{image}^{target}(x_1, y_1)$ while keeping the phase term obtained in the first iteration: $U_{image}^1(x_1, y_1) = A_{image}^{target}(x_1, y_1) \exp(i\phi_{image}^1(x_1, y_1))$, as shown in Figure 3.3–2(e). The corresponding complex amplitude in the hologram plane is obtained again by FT, Figure 3.3–2(b): $U_{hologram}^1(x, y) = A_{hologram}^1(x, y) \exp(i\phi_{hologram}^1(x, y))$. Already after that first iteration, the amplitude modulation of $A_{hologram}^1(x, y)$ is smaller than that of $A_{hologram}^0(x, y)$, which indicates that after multiple iterations the amplitudes will eventually become constant. The second iterations proceeds in a similar way, by first keeping the phase term and assigning a constant amplitude, Figure 3.3–2(c): $U_{hologram}^1(x, y) = 1 \exp(i\phi_{hologram}^1(x, y))$, and then converting back to the image plane, Figure 3.3–2(d): $U_{image}^2(x_1, y_1) = A_{image}^2(x_1, y_1) \exp(i\phi_{image}^2(x_1, y_1))$.

As the iterations progress, the amplitude in the image plane converges toward that of the target image. This is shown in Figure 3.3–2(f), where we report the root mean square difference between the target image amplitude and that in the image as a function of the iteration n ,

$$Error^n = \left(\sum_{x,y} [A_{image}^{target}(x, y) - A_{image}^n(x, y)]^2 \right)^{1/2}, \quad (3.3.1)$$

where the sum runs on all the pixels in the metahologram. The error drops rapidly, meaning that while at each iteration the amplitude in the hologram plane becomes more constant, the phase modulation is able to better reproduce the target image. After about 100 iterations, which takes less than 1 second with a conventional desktop computer, the hologram with constant amplitude and modulated phase is able to reconstruct the target image, as shown in Figure 3.3–2(g). Nevertheless, we use 1'000 iterations to ensure perfect convergence. Although rarely used in metaholograms, it is straightforward to adapt this iterative process to produce a hologram with constant phase and modulating only the amplitude. The design of metaholograms where both the amplitude and the phase are modulated is also possible [126, 128, 129].

Phase discretization

The previous iterative procedure provides a phase distribution for the metahologram with arbitrary spatial resolution and a continuously varying phase between 0 and 2π . The next step is to discretize this continuous range into a small number of discrete levels, each corresponding to a different meta-atom. The number of these discrete phase modulation levels produces slightly different images, as illustrated in Figure 3.3–3(a). Using the continuously varying phase values provides the best contrast, with very dark regions. However, using only 4-levels already provides a good contrast, while the background becomes greyish for 3-levels. Note that for fabrication purposes, only a limited number of levels is feasible since each meta-atom has a specific footprint. Interestingly, a 2-level device produces twin images that are

point-symmetric. This fact is well-known from classical binary holograms, such as those produced with a spatial light modulator [130, 131].

The efficiency of these holograms is studied quantitatively in Figure 3.3–3(b) as a function of the design iteration. The efficiency is defined as the intensity of the reconstructed image divided by that of the target image. One can easily conclude that the higher the number of modulation levels, the higher the efficiency: when the continuously varying phase is used, the efficiency reaches 89.1%; it reaches 73.4% for 4-level, 63.2% for 3-level, and only 40.8% for 2-level. Note that for the 2-level device, the efficiency reported in Figure 3.3–3(b) corresponds only to one of the twin images. While it is not possible to get rid of one of the twin images [132], one can make good use of them by designing a metahologram where both images are superimposed, leading to a very efficient system up to 81.6% from Figure 3.3–3(b). This is the case when the target image has two mirror symmetry planes. It is interesting to note that some particularly efficient binary metaholograms use such an image, see e.g. Fig. 3 in Ref. [133], where an efficiency as high as 75% is observed.

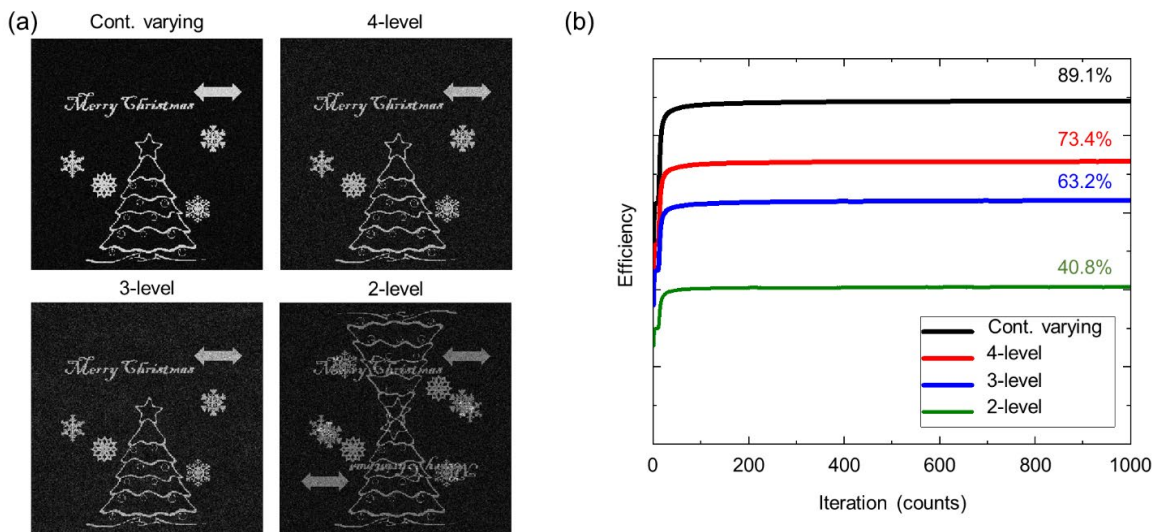


Figure 3.3–3 Efficiencies of metaholograms with different modulation levels. (a) Reconstructed images after 1'000 iterations for different phase discretization levels. Note the twin images for the 2-level metahologram. (b) Efficiencies for different phase discretization levels. For the 2-level metahologram, only one of the twin images is considered, see text for details.

3.3.2 Results and discussion

Having described how to design a metahologram, we now discuss the specific issues associated with the reconstruction of the image; especially the relation between the pixel and image sizes. Before doing so, we would like to mention an important issue that has sometimes been overlooked in the literature and leads to the scrambling of reconstructed images. This phenomenon arises from the usage of fast Fourier transforms in the phase iteration during the metahologram design. Let us consider for example the target image in Figure 3.3–4(a), where the different elements are indexed as in a matrix. The phase distribution for the corresponding 300 by 300 pixels metahologram has been determined using the procedure described in Sec. 2, with 1'000 iterations, then discretized using 4-levels and fabricated in a real device that operates at the wavelength $\lambda = 632$ nm. The fabrication of this silver metasurface with electron beam lithography is described in Figure 3.3–5. We observe in Figure 3.3–4(b) that the reconstructed image is scrambled with each of the four quadrants located at its symmetric position (for example the top left quadrant that begins with "11 12..." is located in the bottom right corner of the image). Surprisingly, the computer image that was used to produce the metahologram and is shown as an inset in Figure 3.3–4(b) is not scrambled. The reason for this is the fact that the fast Fourier transform algorithm does not put the zero frequency in the middle of the transformed vector, but at the beginning [134]. Consequently, the four outermost corners of the image, with numbers "11", "15", "55" and "51" in our example, appear in the center of the reconstructed image, Figure 3.3–4(b). Since the metahologram design involves always a pair of FT and iFT, the corresponding computed images are not scrambled. It is only when an image is physically reconstructed with light

propagating from the metahologram to the screen that the zero order frequency must be placed at the middle of the hologram, not at the edge. Hence, a shifting step must be included between each Fourier transform pair to obtain the correct physical image, as shown in Figure 3.3–4(c) where this additional shifting step has been included in the design of the corresponding metahologram. We insist that this effect appears only during light propagation and does not modify the corresponding computed images, as indicated in the insets of Figure 3.3–4(b) and (c).

Practical applications require the reconstructed image to have specific physical dimensions and sufficient optical contrast. Unfortunately, because the meta-atoms are very small (300 nm in our case), the image reconstructed, for example with our metahologram that includes 300 by 300 different pixels – viz. 300 by 300 meta-atoms – the image diverges significantly and only the center is reconstructed, as visible in Figure 3.3–6(a). This limitation can be alleviated by simply repeating each pixel (each meta-atom) N times in x - and y - directions, forming an $N \times N$ array of the same pixel (meta-atom), as illustrated in Figure 3.3–5(c). Sometimes, this array of $N \times N$ similar meta-atoms is called a super-pixel.

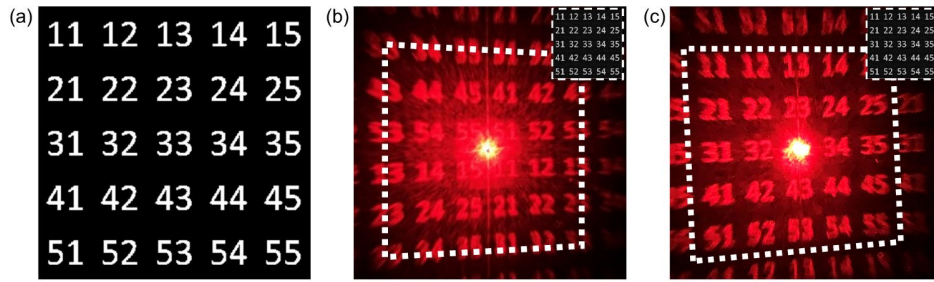


Figure 3.3–4 Target image and its reconstruction using a 4-level metahologram fabricated in silver. (a) Desired target image. Care must be taken in designing the metahologram with fast Fourier transforms to make sure that the zero frequency is positioned at the middle of the hologram. (b) The image is scrambled when this is not the case, (c) while it is perfectly reconstructed when this is the case. Note that this issue does not arise in the computed images shown in the insets.

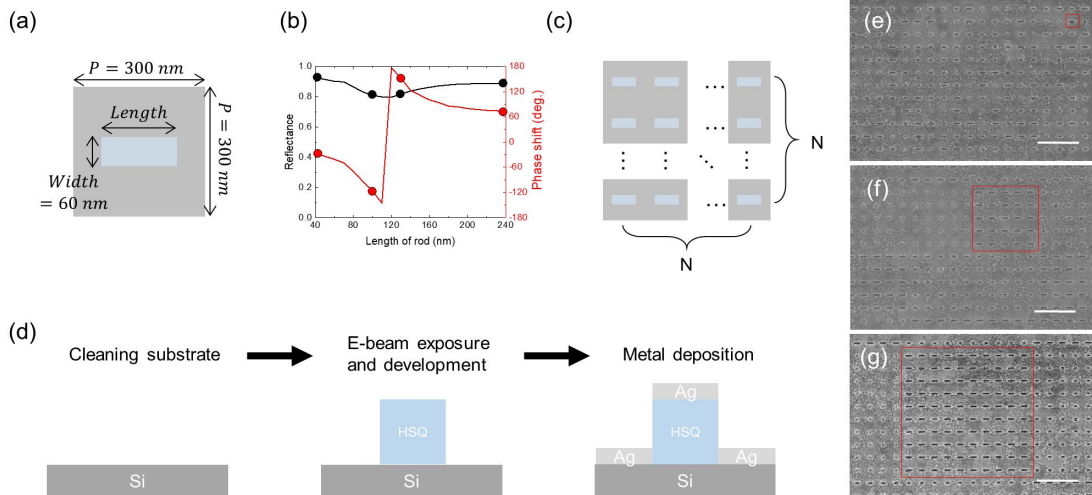


Figure 3.3–5 Simulation and fabrication details of the meta-atoms used for generating phase-modulation-only metaholograms. (a) Top view of the meta-atom with dimensions. The meta-atom has a square period of 300 nm and a 150-nm-tall pillar supporting from the substrate. This pillar is simply built from a negative electron beam photoresist as described in panel (d). The width of the silver rod is 60 nm, while its length is modified to tune the phase. (b) Reflectance and phase shift as a function of the length of the rod computed with Comsol Multiphysics vers. 5.6. Circles in black and red indicate the reflectance and phase shift for rods with lengths 40, 100, 130, and 240 nm. (c) Repeating the meta-atoms in x - and y -directions, forming an $N \times N$ array of similar meta-atoms that build a super-pixel for the metahologram. (d) Fabrication process of the meta-atoms: First, cleaning a silicon substrate and spin-coating 150 nm-thick negative photoresist (HSQ, DuPont). Second, using E-beam lithography to define the dimensions of rods and development. Third, thermal evaporation of 40 nm-thick silver using a procedure reported elsewhere[135, 136]. SEM image of the fabricated metaholograms with super-pixel size (e) 300 nm ($N = 1$), (f) 1.5 μm ($N = 5$), and (g) 3 μm ($N = 10$). The red squares indicate the corresponding super-pixel on the metahologram; the scale bars are 1 μm .

The super-pixel size influences the measurements conditions, including the distance to reconstruct the image, the field of view or viewing angle, and the locations of higher-order images. To study this, we have fabricated metaholograms with three different super-pixel sizes corresponding to multiples N of the pixel size ($P = 300$ nm): 300 nm (corresponding to $N = 1$, Figure 3.3–5(e)), 1.5 μm (corresponding to $N = 5$, Figure 3.3–5(f)), and 3 μm (corresponding to $N = 10$, Figure 3.3–5(g)). The measurement setup is described in Figure 3.3–7(a). The corresponding images reconstructed on the screen are shown in Figure 3.3–6a-c and are very different from one another. For the metahologram with $N = 1$, the reconstructed image propagates in the shape of a spherical wavefront, such that only the region close to normal reflection is projected on the screen, Figure 3.3–6(a). As meta-atoms are repeated, e.g. for $N = 5$, the image becomes more compact and the zero order image can be completely reconstructed with some parts of the neighboring first-order images, Figure 3.3–6(b). For larger repetitions, e.g., $N = 10$ corresponding to a 3 μm super-pixel, the overall intensity distribution is within the diffraction pattern of a square aperture, Figure 3.3–6(c). The insets in Figures 5(a)-(c) show optical microscope images of the corresponding metahologram and emphasize the relationship between the metahologram size and its reconstructed image.

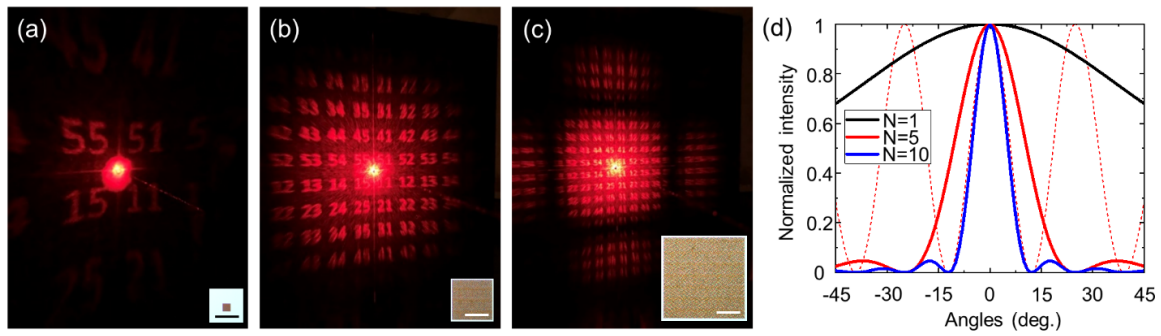


Figure 3.3–6 Imaging of metaholograms with different super-pixel sizes. (a) $N = 1$, (b) $N = 5$, and (c) $N = 10$. Since each hologram includes 300 by 300 super-pixels, its size increases as the super-pixel size increases, as indicated by the optical microscope images shown in the corresponding insets (Scale bars 250 μm). (d) The image projected by the metahologram can be understood in terms of multiple slits diffraction, see text for details.

The multiple slits diffraction formula provides also simple insights into the image formation of metaholograms [80]: each super-pixel can be assigned to a slit with the width PN , which is then repeated periodically 300 times in our example. Narrow slits, corresponding to a small super-pixel size, for example $N = 1$, produce a wide diffraction pattern, see the black line in Figure 3.3–6(d). Increasing the super-pixel size, for example to $N = 5$, or $N = 10$, concentrates the image more, as visible for the red and blue lines in Figure 3.3–6(d). This is also visible when comparing Figure 3.3–6(b) and Figure 3.3–6(c). Looking carefully in the latter figure, one notices that a faint repetition of the image is visible at the edge of the first diffraction order, close to the dark area. The reason for this is that the interference pattern modulates the main diffraction envelope in multiple slits diffraction, as illustrated with red dash line for $N = 5$ in Figure 3.3–6(d). Consequently, additional images can appear outside the main peaks of the diffraction envelope. To one's notice, the intensity of the first order image drops to less than 0.1 with respect to the zero order image located at the center.

Finally, let us observe the dispersion and polarization properties of the metahologram considered here. The meta-atoms have varying dimensions in x -direction only, Figure 3.3–8. Therefore, the images will only be reconstructed with light polarized along that direction. This is visible in Figure 3.3–8, where clear images are reproduced in the upper row for horizontal (parallel to the x -direction) polarization: For the orthogonal polarization, light can barely generate the images, Figure 3.3–8, bottom row. Surprisingly, the fabricated metahologram – initially designed at the wavelength of 632 nm – exhibits a rather broadband response, ranging throughout most of the visible spectral range.

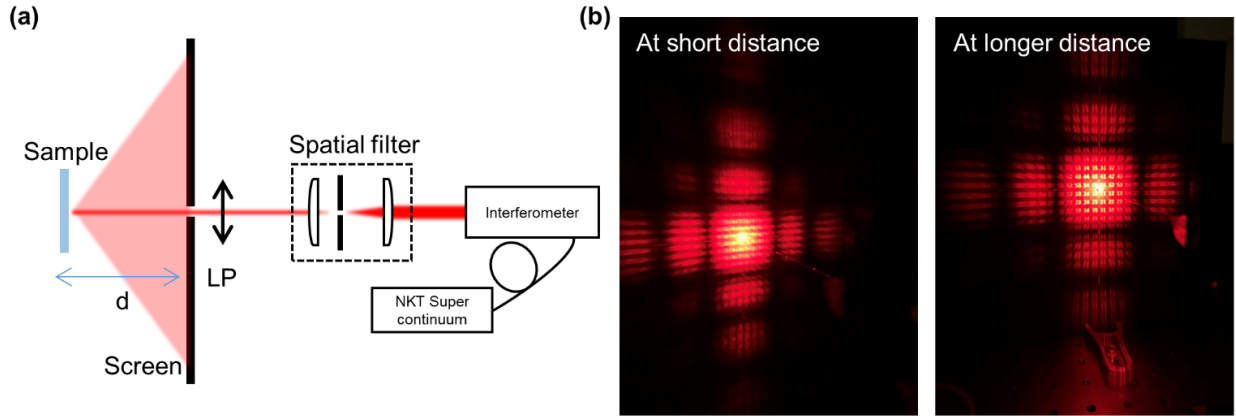


Figure 3.3-7 Measurement setup and reconstructed image at a specific distance. (a) Schematic of the measurement setup. A sufficiently coherent light source from a supercontinuum laser (SuperK Fianium FIU-15-PP-01) passing through the interferometer (SuperK VARIA) emits at the wavelength of 632 nm in free space. The laser beam spot is shrunk by the spatial filter and becomes linearly polarized through the linear polarizer. To ensure the sample is under normal incidence, a hole on the screen is prepared such that the linearly polarized light penetrates through that hole, without blocking the incident light source. The screen is placed at a distance d away from the sample. (b) Reconstructed images for the metahologram with a $3\mu\text{m}$ super-pixel ($N = 10$) at the distance of 15 cm and 30 cm. Due to the low sampling at short distance, the zero-order image is not well reconstructed. Finer details of the image begin to emerge as the distance increases.

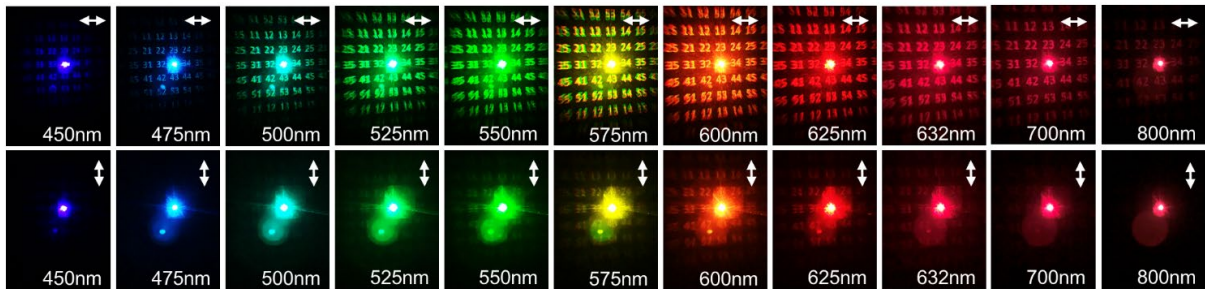


Figure 3.3-8 Dispersion and polarization properties of the fabricated metaholograms. A fair reproduction can be obtained over most of the visible spectrum, as long as the correct polarization is used.

3.3.3 Conclusion

We have described in detail a general method for the design of Fraunhofer metaholograms. Beginning with the target image, the phase distribution required for the metahologram is built iteratively by using direct and inverse Fourier transforms. The process is fast and converges very rapidly toward the final phase distribution. For the practical realization of a metahologram, this continuously varying phase distribution must be discretized with a limited number of discrete levels, corresponding to the different meta-atoms that will be used. The influence of the number of levels on the reconstructed image has been investigated, with 4-levels providing already a very efficient metahologram, whilst remaining feasible physically. The particular case of 2-level metaholograms has also been discussed: as known from classical binary holograms, this phase discretization produces twin images. However, if the target image has mirror symmetries, it is possible to superpose the twin images to produce a 2-level hologram that surpasses the efficiency of 4-level devices.

Additional subtleties associated with the reconstruction of the image from a metahologram have been discussed. They include pitfalls in the utilization of the fast Fourier transform and the repetition of similar meta-atoms to produce a

super-pixel that improves image viewing. These theoretical findings were supported by experiments using nanofabricated metaholograms in silver. The agreement between the two is very good. Finally, we have shown that the fabricated metaholograms exhibit a broadband response and can be operated over the entire visible range, as long as the correct polarization is chosen.

3.4 Robustness analysis

This section was published in ACS Photonics in press (2022), doi: 10.1021/acsp Photonics.2c00563

Title: Metasurfaces Robustness Analysis: Perfect Structures are not always the Best

Authors: Hsiang-Chu Wang, Karim Achouri, and Olivier J.F. Martin*

Abstract: Optical metasurfaces rely on subwavelength scale nanostructures, which puts significant constraints on nanofabrication accuracies. These constraints are becoming increasingly important, as metasurfaces are maturing toward real applications that require the fabrication of very large area samples. Here, we focus on beam steering gradient metasurfaces and show that perfect nanofabrication does not necessarily equate to the best performance: metasurfaces with missing elements can actually be more efficient than intact metasurfaces. Both plasmonic metasurfaces in reflection and dielectric metasurfaces in transmission are investigated. These findings are substantiated by experiments on purposely misfabricated metasurfaces and full-wave calculations. A very efficient quasi-analytical model is also introduced for the design and simulations of metasurfaces; it agrees very well with full-wave calculations. Our findings indicate that the substrate properties play a key role in the robustness of a metasurface and the smoothness of the approximated phase gradient controls the device efficiency.

3.4.1 Introduction

Already at the turn of the 21st century, it was recognized that metallic nanostructures organized on a surface could mold the flow of light by manipulating its phase [137]. A few years later, this field of research developed vividly into that of optical metasurfaces: first at microwave and radio frequencies [97, 138, 139], later in the infrared [140-146], and finally in the visible part of the optical spectrum [92, 102, 147-149]. This spectral evolution was made possible by tremendous progress in nanofabrication since the dimensions of the structures building the device – the so-called meta-atoms – must be smaller than the operation wavelength to produce a homogeneous response [150, 151].

Significant efforts have been devoted to the development of precise nanofabrication techniques for metasurfaces [106, 152, 153]. In most cases the meta-atoms are defined using electron-beam (E-beam) lithography [23, 31, 43, 104, 154-158]; sometimes ultraviolet photolithography is used [159-162], or they are directly carved using focused ion beam [163-165]. Meta-atoms are fabricated in either dielectrics [102, 166, 167] or plasmonic metals [168, 169]. The latter have an especially important interaction with light, due to the excitation of free electron resonances [170]. After the exposure step, the meta-atoms are created either by lift-off or by etching [171]. Irrespective of the approach, nanofabrication is definitely a rather challenging activity, often with a relatively low yield. Over an entire wafer, it is difficult to fabricate structures that are as perfect as the original design. The size of the meta-atoms can vary with the lithography dose; some nanostructures may be deformed during the lithography by proximity effects associated with neighboring nanostructures [172], the adhesion of some meta-atoms can be poor, such that they disappear during the process – this is especially the case for metal nanostructures on dielectric substrates [173-175]. The metal evaporation can produce nanostructures with slanted sides as the photoresist is clogged up during deposition [176].

The aim of this paper is to study the influence of such inaccuracies in nanofabrication on the overall response of metasurfaces; especially the tolerance on nanofabrication that is acceptable without corrupting the optical response excessively. Both a quasi-analytical model and full-wave electromagnetic simulations are used to determine the influence of such fabrication misshapes. In addition, purposely misfabricated samples are studied experimentally to gain

insights into the mechanisms that control the performance of metasurfaces. Although the present study focuses on beam steering gradient plasmonic metasurfaces using gap plasmon meta-atoms [25, 86, 177], the findings reported herein can also be applied to other metasurface designs and materials [87, 178, 179], since the nanofabrication techniques are very similar.

3.4.2 Results and discussion

The metasurface considered here is based on gold nanostructures of varying dimensions deposited above a gold mirror using a SiO₂ spacer, Figure 3.4–1. This reflecting substrate provides additional phase to the scattered light, such that a full 2π phase range can be engineered for the metasurface response [180]. The metasurface is fabricated using E-beam lithography and Ion beam etching as described in the Methods section. In spite of a careful nanofabrication procedure, including dose tests for the electron beam lithography and optimized etching time, it is almost impossible to avoid imperfections in the fabricated metasurface, especially over the relatively large area (typically tens of μm^2) required to implement a meaningful optical function. Misfabrication leads to defects such as missing elements, Figure 1(a) and (b), displaced elements, Figure 3.4–1(a) and (c), or bloated elements, Figure 3.4–1(d) and (e). The aim of this paper is to study theoretically and experimentally the influence of such defective elements on the overall metasurface response.

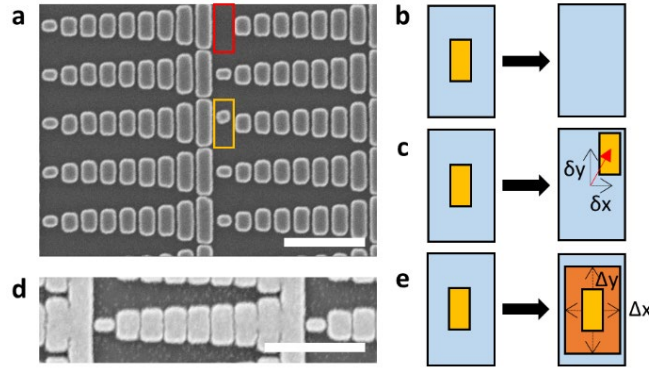


Figure 3.4–1 Examples of possible imperfections that can occur during the nanofabrication of an 8-level metasurface. (a) SEM image of an area of the metasurface with defects such as (b) missing element or (c) displaced element. (d) SEM image of an overexposed metasurface, with oversized elements (e) (Scale bars 500 nm).

The metasurface unit cell is illustrated in Figure 3.4–2: $h = 30$ nm thick Au nanostructures (meta-atoms) with a width $w = 140$ nm and different lengths L are deposited atop a gold mirror (thickness 150 nm, such that the mirror can be considered as semi-infinite) with a $t = 40$ nm SiO₂ spacer, Figure 2a. The system builds unit cells with dimensions $P_x = 180$ nm and $P_y = 430$ nm in x - and y -directions, respectively.

Changing the nanostructure length L controls the phase of the reflected light for illumination with y -polarized light, as shown in Figure 3.4–2(b) for the operation wavelength $\lambda = 980$ nm. These data were obtained using full-wave simulations, as described in the Methods section. Varying the nanostructure length L between 0 and 400 nm changes the phase of the reflected light over a 2π range, while maintaining the amplitude of the reflection coefficient relatively constant around unity, except for $L = 150$ nm, where the excitation of a localized resonance increases absorption and reduces reflectance. To analyze missing meta-atoms, we replace the missing element with a bare substrate, i.e. with its corresponding amplitude (0.99) and phase (107°) of the reflection coefficient, computed at the same height as the other elements.

The deflection angle θ for a beam steering device under normal incidence illumination is defined as $\theta = \sin^{-1}(\lambda/\Lambda)$, where λ is the working wavelength and Λ the superlattice period, which is $\Lambda = nP_x$, where n represents the number of discretized elements used for the metasurface, which is 8 in this work. Two different designs can achieve the same beam-steering functionality: an 8-level design, which maximizes the phase discretization levels and has a smoother

phase gradient, Figure 3.4–2(c); or a 4-level design, with a coarser phase discretization, Figure 3.4–2(d). Both designs have been reported in the literature [92, 97, 147]. Since they have the same superlattice period Λ , they deflect light in the same direction $\theta \cong 43^\circ$ ($\lambda = 980$ nm) and their robustness and performance can be compared in the following.

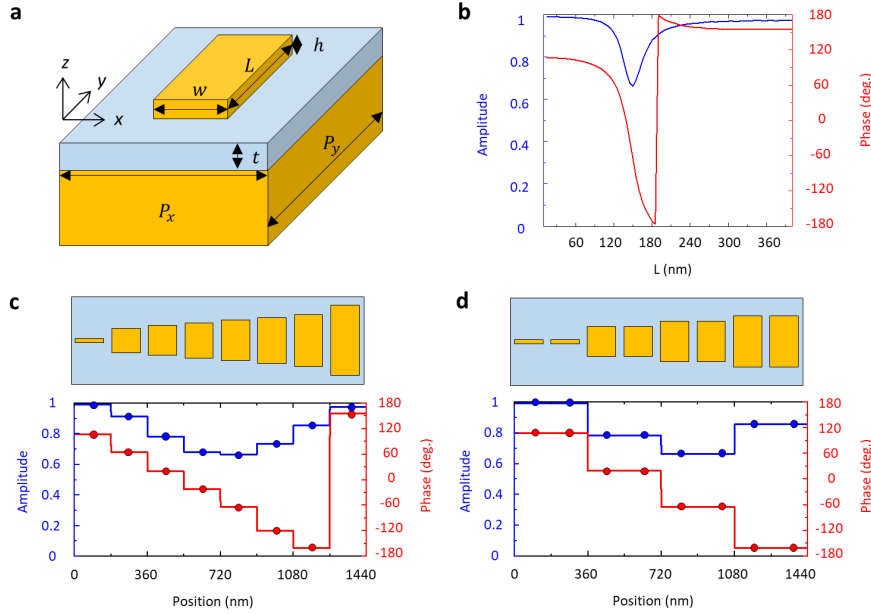


Figure 3.4–2 Optical properties of unit cells for beam-steering device and two designs for same functionality. (a) Schematic of the metallic meta-atom and (b) corresponding amplitude and phase of the reflection coefficient as a function of the length L of the gold nano-rod at $\lambda = 980$ nm. Two common configurations to achieve beam steering with a phase gradient metasurface covering a full 2π range for the phase modulation with (c) an 8-level unit cell with meta-atoms of lengths $L = 20, 120, 135, 143, 150, 160, 175, \text{ and } 345$ nm and (d) a 4-level unit cell with meta-atoms of lengths $L = 20, 135, 150, \text{ and } 175$ nm (each element being repeated). The discrete elements used for the corresponding simplified model are shown beneath panels (c) and (d).

A simple quasi-analytical model is derived in the Methods section to compute the momentum provided by the metasurface upon reflection. Based on Fourier transforms, this model is extremely efficient for computing the metasurface response and can be used to evaluate its performance. In short, the superlattice period is replaced by a collection of discrete points, each representing one meta-atom by its reflection amplitude and phase, as illustrated at the bottom of Figure 3.4–2(c) and (d). These amplitude and phase values were obtained from full-wave simulations, as described in the Methods section. With this approach, it is also very simple to compute the response of a metasurface with one or several missing meta-atoms, which are then replaced by the amplitude and phase of the substrate reflection.

Let us first use this model to study in Figure 3.4–3 the performance of 8-level metasurfaces with different missing elements. We label the intact structure as Sample #0 and a metasurface where the meta-atom m is missing as Sample # m . For a perfect 8-level device, the efficiency is 0.66, meaning that 66% of the incoming energy is redirected into the diffraction order at an angle θ , see Sample #0 in Figure 3.4–3(a). The remaining energy is absorbed in and scattered by the device. When one element is missing, light is still redirected into the direction θ , but part of the energy is also specularly reflected and absorbed, making the device less efficient, see for example Sample #5 in Figure 3.4–3(a), which has only an efficiency of 37%. Surprisingly, each meta-atom does not have the same influence on the performance, as summarized in Figure 3.4–3(c): counterintuitively, it is not when the largest elements #7 or #8 are removed that the efficiency deteriorates most; but rather missing elements around #5 appear especially detrimental to the metasurface performance. On the other hand, when the first meta-atom is missing (Sample #1) the performance is the same as the complete structure (Sample #0), because both the substrate and the first meta-atom ($L = 20$ nm) produce the same amplitude and phase for the reflected field, see Figure 3.4–2(b).

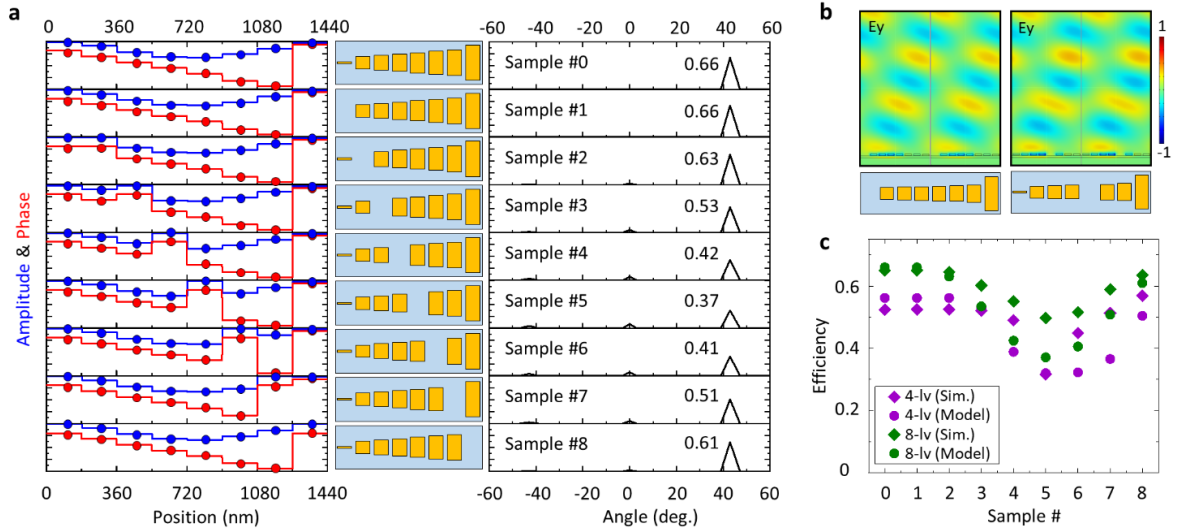


Figure 3.4–3 Performance of metasurfaces with a missing element. (a) Phase and amplitude of the reflection coefficient used for each element in the simplified model (left panel), schematics of the corresponding unit cell (middle panel), and angular response obtained with the simple model (right panel). (b) Full-wave calculations of the total (incident + reflected) electric field E_y component amplitude distribution for sample #1 (left panel) or sample #5 (right panel). (c) Metasurfaces performance as a function of the sample number for 8-level and 4-level metasurfaces, computed using full-wave simulations or the simplified model.

The special role of element #5 is also observed for a 4-level device, as indicated in Figure 3.4–3(c). Those devices have a somewhat lower performance than the 8-level devices, with an efficiency of only 56% for the perfect metasurface due to the coarser phase gradient. However, the decrease in performance caused by element #5 missing is similar for 8- and 4-level devices. On the other hand, the scattering direction θ is maintained for both devices, even when a meta-atom is missing.

Figure 3.4–3(c) also provides the efficiency for the defective devices computed with full-wave simulations. The agreement between those simulations and the simple model is very good and we also recover, with full-wave simulations, the strong influence of element #5. The small differences between the full-wave simulations and the model stem from the fact that the latter does not include the near-field interactions between neighboring elements. The efficiency computed with full-wave simulations for the 4-level device is quite surprising: sample #8 – with a missing element – has a higher efficiency (56%) than the perfect one (52%), and only sample #5 drops noticeably in performance (31%), see the purple diamonds in Figure 3c. To gain insights into the underlying mechanisms, Figure 3.4–3(b) shows the amplitude of the total electric field for Samples #1 (left part) and #5 (right part). Surprisingly, it is very difficult to distinguish in the electric field distribution any difference between both devices.

To investigate this further, we have fabricated samples for both 8-level, Figure 3.4–4(a), and 4-level devices, Figure 3.4–4(b). Purposely misfabricated samples with missing specific elements were realized, as described in Figure 2.2–9. The left parts of Figure 3.4–4(a) and Figure 3.4–4(b) illustrate the large area samples that were produced; this was also the case for the misfabricated metasurfaces, of which only excerpts are shown in the right parts. Complete misfabricated metasurfaces are shown in Figure 2.2–10 for 8-level devices and in Figure 2.2–11 for 4-level devices. The optical response of these different metasurfaces was measured using an optical microscope as detailed in Figure 2.3–10. Figure 3.4–4(c) shows the measured intensity profiles for both devices (purple lines for the 4-level devices and green lines for the 8-level devices). For each device, the efficiency is computed as the power integrated over the entire deflected beam with its center at the angle $\theta \approx 43^\circ$, divided by the measured power reflected by a mirror that replaces the sample. The corresponding values are reported in Figure 3.4–4(d), where the error bars correspond to a series of measurements with different measurement areas, as described in Figure 2.3–10. According to the experimental results, for the 8-level device (green squares): as expected, Sample #1 has almost the same performance as the perfect sample (sample #0). Surprisingly, Sample #2 and #3 have higher performance than the perfect one, while the others follow a similar trend as the semi-analytical model and the full-wave simulations with Sample #5 exhibiting the lowest performance. For the

4-level devices (purple squares in Figure 4(d)), as expected from the calculations, sample #8 has an outstanding performance, while Samples #3 and #4 perform also better than the perfect one (Sample #0). In addition to Sample #5, Sample #7 also has the lowest efficiency.

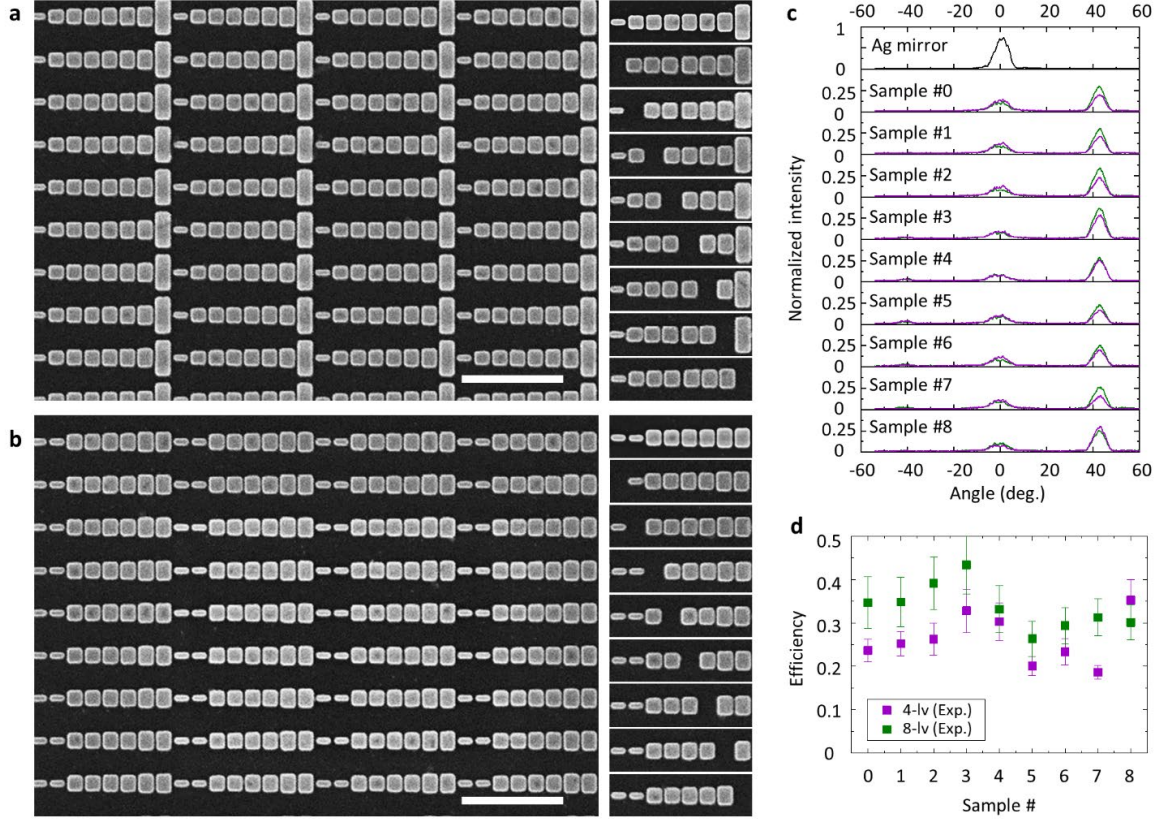


Figure 3.4-4 Experimental results for 8-level and 4-level devices. Fabricated samples (a) for the 8-level devices and (b) for the 4-level devices. The images on the left show part of the perfect sample #0 (Scale bars 1 μ m), while the images on the right show excerpts taken out of the misfabricated samples (the complete misfabricated samples are shown in the Supporting Information Figures S2 and S3). (c) Intensity profiles measured in the Fourier plane (green for the 8-level devices and purple for the 4-level devices). (d) Measured efficiency for each device at the deflection angle $\theta = 43^\circ$ (see text for details).

Next, we elucidate why the fifth element has such a significant influence on the metasurface performance: when it is missing and replaced by the highly reflective substrate the efficiency decreases most. After investigating different parameters, we came to the conclusion that this behavior is related to the phase provided by the substrate upon reflection. In Figure 3.4-5(a), we take the same configuration of an 8-level device as in Figure 3.4-2(c), but this time we keep the reflection amplitude of each meta-atom as unity, while keeping the phase gradient values as derived from full-wave simulations, such that we can clearly see how the phase of the substrate directly affects the device performance. We compute again with the simple model the device efficiency when one meta-atom is missing (Samples #0 ... #8). In addition, we modify the phase associated with the substrate reflection φ_{sub} increasing it gradually from 0° to 315° , Figure 3.4-5(c). First, we notice that for the same substrate as used previously, with a reflection phase of 107° , we recover the results obtained in Figure 3.4-3(c) – a with the strong efficiency loss for Sample #5 – in spite of keeping the reflection amplitude constant. When we change the substrate reflection phase, we observe in Figure 3.4-5(c) that different elements dominate the metasurface efficiency. For example, it is element #7 that dominates the efficiency when the substrate reflection phase is 0° . From the data in Figure 3.4-5(c) we can conclude that the lowest efficiency occurs when one removes the element which phase difference with that of the substrate is the largest (180° in this case). From an experimental point of view, let us note that the phase produced by the substrate strongly depends on the dielectric spacing layer [180].

A similar analysis is performed in Figure 3.4–5(d)–(f) for 4-level devices. In this case, we observe that the overall device efficiencies are lower than their 8-level counterparts. Even for the ideal case used in the simplified model, where each element reflects an amplitude equal to 1, the performance is only 83% due to the coarser phase gradient (it reaches 97% for the 8-level devices, Figure 3.4–5). The surprising fact that a metasurface with missing element can perform as well or even better than a complete metasurface, can easily be understood by the fact that it approximates the phase gradient better. For example, if we consider the phase substrate $\varphi_{\text{sub}} = 0^\circ$ and remove the meta-atom #4, which provides the best performance, the corresponding phase distribution – shown in in Figure 3.4–5(e) – is very smooth. Since in a 4-level metasurface both meta-atoms #3 and #4 produce the same phase, one could think that having either of them missing would deteriorate the performance in a similar fashion. Figure 3.4–5(f) indicates that this is not the case and, from the previous discussion, we have learned that the origin is the worse phase discretization when #3 is replaced by the substrate. Note that one could make good use of these observations to optimize device performances.

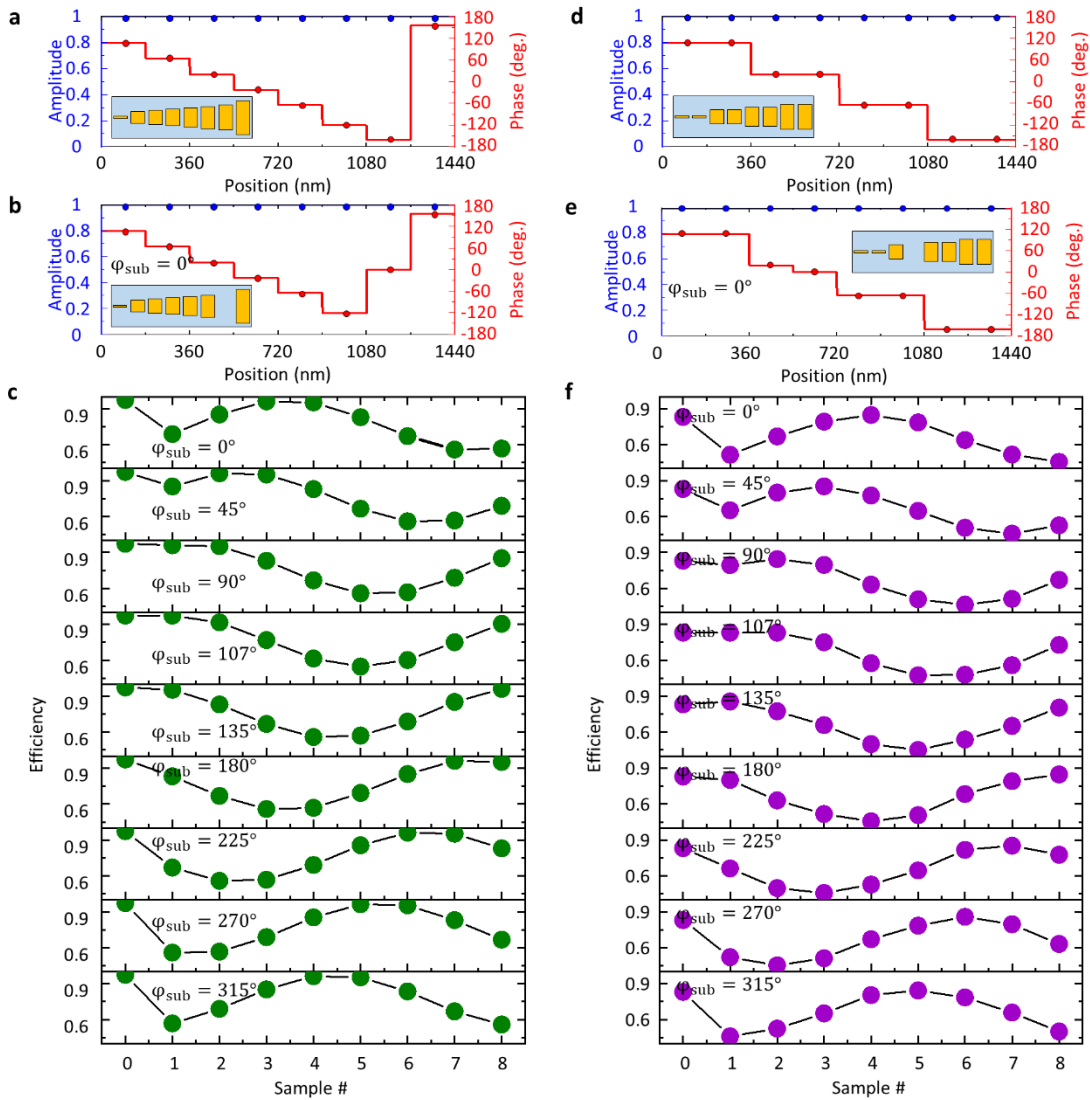


Figure 3.4–5 Efficiency of an artificial 8-level and an artificial 4-level device calculated with the simple model, neglecting the variations of amplitude. (a) Phase values from previous full-wave simulation and the artificial unit amplitudes used. (b) An example of missing element, which is replaced by substrate with phase shift 0° . (c) Metasurface performance as a function of the sample number, i.e. of the missing element for nine substrates with different reflection phases indicated in the inset. (d-f) the counterpart for 4-level device. The efficiency minimum occurs when the phase difference between the missing element and the substrate is 180° .

We now resort to full-wave simulations to study other imperfections such as displaced or bloated nanostructures. In Figure 3.4–6(a), the performance of the 8-level device is not significantly affected by the displacement of a single nanostructure in x -, y - or xy -directions. Maximum possible displacements are $\delta x = 35$ nm and $\delta y = 30$ nm (for larger δy the largest meta-atom would overflow the unit cell). Since the spacing along the x -direction between two adjacent nano-rods is only 40 nm in the original design, a $\delta x = 35$ nm displacement for one nanostructure leaves only 5 nm between neighboring nanostructures. Surprisingly, those displacements barely influence the overall device performance. This observation holds for displacements along both directions, as well as in the diagonal: overall, the exact nanostructure alignment is not required for the device performance; it does not influence the steering angle θ either.

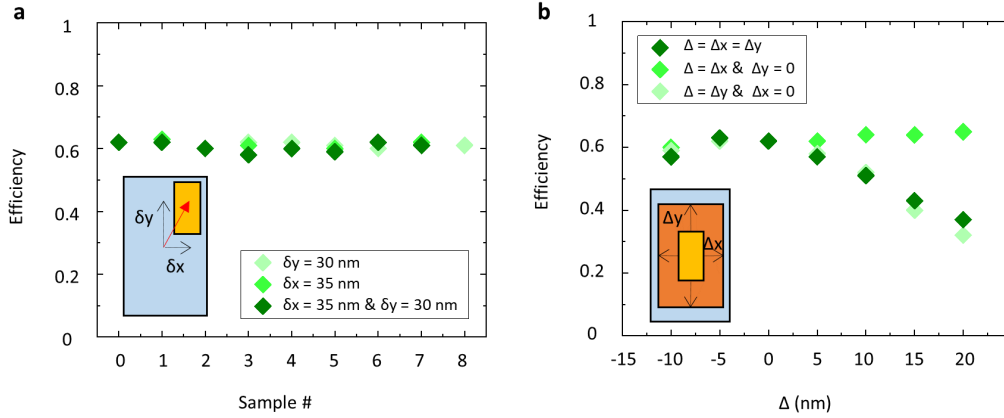


Figure 3.4–6 Performance computed for an 8-level metasurface with individual displaced element or simultaneous size change. (a) one element displaced along one direction (δx , or δy) or along both directions. (b) Performance plot as a function of the size change for all the meta-atoms.

We also study in Figure 3.4–6(b) the influence of the meta-atoms size on the metasurface performance for an 8-level device. Structures that are larger or smaller than the original design are usually the result of an over- or under-exposed lithographic process and all structures will be affected in a similar way. Hence, we consider here that all the eight structures that build the metasurface superlattice are modified in a similar amount in either x -, y - or xy -directions. Both a positive (enlarged nanostructures) and a negative (shrunk nanostructures) variation Δ is considered. We observe in Figure 3.4–6(b) that size variations in x -direction do not influence much the device performance, since the light of interest is polarized in the y -direction. On the other hand, over- or under-sized nanostructures in the y -direction deteriorate the device performance since a change in the nanostructure length L modifies the amplitude and phase of the reflected light (see Figure 3.4–2(b)). This effect is however marginal for variations between $\Delta y = -10$ nm and $\Delta y = 5$ nm, leading to a maximal efficiency reduction of only 5%. For larger variations, the performance begins to be affected significantly, for example for $\Delta y = 20$ nm the efficiency drops to half that of the perfect one, although the steering angle θ is not affected by all these changes.

Let us now briefly investigate another type of device: dielectric metasurfaces that operate in transmission. The meta-atoms are TiO_2 cylinders with a fixed height $H = 600$ nm and varying diameters D , Figure 3.4–7. Changing D tunes the phase shift of the transmitted light over 2π , while keeping the transmission amplitude constant, Figure 3.4–7b. Similar to the metallic metasurface, we investigate both 8-level and 4-level devices (Figure 3.4–7(c) and (d)), and study with full-wave calculations the response of imperfect metasurfaces with a missing element # m . The efficiency as a function of sample number is summarized in Figure 3.4–7(e). For the 8-level dielectric devices, sample #8 has about the same performance (79%) as sample #0 (the complete device). For sample #2 the efficiency drops to only 63%. Surprisingly, sample #8 for the 4-level dielectric device has the highest performance (83%), which is 18% higher than the perfect sample #0 (65%).

It is very surprising that some imperfect metasurfaces – both dielectric and metallic – can outperform perfect devices. To shed some light on this phenomenon, we use full-wave electromagnetic simulations in Figure 3.4–7(f)–(h) to compute the field distribution for perfect and imperfect dielectric devices. 4-level metasurfaces are chosen because sample #8 outperforms the ideal structure most for those devices. By comparing the different phase distributions, we observe that sample #8 exhibits a smoother phase gradient, compared to sample #0. On the other hand, sample #5, which has the worst efficiency, produces a very rough phase distribution, Figure 3.4–7(g). Consequently, although sample #8 is imperfect, its steady state electric field distribution has a better fitting with the designed phase gradient and gives rise to a higher efficiency.

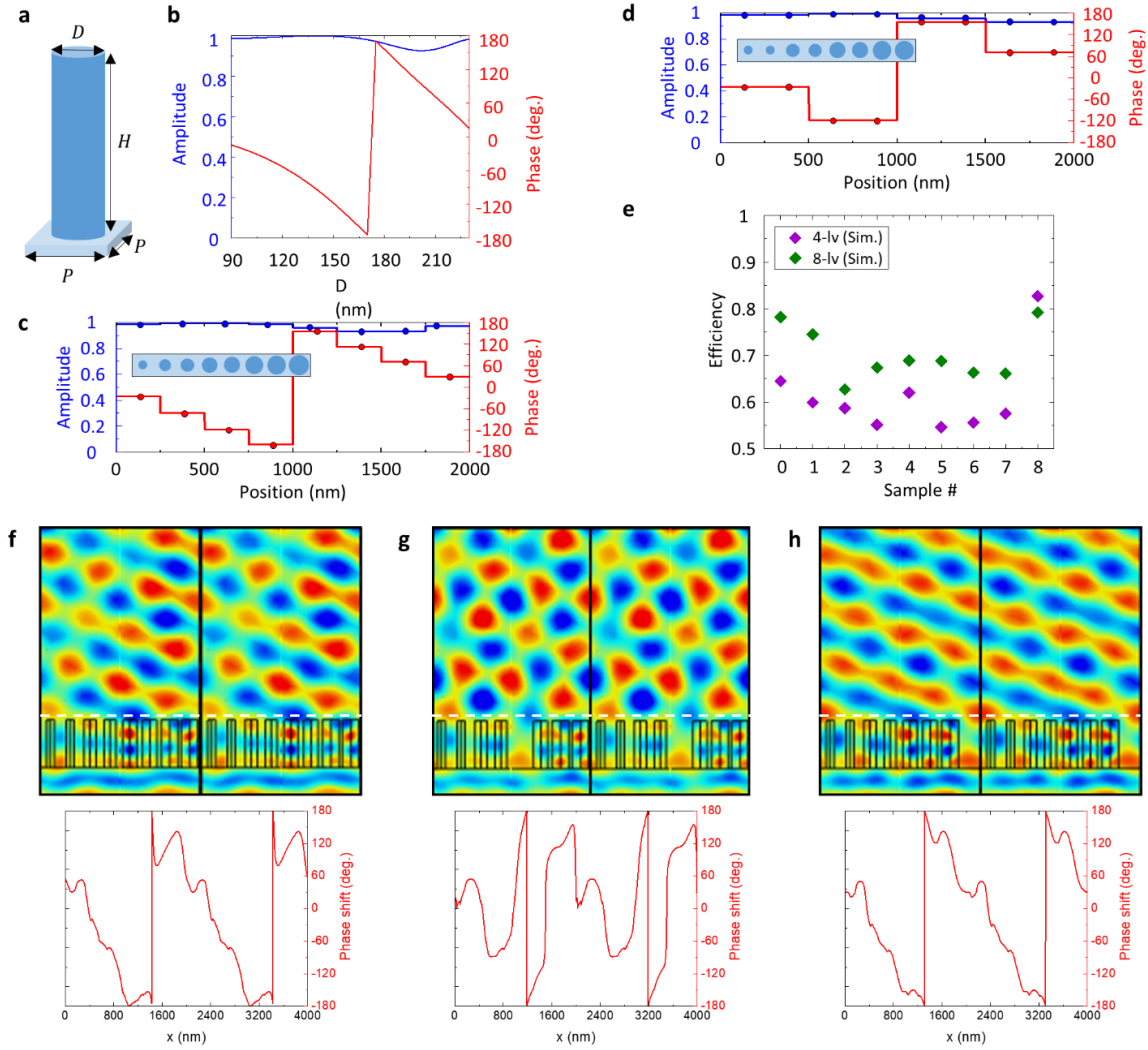


Figure 3.4–7 Another example of beam steering devices made of dielectric meta-atoms in transmission. (a) Schematic of the dielectric meta-atom: a TiO₂ cylinder (varying diameter D and fixed height $H = 600$ nm) supported by a glass substrate with the periodicity $P = 250$ nm. (b) Corresponding amplitude and phase shift in transmission as a function of D at $\lambda = 632$ nm. (c) 8-level unit cell with dielectric meta-atoms of diameters $D = 100, 130, 150, 165, 180, 195, 210$, and 225 nm and (d) 4-level unit cell with meta-atoms of diameters $D = 100, 150, 180$, and 210 nm (each element being repeated once). The discrete elements used for the full-wave simulations are shown in the insets of panels (c) and (d). (e) Metasurfaces performance as a function of the sample number for 8-level and 4-level metasurfaces, computed using full-wave simulations. Total electric field (E_y) amplitude distribution (top) and phase (bottom) for 4-level dielectric beam-steering metasurfaces: (f) sample #0 (perfect structure), (g) sample #5, and (h) sample #8. The phase is retrieved along the white dashed line.

3.4.3 Conclusion

In summary, we have analyzed theoretically and experimentally the robustness of phase gradient metasurfaces to fabrication inaccuracies, considering both metallic devices in reflection and dielectric devices in transmission. To this end, a simple semi-analytical model has been developed, which provides the response of a metasurface at almost no numerical costs and is in very good agreement with full-wave numerical simulations. This simple model could be used to design more complex metasurfaces, such as metaholograms, for example.

Missing meta-atoms are the defects that deteriorate most the device efficiency, reducing it typically by 20%. In that context, and quite surprisingly, it is not the meta-atom size that matters most, but rather its associated phase, with respect to the phase provided by the substrate. Elements which have the largest phase difference with the substrate (e.g. in the order of 180°) are the most sensitive ones. Consequently, by modifying the phase associated with the substrate, one can decide which element is going to be the most sensitive one.

A metasurface is relatively immune to the meta-atom placement within the unit cell. Although it seems that the elements can be located very closed together on the y-axis without influencing the overall performance, we must keep in mind that a single defect was investigated. The phase would in the end also vary with its neighboring units since the same structures are repeated during the design procedure. It is possible to make cells with smaller P_y , but the phase requires to be re-designed since the structural period is changed. On the other hand, sizes variations can rapidly affect the overall efficiency. These findings hold both for 8-level and 4-level metasurfaces and for both types of devices, we notice that the steering angle is not influenced by such defects θ .

Measurements on misfabricated metallic metasurfaces – both 8-level and 4-level – fully support these findings, which indicate that one can design a metasurface with less stringent considerations than anticipated. This work paves the way for revisiting the design of metasurfaces afresh, beyond the constraints of a periodic perfect lattice, possibly with the help of a deep learning approach [181].

3.5 Outlook

Metasurfaces in general have been developed for a decade, and many proof-of-concept devices have been demonstrated in the laboratory stage. It is time to address industry needs and concerns for mass production. These two fundamental studies concerning the experimental environment for reconstructing metaholograms and the high tolerance to defects, imply that devices made from metasurfaces can be useful and robust in the field of holography. To achieve higher efficiency regardless of the traditional physical design, one can generate a database with numerical simulations for training neural networks. In recent years, many studies have started to apply deep learning, data driven approaches, for free-form optical designs, which will be introduced in Section 4.3.

Chapter 4 Spectral manipulation

Spectral responses, for instance, reflectance, of periodic meta-atoms with polarized light are discussed. Although the resonant curve of plasmonics on a spectrum has the shape of a Lorentz function, the reflection spectrum, however, is complicated and depends on the geometry and structural design of a meta-atom.

4.1 Introduction

In the first section, rectangular shaped nanorods are investigated due to a counter-intuitive observation, wherein structural colors of horizontal nanorods turn vivid when illuminated with polarized light in a diagonal direction. If the polarization direction is along the tuned dimension, the colors are muted. Existing literature can hardly explain this phenomenon and plasmonic absorption is not a valid explanation either because there should be no loss for silver in the visible regime. After a thorough study on this mechanism, we demonstrate nanoprinting and encryption as examples for plasmonic applications. In the second section, an ongoing collaborative work is presented, where I am in charge of the simulated database, fabrication, and measurement. Because the spectral response of a meta-atom varies with its dimension and geometry, one can think about using machine learning to predict potential geometries of the meta-atoms, which is an approach that will be discussed in the second section.

4.2 Chromo-encryption

This section has been submitted to *Advanced Optical Materials*.

Title: Polarization-controlled chromo-encryption

Authors: Hsiang-Chu Wang and Olivier J.F. Martin*

Abstract: The response of simple plasmonic nanorods to polarized illumination is studied in detail. Depending on the orientation of that polarization with respect to the symmetry axes of the nanostructure, a chiral response can occur. This response can be analyzed through a second polarizer in order to control the spectral response of the system. Specifically, for the Ag nanorods fabricated here, a broad variety of colors can be produced that cover half of the chromaticity diagram. Depending on the illumination and detection polarizations, these colors range from white to vivid colors or even black, in spite of the fact that the material at hand does not absorb much light. By exploiting two additional degrees of freedom, namely the nanorod length and its orientation within the unit cell, it is possible to produce a very rich palette of optical effects that are controlled by the polarization of light. Their use in reproducing artwork is demonstrated, together with their operation as an encryption system, where the polarizations are used as keys and the message is encrypted in a quaternary color subset.

4.2.1 Introduction

Structural colors [182-186], with their stability, environmental friendliness, and extremely high spatial resolution, enable applications in passive colors for decoration, display [187-190], high-density optical storage [191], information processing [192] and encryption [193]. Different types of structures have been demonstrated for those applications, including grooves [194-197], gratings [198-205], films [206, 207], apertures, nanoparticles [51, 58, 59, 70, 72, 76, 154, 156, 208-213], and related structures [63, 214-218]. In order to increase the information density, the variation of optical

responses under different polarization states has also been used with geometries such as rectangles [61, 74, 219-221], crosses [222-225], and ellipses [226, 227].

Optical cryptography involves recording or transmitting concealed information by means of light where only the employment of correct keys enable the interpretation of the original information. Conventional methods, in general, utilize a phase key to encrypt the original information and a corresponding phase key to decrypt the encrypted information [228]. This concept has been adopted in meta-holograms by illuminating a metasurface (encrypted information) with a modulated incident light (key) [115, 229, 230]. Another group patterns the encrypted information by encoding the orbital angular momentum (OAM) helical phase and Fourier transform lens such that when decrypting with correct keys (time-dependent OAM incident beams), the encrypted information becomes comprehensive [231]. In addition to reconstructing the information in the far field like holograms, encrypted metasurfaces composed of complex-amplitude units can be arranged into gray scale or color images [31, 232-238]. Combining the channels in the far field and near field makes optical encryption more versatile, like in binary or color QR code [62, 239-241]. Since the spectral response of nanostructures is generally sensitive to polarization orientation it can serve as key to decrypt information [64, 65, 68, 118, 242, 243]. However, these encryption concepts are not yet utilized to their full potential. In this work, we use a simple geometry to demonstrate a plethora of spectral responses, which are then employed for encryption using a quaternary system.

Here, we resort to silver (Ag) for its low losses in the visible [17]. Each color pixel (unit cell) contains a rectangular Ag nanorod on a dielectric pedestal that forms an aperture of similar geometry within an Ag mirror underneath (see Methods). The unit cells are placed on a square array with period 300 nm, which prevents grating diffraction orders and Wood-Rayleigh anomalies at the visible wavelength of interest [244]. The coupling between the nanostructures and the mirror plane is negligible since the pedestal height is larger than 80 nm [71]. The readout scheme is illustrated in Figure 4.2–1(a), incident light (in black), passing through a linear polarizer and a polarization insensitive beam splitter, impinges on the sample. The reflected light (in red) is then analyzed with another polarizer (analyzer). When both polarizers are parallel with the nanostructures (horizontal, H-direction, Figure 4.2–1(b)), the observed colors are muted, with a low chroma caused by the low Ag absorption. When rotating both polarizers perpendicular to the nanostructures (vertical, V-direction, Figure 4.2–1(c)), all the colors appear grey due to the lack of dimensional variations in this direction. However, the colors become vivid and saturated when both polarizers are in the diagonal direction (+45°, D-direction), Figure 4.2–1(d). This difference of color contrast controlled by the mere orientation of the polarization is quite baffling, since it contradicts our intuition that the response for diagonal polarization could be inferred from the superposition of the responses for H- and V-directions. There is however a flaw in the simple application of the principle of superposition, as explained next. The strong dependence of the color contrast on polarization observed in Figure 4.2–1 forms the foundation for the chromo-encryption presented here.

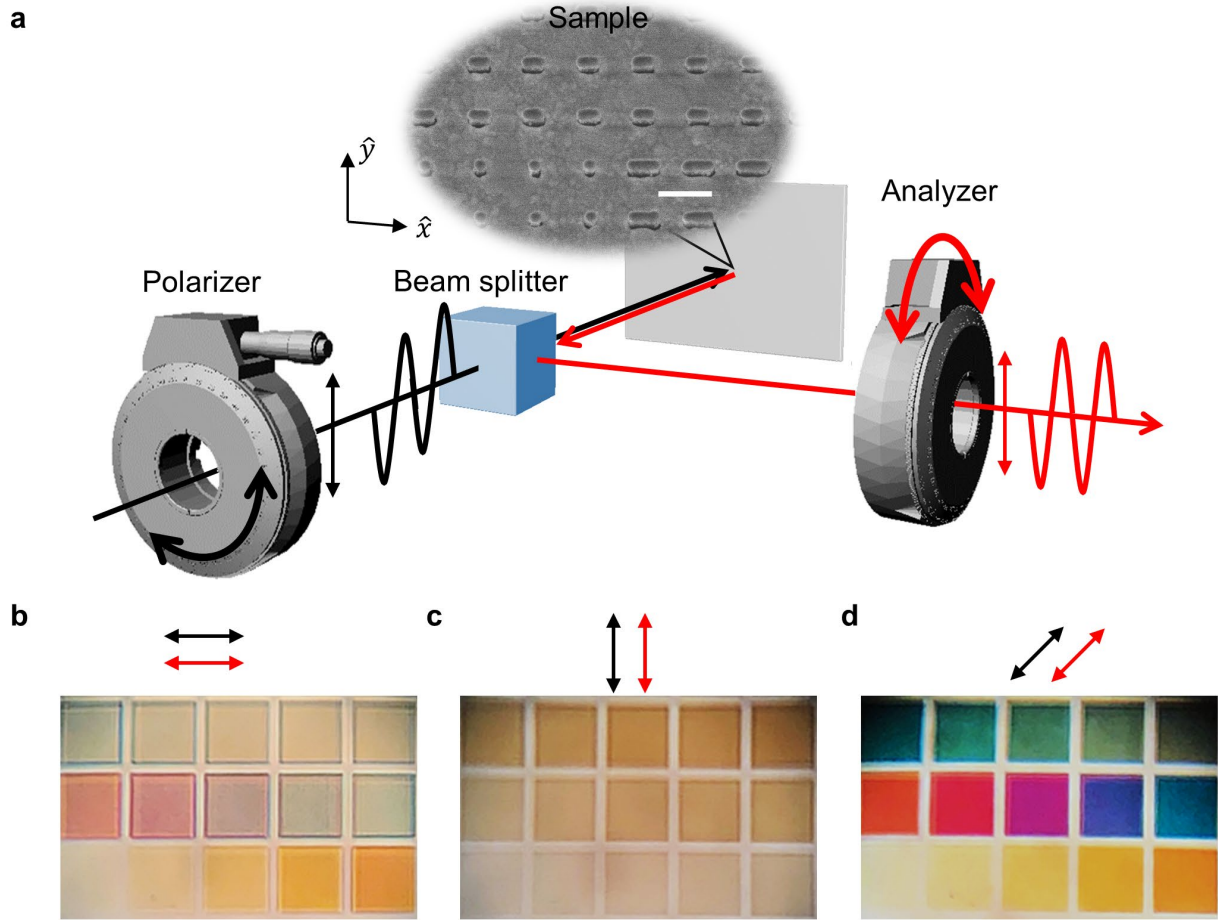


Figure 4.2–1 Color contrast controlled by polarization. (a) Readout principle: each color pixel contains a rectangular Ag nanostructure (scale bar 300 nm). The incident polarization is controlled with a polarizer and the scattered light goes through another polarizer (analyzer). (b) Muted colors with low chroma are generated when the polarizer and analyzer are parallel to the nanostructures axis (horizontal polarization). (c) When rotating both polarizers perpendicular to the nanostructures axis, all the colors appear greyish (vertical polarization). (d) when both polarizers are rotated by 45°, along the diagonal direction, vivid and saturated colors are observed.

Principle of superposition and polarization-induced chirality

The principle of superposition, which stems from the linearity of Maxwell's equations, is ubiquitous in photonics, to the extent that it can pervert our intuition. For example, one would intuitively assume that the optical response of an optical system under diagonal illumination can be inferred from the combined responses for horizontal and vertical illuminations. However, the bleak colors observed under horizontal polarization (H-direction, Figure 4.2–1(b)) or vertical polarization (V-direction, Figure 4.2–1(c)) are turning vivid under diagonal polarization (+45°, D-direction, Figure 4.2–1(d)). This implies that the reflected light intensity under diagonal illumination cannot be deduced from the mere superposition of those along H- and V-directions by applying the principle of superposition naively. As a matter of fact, the principle of superposition cannot be applied to the intensity of light, but is only valid for its amplitude. It is however possible to make a link between the light detected diagonally and the horizontal and vertical components of the illumination field by introducing E_{β}^{α} for the electric field amplitude reflected from the sample, where α indicates the polarization of the incident field and β the polarization of the reflected light. The reflected intensity measured under unit amplitude diagonal polarization can then be written as

$$\begin{aligned}
R^D &= \left| (E_H^H + E_H^V) \hat{h} + (E_V^V + E_V^H) \hat{v} \right|^2 = \left[(E_H^H + E_H^V)^2 + (E_V^V + E_V^H)^2 \right] \\
&= \left[(E_H^H)^2 + 2E_H^H E_H^V + (E_H^V)^2 + (E_V^V)^2 + 2E_V^V E_V^H + (E_V^H)^2 \right],
\end{aligned} \tag{4.2.1}$$

where \hat{h} and \hat{v} are unit vectors along the horizontal and vertical directions. Obviously, this intensity is different from the sum of those reflected at 0° and 90° ,

$$R^D \neq R^H + R^V = \left[(E_H^H)^2 + (E_V^V)^2 \right], \tag{4.2.2}$$

Except for the very special case when all cross polarization terms vanish: $E_H^V = E_V^H = 0$. This condition occurs very rarely; it would for example be the case for a perfectly cylindrical scatterer. For most structures, including the nanorod pixel considered here, the response is always anisotropic or chiral, meaning that the cross-polarization terms do not vanish and the optical response under diagonal polarization can be very different from that under horizontal or vertical polarizations, as visible in Figure 4.2–1(b)–(d).

It might be surprising that a very simple structure with two mirror symmetry planes like the nanorod considered here exhibits chirality. In the scientific literature, quite complicated structures, like the gammadion represent the archetype of a chiral structure [245–248]. However, as described in details by Okamoto [69], a nanorod exhibits chirality as soon as it is illuminated with light polarized different from one of its symmetry axes (H- or V-directions in the case of Figure 4.2–1).

4.2.2 Results and discussion

Polarization controls colors

Let us first study numerically the cross-polarization terms for the unit cell depicted in Figure 4.2–4a using full-wave simulations with periodic boundary conditions. Such a structure is easy to achieve by two-step fabrication (see Methods). The only variable is the length L of the rectangular structures; the simulated and measured reflectance spectra for L between 40 nm and 200 nm are presented in Figure 4.2–2.

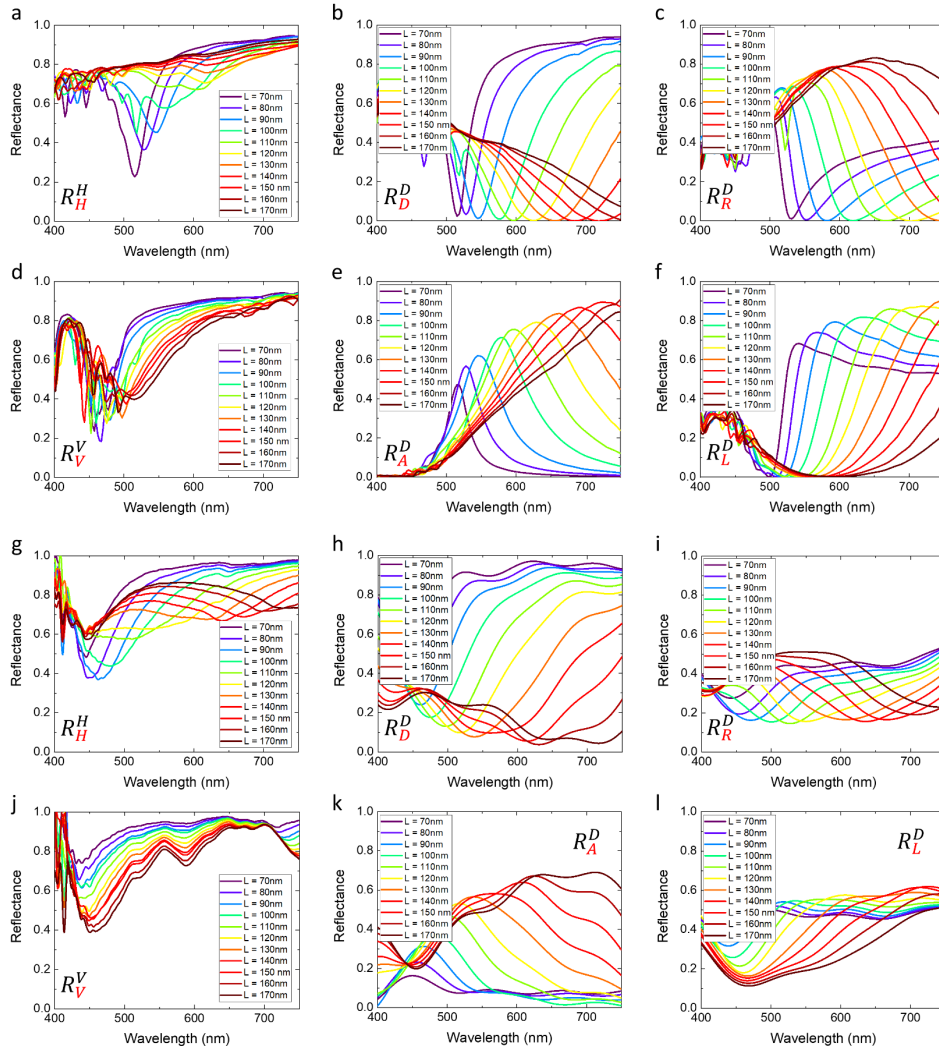


Figure 4.2-2 Simulated and measured spectra as a function of L . (a) Under H-polarized illumination and detection in H-direction. (b) Under D-polarized illumination and detection in D-direction. (c) Under D-polarized illumination and detection in R-direction. (d) Under V-polarized illumination and detection in V-direction. (e) Under D-polarized illumination and detection in A-direction. (f) Under D-polarized illumination and detection in L-direction. (g)-(l), counterparts of measured spectra.

As an example, let us discuss the sample with $L = 100$ nm: the tilted SEM image of a typical Ag rectangular array is displayed in Figure 4.2-4(b). The simulated spectra for reflectance and phase shift are plotted in Figure 4.2-4(c). To study the effect of the illumination and detection polarizations, we introduce a similar notation for the reflectance: R_{β}^{α} , where α indicates the polarization of the incident field (polarizer in Figure 4.2-1a) and β that of the reflected field (analyzer in Figure 4.2-1(a)). When both polarizations are collinear, the reflectance is not strongly modulated, see R_H^H and R_V^V in Figure 4.2-1(c), leading to the muted colors visible in Figure 4.2-1(b) and (c). For cross polarizations, R_H^V and R_V^H , the reflectance is so small that it cannot be shown in Figure 4.2-4(c) and the structures appear black. On the other hand, vivid colors are observed in Figure 4.2-1(d) under diagonal illumination and detection. The reason for this effect can be understood by studying the corresponding phase shift and reflectance spectra under H- and V-polarized illumination in Figure 4.2-4(d). The spectrum under diagonal polarized illumination R_D^D is drawn in brown; it has the deepest trough among the different polarizations investigated, indicative of the strongest color. Since Ag is a low-loss plasmonic material, it is hard to explain this deep trough with absorption [249]. On the other hand, the phase shift associated with the reflectance provides a clue on the phenomenon. The three purple arrows in Figure 4.2-4(c) and (d) indicate the

spectral locations where the phase shift differences τ between R_H^H and R_V^V , defined as $\tau = \Phi_H^H - \Phi_V^V$, amount to $+90^\circ$, 180° , and -90° , respectively (from left to right). These values correspond to special polarizations, namely right circular (R), anti-diagonal (A), and left circular (L) polarization states, respectively. In fact, the phase shift difference τ determines the conversion of polarization states. The polarization states can be easily interpreted through the observation of the electric fields that oscillate with time. The oscillation patterns of different polarization states are presented in Figure 4.2–3.

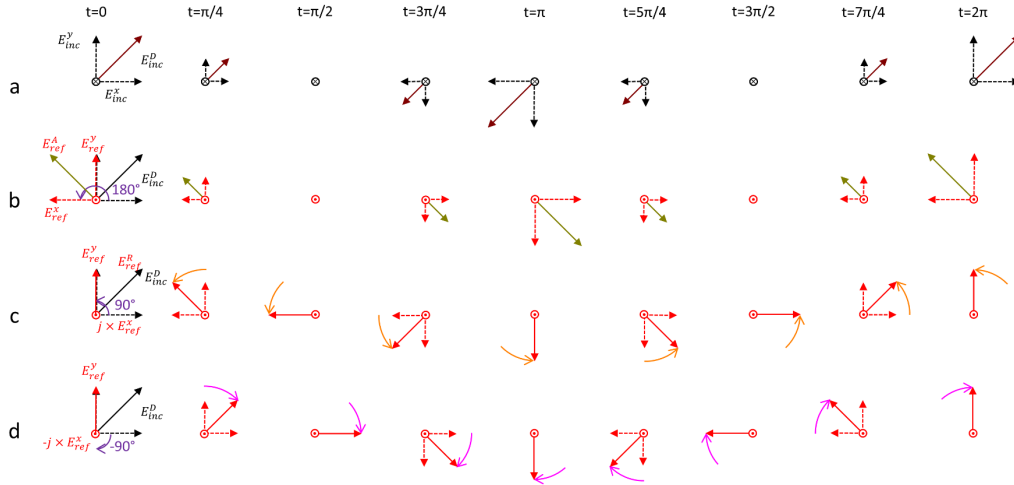


Figure 4.2–3 Oscillation patterns of the reflected light with different τ in a cycle. (a) Unity incident light (in brown arrows) polarized in D-direction propagating in -z direction. The electric field of incident light is decomposed into E_x and E_y components (dashed black arrows), which oscillate with time. When $t = 0$, both components are $+1/\sqrt{2}$. In each time step ($t = \pi/4$), both components oscillate in phase, leading to a linear polarization in 45° . (b) Reflected light (in grey green arrows) polarized in A-direction (-45°). The electric field of reflected light is decomposed into E_x and E_y components (dashed red arrows). When the phase shift difference τ is 180° , the oscillation of E_x component is delayed by π , leading to the reflected light oscillating in A-direction. (c) Reflected light (in orange arrows) polarized in R-direction (right circular). The electric field of reflected light is decomposed into E_x and E_y components (dashed red arrows). When the phase shift difference τ is $+90^\circ$, the oscillation of E_x component is $\pi/2$ faster than E_y component. In this case, $E_x = \cos((t + \pi/2) + \tau)/\sqrt{2}$, while $E_y = \cos(t + \pi/2)/\sqrt{2}$. So at $t = 0$, only E_y component is present. At $t = \pi/2$, E_x component has already reached $-1/\sqrt{2}$. Follow this pattern, one can use the right thumb to point out the propagating direction ($+z$) of reflected light, which is defined as R-polarization. (d) Reflected light (in magenta arrows) polarized in L-direction (left circular). When the phase shift difference τ is -90° , the oscillation of E_x component is delayed by $\pi/2$. Follow the sample approach in c, one can point out the propagating direction of reflected light with left hand.

The plot in Figure 4.2–4(d) describes how the incident light is converted by the unit cell under diagonal polarization illumination into a color spectrum. The incident light (black arrow) can be decomposed into E_{inc}^H and E_{inc}^V . When reflected, the phase shift transforms the incident light E_{inc}^H into E_{ref}^α with a different polarization state α : for a phase shift difference of 180° , the unit cell acts as a half-wave plate, while for a phase shift difference of $\pm 90^\circ$, it acts as a quarter-wave plate. The corresponding spectra are simulated in Figure 4.2–4(e). A maximum cross-polarization peak is detected for $\tau = 180^\circ$, leading to the trough in R_D^D . The extreme for right and left circular polarizations are at the intersections of the R_D^D (in brown) and R_A^D (in grey green), where the phase shifts are $\pm 90^\circ$. The corresponding reflectances measured for R_H^H , R_V^V , R_D^D , R_A^D , R_R^D and R_L^D are shown in Figure 4.2–4(f). In Figure 4.2–2, the trough in the spectrum red shifts with increasing lengths L , which generates rainbow colors by changing L . For the cross-polarization spectra R_A^D , the colors are complimentary to the colors of the co-polarization spectra R_D^D . Likewise, the colors of R_R^D are also complimentary to those of R_L^D .

Since the structure exhibits a different response to the polarization throughout the entire visible range, the spectral response varies with the polarization used. This is illustrated in Figure 4.2–5, where we consider nanostructures of varying lengths L between 40 and 200 nm. Six different polarization states (H, V, D, A, R, L) and their most interesting combinations are considered for illumination and detection, Figure 4.2–5(a). These spectra correspond to different colors, as illustrated in Figure 4.2–5(b)–(d) with the Commission internationale de l'éclairage (CIE 1931) diagrams [250]. For example, Figure 4.2–5(b) shows the different colors when illuminating with H-polarized light, and detecting with H, D, A, R, and L: all these colors are muted, centered around the region CIE map region with coordinates x and y are between 0.3 and 0.4. As for the cross-polarization terms R_V^H , denoted as green crosses, they are black due to no contribution to this polarization state (like R_V^H curve in Figure 4.2–4(c)). Note that the CIE chromaticity diagram does not include the brightness information. A similar behavior is observed for illumination with V-polarized light shown in Figure 4.2–4(c) (R_H^V curve). On the contrary, illuminating these horizontally aligned structures with polarization states such as D, A, R, and L can dramatically expand the detected colors, as evident in Figure 4.2–5(c) for D-polarized illumination and in Figure 4.2–5(d) for R-polarized illumination. Additional illumination polarizations are also presented. In any case, colors illuminated along the symmetry axes of these rectangular structures, i.e. with H- or V-polarizations, remain muted. Other geometries could of course unmute these colors and achieve similar possibilities. For the nanorod shapes studied here, although the colors are muted and not very vivid, the human eyes can still notice their subtle differences, as shown in Figure 4.2–1(b).

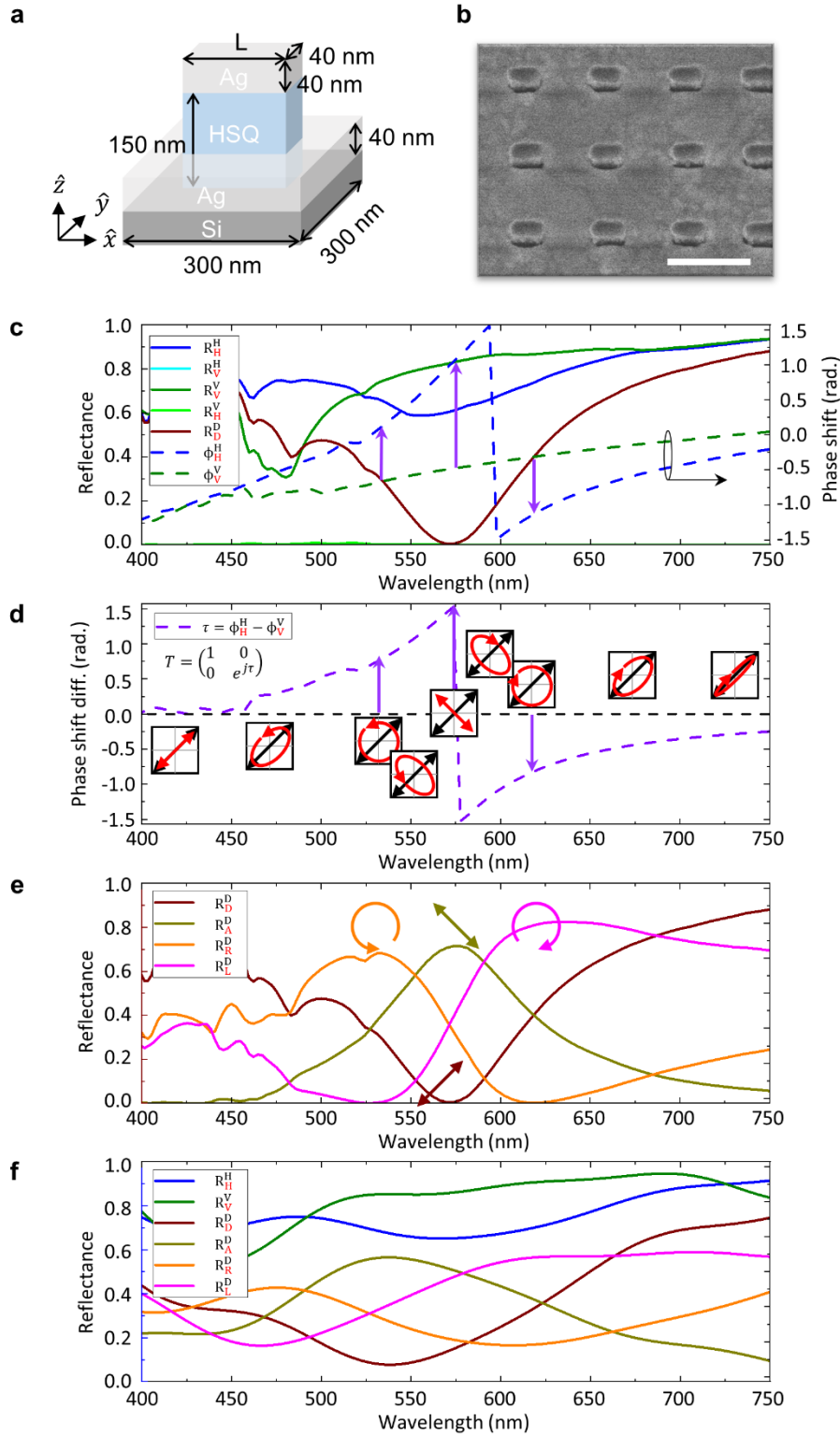


Figure 4.2–4 Colors controlled by the illumination and detection polarizations. (a) Unit cell used in this work, with the nanorod aligned horizontally. (b) Titled SEM image of the fabricated sample, scale bar 300 nm. (c) Computed reflectances R_{β}^{α} and phases Φ_{β}^{α} for different combinations of the illumination polarization α and the detection polarization β . Phase shift between the incident and the reflected lights, induced by the sample (see text for details). (d) Polarization states of reflected light (red arrows) as a function τ under diagonal polarization illumination (black arrows). (e) Computed reflectances for diagonal polarized illumination and four different detection polarizations. (f) Measured reflectance for the sample in b for different polarization combinations. Panels c)-f) are for $L=100$ nm.

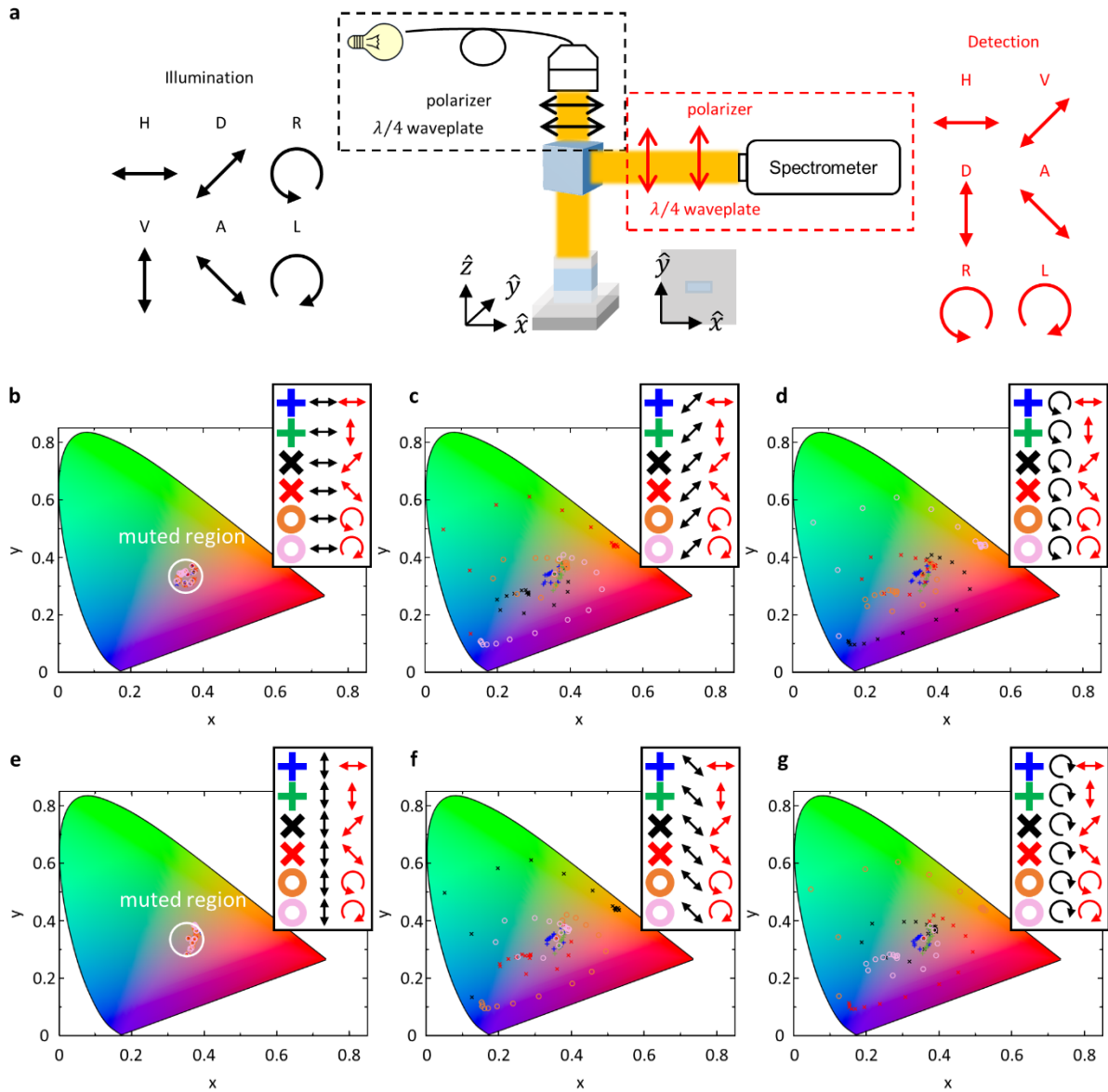


Figure 4.2-5 Reflectance color space covered by changing the nanorod length between $L = 40$ nm and 200 nm for different polarization combinations. (a) Polarizations used for illumination and detection. (b) Horizontal illumination polarization produces muted colors that accumulate in the center of the CIE chromaticity diagram. (c) Diagonal illumination polarization produces vivid colors that cover most of the chromaticity diagram. (d) Right circular illumination polarization produces similar effects with different colors. (e) Vertical illumination polarization produces muted colors that accumulate in the center of the CIE chromaticity diagram. (f) Anti-diagonal illumination polarization produces vivid colors that cover half of the CIE chromaticity diagram. (g) Left circular illumination polarization produces similar effects with different colors.

Based on the idea that colors of nanorods with only one variable L cover broad area on a CIE map, we can utilize these different polarization-controlled colors to reproduce the oil painting Mediterranean Landscape by Pablo Picasso © Succession Picasso / 2022, ProLitteris, Zurich. The original is reproduced in Figure 4.2-9(a). Pixels on the painting are replaced by nanorods with different lengths aligned horizontally. Using the same two-step process of first patterning HSQ with electron beam lithography and then depositing Ag, we obtain a nano-painting ($360 \mu\text{m} \times 235 \mu\text{m}$). Under electron scanning microscope, this nano-painting exhibits a grey scale before (Figure 4.2-9(b)) and after (Figure 4.2-9(c)) Ag deposition. Under polarized white light illumination, it presents different colors depending on the illumination and detection polarizations. (The minor color differences between Figure 4a and 4e is mainly caused by the color quantization described in Figure 4.2-6; in addition some nanofabrication inaccuracies as well as the camera used to take the image in Figure 4e contribute to those color differences). For example, illuminated and detected with both H-polarizations

(Figure 4.2–9(d)) or both V-polarizations (Figure 4.2–9(g)), as expected the colors of the nano-printing are muted, Figure 4.2–5(b). To unmute the colors of these horizontal rods, the polarizations of illumination must differ from H- or V-directions, which is simulated in Figure 4.2–5(c) and (d). In this demonstration, the correct color will be displayed by illuminating and detecting in the D-direction R_D^D as shown in Figure 4.2–9(e), where a color quantized image quite close to the original is recovered. A finer nano-painting can be achieved by applying additional quantized colors [251].

Color quantization is a process of reducing the number of distinct colors used in an image, such that a quantized one is still visually similar to the original image. For example, an original image is composed of more than thousand RGB colors, noted as white dots covering over the RGB color space in a CIE map. Relative few numbers of colors are used to reconstruct the quantized image, which appears similar to the original one as shown in Figure 4.2–6.

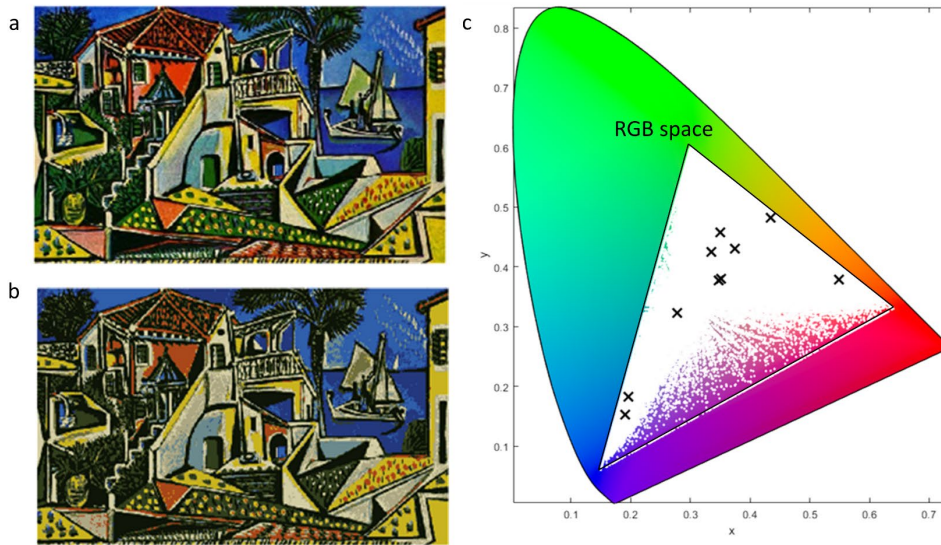


Figure 4.2–6 Color quantization of an image. (a) The original image and (b) its color-quantized image. (c) The color composition of an original image, noted as white dots on a CIE map covering the RGB color space (in a shape of triangle), can be quantized into few number of colors (labelled with black crosses on the CIE map), such that the quantized image is as similar to the original one.

This demonstrated nano-painting utilizes only 9 different rods, including one for a black color. When observed with other polarization pairs such as R_R^D in Figure 4.2–9(f), R_A^D in Figure 4.2–9(h), or R_L^D in Figure 4.2–9(i), other colors are displayed. Let us consider the red building as an example: the wall is designed in red; this color is muted under R_H^H (Figure 4.2–9(d)) and turns grey under R_V^V (Figure 4.2–9(g)). On the other hand, it becomes a strong and saturated red under R_D^D , and switches to the complimentary color – cyan – under R_A^D , Figure 4.2–9(h). When detected with R- or L-polarization, the colors are either blue-shifted or red-shifted. It might appear counterintuitive to achieve black by addition of primary colors, whose mixture normally turns white. Actually, the black color here is achieved by converting the D-polarized incident light into A-polarized light, since the structure of interest has very limited absorption. That is why the dark areas in Figure 4.2–9(e) appear bright in Figure 4.2–9(h). The approach of mixing colors to achieve brighter or darker rainbow colors is to add black or white unit cells into a pixel array, as described in Figure 4.2–7.

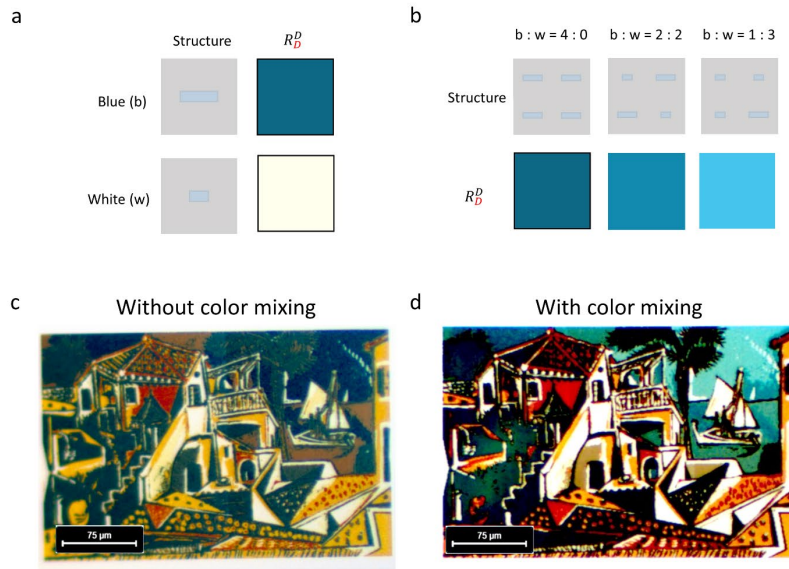


Figure 4.2-7 An example of mixing white unit cell with dark blue color to achieve brighter blue. (a) Schematic of dark blue and white structures and their colors on condition of R_D^D . (b) Strategies of mixing blue and white unit cells in a supercell and the corresponding colors on condition of R_D^D . The optical image (R_D^D) (c) without color mixing and (d) with color mixing. The same strategy applies to adding black structures to achieve darker colors.

Hence, black is composed of two nanorod units, while white is composed of shorter rods with length 60 nm. A pure color such as red is composed of a single length rod in a unit cell. The brighter blue is a mixture of blue and white units: by adding the black and white units into the pure single rod color, we are able to tune the brightness of the rainbow colors (see SEM images in Figure 4.2-8).

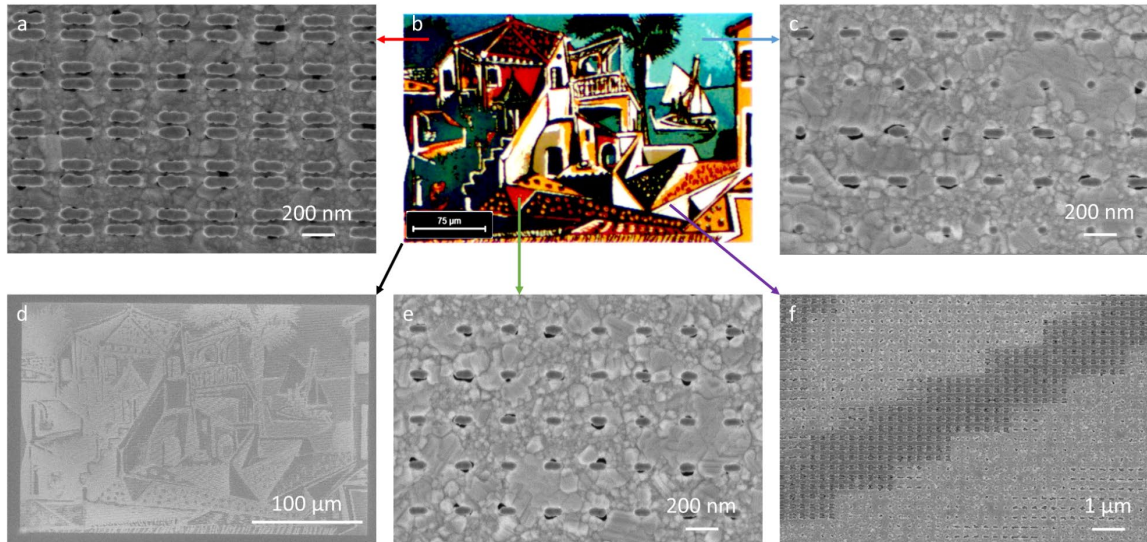


Figure 4.2-8 SEM images of the fabricated nano-printing. (a) SEM image of the two nanorod units for black color for (b) nano-printing designed to reproduce correct colors by D-polarized illuminating and D-polarized detection. (c) The brighter blue color is generated by mixing white color units between dark blue color units. (d) SEM image of the nano-printing made of color mixing unit cells. (e) Pure red color is made by same nanorod (L = 90 nm). (f) SEM image of some other corner in nano-printing.

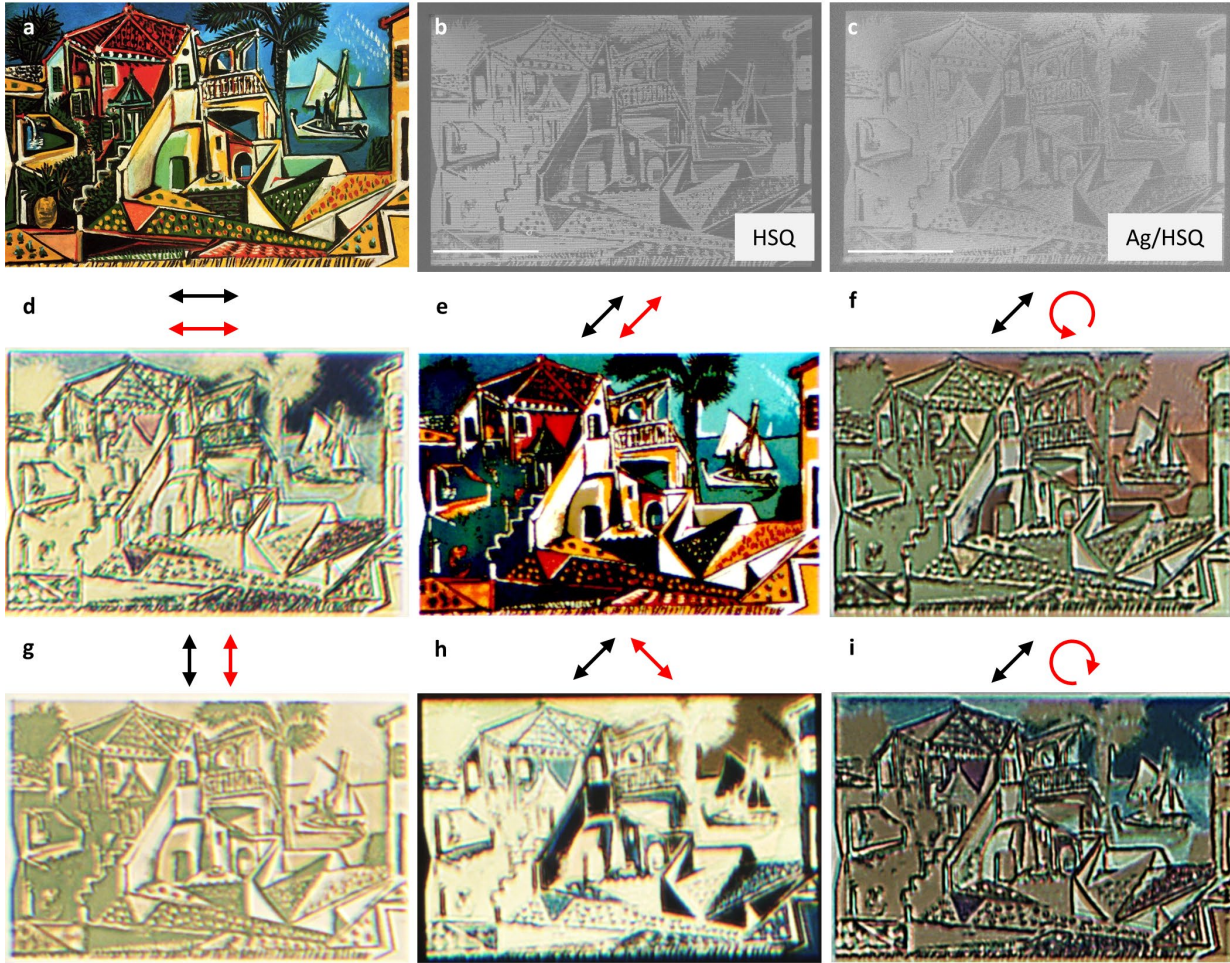


Figure 4.2–9 Nano-printing of the Mediterranean Landscape by Pablo Picasso. (a) Original painting, reproduced from under (license type). SEM images of the sample (b) before and (c) after Ag deposition. Bright field microscope images for different illumination-detection polarization pairs: (d) horizontal-horizontal; (e, diagonal-diagonal; (f) diagonal-RCP; (g) vertical-vertical; (h) diagonal-anti-diagonal; (i) diagonal-LCP.

Chromo-encryption

Now that we have established that the color exhibited by a simple nanorod depends on the illumination and detection polarizations, this optical property can serve as basis for encryption with structural colors. The connection between structural colors and keys in encryption applications is demonstrated in Figure 4.2–11, where the illumination–detection polarization pair represents a key for that encryption system. Although the palette at hand could also support the octal system under proper definitions, we use the quaternary number system[252] for simplicity. In this system, the plain text “Hello!” will be translated into a series of digits 0, 1, 2, and 3. Letters and symbols are defined in ASCII with the binary code that is directly converted it into quaternary digits, 1020 1211 1230 1230 0201 in this example, Figure 4.2–11(a). These digits are later defined on a table of structural colors.

So far, we have focused on nanorods oriented in H-direction only; to increase the utility of keys, we also now include four orientation angles (<1: 0°, <2: 45°, <3: 90°, and <4: 135°). The corresponding colors for different illumination and the detection polarizations are exhibited in the tables shown in Figure 4.2–10. One can notice that the colors are hopping between keys as nanorods rotate. Assuming only linear polarization states (H, V, D, and A) are used for illumination, while detection polarization can be arbitrary, R_H^H , R_V^V , and R_D^D share the color bases; R_A^D is independent from other keys; R_R^D , and R_L^D have the same colors. By applying nanorods possessing high color contrast with orientations, colors read by different keys become multiple. Such approach increases significantly the options to encrypt the digits as a function of nanorod lengths and rotation angles. In the following demonstration, three nanorod lengths ($L = 110$ nm,

130 nm, and 170 nm) with four orientation angles within the unit cell (<1: 0° , <2: 45° , <3: 90° , and <4: 135°) are used. In Figure 4.2–11(b), each structure exhibits different colors under each polarization pairs (keys) of illumination and detection. Yellow colors are labelled as 0, muted colors are assigned as 1, while the remaining distinguishable colors are given 2 and 3 for each polarization pairs, which is compatible with the quaternary coding system. Note that for each polarization pairs, each number can be realized with more than one structure, Figure 4.2–11(b). This provides additional freedom to choose the encrypted structure.

A possible collection of nanostructures with the key illumination-D detection-D is described in Figure 4.2–11(c) for the plain text "Hello!". When decrypted with different keys, different color combinations are observed and the concealed information is successfully decrypted only with the correct key, as shown in Figure 4.2–11(d); applying other keys leads to scrambled messages (Figure 4.2–11(e) to (g), note that we have used here the extended ASCII table that includes 256 characters and sequences such as DC2, EOT, ACK and DC1, which have been underlined to emphasize that they correspond to one single ASCII code). Unlike the binary system, for which an inverted decoding can break the encryption by switching 0 to 1 and vice versa, the quaternary system is very robust and only incorrect messages are produced with the incorrect key, as illustrated in Figure 4.2–11(h) to 5(i).

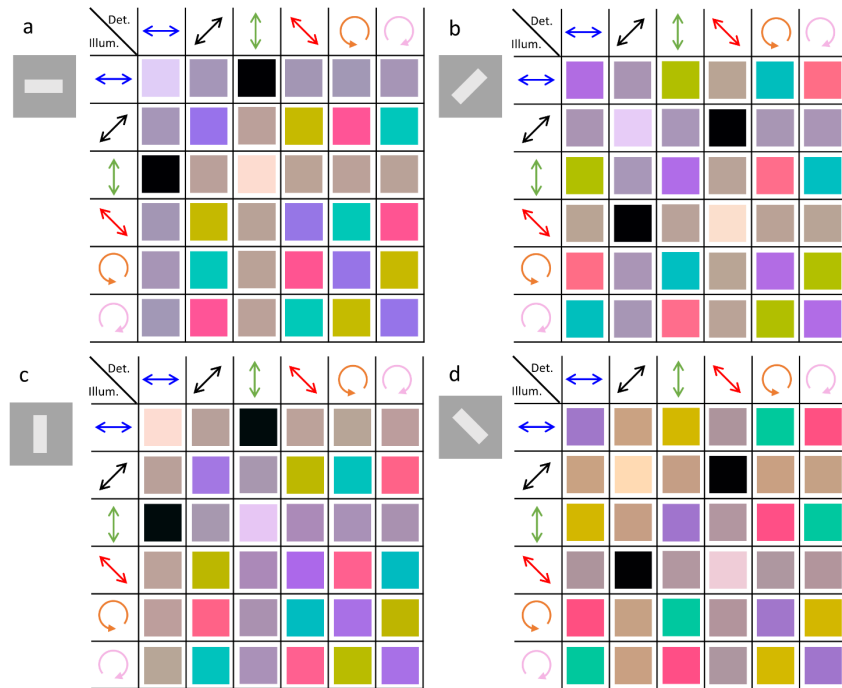


Figure 4.2–10 Computed colors of a single nanorod in different angles with respect to the illumination and the detection polarizations. (a) Nanorod orientated in H-direction (0°). (b) Nanorod orientated in D-direction (45°). (c) Nanorod orientated in V-direction (90°). (d) Nanorod orientated in A-direction (135°).

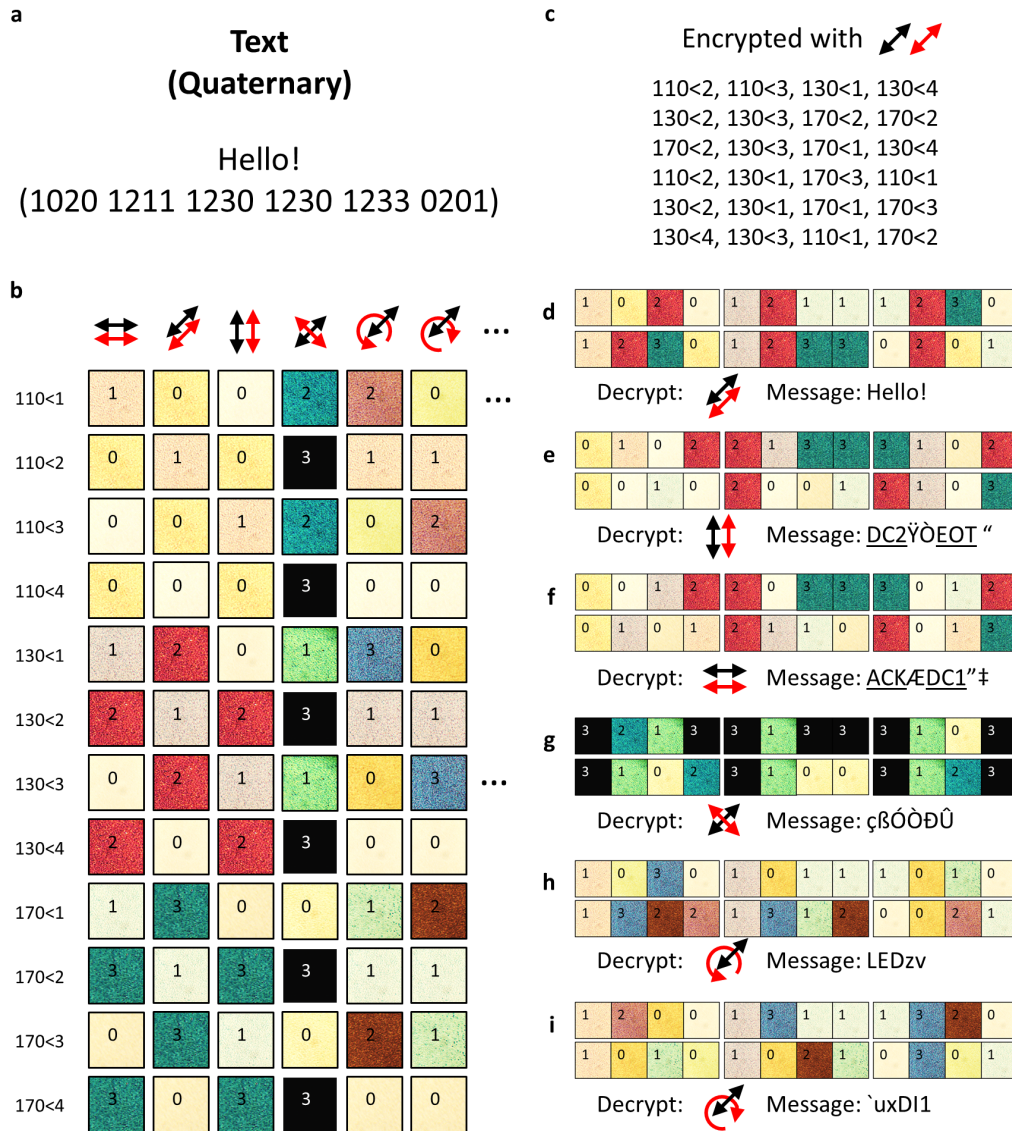


Figure 4.2–11 Polarization-controlled chromo-encryption. a, The secret message "Hello!" is coded with the quaternary system. b, The message is coded using nanorods with three different lengths $L = 110$ nm, 130 nm or 170 nm and four different orientations $\langle 1, \langle 2, \langle 3$, and $\langle 4$ within the unit cell. Depending on the illumination-detection polarizations, different colors – corresponding to different digits within the quaternary system – are observed. c, The 24 digits composing the secret message correspond to 24 nanostructures. d, These 24 nanostructures produce the sequence of colors that corresponds to the secret message when they are illuminated with the correct polarizations. e, – i, any other polarization combination produces a garbage message.

4.2.3 Conclusion

We have described in detail the response of simple plasmonic nanorods to the illumination polarization. Depending on the orientation of that polarization with respect to the symmetry axes of the nanostructure, a chiral response can occur, with the creation of additional field components that were not present in the illumination field. By analyzing this reflected light through a second polarizer, it is possible to control the spectral response of the system at the resolution beyond 80,000 dots per inch. Specifically, for the Ag nanorods fabricated here, a broad variety of colors can be produced that cover 50% of the chromaticity diagram. Depending on the illumination and detection polarizations, these colors range from white to vivid colors or even black, in spite of the fact that the material at hand does not absorb much light. Two additional degrees of freedom have been exploited: the nanorod length, which tunes its spectral response, and the nanorod orientation within the unit cell, which modifies the geometrical relationship between the nanorod and the polarization. These different degrees of freedom provide a very rich palette of optical effects that are controlled by the

polarization of light. Their utilization to reproduce artworks has been demonstrated, together with their operation as encrypting system, where the polarizations are used as keys and the message is encrypted in a quaternary color subset. The diversity of degrees of freedom provided by this system can enable a wealth of applications in solid-state colors, high-density optical data storage and encryption. The polarization-controlled spectral responses demonstrated in this work could be further extended with freeform and unconventional meta-optics[253] and the assistance of artificial intelligence[254, 255].

4.3 Machine learning structural color

This ongoing project started with generating a database of spectra as a function of geometry under a specific polarization state. The database is then used to train a machine learning neural network, called deep convolution generative adversarial network (DCGAN), implemented by André-Pierre Blanchard-Dionne. When the network is properly trained, GAN can produce arbitrary shapes, whose colors are close to the selected point on a CIE map. I am honored to be involved and learn techniques in the field of artificial intelligence for designing and optimizing optical elements.

The following section reports my contribution to this project, that is in preparation for a scientific journal.

Title: Generative Adversarial Network Deep Learning for the inverse design of geometry-dependent plasmonic structural colors

Authors: André-Pierre Blanchard-Dionne, Hsiang-Chu Wang, and Olivier J.F. Martin*

Abstract: Deep learning neural networks have become powerful auxiliary tools in designing complicated optical components and devices. After training, these deep learning neural networks provide designers with multiple possible solutions with similar function or better performance. Take plasmonic structural color systems as an example: their optical responses, or spectra, are very complicated and vary with respect to their geometries and can be sensitive to the incident/reflected polarization states, even though the structure and materials remain unchanged. Besides, it is less efficient for designer to model and simulate free-form structural colors one-by-one. In view of this inconvenience, we make good use of a deep learning algorithm, called deep convolution generative adversarial network (DCGAN), to generate the geometries of a plasmonic structure by giving a determined spectrum. A selection of free-form geometric structures with primary colors, provided by the artificial intelligence, is fabricated with e-beam lithography and great agreement is found between the model and experimental results. The proposed deep learning neural network can save considerable time and serves as a benchmark for designing such intricate systems.

4.3.1 introduction

Artificial intelligence or deep learning neural networks, classified as data-driven approaches, has recently been progressing rapidly and stands out as an excellent auxiliary tool in nano-optics [256-262]. Designers can benefit from this approach and acquire surprisingly high efficient devices or relatively good prediction with limited a priori knowledge. With the tremendous reported breakthroughs and upcoming demand for ultra-thin flat optics [27, 149, 263, 264], designing complicated plasmonic devices according to conventional physics- and rule-based methods takes considerable time [265-267]. Such design processes require massive brainstorming and electromagnetic computation to explore the unknown physics as the degrees of freedom increase. Furthermore, sometimes a device designed on pure physics is unknowingly less efficient [268-270], and before fully understanding the underlying physics, data-driven approaches can offer useful venues for optimization.

Let us consider plasmonic structural colors for example, their spectral response can be generated by multiple resonant behaviors associated with their structure and materials, and combinations thereof. Various mechanisms, including modal interaction, resonant cavities, interferences, polarization conversion, and so on, have been proposed to manipulate the spectral response. Empirical rules have also been proposed to control their peaks and troughs. Still, it is

difficult to predict the spectral responses of basic structures without numerical computation [271], not to mention simple structures with arbitrary geometries since the spectral response is extremely sensitive to their shapes. Designers always rely on full-wave simulations and construct models manually to observe and then analyze the potential interactions according to the electromagnetic fields. This process requires significant computational resources when designing free-form optics. Reducing the computational load in simulation represents the focus of this work and has emerged as a promising design approach that enables advanced functionalities [272-274]. Fortunately, this routine work can be achieved by generative networks, which can handle problems with more degrees of freedom (DOF). A similar idea has been applied in 2019 to produce regular geometries with a targeted spectrum [275]. Since this type of neural networks is capable of solving problems with many DOF, we demonstrate here that it can be used to design structural colors with irregular nanostructure shapes. This represents a disruptive step in the design evolution of structural colors, which up to now, has only focused on regular shapes.

In this work, a deep learning neural network called deep convolution generative adversarial network (DCGAN) is implemented to reverse engineer the dimensions of a silver nanoparticle with a given spectrum. In the first part, we describe how the generative adversarial network (GAN) is trained. During the training process, the GAN learns the relation between the spectrum and the geometry by full-wave simulations. After completing its training, the GAN is capable of providing designers with a set of solutions, or geometries, which can produce similar spectra as desired. In the second part, with those solutions supported by numerical simulations, we fabricate the samples with e-beam lithography and measure the spectra. This paves the way for designing nano-optics with artificial intelligence and promises to alleviate the designers' burden of performing considerable computational work to unveil the underlying physics.

Generating a database with FEM based numerical simulation (COMSOL)

The single variable is the geometry of the unit cell, which determines the spectral response. Instead of using regular and common geometries such as disks [71, 72, 156, 176], rectangles [74, 233, 276], crosses [222-224], and other shapes [23, 191], we intend to apply free-form geometries to generate the desired spectra. To improve the precision of prediction of the deep learn neural network, it is necessary to train the network with reliable data. The dispersion data for silver, the silicon substrate, and HSQ are validated with previous experimental work. Likewise, the spectra of the free-form shapes in the unit cell as shown in Figure 4.3–1(a) are simulated with periodic boundaries in a reflection manner under linearly polarized light illumination.

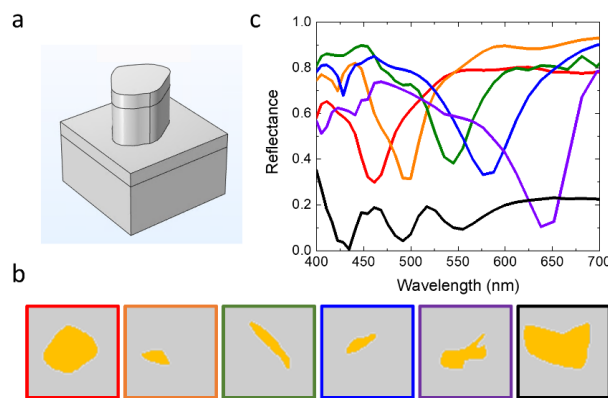


Figure 4.3–1 Geometry-dependent plasmonic structural colors. (a) Schematic of a geometry-dependent unit cell for plasmonic structural colors. (b) Examples of free-form geometries in the dataset. (c) The reflectance varies with geometries.

A geometry generator is implemented to create a free-form geometry in the form of a 64 by 64 matrix consisting of 0 and 1. The resolution of the geometries is 5 nm, which is the fabrication accuracy of EBL. The unit cell periodicity is 320 nm by 320 nm. The area noted as 1 represents the silver nanoparticle raised by an HSQ pillar, while the rest is the thin film deposited on the substrate. Each geometry matrix is imported to COMSOL for modeling in order to obtain its

spectral response. Figure 4.3–1(b) shows the spectra for the geometries in Figure 4.3–1(c). Each spectrum ranges from 400 nm to 700 nm with a 10 nm spectral resolution. From the spectrum, one can easily locate the XYZ coordinates on a CIE map [250]. One can also adjust the parameters such as mesh size, HSQ thickness, silver thickness, periodicity, or even the materials for this type of configuration to obtain another training dataset for machine learning. Here, the dataset is composed of a total of 30,000 geometries (64×64) and their corresponding spectra (1×31) as shown in Figure 4.3–2. The aim is to obtain the geometries of meta-atoms by giving the coordinate on a CIE map with the assistance of a deep learning network. They will be used for training the neural network.

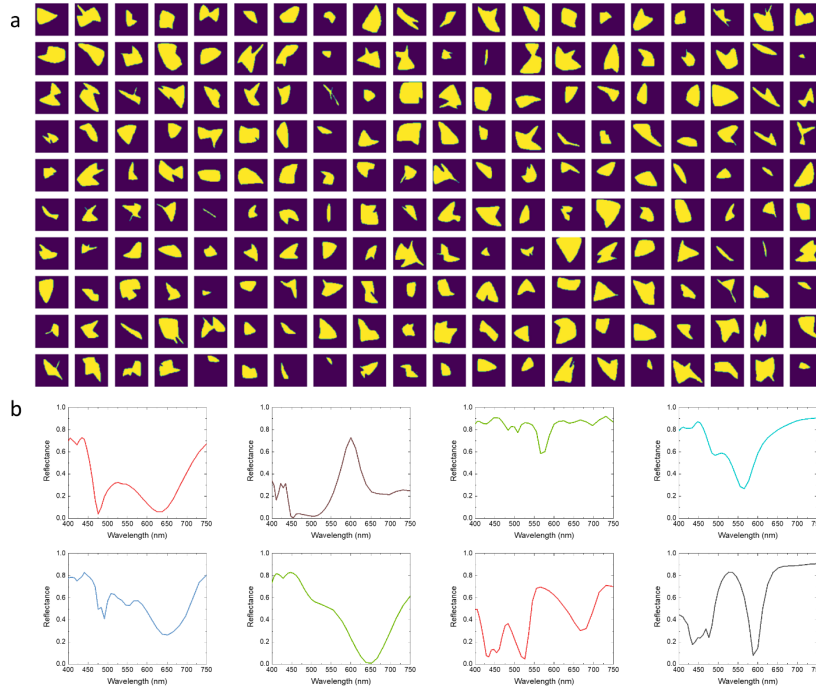


Figure 4.3–2 Database of arbitrary shapes and spectra under polarized illumination. (a) Arbitrary geometries of meta-atoms viewing from above. (b) Simulated spectrum with COMSOL.

4.3.2 Results and discussion

The input of the neural network is xyz on a CIE color map. 5 different points are selected (labelled with black crosses in Figure 4.3–3a), which are outside the training dataset (the boundry is drawn with a dashed line on a CIE map). We choose the geometries given by the network that are the closest points to the selected points for fabrication. The fabrication process is a two-step HSQ EBL along with 40 nm-thick Ag film deposition. We can observe the colors under an optical microscope the colors of these meta-atoms before and after Ag film deposition. The spectra are also measured and compared with those obtained from simulation.

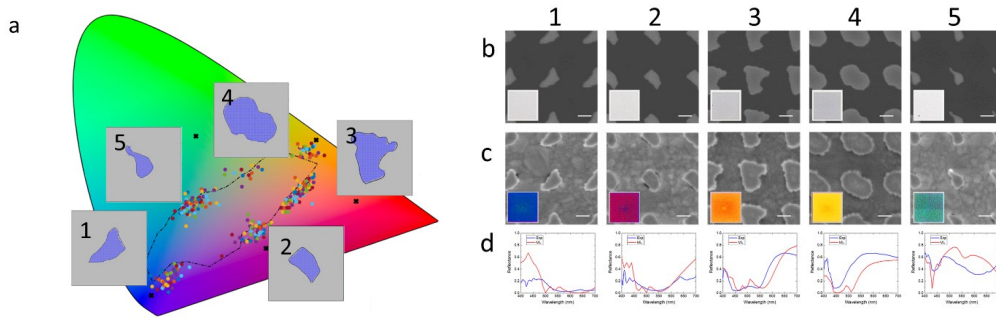


Figure 4.3–3 Fabricated deep learning color pixels and measurements. (a) Representative color groups on a CIE map. (b) SEM images of each pixel before Ag deposition and (c) after Ag deposition. Insets are bright field images under white light illumination with polarization along horizontal direction. (d) Predicted spectra (red line) and measurements (blue line). The scale bars are 100 nm.

4.3.3 Conclusion

We have shown how reverse engineering using deep learning can help the design process for optical nanomaterials based on a free-form design. A generative algorithm was used to precisely find the shape of a particle that can lead to a specific color. This algorithm has then helped push the boundaries of the color space that can be reached by modifying only the particle shape. A wide selection of colors were predicted, fabricated and measured experimentally with very good agreement between the predicted and measured spectra. This approach demonstrates the potential for creative artificial intelligence to revolutionize the traditional design process in nanophotonics.

4.4 Outlook

In this chapter, we investigated the mechanism of structural colors made of nanorod structures. Such a simple geometry can produce a plethora of spectra or colors, which would be affected by the used materials, structure and geometry of the meta-atom, and the polarization states of the incident and reflected lights. In our demonstration, although silver structures are directly exposure to the air, the sample can be stored in a nitrogen chamber to dehydrate it to prevent oxidization[136], or be sealed with a low index transparent materials such as HSQ or PMMA. Different substrates could be investigated for chromo-encryption applications on versatile surfaces. Employing a data-driven approach (machine learning neural network) can be helpful to design more complicated structural colors. For instance, spectra in Section 4.3 are under x-polarized illumination and analyzed with x-polarized reflected light. When more polarization pairs (illumination and detection) are considered, the applications in chromo-encryption or optical storage can be quite robust. The most difficult task is to build a reliable database for training, which will require validating with measurements. Besides, the measurement setup described in Section 2.3.3 provides a robust platform to characterize the optical responses.

Chapter 5 Near-field enhancement

Plasmonic antennas – often used as meta-atoms in this thesis – can be used as efficient transducers to enhance the interaction between light and emitters at the subwavelength scale [277-279]. These nanostructures can both enhance the near-field to increase the excitation and the local density of optical states (LDOS) to enhance the spontaneous emission rate [11, 280, 281]. In this chapter, we study how plasmonic antennas can be used to enhance the upconversion from rare earth compounds [282-286]. The main issue in this case is the extremely large Stokes shift between absorption that occurs in the infrared and emission in the visible. This large shift represents the key asset of those compounds for their utilization to harvest the low energy portion of the sun spectrum and convert it into higher energy that can be processed by photovoltaics. The benefits from an approach based on double resonant silver plasmonic antennas are studied in details.

5.1 Introduction

Optical signals beyond the diffraction limit cannot be detected in the far-field, except if a good transducer can be used to bridge the gap between evanescent and propagating fields. The coupling efficiency between a transducer and an emitter depends on the geometry, size, electromagnetic coupling, and spectral overlap, i.e. the wavelength of the signal should be close to the resonance frequency of the transducer. In principle, it is possible to tune the transducer such as it matches one specific resonance. In this chapter, we wish to extend this concept for upconversion nanoparticles (UCNPs), which require a transducer that can couple at two frequencies: the fundamental frequency and the upconverted frequency.

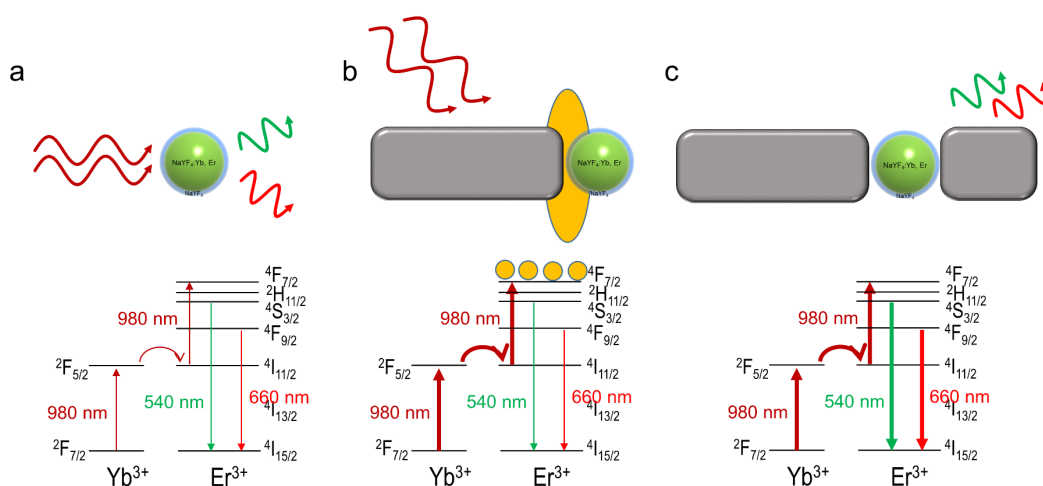


Figure 5.1–1 Schematic of upconversion luminescence with and without the assistance of optical antennas. (a) A single UCNP in this study, illuminated with infrared light at the wavelength of 980nm emits light mainly at the wavelengths of 540 nm and 660 nm. (b) In the vicinity of a plasmonic antenna resonant at the excitation wavelength, the electrons are mostly confined in the excited state with limited decay, leading to a quenching process. (c) To prevent this quenching process, an additional antenna resonant at the emission wavelength – either 540 nm or 660 nm – can favor the emission process. By tuning the antenna, one or the other emission channel can be enhanced.

UCNPs are composed of lanthanide ions in a low-loss host and nanometer-thick shell. They hold great promise for merging low-energy photons into higher-energy ones and thus exhibit an enormous spectral shift [287-289]. Due to their excellent photostability, massive spectral shift, and higher efficiency, UCNPs are useful in bioimaging, lasing, and light harvesting [290-294]. Figure 5.1–1(a), illustrates an UCNP made of NaYF₄: Yb³⁺, Er³⁺ with a few nanometers thick NaYF₄

inert shell. The Yb^{3+} donor absorbs photons at the wavelength of 980 nm and transfers the energy to Er^{3+} , leading to emission at the wavelengths of 540 nm and 660 nm. However, this process is limited by the small scattering cross section of the particle, which is around 20 nm in diameter. To accelerate the electron transitions and achieve higher photoluminescence, external transducers such as dye-molecules and plasmonic nanostructures have been applied [295-298]. Although the enhancement factors are considerably large, these antennas are mostly designed at the excitation wavelength only, as shown in Figure 5.1–1(b). Further enhancement of the emission requires mitigating the spectral mismatch between the emission signal and the transducer.

Plasmonic antennas, composed of nanostructures, can serve as stable optical transducers. By tuning the geometry and size of the plasmonic nanostructures, the local density of optical states (LDOSs) can be engineered [299, 300]. Each LDOS provides a channel for light at a given wavelength to bridge the gap between free-space radiation and near-field. In plasmon-enhanced fluorescence processes with a small Stoke shift, the excitation light and the emission signal share the same channel, which makes it possible to amplify the scattering cross section and accelerate the spontaneous emission rate simultaneously [10, 301]. On the other hand, upconversion photoluminescence undergoes a large Anti-Stoke shift, which produces a spectral mismatch between the emitter and the antenna when the latter exhibits a single resonance. Specifically, applying an antenna only at the excitation wavelength does not enhance the LDOS for the emission to better couple to the far-field, while using an antenna only at the emission wavelength does not increase the scattering cross section for the emitter, which suffers from little excitation. To overcome this dilemma, Figure 5.1–1(c) describes a strategy for boosting the upconversion by using two transducers: one for the excitation wavelength and the other for the emission wavelength.

5.2 Results and discussion

The UCNP in our study is made of $\beta\text{-NaYF}_4\text{:Yb}^{3+}, \text{Er}^{3+}$ as a core with inert NaYF_4 shell (see Figure 5.2–1). We place the UCNP on a thin glass substrate (150 μm thickness) by first diluting them in toluene and then spin coating to form a self-assembled single layer. The number of layers can be controlled by performing several successive spin coatings. This is illustrated in Figure 5.2–2(a), where the left top corner corresponds to a single layer of UCNP, and the right bottom corner corresponds to a double layer of UCNP. Under the same illumination power density, the emission intensity of the UCNP linearly increases with the number of layers (see Figure 5.2–3). The UCNP is illuminated with a CW laser at the wavelength of 980 nm from the top and the emission is collected with an air objective with NA = 0.7, as described in Figure 5.2–6. The spectrum in Figure 5.2–2(b) is the upconversion signal after passing through a short pass filter (cutoff at $\lambda = 750\text{nm}$). There are two major peaks, one at 540 nm and the other at 660 nm. The intensity ratio for green to red is about 2, which means the maximum intensity for green is twice that of red. Apart from the spectrum, the power dependency provides an insight into the process happening in the UCNP: the slopes for green or red emission intensities vs. excitation intensity in a double logarithm plot determines the number of photons participating in the upconversion process. Generally, under weak excitation, the slope is 2 for both red and green emissions since this corresponds to a two-photon absorption process (Figure 5.2–3). In Figure 5.2–2(c), the slopes for green and red emissions 1.5, and 1.4, respectively indicate that the illumination conditions might be close to or within the saturation region. Lowering the excitation to reach a regime where the slopes approach 2, requires longer exposure times or more particles in the field of view to accumulate a strong enough signal. Although we have chosen very efficient UCNP available commercially, the upconversion signal for bare particles is not strong enough under weak excitation.

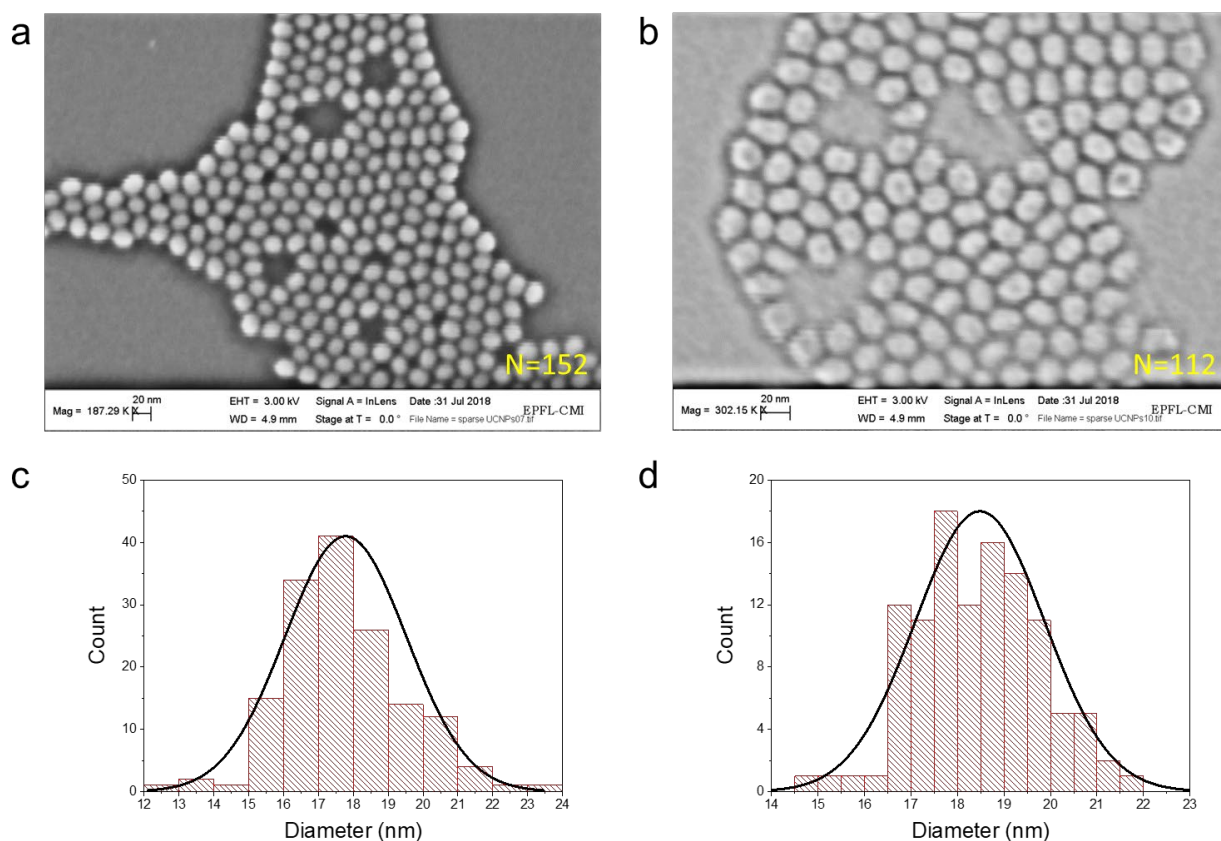


Figure 5.2-1 UCNP sizes distributions. (a) and (b) SEM images on a Si substrate, with the number of upconversion nanoparticles N. (c) and (d) corresponding sizes histograms.

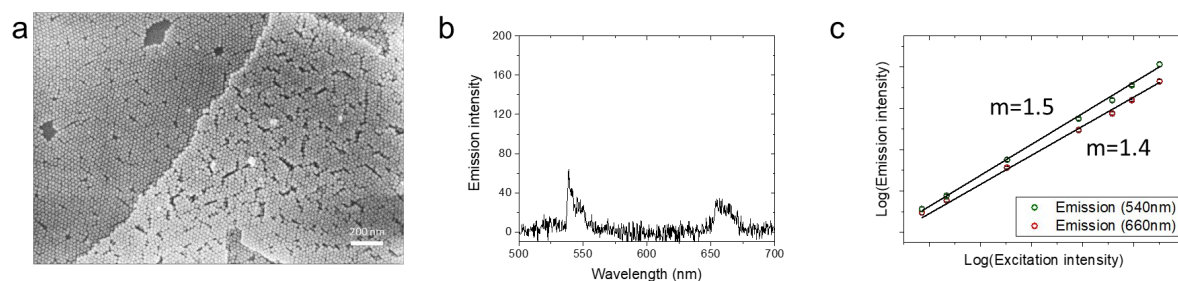


Figure 5.2-2 Optical properties of the UCNP in this study. (a) SEM image of the UCNP spread on a thin glass substrate layer by layer using the spin-coating technique. A single layer is visible in the upper left corner, while the bottom right corner shows a double layer. (b) Emission spectra for a single layer of UCNP illuminated with continuous wave laser at $\lambda = 980$ nm with different excitation powers. (c) Double logarithm plot of the emission intensity vs. excitation power; the slope indicates the number of photons contributing to the process.

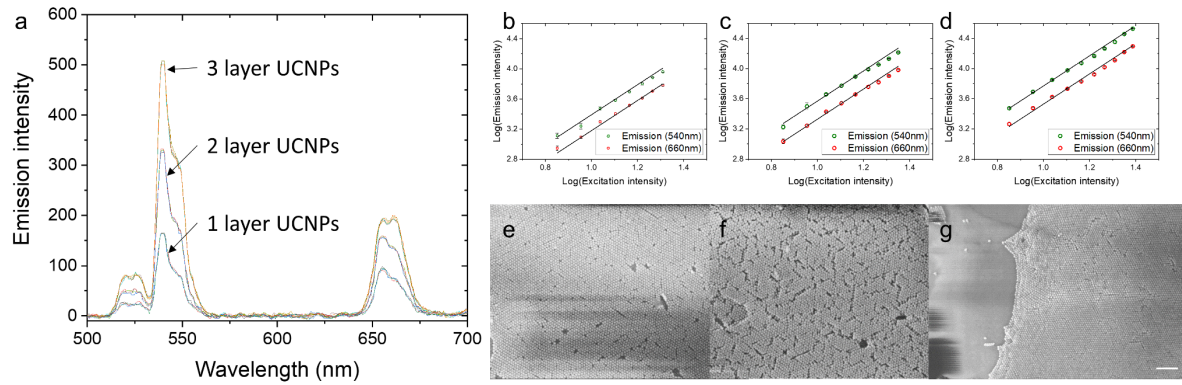


Figure 5.2–3 Linear dependence of the emission intensity on the number of UCNPs layers on a glass substrate. (a) Emission intensity for different layers of UCNPs illuminated with cw laser at $\lambda = 980$ nm. Double logarithm plot of the emission intensity vs. excitation intensity for (b) a single layer; (c) a double layer; and (d) a triple layer of UCNPs. The slope of the black lines in the plot are 2 and independent of the number of layers. Corresponding SEM images for (e) a single layer; (f) a double layer; and (g) a triple layer.

To overcome this limitation, let us resort to plasmonic optical antennas. We chose silver as the plasmonic metal because of its low losses and its ability to cover the entire visible spectrum [West_2011]. We first simulate a monopole silver antenna composed of a nanorod in an effective medium that corresponds to the refractive index of the UCNPs ($n = 1.4748$, since plasmonic antennas are sensitive to their surroundings, the resonant peak will redshift with increasing refractive index) and tune the antennas dimensions to make it resonant at the wavelength of 980nm. Figure 5.2–4(a) shows the near-field enhancement under polarized illumination along the long axis. The near-field is proportional to the LDOS, with strong hot spots located at both ends of the antenna, meaning particles in these regions can be enhanced. The scanning electron microscopy (SEM) image in Figure 5.2–4(b) presents the fabricated sample. The measured reflectance spectrum shown in Figure 5.2–4(c) exhibits a single resonance at the wavelength of 980 nm after covering the system with a single layer of UCNPs. To check the emission enhancement by the designed antenna array, we illuminate the sample in Fig 3b with a continuous wave (cw) laser at the wavelength of 980 nm, with the polarization along the long axis. The black line in Figure 5.2–4(d) represents the emission spectrum for the single layer UCNP on glass, while the red line corresponds to a single layer with the plasmonic antennas. Although the emission intensity enhancement produced by the antennas is about 4 times, we must keep in mind from Figure 5.2–4 that only a very few UCNPs are enhanced and the measured emission enhancement is the average between a few strongly enhanced particles with a large number of particles that do not benefit from the optical antenna. Additional experiments where single resonance antennas are used are shown in Figure 5.2–5. These results indicate that the emission spectrum of the UCNPs can be modified under the same illumination condition. For instance, antennas resonant at a specific wavelength can enhance the upconversion signal individually. This phenomenon of spectral selective enhancement by the plasmonic antennas is analogous to the Purcell effect []. When emitters are in a resonant cavity, the emission can be enhanced at the resonance frequency and in those experiments with single resonance antennas, one single channel – determined by the antenna geometry – is provided to couple the light into the far-field, Figure 5.2–5.

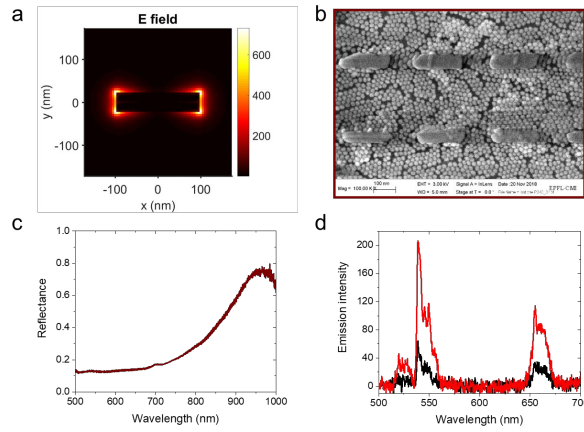


Figure 5.2-4 An optical antenna resonant at 980 nm can enhance the interaction of light with the UCNP. (a) Simulated near-field intensity enhancement around the optical antenna made of a silver nanorod. (b) SEM image of the silver antenna embedded with a single layer of UCNP. (c) Measured reflectance for the sample in panel b. (d) Emission enhancement comparing the situation with (red line) and without (black line) the plasmonic antennas.

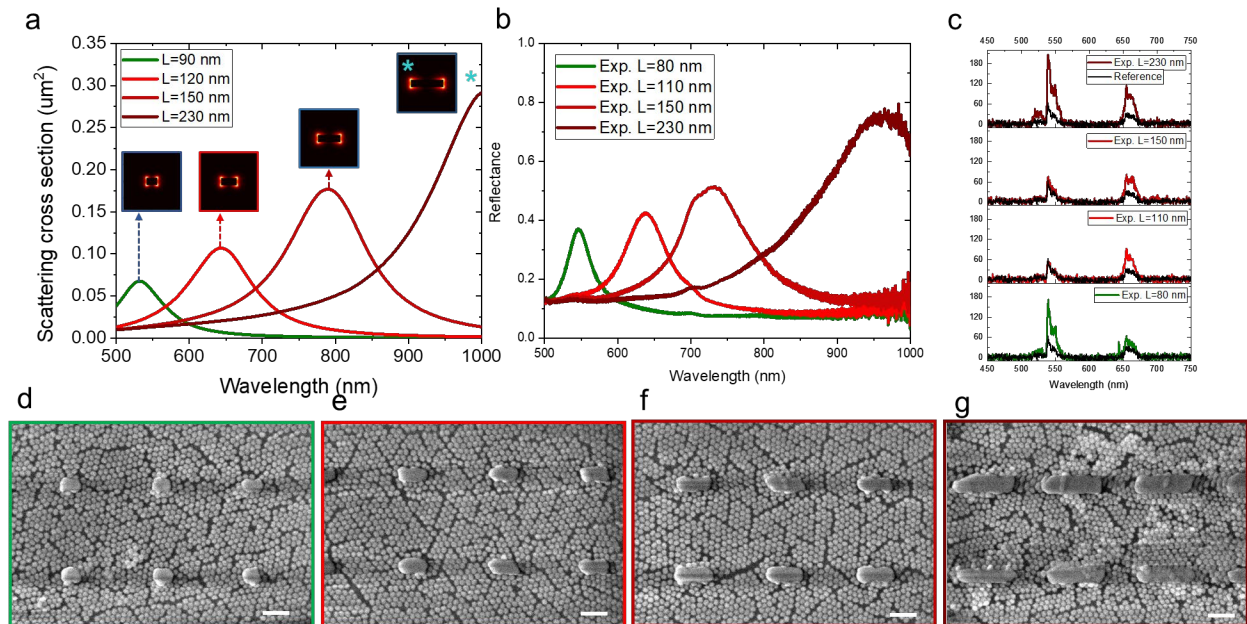


Figure 5.2-5 Influence of single resonance antennas on the emission of the UCNP. (a) Simulated scattering cross sections for different antenna sizes. (b) Reflectance measurements of fabricated antennas. (c) Emission enhancement comparing the situation with (colored line) and without (black line) the plasmonic antennas. (d)-(g) SEM images of corresponding single resonant antennas with a layer of UCNP.

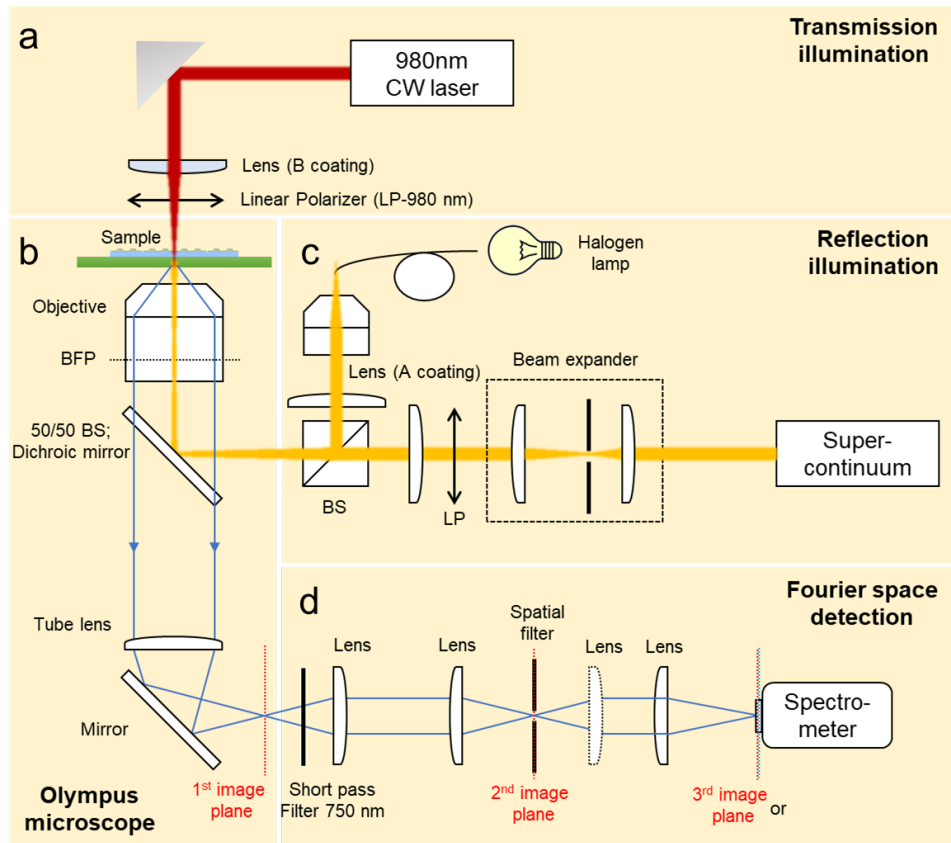


Figure 5.2-6 Schematic of the measurement setup. (a) Transmission illumination used to excite the sample and composed of a cw laser at the wavelength of 980 nm, a focal lens with focal distance 75 mm, and a linear polarizer for 980 nm. (b) Olympus microscope. (c) Reflection illumination used to observe and measure the reflectance of the samples and composed of a halogen lamp and a super continuum laser. (d) Detection path composed of a 4f system with a pinhole in the second image plane as a spatial filter, and a spectrometer.

Let us now turn to double resonant antennas (DRAs) composed of two arms with lengths L_1 and L_2 , illustrated in Figure 5.2-7(a). The benefit of using this type of antenna stems from its two resonance wavelengths, which can be tuned independently by adjusting the length of each arm separately. For example, the short arm L_1 can be used to help the emission, while the long arm L_2 can be used to increase the excitation. Apart from the spectral match, it is important to ensure spatial overlap for the LDOS to simultaneously enhance the excitation and emission. According to the near-field distribution in Figure 5.2-7(b), the field at both wavelengths overlap in the 20 nm gap region, where UCNP can accept the excitation from the long arm and transmit an upconverted signal via the short arm. The SEM image in Figure 5.2-7(c) shows one of the DRAs array covered with two layers of UCNP. From the image, we can see only a few UCNP can fit inside the gap. Two UCNP layers cover the antennas well, such that they are immersed in the corresponding background refractive index, as was the case during their design with numerical simulations.

The reflectance measurements in Figure 5.2-7(d) demonstrate that DRAs arrays provide two channels at the absorption and emission wavelengths. The color of the spectra lines become darker with enhanced excitation. Compared to the enhancement provided by single resonance antennas, the emission spectrum is roughly 4 times stronger. In Figure 5.2-7(e), the emission enhancement by the DRAs is close to a 10-fold enhancement compared to the bare substrate. Note that the intensity for the double UCNP layer is twice that of the single layer UCNP, indicative of the uniformity of the coating technique. Note also that the doubling of the emission intensity with the doubling of the particles layers matches well with the fact that the antennas thickness is 40 nm, while the UCNP have a diameter of 20 nm.

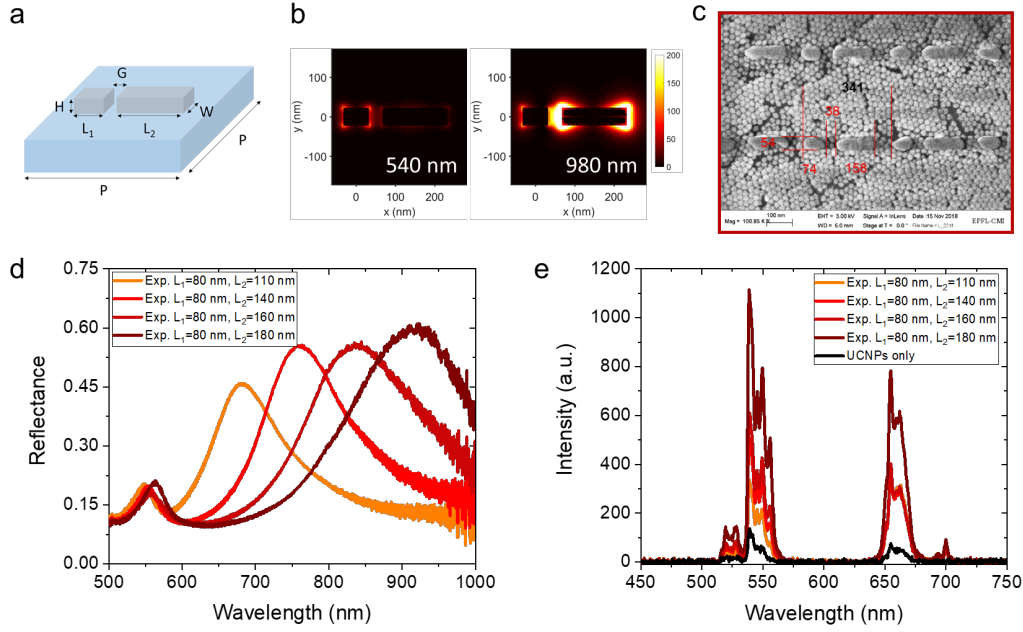


Figure 5.2-7 Upconversion enhancement provided by double resonant antennas. (a) Schematic of a double resonance antenna in Ag composed of two arms. (b) Near-field intensity enhancement at the emission wavelength ($\lambda = 540$ nm) and excitation wavelength ($\lambda = 980$ nm). (c) SEM image of the DRAs embedded into a double layer of UCNPs. (d) Measured reflectance for DRAs with different lengths for the long arm. (e) Measured emission intensity enhanced with the assistance of the DRAs with different long arm lengths.

This principle of simultaneous spectral matching for emission and excitation should also work for the emission in the red. To verify this, we fabricated the DRAs arrays shown in Figure 5.2-8(a), by fixing the long arm at the excitation wavelength ($\lambda = 980$ nm) and tuning the short arm at the red emission wavelength ($\lambda = 660$ nm). The corresponding spectra in Figure 5.2-8(b) show two peaks, one at 980 nm and the other shifting around red emission wavelength. Under the same illumination conditions, as in the previous experiments, the emission spectra in Figure 5.2-8(c) shows an impressive enhancement by the DRA arrays. Unsurprisingly, the red emission now dominates with an enhancement factor close to 40 times. The enhancement is far beyond that obtained with single resonance antenna array. These experiments strongly support the concept of engineering the antennas' resonances to enhance upconversion. A single resonance antenna can either amplify the pumping or accelerate the spontaneous emission rate, depending where it is spectrally tuned. The former phenomenon consists in pumping more electrons into the excited states, while the latter helps the excited electrons decay to the ground state. Under weak excitation, amplifying the pumping can produce a larger enhancement because the excited electrons decay immediately and only a few accumulate in the excited state [302]. Hence, in that weak excitation regime, a single resonant antenna tuned to the emission wavelength provides only marginal benefit. On the contrary, when the excitation intensity increases and one reaches the saturation regime, the power dependence of the emission vs. excitation decreases below 2: the electrons begin to accumulate in the excited state, which happens easily when applying an antenna resonant at the excitation wavelength. In this case, many excited electrons remain in the excited state with a decay rate more or less unchanged, resulting in a limited enhancement. The solution to break through this limitation is to promote the de-excitation channel by adding a resonant structure at the emission wavelength that will enrich the LDOS.

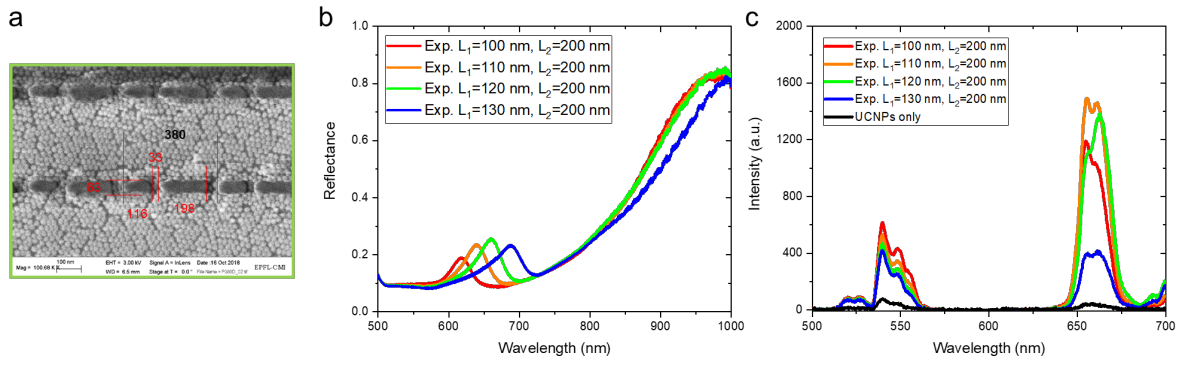


Figure 5.2–8 Selective upconversion emission by spectral tuning of the DRAs. (a) SEM image of DRAs resonant at $\lambda = 660$ nm, embedded into a single layer of UCNPs. (b) Measured reflectance for DRAs with different lengths of the shorter arms, tuned around the red emission wavelength. (c) Measured emission intensity enhancement for DRAs with different shorter arm lengths.

5.3 Conclusion

To sum up, we have experimentally demonstrated the plasmonic enhancement of upconversion photoluminescence by plasmonic antennas resonant both at the emission and excitation wavelengths. Double resonant nanostructure overcome the difficulties associated with the massive spectral shift associated with the upconversion process. Furthermore, these nanostructures provide good spatial overlap at both wavelengths, and a strong near-field to enhance the optical processes in UCNPs. By tuning one of the antenna resonances, it is possible to selectively enhance one or the other bands of the UCNPs. The different illumination conditions have also been studied, demonstrating the benefit arising from DRAs in the saturation regime.

Chapter 6 Conclusion and outlook

In this thesis, we have investigated and characterized meta-atoms for applications in the visible regime, mainly fabricated using silver. Based on numerical calculations, we fabricated the structures and measured their optical responses depending on different needs. Having gone through these three stages (design, fabrication, and measurement), the study can be considered complete. Although each topic seems distinct, they are linked and centered around the central idea that light can be manipulated using subwavelength structures of various forms.

In Chapter 2, we presented a variety of tools and methods used in the different stages of simulation, fabrication, and characterization. In the design stage, the computational approach used depends on what kind of problem is being solved, e.g., is the environment homogeneous or inhomogeneous, are the structures of meta-atoms isolated or periodically arranged, what is the wavelength of interest, and is the phenomenon observable in the near-field or the far-field? The fabrication process requires an understanding of the phenomena occurring at the nanoscale for each material, for example, surface tension, atomic diffusion, adhesion between heterostructures, and so on. As a result, different fabrication process flows are developed for different meta-atoms. After fabrication, SEM is used for examining the dimensions of structures. Characterization of metasurfaces, which are designed to manipulate light, rely on optical approaches. The measurement system implemented as part of this work performs multiple tasks, including spectral measurements, bright field imaging, and Fourier imaging. Precise measurements under polarized illumination are also performed and this approach affects the spectrum and correspondingly, the colors observable on a camera. These tools pave the way for exploration of the following topics: wavefront manipulation, spectral manipulation, and near-field enhancement.

In Chapter 3, meta-atoms have been successfully used to tailor the phase shift of reflected light, leading to diverse applications such as metalenses, metaholograms, and beam-steering phase gradient plates in flat optics. Generally, multiple meta-atoms are used to produce a phase shift between 0 and 2π . As long as one of these applications can be demonstrated, meta-atoms can be used for different purposes in manipulating the propagating direction of light. It is believed that a greater number of modulating levels will give rise to better device performance due to better wavefront approximation, e.g. for a beam-steering device. However, in the demonstration of metaholograms and the subsequent robustness analysis, exceptions are presented. For example, when properly designed, binary metaholograms can lead to a better performance than one with multiple modulation levels. Another example is a 4-level phase gradient beam steering device made of dielectric cylinders, which has higher efficiency than a perfect one with 8 uniformly-modulated levels. These findings encourage designers to reconsider designing based solely on the physical picture (Huygen's principle). Among the demonstrations, metalenses made of two stoichiometric combinations are presented to prove phase modulation by stoichiometry. Functional modification by stoichiometry can be applied to metaholograms as well. Metaholograms can be utilized for optical storage, optical communication, optical encryption, and many other applications that motivate the research on the design of metaholograms. The conditions to reconstruct images for miniaturized metaholograms are different from those of conventional ones and a more complete understanding of these conditions is the next step in pushing these applications towards industry readiness.

In Chapter 4, studies on the spectral responses of meta-atoms have been thoroughly conducted. The approach consists of illuminating rectangular structures with polarized light with different orientations and rotating the structure in different directions. However, the responses were considered complicated and in particular, spectral measurements under polarized light can lead to misleading results if not performed carefully, as discussed in Chapter 2. This issue is rarely discussed in the literature. We, therefore, dug into the core issue to verify the hypothesis with simulations and measured spectra. The findings broaden the study and point toward structural symmetry properties. Even for a simple nanorod structure, the reflectance of a meta-atom can be tremendously subtle. Such a single rectangular meta-atom

possessing two planes of symmetry can generate 36 different optical responses with 6 illumination and 6 detection polarization states. Applying this property, a quaternary numbering system can be easily achieved for optical encryption. As a result, we were able to implement such a system with structural colors. A protocol is needed since there are too many possibilities and variables if this application continues developing. Due to the heavy computational load, machine learning can play an important role in this routine work. A project combining structural colors and artificial intelligence is presented, wherein multiple solutions (geometries) are created after assigning xyz values on a CIE map. The primary result shows the power of machine learning, however, reliable databases are required for training the neural network.

In Chapter 5, the tailoring of the fluorescence of frequency upconversion by plasmonic double resonance antennas is demonstrated. The fluorescence enhancement is successfully explained with the LDOSs provided by the optical antennas, where a strong near-field occurs. We looked into the energy levels of rare-earth ions and the emission power density to derive the number of photons participating in the conversion process. By tuning the LDOSs, we are able to determine the relaxation path of excited electrons. As a result, the emission intensity can be altered. Using plasmonics to couple light from the far-field and confine it in the near-field, the interaction of light and matter can be boosted. This mechanism can be applied to fluorescence containing more complicated energy levels, such that the excitation and relaxation of electrons can be manipulated with plasmonics.

In summary, applications of plasmonics are versatile, depending on the functionalities. They can alter the intrinsic properties of light such as amplitude, phase shift, or wavelength. Engineering these properties enables applications to be used in wavefront manipulation, spectral tailoring, and emission control. Overall, this thesis illustrates that progress in the field of nanophotonics at large and metasurfaces specifically, requires a combination of numerical simulations, advanced nanofabrication techniques, and careful experimental characterization.

Chapter 7 Appendix

7.1 Matlab code of Semi-analytical model

This Matlab code is for the Semi-analytical model in sub-Section 2.1.3.

Matlab code:

```
clc; close all; clear;

% Parameters

Lam_work = 980e-9; % working wavelength

Px = 180e-9; % length of unit cell in x direction

n_level = 8; % number of discrete modulation level

rep = 13; % number of repeating superlattice

Lattice = Px*n_level; % total length of the superlattice

disp(['Expected angle = ', num2str(asind(Lam_work/Lattice))]);

% Fourier transform

i=0;

if i==0

    p = [107,64,19,-23,-65,-121,-161,155]*pi/180;

    a = sqrt([0.98,0.83,0.61,0.46,0.44,0.54,0.73,0.95]);

    % phase and amplitude of the 8-lv device

else

    p = [107,107,19,19,-65,-65,-161,-161]*pi/180;

    a = sqrt([0.98,0.98,0.61,0.61,0.44,0.44,0.73,0.73]);

    % phase and amplitude of the 4-lv device

end

T = a.*exp(-1i*p);

T = repmat(T,1,rep); % extended complex amplitude on the surface

k0 = 2*pi/Lam_work; % wave number

Lrep = rep*Lattice; % total length after repeating the superlattice
```

```
N = length(T);

if mod(length(p),2)

    kx = [-floor(N/2):floor(N/2)]*2*pi/Lrep;

else

    kx = [-floor(N/2):floor(N/2)-1]*2*pi/Lrep;

end

kz = sqrt(k0^2 - kx.^2);    % wave number in z direction

fft_T = fftshift(fft(T))/N;    % Fourier transform of the complex amplitude on the surface

ideal_eff = 4*cos(asin(Lam_work/Lattice))/(1+cos(asin(Lam_work/Lattice)))^2;

y = abs(fft_T).^2.*ideal_eff;    % the ideal efficiency assume the ideal case for the power
of reflected light toward the propagating direction^2

% Plot

figure;

plot(real(asind(kx/k0)), y);

xticks([-90 -60 -30 0 30 60 90]);

axis([-90 90 0 1.]);

xlabel('Angle (deg.)');

ylabel('Efficiency');

grid on;

set(gca,'FontSize',16);
```

List of figures

Figure 2.1–1 SIE method meshes only the surface of a structure into triangular patches.	4
Figure 2.1–2 Optical antenna designs in SIE.	4
Figure 2.1–3 Computing the reflectance of a periodic meta-atom with COMSOL software requires meshing the entire environment and assigning boundary conditions in the frequency domain.	5
Figure 2.1–4 The wavefront reconstructed by a phase gradient with only meta-atoms and its Fourier analysis.	6
Figure 2.2–1 Resonant frequencies of common metallic materials for plasmonics in an electromagnetic spectrum.	7
Figure 2.2–2 The permittivity of gold and silver alloys with different stoichiometry in the visible regime.	8
Figure 2.2–3 XPS images for a 150 nm-thick $\text{Au}_{0.2}\text{Ag}_{0.8}$ film before and after annealing.	9
Figure 2.2–4 XPS images for a 75 nm thick $\text{Au}_{0.5}\text{Pd}_{0.5}$ film before and after annealing.	9
Figure 2.2–5 Factors affecting the measurement configuration in transmission and reflection.	10
Figure 2.2–6 SEM images of Au-Ag and Au-Pd on different substrates after low-temperature annealing.	11
Figure 2.2–7 Schematic of fabricating double resonance antenna with lift-off method.	13
Figure 2.2–8 SEM images of optical antennas fabricated with the lift-off approach.	13
Figure 2.2–9 Schematic of a phase gradient meta-atom in the etching process.	14
Figure 2.2–10 Fabricated 8-level phase gradient beam-steering metasurface devices with intended misfabricated defects.	15
Figure 2.2–11 Fabricated 4-level phase gradient beam-steering metasurface devices with intended misfabricated defects.	15
Figure 2.2–12 Schematic of a polarization-converting meta-atom, or a geometry-sensitive meta-atom, in the fabrication process. .	16
Figure 2.2–13 SEM images of fabricated plasmonic structures in the direct deposition process.	16
Figure 2.3–1 Schematic of the measurement setup for characterizing optical responses.	17
Figure 2.3–2 A $4f$ system with a pair of lenses is widely applied for imaging.	20
Figure 2.3–3 Spectra measurement with a spatial filter (pinhole) at the 2 nd image plane.	21
Figure 2.3–4 Optical images collected by objectives with $NA = 0.7$ and $NA = 0.9$	21
Figure 2.3–5 The concept of the analog Fourier transforms in an optical system.	22
Figure 2.3–6 Images on the Fourier plane are projected with a $4f$ imaging system.	23
Figure 2.3–7 Metahologram sample on the image plane and on the Fourier plane.	24
Figure 2.3–8 Image processing for dark-field images and edge detection.	24
Figure 2.3–9 Angular information of light on the Fourier plane.	25
Figure 2.3–10 Measurement setup for analyzing beam-steering metasurface devices modified from Figure 2.3–1.	26
Figure 2.3–11 The scenario of measuring the focal spot of a lens in transmission type.	27
Figure 2.3–12 Measurement on the Fresnel zone plate lens in a reflection manner.	27
Figure 2.3–13 Polarization states on a Poincare Sphere. Projecting the entire cycle of the oscillation path on a plane perpendicular to the propagating direction of light can clearly observe the pattern of polarization states.	28
Figure 2.3–14 Examples of metasurfaces and the way they modify the polarization of light.	29
Figure 2.3–15 Schematic of the optical system for measuring spectrum of metasurfaces under polarized illumination.	31

Figure 2.3–16 Simulated and measured spectra for the metasurface built from an array of Ag meta-atom rods.	32
Figure 2.3–17 Comparison between the optical responses in terms of polarizations for a plate beam splitter and a cube beam splitter.	33
Figure 2.3–18 Schematic of polarized light propagating in a microscope with a polarization-sensitive plate beam splitter.	34
Figure 2.3–19 Reflectance and phase shift for polarized light reflected by a silver mirror derived from Fresnel coefficients.	35
Figure 3.2–1 Wavefront manipulation achieved by Au-Ag alloy.	38
Figure 3.3–1 Diffraction theories and applicable approximations to reconstruct the image produced by a metahologram under plane wave illumination.	40
Figure 3.3–2 Algorithm for generating a phase-modulation-only metahologram.	41
Figure 3.3–3 Efficiencies of metaholograms with different modulation levels.	43
Figure 3.3–4 Target image and its reconstruction using a 4-level metahologram fabricated in silver.	44
Figure 3.3–5 Simulation and fabrication details of the meta-atoms used for generating phase-modulation-only metaholograms.	44
Figure 3.3–6 Imaging of metaholograms with different super-pixel sizes.	45
Figure 3.3–7 Measurement setup and reconstructed image at a specific distance.	46
Figure 3.3–8 Dispersion and polarization properties of the fabricated metaholograms.	46
Figure 3.4–1 Examples of possible imperfections that can occur during the nanofabrication of an 8-level metasurface.	48
Figure 3.4–2 Optical properties of unit cells for beam-steering device and two designs for same functionality.	49
Figure 3.4–3 Performance of metasurfaces with a missing element.	50
Figure 3.4–4 Experimental results for 8-level and 4-level devices.	51
Figure 3.4–5 Efficiency of an artificial 8-level and an artificial 4-level device calculated with the simple model, neglecting the variations of amplitude.	52
Figure 3.4–6 Performance computed for an 8-level metasurface with individual displaced element or simultaneous size change.	53
Figure 3.4–7 Another example of beam steering devices made of dielectric meta-atoms in transmission.	54
Figure 4.2–1 Color contrast controlled by polarization.	58
Figure 4.2–2 Simulated and measured spectra as a function of L	60
Figure 4.2–3 Oscillation patterns of the reflected light with different τ in a cycle.	61
Figure 4.2–4 Colors controlled by the illumination and detection polarizations.	63
Figure 4.2–5 Reflectance color space covered by changing the nanorod length between $L = 40$ nm and 200 nm for different polarization combinations.	64
Figure 4.2–6 Color quantization of an image.	65
Figure 4.2–7 An example of mixing white unit cell with dark blue color to achieve brighter blue.	66
Figure 4.2–8 SEM images of the fabricated nano-printing.	66
Figure 4.2–9 Nano-printing of the Mediterranean Landscape by Pablo Picasso.	67
Figure 4.2–10 Computed colors of a single nanorod in different angles with respect to the illumination and the detection polarizations.	68
Figure 4.2–11 Polarization-controlled chromo-encryption.	69
Figure 4.3–1 Geometry-dependent plasmonic structural colors.	71
Figure 4.3–2 Database of arbitrary shapes and spectra under polarized illumination.	72
Figure 4.3–3 Fabricated deep learning color pixels and measurements.	73

Figure 5.1–1 Schematic of upconversion luminescence with and without the assistance of optical antennas.	74
Figure 5.2–1 UCNPs sizes distributions.	76
Figure 5.2–2 Optical properties of the UCNPs in this study.	76
Figure 5.2–3 Linear dependence of the emission intensity on the number of UCNPs layers on a glass substrate.	77
Figure 5.2–4 An optical antenna resonant at 980 nm can enhance the interaction of light with the UCNPs.	78
Figure 5.2–5 Influence of single resonance antennas on the emission of the UCNPs.	78
Figure 5.2–6 Schematic of the measurement setup.	79
Figure 5.2–7 Upconversion enhancement provided by double resonant antennas.	80
Figure 5.2–8 Selective upconversion emission by spectral tuning of the DRAs.	81

List of tables

Table 2-1 The substrates used in the thesis..... 10

Table 2-2 Table of optical components in Figure 2.3–1..... 19

References

- [1] N. Yu, F. Aieta, P. Genevet, M. A. Kats, Z. Gaburro, and F. Capasso, "A Broadband, Background-Free Quarter-Wave Plate Based on Plasmonic Metasurfaces," *Nano Letters*, vol. 12, pp. 6328-6333, 2012. <https://doi.org/10.1021/nl303445u>
- [2] S. Wang, P. C. Wu, V.-C. Su, Y.-C. Lai, M.-K. Chen, H. Y. Kuo et al., "A broadband achromatic metalens in the visible," *Nature Nanotechnology*, vol. 13, pp. 227-232, 2018. <https://doi.org/10.1038/s41565-017-0052-4>
- [3] M. L. Tseng, M. Semmlinger, M. Zhang, C. Arndt, T.-T. Huang, J. Yang et al., "Vacuum ultraviolet nonlinear metalens," *Science Advances*, vol. 8, pp. eabn5644, 2022. <https://doi.org/doi:10.1126/sciadv.abn5644>
- [4] X. Ni, A. V. Kildishev, and V. M. Shalaev, "Metasurface holograms for visible light," *Nat Commun*, vol. 4, pp. 2807, 2013. <https://doi.org/10.1038/ncomms3807>
- [5] Y. Lei, M. Sakakura, L. Wang, Y. Yu, H. Wang, G. Shayeganrad et al., "High speed ultrafast laser anisotropic nanostructuring by energy deposition control via near-field enhancement," *Optica*, vol. 8, pp. 1365-1371, 2021. <https://doi.org/10.1364/OPTICA.433765>
- [6] D. B. Davidson, "Computational Electromagnetics for RF and Microwave Engineering," Cambridge, Cambridge University Press, 2010. <https://doi.org/10.1017/CBO9780511778117>
- [7] B. Gallinet, J. Butet, and O. J. F. Martin, "Numerical methods for nanophotonics: standard problems and future challenges," *Laser & Photonics Reviews*, vol. 9, pp. 577-603, 2015.
- [8] A. M. Kern, and O. J. F. Martin, "Surface integral formulation for 3D simulations of plasmonic and high permittivity nanostructures," *J. Opt. Soc. Am. A*, vol. 26, pp. 732-740, 2009. <https://doi.org/10.1364/JOSAA.26.000732>
- [9] P. Bharadwaj, B. Deutsch, and L. Novotny, "Optical Antennas," *Advances in Optics and Photonics*, vol. 1, pp. 438-483, 2009. <https://doi.org/10.1364/AOP.1.000438>
- [10] A. M. Kern, and O. J. F. Martin, "Excitation and Reemission of Molecules near Realistic Plasmonic Nanostructures," *Nano Letters*, vol. 11, pp. 482-487, 2011. <https://doi.org/10.1021/nl1032588>
- [11] M. W. Knight, L. Liu, Y. Wang, L. Brown, S. Mukherjee, N. S. King et al., "Aluminum Plasmonic Nanoantennas," *Nano Letters*, vol. 12, pp. 6000-6004, 2012. <https://doi.org/10.1021/nl303517v>
- [12] C. Caloz, and K. Achouri, "Electromagnetic Metasurfaces: Theory and Applications," John Wiley & Sons, 2021.
- [13] S. A. Maier, "Plasmonics : fundamentals and applications," vol. pp. 2007. <http://public.ebookcentral.proquest.com/choice/publicfullrecord.aspx?p=372512>
- [14] M. W. Knight, N. S. King, L. Liu, H. O. Everitt, P. Nordlander, and N. J. Halas, "Aluminum for Plasmonics," *ACS Nano*, vol. 8, pp. 834-840, 2013. <https://doi.org/10.1021/nn405495q>
- [15] J.-M. Guay, A. Calà Lesina, G. Côté, M. Charron, D. Poitras, L. Ramunno et al., "Laser-induced plasmonic colours on metals," *Nat. Commun.*, vol. 8, pp. 16095, 2017. <https://doi.org/10.1038/ncomms16095>
- [16] G. H. Chan, J. Zhao, G. C. Schatz, and R. P. V. Duyne, "Localized Surface Plasmon Resonance Spectroscopy of Triangular Aluminum Nanoparticles," pp. 13958-13963 (2008).
- [17] X. Wang, C. Santschi, and O. J. F. Martin, "Strong Improvement of Long-Term Chemical and Thermal Stability of Plasmonic Silver Nanoantennas and Films," *Small*, vol. 13, pp. 1700044, 2017. <https://doi.org/10.1002/smll.201700044>
- [18] D. Rioux, S. Vallières, S. Besner, P. Muñoz, E. Mazur, and M. Meunier, "An Analytic Model for the Dielectric Function of Au, Ag, and their Alloys," *Advanced Optical Materials*, vol. 2, pp. 176-182, 2014. <https://doi.org/10.1002/adom.201300457>
- [19] D. Ray, H.-C. Wang, J. Kim, C. Santschi, and O. J. F. Martin, "A Low-Temperature Annealing Method for Alloy Nanostructures and Metasurfaces: Unlocking a Novel Degree of Freedom," *Advanced Materials*, vol. 34, pp. 2108225, 2022. <https://doi.org/10.1002/adma.202108225>
- [20] H. R. Yu, A. Conde-Rubio, H. C. Wang, O. J. F. Martin, G. Boero, and J. Brugger, "Precise Capillary-Assisted Nanoparticle Assembly in Reusable Templates," *Particle & Particle Systems Characterization*, vol. pp. 2022. <https://doi.org/10.1002/ppsc.202100288>
- [21] G. B. Arfken, and H. J. Weber, "Mathematical Methods for Physicists," Elsevier Academic Press, 2005.
- [22] H.-C. Wang, K. Achouri, and O. J. F. Martin, "Robustness Analysis of Metasurfaces: Perfect Structures Are Not Always the Best," *ACS Photonics*, vol. pp. 2022. <https://doi.org/10.1021/acsp Photonics.2c00563>
- [23] C. Yan, K.-Y. Yang, and O. J. F. Martin, "Fano-resonance-assisted metasurface for color routing," *Light: Science & Applications*, vol. 6, pp. e17017, 2017. <https://doi.org/10.1038/lsa.2017.17>
- [24] J. Mertz, "Introduction to Optical Microscopy," Cambridge, Cambridge University Press, 2019. <https://doi.org/DOI:10.1017/9781108552660>
- [25] F. Ding, Y. Yang, R. A. Deshpande, and S. I. Bozhevolnyi, "A review of gap-surface plasmon metasurfaces: fundamentals and applications," *Nanophotonics*, vol. 7, pp. 1129-1156, 2018. <https://doi.org/doi:10.1515/nanoph-2017-0125>
- [26] J. Scheuer, "Optical Metasurfaces Are Coming of Age: Short- and Long-Term Opportunities for Commercial Applications," *ACS Photonics*, vol. 7, pp. 1323-1354, 2020. <https://doi.org/10.1021/acsp Photonics.9b01719>
- [27] M. K. Chen, Y. Wu, L. Feng, Q. Fan, M. Lu, T. Xu et al., "Principles, Functions, and Applications of Optical Meta-Lens," *Advanced Optical Materials*, vol. 9, pp. 2001414, 2021. <https://doi.org/https://doi.org/10.1002/adom.202001414>

- [28] Y. Deng, Z. Cai, Y. Ding, S. I. Bozhevolnyi, and F. Ding, "Recent progress in metasurface-enabled optical waveplates," *Nanophotonics*, vol. pp. 2022. <https://doi.org/doi:10.1515/nanoph-2022-0030>
- [29] J. Kim, J. Seong, Y. Yang, S.-W. Moon, T. Badloe, and J. Rho, "Tunable metasurfaces towards versatile metalenses and metaholograms: a review," *Advanced Photonics*, vol. 4, pp. 024001, 2022. <https://doi.org/10.1117/1.AP.4.2.024001>
- [30] H. J. Chen, L. Shao, Q. Li, and J. F. Wang, "Gold nanorods and their plasmonic properties," *Chemical Society Reviews*, vol. 42, pp. 2679-2724, 2013. <https://doi.org/10.1039/c2cs35367a>
- [31] P. C. Wu, W.-Y. Tsai, W. T. Chen, Y.-W. Huang, T.-Y. Chen, J.-W. Chen et al., "Versatile Polarization Generation with an Aluminum Plasmonic Metasurface," *Nano Letters*, vol. 17, pp. 445-452, 2017. <https://doi.org/10.1021/acs.nanolett.6b04446>
- [32] Y. Cao, L. Tang, J. Li, C. Lee, and Z.-G. Dong, "Four-channel display and encryption by near-field reflection on nanoprinting metasurface," *Nanophotonics*, vol. 11, pp. 3365-3374, 2022. <https://doi.org/doi:10.1515/nanoph-2022-0216>
- [33] B. H. Chen, P. C. Wu, V.-C. Su, Y.-C. Lai, C. H. Chu, I. C. Lee et al., "GaN Metalens for Pixel-Level Full-Color Routing at Visible Light," *Nano Letters*, vol. 17, pp. 6345-6352, 2017. <https://doi.org/10.1021/acs.nanolett.7b03135>
- [34] L. Guo, Z. Hu, R. Wan, L. Long, T. Li, J. Yan et al., "Design of aluminum nitride metalens for broadband ultraviolet incidence routing," *Nanophotonics*, vol. 8, pp. 171-180, 2019. <https://doi.org/doi:10.1515/nanoph-2018-0151>
- [35] A. Leitis, A. Heßler, S. Wahl, M. Wuttig, T. Taubner, A. Tittl et al., "All-Dielectric Programmable Huygens' Metasurfaces," *Advanced Functional Materials*, vol. 30, pp. 1910259, 2020. <https://doi.org/https://doi.org/10.1002/adfm.201910259>
- [36] F. Ali, and S. Aksu, "A hybrid broadband metalens operating at ultraviolet frequencies," *Scientific Reports*, vol. 11, pp. 2303, 2021. <https://doi.org/10.1038/s41598-021-81956-4>
- [37] P. Zheng, J. Li, Z. Li, M. Ge, S. Zhang, G. Zheng et al., "Compressive Imaging Encryption with Secret Sharing Metasurfaces," *Advanced Optical Materials*, vol. pp. 2200257, 2022. <https://doi.org/https://doi.org/10.1002/adom.202200257>
- [38] O. Khatib, S. Ren, J. Malof, and W. J. Padilla, "Learning the Physics of All-Dielectric Metamaterials with Deep Lorentz Neural Networks," *Advanced Optical Materials*, vol. pp. 2200097, 2022. <https://doi.org/https://doi.org/10.1002/adom.202200097>
- [39] Z.-Y. Chiao, Y.-C. Chen, J.-W. Chen, Y.-C. Chu, J.-W. Yang, T.-Y. Peng et al., "Full-color generation enabled by refractory plasmonic crystals," *Nanophotonics*, vol. 11, pp. 2891-2899, 2022. <https://doi.org/doi:10.1515/nanoph-2022-0071>
- [40] H. Liu, H. Peng, K. Li, L. Lu, J. Deng, Y. Liu et al., "Transfer Printing of Solution-Processed 3D ZnO Nanostructures with Ultra-High Yield for Flexible Metasurface Color Filter," *Adv. Mater. Interfaces*, vol. n/a, pp. 2101963, 2022. <https://doi.org/https://doi.org/10.1002/admi.202101963>
- [41] Q. Fan, W. Xu, X. Hu, W. Zhu, T. Yue, C. Zhang et al., "Trilobite-inspired neural nanophotonic light-field camera with extreme depth-of-field," *Nat. Commun.*, vol. 13, pp. 2130, 2022. <https://doi.org/10.1038/s41467-022-29568-y>
- [42] R. Guo, E. Rusak, I. Staude, J. Dominguez, M. Decker, C. Rockstuhl et al., "Multipolar Coupling in Hybrid Metal-Dielectric Metasurfaces," *ACS Photonics*, vol. 3, pp. 349-353, 2016. <https://doi.org/10.1021/acsphotonics.6b00012>
- [43] D. Ray, T. V. Raziman, C. Santschi, D. Etezadi, H. Altug, and O. J. F. Martin, "Hybrid Metal-Dielectric Metasurfaces for Refractive Index Sensing," *Nano Letters*, vol. 20, pp. 8752-8759, 2020. <https://doi.org/10.1021/acs.nanolett.0c03613>
- [44] J.-H. Yang, and K.-P. Chen, "Hybridization of plasmonic and dielectric metasurfaces with asymmetric absorption enhancement," *Journal of Applied Physics*, vol. 128, pp. 133101, 2020. <https://doi.org/10.1063/5.0019449>
- [45] R. A. Chipman, W. S. T. Lam, and G. Young, "Polarized light and optical systems," Boca Raton, CRC Press, 2019.
- [46] S. Sun, K.-Y. Yang, C.-M. Wang, T.-K. Juan, W. T. Chen, C. Y. Liao et al., "High-Efficiency Broadband Anomalous Reflection by Gradient Meta-Surfaces," *Nano Letters*, vol. 12, pp. 6223-6229, 2012. <https://doi.org/10.1021/nl3032668>
- [47] Y. Tan, K. Qu, K. Chen, J. Wu, L. Feng, S. Yang et al., "Free-Standing Single-Layer Metasurface for Efficient and Broadband Tailoring of Terahertz Wavefront," *Advanced Optical Materials*, vol. pp. 2200565, 2022. <https://doi.org/https://doi.org/10.1002/adom.202200565>
- [48] A. Arbabi, Y. Horie, M. Bagheri, and A. Faraon, "Dielectric metasurfaces for complete control of phase and polarization with subwavelength spatial resolution and high transmission," *Nature Nanotechnology*, vol. 10, pp. 937-943, 2015. <https://doi.org/10.1038/nnano.2015.186>
- [49] S. Wang, P. C. Wu, V.-C. Su, Y.-C. Lai, C. Hung Chu, J.-W. Chen et al., "Broadband achromatic optical metasurface devices," *Nat. Commun.*, vol. 8, pp. 187, 2017. <https://doi.org/10.1038/s41467-017-00166-7>
- [50] P. Chen, B. Fang, J. Li, X. Jing, M. Kong, and Z. Hong, "Enhancement of efficiency on the Pancharatnam-Berry geometric phase metalens in the terahertz region," *Applied Optics*, vol. 60, pp. 7849-7857, 2021. <https://doi.org/10.1364/AO.433115>
- [51] M. Jiang, S. Y. Siew, J. Y. E. Chan, J. Deng, Q. Y. S. Wu, L. Jin et al., "Patterned resist on flat silver achieving saturated plasmonic colors with sub-20-nm spectral linewidth," *Materials Today*, vol. 35, pp. 99-105, 2020. <https://doi.org/https://doi.org/10.1016/j.mattod.2019.10.020>
- [52] F. Ding, S. Tang, and S. I. Bozhevolnyi, "Recent Advances in Polarization-Encoded Optical Metasurfaces," *Advanced Photonics Research*, vol. 2, pp. 2000173, 2021. <https://doi.org/https://doi.org/10.1002/adpr.202000173>
- [53] Z. Cai, Y. Deng, C. Wu, C. Meng, Y. Ding, S. I. Bozhevolnyi et al., "Dual-Functional Optical Waveplates Based on Gap-Surface Plasmon Metasurfaces," *Advanced Optical Materials*, vol. 9, pp. 2002253, 2021. <https://doi.org/https://doi.org/10.1002/adom.202002253>
- [54] Z. Yue, J. Li, J. Liu, J. Li, C. Zheng, G. Wang et al., "Versatile Polarization Conversion and Wavefront Shaping Based on Fully Phase-Modulated Metasurface with Complex Amplitude Modulation," *Advanced Optical Materials*, vol. pp. 2200733, 2022. <https://doi.org/https://doi.org/10.1002/adom.202200733>
- [55] C. Zheng, J. Li, Z. Yue, J. Li, J. Liu, G. Wang et al., "All-Dielectric Trifunctional Metasurface Capable of Independent Amplitude and Phase Modulation," *Laser & Photonics Reviews*, vol. pp. 2200051, 2022. <https://doi.org/https://doi.org/10.1002/lpor.202200051>

- [56] W. Zhang, B. Gallinet, and O. J. F. Martin, "Symmetry and selection rules for localized surface plasmon resonances in nanostructures," *Physical Review B*, vol. 81, pp. 233407, 2010. <http://link.aps.org/doi/10.1103/PhysRevB.81.233407>
- [57] J. Jang, T. Badloe, Y. Yang, T. Lee, J. Mun, and J. Rho, "Spectral Modulation through the Hybridization of Mie-Scatterers and Quasi-Guided Mode Resonances: Realizing Full and Gradients of Structural Color," *ACS Nano*, vol. 14, pp. 15317-15326, 2020. <https://doi.org/10.1021/acsnano.0c05656>
- [58] X. Liu, Z. Huang, and J. Zang, "All-Dielectric Silicon Nanoring Metasurface for Full-Color Printing," *Nano Letters*, vol. 20, pp. 8739-8744, 2020. <https://doi.org/10.1021/acs.nanolett.0c03596>
- [59] W. Yang, S. Xiao, Q. Song, Y. Liu, Y. Wu, S. Wang et al., "All-dielectric metasurface for high-performance structural color," *Nat. Commun.*, vol. 11, pp. 1864, 2020. <https://doi.org/10.1038/s41467-020-15773-0>
- [60] M. R. Foreman, and P. Torok, "Computational methods in vectorial imaging," *Journal of Modern Optics*, vol. 58, pp. 339-364, 2011. <https://doi.org/10.1080/09500340.2010.525668>
- [61] E. Panchenko, L. Wesemann, D. E. Gómez, T. D. James, T. J. Davis, and A. Roberts, "Ultracompact Camera Pixel with Integrated Plasmonic Color Filters," *Advanced Optical Materials*, vol. 7, pp. 1900893, 2019. <https://doi.org/https://doi.org/10.1002/adom.201900893>
- [62] J. Jang, H. Jeong, G. Hu, C.-W. Qiu, K. T. Nam, and J. Rho, "Kerker-Conditioned Dynamic Cryptographic Nanoprints," *Advanced Optical Materials*, vol. 7, pp. 1801070, 2019. <https://doi.org/https://doi.org/10.1002/adom.201801070>
- [63] C. U. Hail, G. Schnoering, M. Damak, D. Poulikakos, and H. Eghlidi, "A Plasmonic Painter's Method of Color Mixing for a Continuous Red-Green-Blue Palette," *ACS Nano*, vol. 14, pp. 1783-1791, 2020. <https://doi.org/10.1021/acsnano.9b07523>
- [64] Q. Dai, N. Zhou, L. Deng, J. Deng, Z. Li, and G. Zheng, "Dual-Channel Binary Gray-Image Display Enabled with Malus-Assisted Metasurfaces," *Physical Review Applied*, vol. 14, pp. 034002, 2020. <https://doi.org/10.1103/PhysRevApplied.14.034002>
- [65] L. Deng, J. Deng, Z. Guan, J. Tao, Y. Chen, Y. Yang et al., "Malus-metasurface-assisted polarization multiplexing," *Light: Science & Applications*, vol. 9, pp. 101, 2020. <https://doi.org/10.1038/s41377-020-0327-7>
- [66] Y. Zhang, Y. Cheng, M. Chen, R. Xu, and L. Yuan, "Ultracompact metaimage display and encryption with a silver nanopolarizer based metasurface," *Applied Physics Letters*, vol. 117, pp. 021105, 2020. <https://doi.org/10.1063/5.0014987>
- [67] P. C. Wu, R. Sokhoyan, G. K. Shirmanesh, W.-H. Cheng, and H. A. Atwater, "Near-Infrared Active Metasurface for Dynamic Polarization Conversion," *Advanced Optical Materials*, vol. 9, pp. 2100230, 2021. <https://doi.org/https://doi.org/10.1002/adom.202100230>
- [68] P. Zheng, Q. Dai, Z. Li, Z. Ye, J. Xiong, H.-C. Liu et al., "Metasurface-based key for computational imaging encryption," *Science Advances*, vol. 7, pp. eabg0363, 2021. <https://doi.org/10.1126/sciadv.abg0363>
- [69] H. Okamoto, "Local optical activity of nano- to microscale materials and plasmons," *Journal of Materials Chemistry C*, vol. 7, pp. 14771-14787, 2019. <https://doi.org/10.1039/C9TC05141D>
- [70] K. Kumar, H. Duan, R. S. Hegde, S. C. W. Koh, J. N. Wei, and J. K. W. Yang, "Printing colour at the optical diffraction limit," *Nat Nano*, vol. 7, pp. 557-561, 2012. <https://doi.org/10.1038/nnano.2012.128>
- [71] J. S. Clausen, E. Højlund-Nielsen, A. B. Christiansen, S. Yazdi, M. Grajower, H. Taha et al., "Plasmonic Metasurfaces for Coloration of Plastic Consumer Products," *Nano Letters*, vol. 14, pp. 4499-4504, 2014. <https://doi.org/10.1021/nl5014986>
- [72] S. J. Tan, L. Zhang, D. Zhu, X. M. Goh, Y. M. Wang, K. Kumar et al., "Plasmonic Color Palettes for Photorealistic Printing with Aluminum Nanostructures," *Nano Letters*, vol. 14, pp. 4023-4029, 2014. <https://doi.org/10.1021/nl501460x>
- [73] X. Zhu, C. Vannahme, E. Højlund-Nielsen, N. A. Mortensen, and A. Kristensen, "Plasmonic colour laser printing," *Nat Nano*, vol. advance online publication, pp. 2015. <https://doi.org/10.1038/nnano.2015.285>
- [74] T. D. James, P. Mulvaney, and A. Roberts, "The Plasmonic Pixel: Large Area, Wide Gamut Color Reproduction Using Aluminum Nanostructures," *Nano Letters*, vol. 16, pp. 3817-3823, 2016. <https://doi.org/10.1021/acs.nanolett.6b01250>
- [75] B.-R. Lu, C. Xu, J. Liao, J. Liu, and Y. Chen, "High-resolution plasmonic structural colors from nanohole arrays with bottom metal disks," *Optics Letters*, vol. 41, pp. 1400-1403, 2016. <https://doi.org/10.1364/OL.41.001400>
- [76] R. Mudachathi, and T. Tanaka, "Up Scalable Full Colour Plasmonic Pixels with Controllable Hue, Brightness and Saturation," *Scientific Reports*, vol. 7, pp. 1199, 2017. <https://doi.org/10.1038/s41598-017-01266-6>
- [77] J. Zhao, X. Yu, K. Zhou, X. Yang, and Y. Yu, "Wide-Gamut and Polarization-Independent Structural Color at Optical Sub-diffraction-Limit Spatial Resolution Based on Uncoupled LSPs," *Nanoscale Research Letters*, vol. 14, pp. 214, 2019. <https://doi.org/10.1186/s11671-019-3050-7>
- [78] J. Zhang, R. Wei, and C. Guo, "Simultaneous implementation of antireflection and antitransmission through multipolar interference in plasmonic metasurfaces and applications in optical absorbers and broadband polarizers," *Nanophotonics*, vol. 9, pp. 4529-4538, 2020. <https://doi.org/10.1515/nanoph-2020-0325>
- [79] M. F. Shahin Shahidan, J. Song, T. D. James, and A. Roberts, "Vivid plasmonic color under ambient light," *Optics Express*, vol. 29, pp. 40710-40720, 2021. <https://doi.org/10.1364/OE.443853>
- [80] S. L. Ariel Lipson, Henry Lipson, "Optical Physics," Cambridge, Cambridge University Press, 2010. <https://doi.org/10.1017/CBO9780511763120>
- [81] P. B. Johnson, and R. W. Christy, "Optical Constants of the Noble Metals," *Phys. Rev. B*, vol. 6, pp. 4370-4379, 1972.
- [82] N. Yu, P. Genevet, M. A. Kats, F. Aieta, J.-P. Tetienne, F. Capasso et al., "Light Propagation with Phase Discontinuities: Generalized Laws of Reflection and Refraction," *Science*, vol. 334, pp. 333-337, 2011. <https://doi.org/10.1126/science.1210713>
- [83] L. Huang, X. Chen, H. Mühlenbernd, H. Zhang, S. Chen, B. Bai et al., "Three-dimensional optical holography using a plasmonic metasurface," *Nat Commun*, vol. 4, pp. 2808, 2013. <https://doi.org/10.1038/ncomms3808>

- [84] Y. He, B. Song, and J. Tang, "Optical metalenses: fundamentals, dispersion manipulation, and applications," *Frontiers of Optoelectronics*, vol. 15, pp. 24, 2022. <https://doi.org/10.1007/s12200-022-00017-4>
- [85] D. K. Gramotnev, and S. I. Bozhevolnyi, "Plasmonics beyond the diffraction limit," *Nature Photonics*, vol. 4, pp. 83-91, 2010. <https://doi.org/10.1038/nphoton.2009.282>
- [86] G. L  v  que, and O. J. F. Martin, "Optical interactions in a plasmonic particle coupled to a metallic film," *Optics Express*, vol. 14, pp. 9971-9981, 2006. <https://doi.org/10.1364/OE.14.009971>
- [87] F. Ding, A. Pors, and S. I. Bozhevolnyi, "Gradient metasurfaces: a review of fundamentals and applications," *Reports on Progress in Physics*, vol. 81, pp. 026401, 2018. <http://stacks.iop.org/0034-4885/81/i=2/a=026401>
- [88] B. Gallinet, A. M. Kern, and O. J. F. Martin, "Accurate and versatile modeling of electromagnetic scattering on periodic nanostructures with a surface integral approach," *Journal of the Optical Society of America A*, vol. 27, pp. 2261-2271, 2010. <https://doi.org/10.1364/JOSAA.27.002261>
- [89] L. Gao, F. Lemarchand, and M. Lequime, "Refractive index determination of SiO₂ layer in the UV/Vis/NIR range: spectrophotometric reverse engineering on single and bi-layer designs," 2013. https://www.jeos.org/index.php/jeos_rp/article/view/13010
- [90] Y. Z. Ho, B. H. Cheng, W.-L. Hsu, C.-M. Wang, and D. P. Tsai, "Anomalous reflection from metasurfaces with gradient phase distribution below 2π ," *Applied Physics Express*, vol. 9, pp. 072502, 2016. <https://doi.org/10.7567/apex.9.072502>
- [91] Y.-W. Huang, W. T. Chen, W.-Y. Tsai, P. C. Wu, C.-M. Wang, G. Sun et al., "Aluminum Plasmonic Multicolor Meta-Hologram," *Nano Letters*, vol. 15, pp. 3122-3127, 2015. <https://doi.org/10.1021/acs.nanolett.5b00184>
- [92] L. Huang, S. Zhang, and T. Zentgraf, "Metasurface holography: from fundamentals to applications," *Nanophotonics*, vol. 7, pp. 1169-1190, 2018. <https://doi.org/10.1515/nanoph-2017-0118>
- [93] Q. Jiang, G. Jin, and L. Cao, "When metasurface meets hologram: principle and advances," *Advances in Optics and Photonics*, vol. 11, pp. 518-576, 2019. <https://doi.org/10.1364/AOP.11.000518>
- [94] R. Zhao, L. Huang, and Y. Wang, "Recent advances in multi-dimensional metasurfaces holographic technologies," *PhotonIX*, vol. 1, pp. 20, 2020. <https://doi.org/10.1186/s43074-020-00020-y>
- [95] Z.-L. Deng, Li Xiangping, Li Guixin, "Metasurface Holography," Morgan & Claypool, 2020. <https://doi.org/10.2200/S01008ED1V01Y202004MOP004>
- [96] Z.-L. Deng, Z.-Q. Wang, F.-J. Li, M.-X. Hu, and X. Li, "Multi-freedom metasurface empowered vectorial holography," *Nanophotonics*, vol. 11, pp. 1725-1739, 2022. <https://doi.org/doi:10.1515/nanoph-2021-0662>
- [97] A. B. Li, S. Singh, and D. Sievenpiper, "Metasurfaces and their applications," *Nanophotonics*, vol. 7, pp. 989-1011, 2018. <https://doi.org/10.1515/nanoph-2017-0120>
- [98] A. W. Lohmann, R. G. Dorsch, D. Mendlovic, Z. Zalevsky, and C. Ferreira, "Space-bandwidth product of optical signals and systems," *Journal of the Optical Society of America A*, vol. 13, pp. 470-473, 1996. <https://doi.org/10.1364/JOSAA.13.000470>
- [99] D. Frese, B. Sain, H. Zhou, Y. Wang, L. Huang, and T. Zentgraf, "A wavelength and polarization selective photon sieve for holographic applications," *Nanophotonics*, vol. 10, pp. 4543-4550, 2021. <https://doi.org/doi:10.1515/nanoph-2021-0440>
- [100] Y. Hu, X. Luo, Y. Chen, Q. Liu, X. Li, Y. Wang et al., "3D-Integrated metasurfaces for full-colour holography," *Light: Science & Applications*, vol. 8, pp. 86, 2019. <https://doi.org/10.1038/s41377-019-0198-y>
- [101] G. Yoon, D. Lee, K. T. Nam, and J. Rho, "Pragmatic Metasurface Hologram at Visible Wavelength: The Balance between Diffraction Efficiency and Fabrication Compatibility," *Acs Photonics*, vol. 5, pp. 1643-1647, 2018. <https://doi.org/10.1021/acsp Photonics.7b01044>
- [102] S. M. Kamali, E. Arbabi, A. Arbabi, and A. Faraon, "A review of dielectric optical metasurfaces for wavefront control," *Nanophotonics*, vol. 7, pp. 1041-1068, 2018. <https://doi.org/10.1515/nanoph-2017-0129>
- [103] C. R. de Galarreta, I. Sinev, A. M. Alexeev, P. Trofimov, K. Ladutenko, S. G. C. Carrillo et al., "Reconfigurable multilevel control of hybrid all-dielectric phase-change metasurfaces," *Optica*, vol. 7, pp. 476-484, 2020. <https://doi.org/10.1364/optica.384138>
- [104] C. H. Chu, M. L. Tseng, J. Chen, P. C. Wu, Y.-H. Chen, H.-C. Wang et al., "Active dielectric metasurface based on phase-change medium," *Laser & Photonics Reviews*, vol. 10, pp. 986-994, 2016. <https://doi.org/https://doi.org/10.1002/lpor.201600106>
- [105] Y. Hu, X. Wang, X. Luo, X. Ou, L. Li, Y. Chen et al., "All-dielectric metasurfaces for polarization manipulation: principles and emerging applications," *Nanophotonics*, vol. 9, pp. 3755-3780, 2020. <https://doi.org/doi:10.1515/nanoph-2020-0220>
- [106] H.-H. Hsiao, C. H. Chu, and D. P. Tsai, "Fundamentals and Applications of Metasurfaces," *Small Methods*, vol. 1, pp. 1600064, 2017. <https://doi.org/https://doi.org/10.1002/smt.201600064>
- [107] H. Sattari, T. Graziosi, M. Kiss, T. J. Seok, S. Han, M. C. Wu et al., "Silicon Photonic MEMS Phase-Shifter," *Optics Express*, vol. 27, pp. 18959-18969, 2019. <https://doi.org/10.1364/OE.27.018959>
- [108] Z. Li, S. Yu, and G. Zheng, "Advances in exploiting the degrees of freedom in nanostructured metasurface design: from 1 to 3 to more," *Nanophotonics*, vol. 9, pp. 3699-3731, 2020. <https://doi.org/doi:10.1515/nanoph-2020-0127>
- [109] Q. Wei, L. Huang, T. Zentgraf, and Y. Wang, "Optical wavefront shaping based on functional metasurfaces," *Nanophotonics*, vol. 9, pp. 987-1002, 2020. <https://doi.org/doi:10.1515/nanoph-2019-0478>
- [110] J. Sung, G.-Y. Lee, and B. Lee, "Progresses in the practical metasurface for holography and lens," *Nanophotonics*, vol. 8, pp. 1701-1718, 2019. <https://doi.org/doi:10.1515/nanoph-2019-0203>
- [111] Q. Song, S. Khadir, S. V  zian, B. Damilano, P. d. Mierry, S. Chenot et al., "Printing polarization and phase at the optical diffraction limit: near- and far-field optical encryption," *Nanophotonics*, vol. 10, pp. 697-704, 2021. <https://doi.org/doi:10.1515/nanoph-2020-0352>

- [112] Z. Li, M. Premaratne, and W. Zhu, "Advanced encryption method realized by secret shared phase encoding scheme using a multi-wavelength metasurface," *Nanophotonics*, vol. 9, pp. 3687-3696, 2020. <https://doi.org/doi:10.1515/nanoph-2020-0298>
- [113] H. Rajabalipanah, K. Rouhi, A. Abdolali, S. Iqbal, L. Zhang, and S. Liu, "Real-time terahertz meta-cryptography using polarization-multiplexed graphene-based computer-generated holograms," *Nanophotonics*, vol. 9, pp. 2861-2877, 2020. <https://doi.org/doi:10.1515/nanoph-2020-0110>
- [114] H. Q. Zhou, Y. T. Wang, X. W. Li, Q. Wang, Q. S. Wei, G. Z. Geng et al., "Switchable active phase modulation and holography encryption based on hybrid metasurfaces," *Nanophotonics*, vol. 9, pp. 905-912, 2020. <https://doi.org/10.1515/nanoph-2019-0519>
- [115] G. Qu, W. Yang, Q. Song, Y. Liu, C.-W. Qiu, J. Han et al., "Reprogrammable meta-hologram for optical encryption," *Nat. Commun.*, vol. 11, pp. 5484, 2020. <https://doi.org/10.1038/s41467-020-19312-9>
- [116] K. L. Tsakmakidis, A. D. Boardman, and O. Hess, "'Trapped rainbow' storage of light in metamaterials," *Nature*, vol. 450, pp. 397-401, 2007. <https://doi.org/10.1038/nature06285>
- [117] S. G. C. Carrillo, L. Trimby, Y. Y. Au, V. K. Nagareddy, G. Rodriguez-Hernandez, P. Hosseini et al., "A Nonvolatile Phase-Change Metamaterial Color Display," *Advanced Optical Materials*, vol. 7, pp. 2019. <https://doi.org/10.1002/adom.201801782>
- [118] M. Song, D. Wang, Z. A. Kudyshev, Y. Xuan, Z. Wang, A. Boltasseva et al., "Enabling Optical Steganography, Data Storage, and Encryption with Plasmonic Colors," *Laser & Photonics Reviews*, vol. 15, pp. 2000343, 2021. <https://doi.org/https://doi.org/10.1002/lpor.202000343>
- [119] U. Schnars, and W. P. O. J ptner, "Digital recording and numerical reconstruction of holograms," *Measurement Science and Technology*, vol. 13, pp. R85-R101, 2002. <https://doi.org/10.1088/0957-0233/13/9/201>
- [120] S. Mehrabkhani, and T. Schneider, "Is the Rayleigh-Sommerfeld diffraction always an exact reference for high speed diffraction algorithms?," *Optics Express*, vol. 25, pp. 30229-30240, 2017. <https://doi.org/10.1364/OE.25.030229>
- [121] R. Yang, J. Wang, C. Chen, Y. Wu, B. Li, Y. Li et al., "Fast Diffraction Calculation for Spherical Computer-Generated Hologram Using Phase Compensation Method in Visible Range," *Applied Sciences*, vol. 10, pp. 5784, 2020. <https://doi.org/10.3390/app10175784>
- [122] R. W. Gerchberg, "A practical algorithm for the determination of phase from image and diffraction plane pictures," *Optik*, vol. 35, pp. 237-246, 1972. <https://asset-pdf.scinapse.io/prod/1484412996/1484412996.pdf>
- [123] I. J. Cooper, C. J. R. Sheppard, and M. Sharma, "Numerical integration of diffraction integrals for a circular aperture," *Optik*, vol. 113, pp. 293-298, 2002. <https://doi.org/10.1078/0030-4026-00170>
- [124] J. Braat, and P. Török, "Imaging Optics," Cambridge, Cambridge University Press, 2019. <https://doi.org/10.1017/9781108552264>
- [125] D. Hu, J. Zheng, E. Liao, T. Syu, and A. Du, "Modulating both amplitude and phase in a single-spatial light modulator (SLM)," *SPIE*, 2022. <https://doi.org/10.1117/12.2607186>
- [126] R. Fu, X. Shan, L. G. Deng, Q. Dai, Z. Q. Guan, Z. L. Li et al., "Multiplexing meta-hologram with separate control of amplitude and phase," *Optics Express*, vol. 29, pp. 27696-27707, 2021. <https://doi.org/10.1364/oe.435986>
- [127] F. Wyrowski, and O. Bryngdahl, "Iterative Fourier-transform algorithm applied to computer holography," *Journal of the Optical Society of America A*, vol. 5, pp. 1058-1065, 1988. <https://doi.org/10.1364/JOSAA.5.001058>
- [128] Y. Mu, M. Zheng, J. Qi, H. Li, and J. Qiu, "A large field-of-view metasurface for complex-amplitude hologram breaking numerical aperture limitation," *Nanophotonics*, vol. 9, pp. 4749-4759, 2020. <https://doi.org/doi:10.1515/nanoph-2020-0448>
- [129] W. Wei, P. Tang, J. Shao, J. Zhu, X. Zhao, and C. Wu, "End-to-end design of metasurface-based complex-amplitude holograms by physics-driven deep neural networks," *Nanophotonics*, vol. 11, pp. 2921-2929, 2022. <https://doi.org/doi:10.1515/nanoph-2022-0111>
- [130] A. W. Lohmann, and D. P. Paris, "Binary Fraunhofer Holograms, Generated by Computer," *Applied Optics*, vol. 6, pp. 1739-1748, 1967. <https://doi.org/10.1364/AO.6.001739>
- [131] J. A. Davis, G. W. Bach, D. M. Cottrell, and R. A. Lilly, "Suppression of selected diffraction orders with programmable masks written on spatial light modulators," *Applied Optics*, vol. 27, pp. 2949-2953, 1988. <https://doi.org/10.1364/AO.27.002949>
- [132] M. A. A. Neil, and E. G. S. Paige, "Breaking of inversion symmetry in 2-level binary, Fourier holograms," 1993 *Fourth International Conference on Holographic Systems, Components and Applications* 85-90 (1993). <https://ieeexplore.ieee.org/stamp/stamp.jsp?tp=&arnumber=263315>
- [133] M. Khorasaninejad, A. Ambrosio, P. Kanhaiya, and F. Capasso, "Broadband and chiral binary dielectric meta-holograms," *Science Advances*, vol. 2, pp. e1501258, 2016. <https://doi.org/10.1126/sciadv.1501258>
- [134] B. F. William H., Saul Teukolsky, William Vetterling, "Numerical Recipes in C: The Art of Scientific Computing," Cambridge University Press, 1992. <https://www.amazon.com/Numerical-Recipes-Scientific-Computing-Second/dp/0521431085>
- [135] K. Thyagarajan, C. Santschi, P. Langlet, and O. J. F. Martin, "Highly Improved Fabrication of Ag and Al Nanostructures for UV and Nonlinear Plasmonics," *Advanced Optical Materials*, vol. 4, pp. 871-876, 2016. <https://doi.org/10.1002/adom.201500740>
- [136] X. Wang, C. Santschi, and O. J. F. Martin, "Strong Improvement of Long-Term Chemical and Thermal Stability of Plasmonic Silver Nanoantennas and Films," *Small*, vol. 13, pp. 1700044, 2017. <https://doi.org/10.1002/sml.201700044>
- [137] Z. e. Bomzon, V. Kleiner, and E. Hasman, "Space-variant polarization state manipulation with computer-generated subwavelength metal stripe gratings," *Optics Communications*, vol. 192, pp. 169-181, 2001. [https://doi.org/10.1016/S0030-4018\(01\)01196-8](https://doi.org/10.1016/S0030-4018(01)01196-8)

- [138] D. F. Sievenpiper, J. H. Schaffner, H. J. Song, R. Y. Loo, and G. Tangonan, "Two-dimensional beam steering using an electrically tunable impedance surface," *IEEE Transactions on Antennas and Propagation*, vol. 51, pp. 2713-2722, 2003. <https://doi.org/10.1109/tap.2003.817558>
- [139] S. J. Lim, C. Caloz, and T. Itoh, "Metamaterial-based electronically controlled transmission-line structure as a novel leaky-wave antenna with tunable radiation angle and beamwidth," *IEEE Trans. Microw. Theory Tech.*, vol. 52, pp. 2678-2690, 2004. <https://doi.org/10.1109/tmtt.2004.838302>
- [140] Q. Feng, M. B. Pu, C. G. Hu, and X. G. Luo, "Engineering the dispersion of metamaterial surface for broadband infrared absorption," *Optics Letters*, vol. 37, pp. 2133-2135, 2012. <https://doi.org/10.1364/ol.37.002133>
- [141] C. Pfeiffer, and A. Grbic, "Cascaded metasurfaces for complete phase and polarization control," *Applied Physics Letters*, vol. 102, pp. 231116, 2013. <https://doi.org/10.1063/1.4810873>
- [142] Y. Yao, R. Shankar, M. A. Kats, Y. Song, J. Kong, M. Loncar et al., "Electrically Tunable Metasurface Perfect Absorbers for Ultrathin Mid-Infrared Optical Modulators," *Nano Letters*, vol. 14, pp. 6526-6532, 2014. <https://doi.org/10.1021/nl503104n>
- [143] K. B. Fan, J. Y. Suen, X. Y. Liu, and W. J. Padilla, "All-dielectric metasurface absorbers for uncooled terahertz imaging," *Optica*, vol. 4, pp. 601-604, 2017. <https://doi.org/10.1364/optica.4.000601>
- [144] P. N. Li, I. Dolado, F. J. Alfaro-Mozaz, F. Casanova, L. E. Hueso, S. Liu et al., "Infrared hyperbolic metasurface based on nanostructured van der Waals materials," *Science*, vol. 359, pp. 892-+, 2018. <https://doi.org/10.1126/science.aag1704>
- [145] J. W. He, T. Dong, B. H. Chi, and Y. Zhang, "Metasurfaces for Terahertz Wavefront Modulation: a Review," *Journal of Infrared Millimeter and Terahertz Waves*, vol. 41, pp. 607-631, 2020. <https://doi.org/10.1007/s10762-020-00677-3>
- [146] Z. H. Wang, Y. L. Wu, D. F. Qi, W. H. Yu, and H. Y. Zheng, "Progress in the design, nanofabrication, and performance of metalenses," *Journal of Optics*, vol. 24, pp. 2022. <https://doi.org/10.1088/2040-8986/ac44d8>
- [147] N. Yu, and F. Capasso, "Flat optics with designer metasurfaces," *Nature Materials*, vol. 13, pp. 139-150, 2014. <https://doi.org/10.1038/nmat3839>
- [148] S. Sun, Q. He, J. Hao, S. Xiao, and L. Zhou, "Electromagnetic metasurfaces: physics and applications," *Advances in Optics and Photonics*, vol. 11, pp. 380-479, 2019. <https://doi.org/10.1364/AOP.11.000380>
- [149] W. T. Chen, A. Y. Zhu, and F. Capasso, "Flat optics with dispersion-engineered metasurfaces," *Nature Reviews Materials*, vol. 5, pp. 604-620, 2020. <https://doi.org/10.1038/s41578-020-0203-3>
- [150] K. Achouri, G. D. Bernasconi, J. Butet, and O. J. F. Martin, "Homogenization and Scattering Analysis of Second-Harmonic Generation in Nonlinear Metasurfaces," *Ieee Transactions on Antennas and Propagation*, vol. 66, pp. 6061-6075, 2018. <https://doi.org/10.1109/tap.2018.2863116>
- [151] A. M. Shaltout, K. G. Lagoudakis, J. van de Groep, S. J. Kim, J. Vučković, V. M. Shalaev et al., "Spatiotemporal light control with frequency-gradient metasurfaces," *Science*, vol. 365, pp. 374-377, 2019. <https://doi.org/10.1126/science.aax2357>
- [152] G. Yoon, T. Tanaka, T. Zentgraf, and J. Rho, "Recent progress on metasurfaces: applications and fabrication," *J. Phys. D-Appl. Phys.*, vol. 54, pp. 2021. <https://doi.org/10.1088/1361-6463/ac0faa>
- [153] A. M. Baracu, M. A. Avram, C. Breazu, M. C. Bunea, M. Socol, A. Stanculescu et al., "Silicon Metalens Fabrication from Electron Beam to UV-Nanoimprint Lithography," *Nanomaterials*, vol. 11, pp. 2021. <https://doi.org/10.3390/nano11092329>
- [154] A. S. Roberts, A. Pors, O. Albrechtsen, and S. I. Bozhevolnyi, "Subwavelength Plasmonic Color Printing Protected for Ambient Use," *Nano Letters*, vol. 14, pp. 783-787, 2014. <https://doi.org/10.1021/nl404129n>
- [155] K.-Y. Yang, R. Verre, J. Butet, C. Yan, T. J. Antosiewicz, M. Käll et al., "Wavevector-Selective Nonlinear Plasmonic Metasurfaces," *Nano Letters*, vol. 17, pp. 5258-5263, 2017. <https://doi.org/10.1021/acs.nanolett.7b01412>
- [156] H. Wang, X. Wang, C. Yan, H. Zhao, J. Zhang, C. Santschi et al., "Full Color Generation Using Silver Tandem Nanodisks," *ACS Nano*, vol. 11, pp. 4419-4427, 2017. <https://doi.org/10.1021/acsnano.6b08465>
- [157] F. Ding, R. Deshpande, and S. I. Bozhevolnyi, "Bifunctional gap-plasmon metasurfaces for visible light: polarization-controlled unidirectional surface plasmon excitation and beam steering at normal incidence," *Light: Science & Applications*, vol. 7, pp. 17178-17178, 2018. <https://doi.org/10.1038/lsa.2017.178>
- [158] H.-C. Wang, C. H. Chu, P. C. Wu, H.-H. Hsiao, H. J. Wu, J.-W. Chen et al., "Ultrathin Planar Cavity Metasurfaces," *Small*, vol. 14, pp. 1703920, 2018. <https://doi.org/10.1002/smll.201703920>
- [159] T. Hu, C. K. Tseng, Y. H. Fu, Z. J. Xu, Y. Dong, S. J. Wang et al., "Demonstration of color display metasurfaces via immersion lithography on a 12-inch silicon wafer," *Optics Express*, vol. 26, pp. 19548-19554, 2018. <https://doi.org/10.1364/oe.26.019548>
- [160] N. X. Li, Y. H. Fu, Y. Dong, T. Hu, Z. J. Xu, Q. Z. Zhong et al., "Large-area pixelated metasurface beam deflector on a 12-inch glass wafer for random point generation," *Nanophotonics*, vol. 8, pp. 1855-1861, 2019. <https://doi.org/10.1515/nanoph-2019-0208>
- [161] Y. Dong, Z. J. Xu, N. X. Li, J. C. Tong, Y. H. Fu, Y. Y. Zhou et al., "Si metasurface half-wave plates demonstrated on a 12-inch CMOS platform," *Nanophotonics*, vol. 9, pp. 149-157, 2020. <https://doi.org/10.1515/nanoph-2019-0364>
- [162] C. A. Dirdal, G. U. Jensen, H. Angelskar, P. Conrad, V. Thrane, J. Gjessing et al., "Towards high-throughput large-area metalens fabrication using UV-nanoimprint lithography and Bosch deep reactive ion etching," *Optics Express*, vol. 28, pp. 15542-15561, 2020. <https://doi.org/10.1364/oe.393328>
- [163] P. Cencillo-Abad, J. Y. Ou, E. Plum, J. Valente, and N. I. Zheludev, "Random access actuation of nanowire grid metamaterial," *Nanotechnology*, vol. 27, pp. 2016. <https://doi.org/10.1088/0957-4484/27/48/485206>
- [164] Z. G. Liu, H. F. Du, Z. Y. Li, N. X. Fang, and J. F. Li, "Invited Article: Nano-kirigami metasurfaces by focused-ion-beam induced close-loop transformation," *Appl Photonics*, vol. 3, pp. 2018. <https://doi.org/10.1063/1.5043065>

- [165] M. Semple, A. C. Hryciw, P. Li, E. Flaim, and A. K. Iyer, "Patterning of Complex, Nanometer-Scale Features in Wide-Area Gold Nanoplasmonic Structures Using Helium Focused Ion Beam Milling," *Acs Applied Materials & Interfaces*, vol. 13, pp. 43209-43220, 2021. <https://doi.org/10.1021/acsami.1c09295>
- [166] P. R. West, J. L. Stewart, A. V. Kildishev, V. M. Shalae, V. V. Shkunov, F. Strohkindl et al., "All-dielectric subwavelength metasurface focusing lens," *Optics Express*, vol. 22, pp. 26212-26221, 2014. <https://doi.org/10.1364/oe.22.026212>
- [167] B. Sain, C. Meier, and T. Zentgraf, "Nonlinear optics in all-dielectric nanoantennas and metasurfaces: a review," *Advanced Photonics*, vol. 1, pp. 024002, 2019. <https://doi.org/10.1117/1.AP.1.2.024002>
- [168] I. P. Radko, V. S. Volkov, J. Beermann, A. B. Evlyukhin, T. S ndergaard, A. Boltasseva et al., "Plasmonic metasurfaces for waveguiding and field enhancement," *Laser & Photonics Reviews*, vol. 3, pp. 575-590, 2009. <https://doi.org/10.1002/lpor.200810071>
- [169] P. Genevet, F. Capasso, F. Aieta, M. Khorasaninejad, and R. Devlin, "Recent advances in planar optics: from plasmonic to dielectric metasurfaces," *Optica*, vol. 4, pp. 139-152, 2017. <https://doi.org/10.1364/OPTICA.4.000139>
- [170] J. P. Kottmann, O. J. F. Martin, D. R. Smith, and S. Schultz, "Non-regularly shaped plasmon resonant nanoparticle as localized light source for near-field microscopy," *Journal of Microscopy*, vol. 202 pt. 1, pp. 60-65, 2001.
- [171] B. Abasahl, C. Santschi, T. V. Raziman, and O. J. F. Martin, "Fabrication of plasmonic structures with well-controlled nanometric features: a comparison between lift-off and ion beam etching," *Nanotechnology*, vol. 32, pp. 475202, 2021. <https://doi.org/10.1088/1361-6528/ac1a93>
- [172] S. Okazaki, "High resolution optical lithography or high throughput electron beam lithography: The technical struggle from the micro to the nano-fabrication evolution," *Microelectronic Engineering*, vol. 133, pp. 23-35, 2015. <https://doi.org/10.1016/j.mee.2014.11.015>
- [173] H. Aouani, J. Wenger, D. Gerard, H. Rigneault, E. Devaux, T. W. Ebbesen et al., "Crucial Role of the Adhesion Layer on the Plasmonic Fluorescence Enhancement," *Acs Nano*, vol. 3, pp. 2043-2048, 2009. <https://doi.org/10.1021/nn900460t>
- [174] X. Jiao, J. Goeckeritz, S. Blair, and M. Oldham, "Localization of Near-Field Resonances in Bowtie Antennae: Influence of Adhesion Layers," *Plasmonics*, vol. 4, pp. 37-50, 2009. <https://doi.org/10.1007/s11468-008-9075-x>
- [175] T. Siegfried, Y. Ekinici, O. J. F. Martin, and H. Sigg, "Engineering Metal Adhesion Layers That Do Not Deteriorate Plasmon Resonances," *ACS Nano*, vol. 7, pp. 2751-2757, 2013. <https://doi.org/10.1021/nn4002006>
- [176] Y. Ekinici, A. Christ, M. Agio, O. J. F. Martin, H. H. Solak, and J. F. L ffler, "Electric and magnetic resonances in arrays of coupled gold nanoparticle in-tandem pairs," *Opt. Express*, vol. 16, pp. 13287-13295, 2008. <https://doi.org/10.1364/OE.16.013287>
- [177] A. Pors, and S. I. Bozhevolnyi, "Plasmonic metasurfaces for efficient phase control in reflection," *Optics Express*, vol. 21, pp. 27438-27451, 2013. <https://doi.org/10.1364/OE.21.027438>
- [178] A. V. Kildishev, A. Boltasseva, and V. M. Shalae, "Planar Photonics with Metasurfaces," *Science*, vol. 339, pp. 2013. <https://doi.org/10.1126/science.1232009>
- [179] K. Achouri, and C. Caloz, "Design, concepts, and applications of electromagnetic metasurfaces," *Nanophotonics*, vol. 7, pp. 1095, 2018. <https://doi.org/10.1515/nanoph-2017-0119>
- [180] C. Yan, T. V. Raziman, and O. J. F. Martin, "Phase Bifurcation and Zero Reflection in Planar Plasmonic Metasurfaces," *ACS Photonics*, vol. 4, pp. 852-860, 2017. <https://doi.org/10.1021/acsp Photonics.6b00914>
- [181] A.-P. Blanchard-Dionne, and O. J. F. Martin, "Successive training of a generative adversarial network for the design of an optical cloak," *OSA Continuum*, vol. 4, pp. 87-95, 2021. <https://doi.org/10.1364/OSAC.413394>
- [182] A. Kristensen, J. K. W. Yang, S. I. Bozhevolnyi, S. Link, P. Nordlander, N. J. Halas et al., "Plasmonic colour generation," *Nature Reviews Materials*, vol. 2, pp. 16088, 2016. <https://doi.org/10.1038/natrevmats.2016.88>
- [183] T. Lee, J. Jang, H. Jeong, and J. Rho, "Plasmonic- and dielectric-based structural coloring: from fundamentals to practical applications," *Nano Convergence*, vol. 5, pp. 1, 2018. <https://doi.org/10.1186/s40580-017-0133-y>
- [184] M. Song, D. Wang, S. Peana, S. Choudhury, P. Nyga, Z. A. Kudyshev et al., "Colors with plasmonic nanostructures: A full-spectrum review," *Applied Physics Reviews*, vol. 6, pp. 041308, 2019. <https://doi.org/10.1063/1.5110051>
- [185] S. Daqiqeh Rezaei, Z. Dong, J. You En Chan, J. Trisno, R. J. H. Ng, Q. Ruan et al., "Nanophotonic Structural Colors," *ACS Photonics*, vol. 8, pp. 18-33, 2021. <https://doi.org/10.1021/acsp Photonics.0c00947>
- [186] Z. Xuan, J. Li, Q. Liu, F. Yi, S. Wang, and W. Lu, "Artificial Structural Colors and Applications," *The Innovation*, vol. 2, pp. 2021. <https://doi.org/10.1016/j.xinn.2021.100081>
- [187] J. Olson, A. Manjavacas, T. Basu, D. Huang, A. E. Schlather, B. Zheng et al., "High Chromaticity Aluminum Plasmonic Pixels for Active Liquid Crystal Displays," *ACS Nano*, vol. 10, pp. 1108-1117, 2016. <https://doi.org/10.1021/acsnano.5b06415>
- [188] L. Wen, Q. Chen, X. Hu, H. Wang, L. Jin, and Q. Su, "Multifunctional Silicon Optoelectronics Integrated with Plasmonic Scattering Color," *ACS Nano*, vol. 10, pp. 11076-11086, 2016. <https://doi.org/10.1021/acsnano.6b05960>
- [189] Y. Lee, M.-K. Park, S. Kim, J. H. Shin, C. Moon, J. Y. Hwang et al., "Electrical Broad Tuning of Plasmonic Color Filter Employing an Asymmetric-Lattice Nanohole Array of Metasurface Controlled by Polarization Rotator," *ACS Photonics*, vol. 4, pp. 1954-1966, 2017. <https://doi.org/10.1021/acsp Photonics.7b00249>
- [190] M. L. Tseng, J. Yang, M. Semmlinger, C. Zhang, P. Nordlander, and N. J. Halas, "Two-Dimensional Active Tuning of an Aluminum Plasmonic Array for Full-Spectrum Response," *Nano Letters*, vol. 17, pp. 6034-6039, 2017. <https://doi.org/10.1021/acs.nanolett.7b02350>
- [191] J. Zhao, X. Yu, K. Zhou, W. Zhang, W. Yuan, and Y. Yu, "Polarization-sensitive subtractive structural color used for information encoding and dynamic display," *Optics and Lasers in Engineering*, vol. 138, pp. 106421, 2021. <https://doi.org/10.1016/j.optlaseng.2020.106421>

- [192] Z. Li, Q. Dai, L. Deng, G. Zheng, and G. Li, "Structural-color nanoprinting with hidden watermarks," *Optics Letters*, vol. 46, pp. 480-483, 2021. <https://doi.org/10.1364/OL.417026>
- [193] J. Cai, C. Zhang, and W.-D. Li, "Dual-Color Flexible Metasurfaces with Polarization-Tunable Plasmons in Gold Nanorod Arrays," *Advanced Optical Materials*, vol. 9, pp. 2001401, 2021. <https://doi.org/https://doi.org/10.1002/adom.202001401>
- [194] W. Wang, D. Rosenmann, D. A. Czaplewski, X. Yang, and J. Gao, "Realizing structural color generation with aluminum plasmonic V-groove metasurfaces," *Optics Express*, vol. 25, pp. 20454-20465, 2017. <https://doi.org/10.1364/OE.25.020454>
- [195] M. Song, X. Li, M. Pu, Y. Guo, K. Liu, H. Yu et al., "Color display and encryption with a plasmonic polarizing metamirror," *Nanophotonics*, vol. 7, pp. 323-331, 2018. <https://doi.org/doi:10.1515/nanoph-2017-0062>
- [196] L. Cheng, J. Mao, K. Wang, J. Lu, K. Huang, Y. Zhang et al., "Rational design of colorimetric sensing for a customer-oriented index range using plasmonic substrates," *Journal of the Optical Society of America B*, vol. 36, pp. 3168-3173, 2019. <https://doi.org/10.1364/JOSAB.36.003168>
- [197] E. G. Melo, A. L. A. Ribeiro, R. S. Benevides, A. A. G. V. Zuben, M. V. Puydinger dos Santos, A. A. Silva et al., "Bright and Vivid Diffractive-Plasmonic Reflective Filters for Color Generation," *ACS Applied Nano Materials*, vol. 3, pp. 1111-1117, 2020. <https://doi.org/10.1021/acsnanm.9b02508>
- [198] E. Schonbrun, G. Möller, and G. Di Caprio, "Polarization encoded color camera," *Optics Letters*, vol. 39, pp. 1433-1436, 2014. <https://doi.org/10.1364/OL.39.001433>
- [199] L. Duempelmann, D. Casari, A. Luu-Dinh, B. Gallinet, and L. Novotny, "Color Rendering Plasmonic Aluminum Substrates with Angular Symmetry Breaking," *ACS Nano*, vol. 9, pp. 12383-12391, 2015. <https://doi.org/10.1021/acsnano.5b05710>
- [200] V. Raj Shrestha, S.-S. Lee, E.-S. Kim, and D.-Y. Choi, "Polarization-tuned Dynamic Color Filters Incorporating a Dielectric-loaded Aluminum Nanowire Array," *Scientific Reports*, vol. 5, pp. 12450, 2015. <https://doi.org/10.1038/srep12450>
- [201] L. Duempelmann, A. Luu-Dinh, B. Gallinet, and L. Novotny, "Four-Fold Color Filter Based on Plasmonic Phase Retarder," *ACS Photonics*, vol. 3, pp. 190-196, 2016. <https://doi.org/10.1021/acsp Photonics.5b00604>
- [202] I. Koirala, V. R. Shrestha, C.-S. Park, S.-S. Lee, and D.-Y. Choi, "Polarization-Controlled Broad Color Palette Based on an Ultrathin One-Dimensional Resonant Grating Structure," *Scientific Reports*, vol. 7, pp. 40073, 2017. <https://doi.org/10.1038/srep40073>
- [203] Y. Kim, K. Jung, J. Cho, and J. K. Hyun, "Realizing Vibrant and High-Contrast Reflective Structural Colors from Lossy Metals Supporting Dielectric Gratings," *ACS Nano*, vol. 13, pp. 10717-10726, 2019. <https://doi.org/10.1021/acsnano.9b05382>
- [204] J. S. Lee, J. Y. Park, Y. H. Kim, S. Jeon, O. Ouellette, E. H. Sargent et al., "Ultrahigh resolution and color gamut with scattering-reducing transmissive pixels," *Nat. Commun.*, vol. 10, pp. 4782, 2019. <https://doi.org/10.1038/s41467-019-12689-2>
- [205] S. Mader, and O. J. F. Martin, "Remarkable Color Gamut Enhancement of Dye Lacquers Using Corrugated Surfaces," *Advanced Photonics Research*, vol. 3, pp. 2100245, 2021. <https://doi.org/https://doi.org/10.1002/adpr.202100245>
- [206] H. A. Macleod, "Thin-film optical filters," Boca Raton, CRC Press, 2018.
- [207] S. Mader, and O. J. F. Martin, "Engineerin multi-state transparency on demand," *Light: Advanced Manufacturing*, vol. 2, pp. 385-394, 2021.
- [208] F. Cheng, J. Gao, T. S. Luk, and X. Yang, "Structural color printing based on plasmonic metasurfaces of perfect light absorption," *Scientific Reports*, vol. 5, pp. 11045, 2015. <https://doi.org/10.1038/srep11045>
- [209] M. Miyata, H. Hatada, and J. Takahara, "Full-Color Subwavelength Printing with Gap-Plasmonic Optical Antennas," *Nano Letters*, vol. 16, pp. 3166-3172, 2016. <https://doi.org/10.1021/acs.nanolett.6b00500>
- [210] V. Flauraud, M. Reyes, R. Paniagua-Domínguez, A. I. Kuznetsov, and J. Brugger, "Silicon Nanostructures for Bright Field Full Color Prints," *ACS Photonics*, vol. 4, pp. 1913-1919, 2017. <https://doi.org/10.1021/acsp Photonics.6b01021>
- [211] B. Yang, W. Liu, Z. Li, H. Cheng, D.-Y. Choi, S. Chen et al., "Ultrahighly Saturated Structural Colors Enhanced by Multipolar-Modulated Metasurfaces," *Nano Letters*, vol. 19, pp. 4221-4228, 2019. <https://doi.org/10.1021/acs.nanolett.8b04923>
- [212] L. Li, J. Niu, X. Shang, S. Chen, C. Lu, Y. Zhang et al., "Bright Field Structural Colors in Silicon-on-Insulator Nanostructures," *ACS Applied Materials & Interfaces*, vol. pp. 2021. <https://doi.org/10.1021/acsam.0c19126>
- [213] P. Huo, M. Song, W. Zhu, C. Zhang, L. Chen, H. J. Lezec et al., "Photorealistic full-color nanopainting enabled by a low-loss metasurface," *Optica*, vol. 7, pp. 1171-1172, 2020. <https://doi.org/10.1364/OPTICA.403092>
- [214] Y. Liu, H. Wang, J. Ho, R. C. Ng, R. J. H. Ng, V. H. Hall-Chen et al., "Structural color three-dimensional printing by shrinking photonic crystals," *Nat. Commun.*, vol. 10, pp. 4340, 2019. <https://doi.org/10.1038/s41467-019-12360-w>
- [215] A. S. Roberts, S. M. Novikov, Y. Yang, Y. Chen, S. Boroviks, J. Beermann et al., "Laser Writing of Bright Colors on Near-Percolation Plasmonic Reflector Arrays," *ACS Nano*, vol. 13, pp. 71-77, 2019. <https://doi.org/10.1021/acsnano.8b07541>
- [216] C. Liu, S. A. Maier, and G. Li, "Genetic-Algorithm-Aided Meta-Atom Multiplication for Improved Absorption and Coloration in Nanophotonics," *ACS Photonics*, vol. 7, pp. 1716-1722, 2020. <https://doi.org/10.1021/acsp Photonics.0c00266>
- [217] A. Weissman, M. Galanty, D. Gachet, E. Segal, O. Shavit, and A. Salomon, "Spatial Confinement of Light onto a Flat Metallic Surface Using Hybridization between Two Cavities," *Advanced Optical Materials*, vol. 5, pp. 1700097, 2017. <https://doi.org/https://doi.org/10.1002/adom.201700097>
- [218] L. V. Poulikakos, M. Lawrence, D. R. Barton, S. S. Jeffrey, and J. A. Dionne, "Guided-Mode-Resonant Dielectric Metasurfaces for Colorimetric Imaging of Material Anisotropy in Fibrous Biological Tissue," *ACS Photonics*, vol. 7, pp. 3216-3227, 2020. <https://doi.org/10.1021/acsp Photonics.0c01303>
- [219] Y. Nagasaki, M. Suzuki, and J. Takahara, "All-Dielectric Dual-Color Pixel with Subwavelength Resolution," *Nano Letters*, vol. 17, pp. 7500-7506, 2017. <https://doi.org/10.1021/acs.nanolett.7b03421>
- [220] M. Song, Z. A. Kudyshev, H. Yu, A. Boltasseva, V. M. Shalae, and A. V. Kildishev, "Achieving full-color generation with polarization-tunable perfect light absorption," *Optical Materials Express*, vol. 9, pp. 779-787, 2019. <https://doi.org/10.1364/OME.9.000779>

- [221] X. Wang, D. Xu, B. Jaquet, Y. Yang, J. Wang, H. Huang et al., "Structural Colors by Synergistic Birefringence and Surface Plasmon Resonance," *ACS Nano*, vol. 14, pp. 16832-16839, 2020. <https://doi.org/10.1021/acsnano.0c05599>
- [222] T. Ellenbogen, K. Seo, and K. B. Crozier, "Chromatic Plasmonic Polarizers for Active Visible Color Filtering and Polarimetry," *Nano Letters*, vol. 12, pp. 1026-1031, 2012. <https://doi.org/10.1021/nl204257g>
- [223] Z. Li, A. W. Clark, and J. M. Cooper, "Dual Color Plasmonic Pixels Create a Polarization Controlled Nano Color Palette," *ACS Nano*, vol. 10, pp. 492-498, 2016. <https://doi.org/10.1021/acsnano.5b05411>
- [224] E. Heydari, J. R. Sperling, S. L. Neale, and A. W. Clark, "Plasmonic Color Filters as Dual-State Nanopixels for High-Density Microimage Encoding," *Advanced Functional Materials*, vol. 27, pp. 1701866, 2017. <https://doi.org/https://doi.org/10.1002/adfm.201701866>
- [225] V. Vashistha, G. Vaidya, P. Gruszecki, A. E. Serebryannikov, and M. Krawczyk, "Polarization tunable all-dielectric color filters based on cross-shaped Si nanoantennas," *Scientific Reports*, vol. 7, pp. 8092, 2017. <https://doi.org/10.1038/s41598-017-07986-z>
- [226] X. M. Goh, Y. Zheng, S. J. Tan, L. Zhang, K. Kumar, C.-W. Qiu et al., "Three-dimensional plasmonic stereoscopic prints in full colour," *Nat Commun*, vol. 5, pp. 2014. <https://doi.org/10.1038/ncomms6361>
- [227] B. Yang, W. Liu, Z. Li, H. Cheng, S. Chen, and J. Tian, "Polarization-Sensitive Structural Colors with Hue-and-Saturation Tuning Based on All-Dielectric Nanopixels," *Advanced Optical Materials*, vol. 6, pp. 1701009, 2018. <https://doi.org/https://doi.org/10.1002/adom.201701009>
- [228] "Optical Encryption and Decryption," in *Generalized Phase Contrast* J. Glückstad, and D. Palima, Eds., pp. 273-298, Springer Netherlands, Dordrecht (2009).
- [229] X. Li, R. Zhao, Q. Wei, G. Geng, J. Li, S. Zhang et al., "Code Division Multiplexing Inspired Dynamic Metasurface Holography," *Advanced Functional Materials*, vol. 31, pp. 2103326, 2021. <https://doi.org/https://doi.org/10.1002/adfm.202103326>
- [230] P. Georgi, Q. Wei, B. Sain, C. Schlickriede, Y. Wang, L. Huang et al., "Optical secret sharing with cascaded metasurface holography," *Science Advances*, vol. 7, pp. eabf9718, 2021. <https://doi.org/10.1126/sciadv.abf9718>
- [231] H. Ren, X. Fang, J. Jang, J. Bürger, J. Rho, and S. A. Maier, "Complex-amplitude metasurface-based orbital angular momentum holography in momentum space," *Nature Nanotechnology*, vol. 15, pp. 948-955, 2020. <https://doi.org/10.1038/s41565-020-0768-4>
- [232] Z. Li, C. Chen, Z. Guan, J. Tao, S. Chang, Q. Dai et al., "Three-Channel Metasurfaces for Simultaneous Meta-Holography and Meta-Nanoprinting: A Single-Cell Design Approach," *Laser & Photonics Reviews*, vol. 14, pp. 2000032, 2020. <https://doi.org/https://doi.org/10.1002/lpor.202000032>
- [233] C. Liang, L. Deng, Q. Dai, Z. Li, G. Zheng, Z. Guan et al., "Single-celled multifunctional metasurfaces merging structural-color nanoprinting and holography," *Optics Express*, vol. 29, pp. 10737-10748, 2021. <https://doi.org/10.1364/OE.420831>
- [234] Q. Dai, Z. Guan, S. Chang, L. Deng, J. Tao, Z. Li et al., "A Single-Celled Tri-Functional Metasurface Enabled with Triple Manipulations of Light," *Advanced Functional Materials*, vol. 30, pp. 2003990, 2020. <https://doi.org/https://doi.org/10.1002/adfm.202003990>
- [235] F. Ding, B. Chang, Q. Wei, L. Huang, X. Guan, and S. I. Bozhevolnyi, "Versatile Polarization Generation and Manipulation Using Dielectric Metasurfaces," *Laser & Photonics Reviews*, vol. 14, pp. 2000116, 2020. <https://doi.org/https://doi.org/10.1002/lpor.202000116>
- [236] M. Liu, P. Huo, W. Zhu, C. Zhang, S. Zhang, M. Song et al., "Broadband generation of perfect Poincaré beams via dielectric spin-multiplexed metasurface," *Nat. Commun.*, vol. 12, pp. 2230, 2021. <https://doi.org/10.1038/s41467-021-22462-z>
- [237] A. C. Overvig, S. Shrestha, S. C. Malek, M. Lu, A. Stein, C. Zheng et al., "Dielectric metasurfaces for complete and independent control of the optical amplitude and phase," *Light: Science & Applications*, vol. 8, pp. 92, 2019. <https://doi.org/10.1038/s41377-019-0201-7>
- [238] X. Guo, J. Zhong, B. Li, S. Qi, Y. Li, P. Li et al., "Full-Color Holographic Display and Encryption with Full-Polarization Degree of Freedom," *Advanced Materials*, vol. 34, pp. 2103192, 2022. <https://doi.org/https://doi.org/10.1002/adma.202103192>
- [239] M. Abdolahi, H. Jiang, and B. Kaminska, "Structural colour QR codes for multichannel information storage with enhanced optical security and life expectancy," *Nanotechnology*, vol. 30, pp. 405301, 2019. <https://doi.org/10.1088/1361-6528/ab2d3b>
- [240] X. Luo, Y. Hu, X. Li, Y. Jiang, Y. Wang, P. Dai et al., "Integrated Metasurfaces with Microprints and Helicity-Multiplexed Holograms for Real-Time Optical Encryption," *Advanced Optical Materials*, vol. 8, pp. 1902020, 2020. <https://doi.org/https://doi.org/10.1002/adom.201902020>
- [241] I. Kim, J. Jang, G. Kim, J. Lee, T. Badloe, J. Mun et al., "Pixelated bifunctional metasurface-driven dynamic vectorial holographic color prints for photonic security platform," *Nat. Commun.*, vol. 12, pp. 3614, 2021. <https://doi.org/10.1038/s41467-021-23814-5>
- [242] Z. Li, R. Ren, J. Deng, L. Deng, G. Li, and G. Zheng, "Non-orthogonal-polarization multiplexed metasurfaces for tri-channel gray-imaging," *Opt Express*, vol. 29, pp. 134-144, 2021. <https://doi.org/10.1364/oe.415403>
- [243] R. Ren, Z. Li, L. Deng, X. Shan, Q. Dai, Z. Guan et al., "Non-orthogonal polarization multiplexed metasurfaces for tri-channel polychromatic image displays and information encryption," *Nanophotonics*, vol. pp. 2021. <https://doi.org/doi:10.1515/nanoph-2021-0259>
- [244] F. J. G. de Abajo, "Colloquium: Light scattering by particle and hole arrays," *Reviews of Modern Physics*, vol. 79, pp. 1267-1224, 2007. <http://link.aps.org/abstract/RMP/v79/p1267>
- [245] M. Hentschel, M. Schäferling, X. Duan, H. Giessen, and N. Liu, "Chiral plasmonics," *Science Advances*, vol. 3, pp. 2017. <https://doi.org/10.1126/sciadv.1602735>

- [246] E. Ashalley, K. Acheampong, L. V. Besteiro, P. Yu, A. Neogi, A. O. Govorov et al., "Multitask deep-learning-based design of chiral plasmonic metamaterials," *Photon. Res.*, vol. 8, pp. 1213-1225, 2020. <https://doi.org/10.1364/PRJ.388253>
- [247] S. Choi, H. Son, and B. Lee, "Chirality-selective all-dielectric metasurface structural color display," *Optics Express*, vol. 29, pp. 41258-41267, 2021. <https://doi.org/10.1364/OE.445866>
- [248] E. S. A. Goerlitz, A. S. Puri, J. J. Moses, L. V. Poulikakos, and N. Vogel, "The Beginner's Guide to Chiral Plasmonics: Mostly Harmless Theory and the Design of Large-Area Substrates," *Advanced Optical Materials*, vol. 9, pp. 2021. <https://doi.org/10.1002/adom.202100378>
- [249] P. R. West, S. Ishii, G. V. Naik, N. K. Emani, V. M. Shalae, and A. Boltasseva, "Searching for better plasmonic materials," *Laser & Photonics Reviews*, vol. 4, pp. 795-808, 2010. <https://doi.org/10.1002/lpor.200900055>
- [250] S. Westland, and C. Ripamonti, "Computational colour science using MATLAB," Hoboken, N.J., John Wiley, 2004.
- [251] H. J. Park, K. B. Kim, and E. Y. Cha, "An Effective Color Quantization Method Using Octree-Based Self-Organizing Maps," *Comput Intell Neurosci*, vol. 2016, pp. 5302957, 2016. <https://doi.org/10.1155/2016/5302957>
- [252] B. Tice, "The analysis of binary, ternary and quaternary-based systems for communications theory," SPIE, 2008. <https://doi.org/10.1117/12.798510>
- [253] Y. Fan, H. Liang, J. Li, D. P. Tsai, and S. Zhang, "Emerging Trend in Unconventional Metasurfaces: From Nonlinear, Non-Hermitian to Nonclassical Metasurfaces," *ACS Photonics*, vol. 9, pp. 2872-2890, 2022. <https://doi.org/10.1021/acsp Photonics.2c00816>
- [254] A.-P. Blanchard-Dionne, and O. J. F. Martin, "Teaching optics to a machine learning network," *Optics Letters*, vol. 45, pp. 2922-2925, 2020. <https://doi.org/10.1364/OL.390600>
- [255] M. K. Chen, X. Liu, Y. Sun, and D. P. Tsai, "Artificial Intelligence in Meta-optics," *Chemical Reviews*, vol. 122, pp. 15356-15413, 2022. <https://doi.org/10.1021/acs.chemrev.2c00012>
- [256] J. Fang, A. Swain, R. Unni, and Y. Zheng, "Decoding Optical Data with Machine Learning," *Laser & Photonics Reviews*, vol. 15, pp. 2000422, 2021. <https://doi.org/https://doi.org/10.1002/lpor.202000422>
- [257] C. Qian, B. Zheng, Y. Shen, L. Jing, E. Li, L. Shen et al., "Deep-learning-enabled self-adaptive microwave cloak without human intervention," *Nature Photonics*, vol. 14, pp. 383-390, 2020. <https://doi.org/10.1038/s41566-020-0604-2>
- [258] W. Ma, Z. Liu, Z. A. Kudyshev, A. Boltasseva, W. Cai, and Y. Liu, "Deep learning for the design of photonic structures," *Nature Photonics*, vol. 15, pp. 77-90, 2021. <https://doi.org/10.1038/s41566-020-0685-y>
- [259] Z. Liu, D. Zhu, L. Raju, and W. Cai, "Tackling Photonic Inverse Design with Machine Learning," *Advanced Science*, vol. 8, pp. 2002923, 2021. <https://doi.org/https://doi.org/10.1002/adv.202002923>
- [260] O. Khatib, S. Ren, J. Malof, and W. J. Padilla, "Deep Learning the Electromagnetic Properties of Metamaterials—A Comprehensive Review," *Advanced Functional Materials*, vol. 31, pp. 2101748, 2021. <https://doi.org/https://doi.org/10.1002/adfm.202101748>
- [261] J. Jiang, M. Chen, and J. A. Fan, "Deep neural networks for the evaluation and design of photonic devices," *Nature Reviews Materials*, vol. 6, pp. 679-700, 2021. <https://doi.org/10.1038/s41578-020-00260-1>
- [262] Z. Li, R. Pestourie, Z. Lin, S. G. Johnson, and F. Capasso, "Empowering Metasurfaces with Inverse Design: Principles and Applications," *ACS Photonics*, vol. pp. 2022. <https://doi.org/10.1021/acsp Photonics.1c01850>
- [263] S. Molesky, Z. Lin, A. Y. Piggott, W. Jin, J. Vucković, and A. W. Rodriguez, "Inverse design in nanophotonics," *Nature Photonics*, vol. 12, pp. 659-670, 2018. <https://doi.org/10.1038/s41566-018-0246-9>
- [264] M. Pan, Y. Fu, M. Zheng, H. Chen, Y. Zang, H. Duan et al., "Dielectric metalens for miniaturized imaging systems: progress and challenges," *Light: Science & Applications*, vol. 11, pp. 195, 2022. <https://doi.org/10.1038/s41377-022-00885-7>
- [265] D. Z. Zhu, E. B. Whiting, S. D. Campbell, D. B. Burckel, and D. H. Werner, "Optimal High Efficiency 3D Plasmonic Metasurface Elements Revealed by Lazy Ants," *ACS Photonics*, vol. 6, pp. 2741-2748, 2019. <https://doi.org/10.1021/acsp Photonics.9b00717>
- [266] S. An, B. Zheng, M. Y. Shalaginov, H. Tang, H. Li, L. Zhou et al., "Deep learning modeling approach for metasurfaces with high degrees of freedom," *Optics Express*, vol. 28, pp. 31932-31942, 2020. <https://doi.org/10.1364/OE.401960>
- [267] X. Han, Z. Fan, Z. Liu, C. Li, and L. J. Guo, "Inverse design of metasurface optical filters using deep neural network with high degrees of freedom," *InfoMat*, vol. 3, pp. 432-442, 2021. <https://doi.org/https://doi.org/10.1002/inf2.12116>
- [268] G. Lévêque, and O. J. F. Martin, "Optimization of finite diffraction gratings for the excitation of surface plasmons," *J. Appl. Phys.*, vol. 100, pp. 124301, 2006.
- [269] E. B. Whiting, S. D. Campbell, L. Kang, and D. H. Werner, "Meta-atom library generation via an efficient multi-objective shape optimization method," *Optics Express*, vol. 28, pp. 24229-24242, 2020. <https://doi.org/10.1364/OE.398332>
- [270] F. Wen, J. Jiang, and J. A. Fan, "Robust Freeform Metasurface Design Based on Progressively Growing Generative Networks," *ACS Photonics*, vol. 7, pp. 2098-2104, 2020. <https://doi.org/10.1021/acsp Photonics.0c00539>
- [271] P. Rai, "Plasmonic noble metal@metal oxide core-shell nanoparticles for dye-sensitized solar cell applications," *Sustainable Energy & Fuels*, vol. 3, pp. 63-91, 2019. <https://doi.org/10.1039/C8SE00336J>
- [272] Z. A. Kudyshev, V. M. Shalae, and A. Boltasseva, "Machine Learning for Integrated Quantum Photonics," *ACS Photonics*, vol. 8, pp. 34-46, 2021. <https://doi.org/10.1021/acsp Photonics.0c00960>
- [273] N. J. Dinsdale, P. R. Wiecha, M. Delaney, J. Reynolds, M. Ebert, I. Zeimpekis et al., "Deep Learning Enabled Design of Complex Transmission Matrices for Universal Optical Components," *ACS Photonics*, vol. 8, pp. 283-295, 2021. <https://doi.org/10.1021/acsp Photonics.0c01481>
- [274] H. Ren, W. Shao, Y. Li, F. Salim, and M. Gu, "Three-dimensional vectorial holography based on machine learning inverse design," *Science Advances*, vol. 6, pp. eaaz4261, 2020. <https://doi.org/doi:10.1126/sciadv.aaz4261>

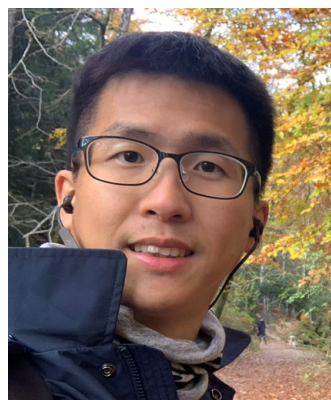
- [275] S. So, and J. Rho, "Designing nanophotonic structures using conditional deep convolutional generative adversarial networks," *Nanophotonics*, vol. 8, pp. 1255-1261, 2019. <https://doi.org/doi:10.1515/nanoph-2019-0117>
- [276] X. Zhu, W. Yan, U. Levy, N. A. Mortensen, and A. Kristensen, "Resonant laser printing of structural colors on high-index dielectric metasurfaces," *Science Advances*, vol. 3, pp. e1602487, 2017. <https://doi.org/doi:10.1126/sciadv.1602487>
- [277] P. Muhlschlegel, H.-J. Eisler, O. J. F. Martin, B. Hecht, and D. W. Pohl, "Resonant optical antennas," *Science*, vol. 308, pp. 1607-1608, 2005.
- [278] L. Novotny, and N. van Hulst, "Antennas for light," *Nat Photon*, vol. 5, pp. 83-90, 2011. <http://dx.doi.org/10.1038/nphoton.2010.237>
- [279] S. A. Maier, M. L. Brongersma, P. G. Kik, S. Meltzer, A. A. G. Requicha, and H. A. Atwater, "Plasmonics—A Route to Nanoscale Optical Devices," *Advanced Materials*, vol. 13, pp. 1501-1505, 2001. [http://dx.doi.org/10.1002/1521-4095\(200110\)13:19<1501::AID-ADMA1501>3.0.CO;2-Z](http://dx.doi.org/10.1002/1521-4095(200110)13:19<1501::AID-ADMA1501>3.0.CO;2-Z)
- [280] S. Viarbitskaya, A. Teulle, R. Marty, J. Sharma, C. Girard, A. Arbouet et al., "Tailoring and imaging the plasmonic local density of states in crystalline nanoprisms," *Nat Mater*, vol. 12, pp. 426-432, 2013. <https://doi.org/10.1038/nmat3581>
- <http://www.nature.com/nmat/journal/v12/n5/abs/nmat3581.html#supplementary-information>
- [281] Y. Wu, J. Xu, E. T. Poh, L. Liang, H. Liu, J. K. W. Yang et al., "Upconversion superburst with sub-2 μ s lifetime," *Nature Nanotechnology*, vol. 14, pp. 1110-1115, 2019. <https://doi.org/10.1038/s41565-019-0560-5>
- [282] R. Esteban, M. Laroche, and J.-J. Greffet, "Influence of metallic nanoparticles on upconversion processes," *Journal of Applied Physics*, vol. 105, pp. 033107, 2009. <https://doi.org/10.1063/1.3075848>
- [283] A. M. Kern, A. J. Meixner, and O. J. F. Martin, "Molecule-Dependent Plasmonic Enhancement of Fluorescence and Raman Scattering near Realistic Nanostructures," *ACS Nano*, vol. 6, pp. 9828-9836, 2012. <https://doi.org/10.1021/nn3033612>
- [284] D. M. Wu, A. García-Etxarri, A. Salleo, and J. A. Dionne, "Plasmon-Enhanced Upconversion," *The Journal of Physical Chemistry Letters*, vol. 5, pp. 4020-4031, 2014. <https://doi.org/10.1021/jz5019042>
- [285] W. Park, D. Lu, and S. Ahn, "Plasmon enhancement of luminescence upconversion," *Chemical Society Reviews*, vol. 44, pp. 2940-2962, 2015. <https://doi.org/10.1039/C5CS00050E>
- [286] J. Dong, W. Gao, Q. Han, Y. Wang, J. Qi, X. Yan et al., "Plasmon-enhanced upconversion photoluminescence: Mechanism and application," *Reviews in Physics*, vol. 4, pp. 100026, 2019. <https://doi.org/https://doi.org/10.1016/j.revip.2018.100026>
- [287] B. Zhou, B. Shi, D. Jin, and X. Liu, "Controlling upconversion nanocrystals for emerging applications," *Nature Nanotechnology*, vol. 10, pp. 924-936, 2015. <https://doi.org/10.1038/nnano.2015.251>
- [288] S. Heer, K. Kömpe, H.-U. Güdel, and M. Haase, "Highly Efficient Multicolour Upconversion Emission in Transparent Colloids of Lanthanide-Doped NaYF₄ Nanocrystals," *Advanced Materials*, vol. 16, pp. 2102-2105, 2004. <https://doi.org/https://doi.org/10.1002/adma.200400772>
- [289] F. Wang, R. Deng, J. Wang, Q. Wang, Y. Han, H. Zhu et al., "Tuning upconversion through energy migration in core-shell nanoparticles," *Nature Materials*, vol. 10, pp. 968-973, 2011. <https://doi.org/10.1038/nmat3149>
- [290] S. Wen, J. Zhou, K. Zheng, A. Bednarkiewicz, X. Liu, and D. Jin, "Advances in highly doped upconversion nanoparticles," *Nat. Commun.*, vol. 9, pp. 2415, 2018. <https://doi.org/10.1038/s41467-018-04813-5>
- [291] Y. Liu, Y. Lu, X. Yang, X. Zheng, S. Wen, F. Wang et al., "Amplified stimulated emission in upconversion nanoparticles for super-resolution nanoscopy," *Nature*, vol. 543, pp. 229-233, 2017. <https://doi.org/10.1038/nature21366>
- [292] Q. Liu, Y. Zhang, C. S. Peng, T. Yang, L.-M. Joubert, and S. Chu, "Single upconversion nanoparticle imaging at sub-10 W cm⁻² irradiance," *Nature Photonics*, vol. 12, pp. 548-553, 2018. <https://doi.org/10.1038/s41566-018-0217-1>
- [293] A. Fernandez-Bravo, K. Yao, E. S. Barnard, N. J. Borys, E. S. Levy, B. Tian et al., "Continuous-wave upconverting nanoparticle microlasers," *Nature Nanotechnology*, vol. 13, pp. 572-577, 2018. <https://doi.org/10.1038/s41565-018-0161-8>
- [294] B. Tian, A. Fernandez-Bravo, H. Najafabadi, N. A. Torquato, M. V. P. Altoe, A. Teitelboim et al., "Low irradiance multiphoton imaging with alloyed lanthanide nanocrystals," *Nat. Commun.*, vol. 9, pp. 3082, 2018. <https://doi.org/10.1038/s41467-018-05577-8>
- [295] D. J. Garfield, N. J. Borys, S. M. Hamed, N. A. Torquato, C. A. Tajon, B. Tian et al., "Enrichment of molecular antenna triplets amplifies upconverting nanoparticle emission," *Nature Photonics*, vol. 12, pp. 402-407, 2018. <https://doi.org/10.1038/s41566-018-0156-x>
- [296] J. Zhou, S. Wen, J. Liao, C. Clarke, S. A. Tawfik, W. Ren et al., "Activation of the surface dark-layer to enhance upconversion in a thermal field," *Nature Photonics*, vol. 12, pp. 154-158, 2018. <https://doi.org/10.1038/s41566-018-0108-5>
- [297] A. Fernandez-Bravo, D. Wang, E. S. Barnard, A. Teitelboim, C. Tajon, J. Guan et al., "Ultralow-threshold, continuous-wave upconverting lasing from subwavelength plasmons," *Nature Materials*, vol. 18, pp. 1172-1176, 2019. <https://doi.org/10.1038/s41563-019-0482-5>
- [298] A. Das, C. Mao, S. Cho, K. Kim, and W. Park, "Over 1000-fold enhancement of upconversion luminescence using water-dispersible metal-insulator-metal nanostructures," *Nat. Commun.*, vol. 9, pp. 4828, 2018. <https://doi.org/10.1038/s41467-018-07284-w>
- [299] O. J. F. Martin, C. Girard, D. R. Smith, and S. Schultz, "Generalized field propagator for arbitrary finite-size photonic band gap structures," *Physical Review Letters*, vol. 82, pp. 315-318, 1999. <https://doi.org/10.1103/PhysRevLett.82.315>
- [300] H. Fischer, and O. J. F. Martin, "Engineering the optical response of plasmonic nanoantennas," *Optics Express*, vol. 16, pp. 9144-9154, 2008. <https://doi.org/10.1364/OE.16.009144>
- [301] A. M. Kern, and O. J. F. Martin, "Strong enhancement of forbidden atomic transitions using plasmonic nanostructures," *Physical Review A*, vol. 85, pp. 022501, 2012. <https://doi.org/10.1103/PhysRevA.85.022501>

- [302] C. Girard, O. J. F. Martin, G. Lévêque, G. C. des Francs, and A. Dereux, "Generalized bloch equations for optical interactions in confined geometries," *Chemical Physics Letters*, vol. 404, pp. 44-48, 2005.
<https://doi.org/https://doi.org/10.1016/j.cplett.2005.01.059>

Curriculum Vitae

Personal Information

Name Hsiang-Chu Wang
Address Av. de Préfaully 4
1022 Chavanne-Prés-Renens
Switzerland
Mobile +41 78 745 0800
Email hsiang-chu.wang@epfl.ch
Date (Place) of Birth 26.12.1989 (Changhua, Taiwan)
Citizenship Taiwan



Education

2017/09 – to date Ph.D., École Polytechnique Fédérale de Lausanne (EPFL), Switzerland
2015/10 – 2017/08 Research assistant, Academia Sinica, Taiwan
2012/09 – 2014/08 Master of Photonics and Optoelectronics, National Taiwan University, Taiwan
2008/09 – 2012/06 Bachelor of Physics, National Tsing-Hua University, Taiwan

Experiences

Ph.D. Project, EPFL, Supervisor: Prof. O. Martin -----2017/09 till now
✓ Design, simulation, fabrication, and measurement of plasmonic metasurfaces for applications in nearfield enhancement, wavefront manipulation, and spectral manipulation.
✓ Construction of a Fourier imaging microscope for optical characterizations.
✓ Scientific performance in peer-reviewed journals and international conferences.
Research assistant, Academia Sinica, Supervisor: Prof. D. P. Tsai-----2015/10-2017/08
✓ Research in ultrathin planar cavity effect for color printing and wavefront manipulation.
✓ Research in phase change materials for reconfigurable metasurfaces.
✓ Attending international conferences.
M. Sc. Project, National Taiwan University, Supervisor: Prof. S. Tseng-----2012/09-2014/08
✓ Development of Finite-Difference Time-Domain method with MATLAB to calculate the refractive index information from Optical Coherent Tomography (OCT) raw data.

Publications

- **H.-C. Wang**, K. Achouri, and O.J.F. Martin, "Robustness Analysis of Metasurfaces: Perfect Structures Are Not Always the Best" *ACS Photonics* (2022).
- D. Ray, **H.-C. Wang**, J. Kim, Ch. Santschi, and O.J.F. Martin, "A Low-Temperature Annealing Method for Alloy Nanostructures and Metasurfaces: Unlocking a Novel Degree of Freedom" *Advanced Materials* (2022).
- H.S.C. Yu, A. Conde-Rubio, **H.-C. Wang**, O.J.F. Martin, G. Boero, and J. Brugger, "Precise Capillary-Assisted Nanoparticle Assembly in Reusable Templates" *Particle and Particle System Characterization* (2022)

- K. Achouri, **H.-C. Wang**, and O.J.F. Martin, "Optical force control using phase-gradient metasurfaces" *Proc. Metamaterials* (2018)
- **H.-C. Wang**, C.H. Chu, P. C. Wu, H.-H. Hsiao, H. J. Wu, J.-W. Chen, W. H. Lee, Y.-C. Lai, Y.-W. Huang, M. L. Tseng, S.-W. Chang, and D. P. Tsai, "Ultrathin Planar Cavity Metasurfaces" *Small* (2018)
- C. H. Chu, M. L. Tseng, J. Chen, P. C. Wu, Y.-H. Chen, **H.-C. Wang**, T.-Y. Chen, W. T. Hsien, H. J. Wu, G. Sun, D. P. Tsai, "Active dielectric metasurface based on phase-change medium" *Laser & Photonics Reviews* (2016)
- S. H. Tseng, W.-L. Ting, **S.-J. Wang**, "2-D PSTD Simulation of the time-reversed ultrasound-encoded deep-tissue imaging technique" *Biomed. Opt. Express* (2014)

Conferences

- **Oral presentation:** "Perfect gradient metasurfaces are not the most efficient", Materials research society spring meeting 2021 (MRS2021), Online, April 17-23, 2021.
- **Oral presentation:** "Hologram generated by alloy metasurfaces", Near-Field Optics 16 online event (NFO16), Online, August 17-21, 2020.
- **Oral presentation:** "Robustness analysis of metasurfaces", Near-Field Optics 16 online event (NFO16), Online, August 17-21, 2020.
- **Oral presentation (Award):** "Plasmonic enhanced frequency upconversion luminescence", Photonics Day, Neuchatel Switzerland, December 6, 2019.
- **Poster:** "Tailoring Upconversion Luminescence with Multi-resonant Antennas", Surface plasmon photonics 9 (SPP9), Copenhagen Denmark, May 26-31, 2019.
- **Poster:** "Upconversion Luminescence Enhanced by Optical Antennas", The 15th International Conference of Near-field Optics and Nanophotonics (NFO15), Troy, France, August 26-31, 2018.
- **Poster:** "Upconversion Luminescence Enhanced by Optical Antennas", Plasmonics and Nanophotonics Gordon Research Conference (GRC), Boston, U.S., July 8-13, 2018.
- **Poster:** "Ultrathin interference cavity for metasurfaces", Surface plasmon photonics 8 (SPP8), Taipei Taiwan, May 22-26, 2017.
- **Poster (Award):** "Visible Light Scattering by Ge₂Sb₂Te₅ Dots", European symposium on Phase-Change and Ovonic Sciences 2016 (EPCOS2016), Cambridge, U.K, 2016
- **Poster:** "Resonant Light Scattering of Ge₂Sb₂Te₅ Dots Fabricated by Laser-induced Forward Transfer", International Symposium on Optical Memory 2016 (ISOM2016), Kyoto, Japan, 2016

Skills

- **Language:** English (Fluent), Chinese (Native), French (Beginner).
- **Engineering:** MATLAB (Programming & Simulink), COMSOL Multiphysics, CST studio, L-edit, Lumerical, Blender.
- **Nanofabrication:** Electron beam lithography, photolithography, thermal evaporation, wet etching, dry etching, scanning electron microscope.